

EXPLICIT SIMULATION OF ICE PARTICLE HABITS IN A
NUMERICAL WEATHER PREDICTION MODEL

by

Tempei Hashino

A dissertation submitted in partial fulfillment of
the requirements for the degree of

Doctor of Philosophy

(Atmospheric and Oceanic Sciences)

At the

UNIVERSITY OF WISCONSIN-MADISON

2007

ABSTRACT

This study develops a scheme for explicit simulation of ice particle habits in Cloud Resolving Models (CRMs), and investigates sensitivity of microphysical processes and distributions of ice particles to habits. The scheme is called Spectral Ice Habit Prediction System (SHIPS), which represents a continuous-property approach to microphysics simulation as opposed to a discrete-property approach such as bulk microphysical parameterization. The characteristics of ice particles are diagnosed based on a series of particle property variables (PPVs) that reflect history of microphysical processes and the mixing between mass bins and air parcels in space.

SHIPS was installed into a CRM, the University of Wisconsin Nonhydrostatic Modeling System (UW-NMS). Two dimensional idealized simulations were employed to simulate a winter orographic storm observed during the IMPROVE-2 campaign. First, ice nucleation and vapor deposition processes with hexagonal monocrystals were tested. The simulations showed that the dynamic advection and sedimentation of ice crystals are keys to produce wide dendritic growth region and capped columns. Comparison of a simulation with columnar growth mode ($T < -20^{\circ}\text{C}$) to aircraft observations cast doubt on the role of the growth mode traditionally thought to be dominant in literature.

Secondly, the vapor deposition process was extended to predict growth of polycrystals with use of a habit frequency data constructed in the laboratory. The simulations with only monocrystals and with monocrystals and polycrystals showed distinct differences in habit distribution due to the nucleated habits at each level and due to sedimentation from upper levels

to lower levels. Sedimentation of the polycrystals from upper levels can be significant and grow dendritic arms on them, which may be considered to spatial dendrites. The immersion (homogeneous) freezing process appeared to be a key process to create planar (columnar and irregular) polycrystals due to the defined frequency map in the temperature, high concentration of available supercooled liquid hydrometeors relative to ice nuclei concentration and the freezing rate. The habit frequencies simulated with the habit frequency dataset showed characteristics similar to observations in stratiform clouds, wave and cirrus clouds.

This study developed a habit-dependent stochastic collection model with use of PPVs. Box simulations with SHIPS showed relationships between mass and dimension, mass and terminal velocity, and dimension and density predicted with aggregation and riming processes moderately agree with empirical relationships. Evolution of PSDs was shown to depend on habits as well as choice of aggregation efficiency model and initial distribution of ice crystals. The difference in habits led to the difference in collection rate by factor of 10 to 100 at given mass. Then, the aggregation process was investigated for the above orographic storm with simulation starting without initial distribution of ice particles. Formation of spatial dendrites was modeled through sedimentation of irregular polycrystals into dendritic zone, and it triggered aggregation by combination of the modeled efficiency and their high concentration produced by immersion freezing nucleation. From ice nucleation processes, SHIPS was able to reproduce sub-exponential particle size distribution (PSD) that consists of pristine crystals and aggregates.

Five more simulations were implemented with all microphysical processes on in order to study effects of aggregation and riming on habit frequency at a given temperature range. In

$T > -10^{\circ}\text{C}$, faster sedimentation of aggregates of plates may have resulted in the increase of frequency of plates. The cases with small IN concentration had high frequency of columnar crystals because active riming process triggered active secondary nucleation process in the temperature. SHIPS showed a dependence of simulated mass content of aggregates on the habits produced by freezing nucleation processes. The average PSDs obtained in the wave cloud section had multiple modes that were similar to typically observed. The inflection points of the PSDs were associated with change of dominant type of ice particles from pristine crystals to aggregates.

Finally, simulations with all microphysical processes were started from initial and boundary condition of ice particles to mimic observed altostratus clouds associated with upper level fronts. A budget analysis of concentration tendency showed that aggregation efficiency can in fact control the evolution of PSD and sedimentation of large particles has a significant effect as well. SHIPS suggests that the observed increase in concentration of small particles with decrease of height is caused by the active nucleation above, sedimentation flux convergence of the particles, and somewhat inefficient aggregation process to remove the small particles. The stochastic collection approach was able to predict relationships among temperature and parameters of PSDs that are consistent with those generally observed in stratiform cloud layers. Uncertainties associated with aggregation efficiency model, habit prediction, and IN concentration were shown to modulate spatial distribution of accumulated precipitation to the same degree.

ACKNOWLEDGEMENT

First, I wish to thank my adviser, Prof. Greg Tripoli for his continuous advice, and constructive critique. His patience and encouragement made this research possible. He gave me a chance to start research in the field of meteorology even though I had engineering background. I would like to thank my other committee members. Prof. Pao Wang has always given me sound advice and insights on research as well as on career. Prof. Grant Petty, Prof. Ralf Bennartz and Prof. Susan Coppersmith have provided me with refreshing insights and discussions from different view points.

I would also like to thank Prof. Allen Bradley, my adviser for master program at the University of Iowa. He recommended me to come here and made it possible for me to learn meteorology in the first year of stay.

I wish to thank my fellow graduate students for friendships and open discussion on weather, culture, politics, and so on.

Thanks are due to my parents. Without their mental and financial support, studying abroad was not possible from the very beginning. To my wife, Noriko, thank you for helping me go through the hardest part of my life.

This research was supported by NASA under the following grants: NNG04GA36G and NNX07AD43G. This support is greatly acknowledged.

TABLE OF CONTENT

ABSTRACT	i
ACKNOWLEDGEMENT.....	iv
LIST OF FIGURES	ix
LIST OF TABLES.....	xvii
Chapter 1 Introduction.....	1
1.1 Studying snow and motivation	1
1.2 Challenge in modeling ice microphysics.....	3
References, Chapter 1	6
Chapter 2 Model description and simulation of vapor deposition process.....	7
2.1 Introduction.....	7
2.2 Spectral Habit Ice Prediction System (SHIPS).....	10
2.2.1 Hybrid bin method.....	11
2.2.2 Particle property variables (PPVs).....	14
2.2.2.1 MASS CONTENT COMPONENTS.....	14
2.2.2.2 LENGTH VARIABLE COMPONENTS	15
2.2.2.3 VOLUME VARIABLE COMPONENTS.....	17
2.2.2.4 AEROSOL MASS CONTENT COMPONENTS	18
2.2.3 Diagnosis of habit and type	19
2.2.4 Outputs and possible applications	20
2.3 Applying hybrid-bin method to the Eulerian dynamics framework.....	21
2.3.1 Continuity equation	21
2.3.2 Weighted terminal velocity and sedimentation	24
2.4 Modeling dependence of depositional growth and terminal velocity on ice crystal habits	26
2.4.1 Vapor deposition process.....	26
2.4.2 Terminal velocity.....	29
2.5 Model setup and experiment design	30

2.5.1 Dynamics	31
2.5.2 Microphysics.....	32
2.5.3 Initial conditions	33
2.5.4 Experiment design	34
2.6 Results.....	35
2.6.1 Vapor deposition process and advection	35
2.6.2 Sensitivity of upper level growth mode.....	38
2.7 Conclusions.....	42
Appendix A Mixing PPVs between bins and grid cells	46
A.1 Length variable components.....	46
A.2 Volume variable components	49
Appendix B Description of microphysical process models.....	49
B.1 Aerosol microphysics (APS).....	50
B.2 Liquid-phase microphysics (SLIPS)	50
B.3 Ice-phase microphysics (SHIPS)	51
B.3.1 ICE NUCLEATION	51
B.3.2 MELTING-SHEDDING PROCESS.....	54
Appendix C List of Symbols	56
References, Chapter 2.....	61
Chapter 3 Simulation of nucleation and depositional growth of polycrystals.....	86
3.1 Introduction.....	86
3.2 Framework to simulate polycrystals with SHIPS.....	89
3.2.1 Brief description of SHIPS	89
3.2.2 Habit diagram and frequency.....	90
3.2.3 Prognostic variables and diagnosis.....	91
3.2.4 Growth rate calculation.....	93
3.2.5 Bin shifting of polycrystal variables.....	95
3.2.6 Terminal velocity.....	96
3.3 Model setup and experiment design	96

3.4 Results.....	98
3.4.1 Habit distributions with and without polycrystals	98
3.4.2 Effect of formation of polycrystals through freezing	101
3.4.3 Effect of ice nucleation concentration	106
3.5 Discussions	107
3.6 Conclusions.....	110
References, Chapter 3	113
Chapter 4 Description and box model simulations of habit-dependence aggregation and riming process	138
4.1 Introduction.....	138
4.2 Modeling aggregation and riming processes with SHIPS	140
4.2.1 SHIPS and quasi-stochastic collection equation.....	140
4.2.2 Diagnosis of semi-axis lengths, aspect ratio, and porosity	142
4.2.3 Aggregation process	143
4.2.3.1 EFFICIENCY	143
4.2.3.2 GROWTH OF PPVs.....	145
4.2.4 Riming process	148
4.2.4.1 EFFICIENCY	148
4.2.4.2 GROWTH OF PPVs.....	149
4.2.5 Hydrodynamic breakup	149
4.3 Box model simulations	150
4.3.1 Aggregation process	151
4.3.2 Riming process	158
4.3.3 Effect of implicit mass sorting assumption	160
4.4 Summary and conclusions	161
Appendix D Description of microphysical process models	164
D.1 Surface temperature diagnosis	164
D.2 Melting and shedding process.....	165
D.3 Secondary nucleation process.....	166
References, Chapter 4.....	168

Chapter 5 Aggregation process and explicit prediction of ice crystal habits in a two dimensional orographic storm.....	190
5.1 Introduction.....	190
5.2 Model setup and experiment design	192
5.2.1 Case study and model set up.....	192
5.2.2 Experiment design	193
5.3 Eulerian simulation without initial ice distribution	195
5.3.1 Aggregation initiation and ice nuclei concentration.....	195
5.3.2 Aggregation initiation and habit dependency.....	200
5.3.3 Evolution of particle size distribution from ice nucleation process	202
5.3.4 Habit frequency analysis.....	205
5.4 Eulerian simulations with initial ice distribution.....	209
5.4.1 Comparison of simulated bulk property	209
5.4.2 Comparison of simulated particle size distribution	212
5.4.3 Comparison of PSDs with observation.....	216
5.4.4 Trajectory analysis.....	218
5.4.5 Effect of aggregation efficiency, prediction of length, and IN concentration on precipitation	222
5.5 Summary and conclusions	225
References, Chapter 5	231
Chapter 6 Conclusions and future works.....	280
6.1 Concept of SHIPS.....	280
6.2 Importance of advection and sedimentation in habit prediction.....	281
6.3 Aggregation and riming process with explicit habit prediction.....	284
6.4 Remarks and future study	289
References, Chapter 6.....	294

LIST OF FIGURES

- Figure 2.1 Schematic of SHIPS. In this example, the mass spectrum of ice particles is divided into five mass bins. The mass content M of each bin consists of four mass content components, M_I , M_A , M_R , and M_W , shown by the square boxes with BIN number above the mass spectrum. From the mass content components, one can diagnose the type of solid hydrometeor for a bin. The largest bin may be diagnosed as graupel because of the dominant rime mass component. The variables in the top two boxes are prognostic variables. Length variable components are used to diagnose the geometry of an ice crystal or habit in an ice particle. Volume variable component is used to diagnose the density and maximum dimension of ice particles. Aerosol mass content components gives solubility of aerosols within an ice particle. Two moments of sub-distribution, concentration N and mass content M %define the sub distribution within a bin. 65
- Figure 2.2 Diagnosis of habit of the representative hydrometeor for a bin. (a) is the dimension of the hexagonal crystal model, and (b) is the diagnosis flow chart..... 66
- Figure 2.3 Diagnosis of type of the representative hydrometeor for a bin. F is set to 0.1 for this study..... 67
- Figure 2.4 Example of terminal velocity that is a continuous function of axis ratios $\phi = c/a$ and $\varphi = d/a$ with use of the hexagonal crystal model. The mass of the crystal used for the calculation has the mass of the hexagonal crystal model with a-axis length $50 \mu\text{m}$ and axis ratio $\phi = 1.0$. The unit of velocity is cm s^{-1} 68
- Figure 2.5 Quasi-steady state after 12 hours of run only with liquid species. Vertical motion (m s^{-1}) and potential temperature (K) are shown in the panel (a). Dark (light) thin line is upward (downward) vertical motion. The contours are given at 0.5, 1, 3, 5 and -0.5, -1, -3, -5. Temperature is shown in the panel (b). Supersaturations over ice and water are shown in the panel (c). Light (dark) thin line is supersaturation over water (ice) with contours of -10 and 0 % (0 to 50 %) by 10 % increment. 69
- Figure 2.6 Horizontally averaged axis lengths of ice crystals at 20 minutes of vapor deposition simulation without advection and sedimentation (EXP1). “Mean” is the horizontally averaged value, “SD” is the standard deviation, and “Max” is the maximum value. 70
- Figure 2.7 Lagrangian simulation of a-axis and c-axis length under water saturation. Time is 1, 5, 10, 15, and 20 minutes from the left, and circle and cross are observation by Takahashi et al.(1991). 71
- Figure 2.8 Comparison of average axis lengths at 20 minutes of vapor deposition simulation with advection and sedimentation (EXP2). The length is given in logarithm of cm..... 72
- Figure 2.9 Comparison of concentrations at 20 minutes of vapor deposition simulation with advection and sedimentation (EXP2). The concentration is given in logarithm of L^{-1} 73

- Figure 2.10 Comparison of average axis ratios at 20 minutes of vapor deposition simulation with advection and sedimentation (EXP2). The left-hand side shows logarithm of $\phi = c/a$ and the right-hand side $\varphi = d/a$ 74
- Figure 2.11 Comparison of (a) concentration of ice crystals ($\log_{10}(L^{-1})$) and (b) concentration tendency by all the ice nucleation processes ($\log_{10}(L^{-1} s^{-1})$) after 90 minutes of vapor deposition simulation (EXP2)..... 75
- Figure 2.12 Comparison of mass contents for diagnosed habits after 90 minutes of vapor deposition simulation (EXP2). The dots contours are 0.01, and 0.05 ($g m^{-3}$) and the solid contours 0.1, 0.2, and 0.3 ($g m^{-3}$)..... 76
- Figure 2.13 Inherent growth ratio. Solid line is Chen and Lamb (1994b), broken line is our parameterization to obtain convergence solution with smaller time step, and thin broken line is defined for sensitivity test EXP3. 77
- Figure 2.14 Same as Figure 12 except that this is a vapor deposition simulation with plate growth at upper level (EXP3)..... 78
- Figure 2.15 Mass spectra of solid hydrometeors at horizontal distance of 194 km from EXP3. (a) is at altitude of 4.4 km, (b) 4.0 km, and (c) 3.7 km. The linear distribution of a mass bin is indicated with 5 points. The circles indicate plates, the squares broad-branched crystals, the triangles dendrites, the crosses columns, and plus symbols capped columns. 79
- Figure 2.16 Size spectra of solid hydrometeors at horizontal distance of 240 km from EXP3, and at from altitude of (a) 5.8 km to (f) 1.55 km. km. The linear distribution of a mass bin is indicated with 5 points. The circles indicate plates, the squares broad-branched crystals, the triangles dendrites, the crosses columns, and plus symbols capped columns. 80
- Figure 3.1 Habit frequency given temperature T and supersaturation over ice s_i . They were constructed from Bailey and Hallett (2004). (a) plates, (b) columnar crystals, (c) polycrystals, (d) columnar polycrystals and (e) planar polycrystals. The frequency of (d) and (e) is conditional frequency given the occurrence of polycrystals, while the frequencies of (a), (b) and (c) add up to unity. 116
- Figure 3.2 Diagnosis of ice crystal habits including polycrystals. n_{exice} is the number of extra crystalline structure, and a_g and c_g are the coordinates of center of gravity of a polycrystal. “M” indicates monocrystals defined in $n_{exice} < 0.5$. Polycrystals are defined in $n_{exice} \geq 0.5$. “PP” (“CP”) indicates planar (columnar) polycrystals defined by $a_g/a \geq c_g/c + 0.5$ ($c_g/c \geq a_g/a + 0.5$). “IP” indicates irregular polycrystals defined between “PP” and “CP” 117
- Figure 3.3 Conceptual models of center of gravity for polycrystals. (a) is bullet rosette, (b) side plane, (c) assemblage of plates, (d) overlapping parallel plates, (e) crossed plates, and (f) scalelike side plane. 118
- Figure 3.4 Extended inherent growth ratios for columnar and planar growth in $T \leq -20^\circ C$. . 119

- Figure 3.5 Vertical profile of horizontally averaged concentration and axis ratios for each habit at 20 minutes of simulation. The upper figures show results from S-HCH, and the lower from S-PCH. The solid line indicates plates, dashed dendrites, dash-dotted columns, gray solid planar polycrystals, gray dash-dotted columnar polycrystals, and gray dashed irregular polycrystals. 120
- Figure 3.6 Vertical profile of temperature and supersaturation. Solid line in (b) indicates supersaturation over ice averaged only for positive values. Dotted lines indicate one standard deviation added or subtracted from the mean, and dashed line supersaturation over water corresponding to the one over ice. 121
- Figure 3.7 Mass-dimensional and mass-terminal velocity relationships at 20 minutes of simulation for S-HCH. The color points for plates and dendrites indicate axis ratio, $\phi = c/a$; $0.5 < \phi$: blue, $0.1 < \phi \leq 0.5$: cyan, and $0.05 < \phi \leq 0.1$: green. Those for columnar crystals $1 \leq \phi < 5$: blue, $5 \leq \phi < 10$: cyan, $10 \leq \phi < 15$: green, $15 \leq \phi < 20$: yellow, $20 \leq \phi < 25$: magenta, $25 \leq \phi < 30$: red, and $30 \leq \phi$: black. HK87 denotes Heymsfield and Kajikawa (1987), K82 Kajikawa (1982), LH74 Locatelli and Hobbs (1974), MZP90 Mitchell et al. (1990), and M96 Mitchell (1996). “Ag” indicates “aggregates of” the habit. 122
- Figure 3.8 Same as Figure 3.5 except that this is at 60 minutes of simulation. 123
- Figure 3.9 Comparison of mass contents for diagnosed habits after 90 minutes of vapor deposition simulation (S-HCH). The dots contours are 0.01, and 0.05 (g/m^3), and the solid contours 0.1, 0.2, and 0.3 (g/m^3). 124
- Figure 3.10 Comparison of mass contents for diagnosed habits after 90 minutes of vapor deposition simulation (S-PCH). The dots contours are 0.01, and 0.05 (g/m^3), and the solid contours 0.1, 0.2, and 0.3 (g/m^3). 125
- Figure 3.11 Concentration tendency of ice nucleation processes for PCH at 20 minutes; (a) deposition-condensation nucleation, (b) contact freezing nucleation, (c) immersion freezing nucleation (d) homogeneous freezing nucleation and (e) total. 126
- Figure 3.12 Initial mass per a single particle produced by ice nucleation processes for PCH at 20 minutes; (a) deposition-condensation nucleation, (b) contact freezing nucleation, (c) immersion freezing nucleation (d) homogeneous freezing nucleation and (e) total. 127
- Figure 3.13 Concentration for diagnosed habits for PCL at 20 minutes. 128
- Figure 3.14 Concentration for diagnosed habits for PCLH at 20 minutes of simulation. 129
- Figure 3.15 Average particle size distribution (left column) and conditional frequency (right column) of habits in the five temperature ranges for PCL at 90 minutes. Open circles in the left column indicate samples. In the right plates, dendrites, and columns are indicated by circles, asterisks, and squares, respectively. Columnar, planar, and irregular polycrystals are indicated by crosses, triangles, and diamonds, respectively. 130
- Figure 3.16 Same as Figure 3.15 except that this is for PCLH at 90 minutes. 131

- Figure 3.17 Comparison of concentration of supercooled liquid hydrometeors (a) and immersion freezing nucleation rate calculated with Bigg's formula (b) at 20 minutes for PCL. The solid line in (b) indicates the freezing probability of a particle per second. ... 132
- Figure 3.18 Comparison of supersaturation over ice for (a) PCH, and (b) PCL. Color-filled contour indicates supersaturation over ice in %, and the red solid lines temperature in Celsius. PCH and PCHH or PCL and PCLH have similar distributions. 133
- Figure 3.19 Comparison of maximum dimension averaged for each diagnosed habit at 90 minutes for PCH. 134
- Figure 3.20 Same as Figure 3.19 except that this is for PCL. 135
- Figure 4.1 growth model of maximum dimension for colliding two plates. 171
- Figure 4.2 Comparison of mass distributions at 60-minute simulation for six different ice crystal habits, namely sphere (S), dendrites (D), plates (P), columns (C), columnar polycrystals (CP), planar polycrystals (PP), and irregular polycrystals (IP). (a) shows the simulation with unit collection efficiency, (b) with efficiency model P, (c) with efficiency model C, and (d) with efficiency model D. 172
- Figure 4.3 Comparison of (a) collection rate, (b) cross section, (c) terminal velocity difference, and (d) coalescence efficiency with the unit collection efficiency. 173
- Figure 4.4 Evolution of size distribution for plates with unit efficiency. 174
- Figure 4.5 Comparison of (a) collection rate, (b) cross section, (c) terminal velocity difference, and (d) coalescence efficiency with interlocking efficiency model P. 175
- Figure 4.6 Comparison of (a) collection rate, (b) cross section, (c) terminal velocity difference, and (d) coalescence efficiency with interlocking efficiency model C. 176
- Figure 4.7 Comparison of (a) collection rate, (b) cross section, (c) terminal velocity difference, and (d) coalescence efficiency with interlocking efficiency model D. 177
- Figure 4.8 Comparison of simulated mass-dimensional relationship with the efficiency model P at 60 minutes. Cross indicates the initial condition, and circle predicted at 60 minutes. HK87 denotes Heymsfield and Kajikawa (1987), K82 Kajikawa (1982), LH74 Locatelli and Hobbs (1974), MZP90 Mitchell et al. (1990), M96 Mitchell (1996), and HI00 Heymsfield and Iaquinta (2000). "Ag" indicates "aggregates of" the habit. 178
- Figure 4.9 Comparison of simulated mass-terminal velocity relationships with the efficiency model P at 60 minutes. Cross indicates the initial condition, and circle predicted at 60 minutes. The reference that empirical formula was taken from is shown in the caption of Figure 4.8. 179
- Figure 4.10 Comparison of simulated max dimension-density relationships with the efficiency model P at 60 minutes. Cross indicates the initial condition, and circle predicted at 60 minutes. Solid line in the figure is aggregates of planar crystals from Magono and Nakamura (1965), long dashed line is aggregates of planar crystals Kajikawa (1982), short

dashed line is aggregates of rosettes obtained by Heymsfield et al. (2002), and dash-dotted line is aggregates of S1-S3 by Heymsfield et al. (2002).	180
Figure 4.11 Mass densities as a function of maximum radius at 90 minutes of simulation with efficiency model P. Ice sphere is denoted by S, dendrites D, plates P, columns C, columnar polycrystals CP, planar polycrystals PP, and irregular polycrystals IP.....	181
Figure 4.12 Comparison of time series of melt diameter of mean mass for (a) initial distribution with mean radius of 0.01 cm and (b) one of 0.05 cm. The efficiency model is P.....	182
Figure 4.13 Comparison of melt diameter of mean mass with initial distribution of mean radius \bar{r} of 5×10^{-2} cm.	183
Figure 4.14 Same as Figure 8, except that these simulations are with the breakup process. ...	184
Figure 4.15 Comparison of size distribution for efficiency model P with (a) and without (b) breakup scheme.	185
Figure 4.16 Comparison of mass distributions among six habits with aggregation, breakup and riming processes at 60 minutes of simulation.....	186
Figure 4.17 Mass components and diagnosed type of ice particles. (a) is the fraction of the aggregation mass component to the total mass for the representative hydrometeor, (b) the fraction of the rimed mass component, and (c) is the diagnosed type of ice particles. In (c), “1” indicates pristine crystals, “2” rimed crystals, “3” aggregates, “4” rimed aggregates, and “5” graupels.	187
Figure 4.18 Property of ice particles simulated with aggregation, breakup, and riming processes at 60 minutes of simulation. (a) is mass-dimensional relationship, (b) is mass-terminal velocity relationship, and (c) is dimension-density relationship.	188
Figure 5.1 Diagnosed habits of all ice particles for MS1 at 20 minutes.....	233
Figure 5.2 Comparison of concentration of diagnosed pristine crystals and aggregates among difference IN concentrations with constant efficiency of 0.1 at 20 minutes. (a) and (b) are pristine crystals and aggregates for 230 L^{-1} (HS1), (c) and (d) for 10 L^{-1} (MS1), and (e) and (f) for 1 L^{-1} (LS1).....	234
Figure 5.3 Horizontal average of mean (solid line) and standard deviation (dashed line) of terminal velocity and cross section area at each grid cell at 20 minutes.	235
Figure 5.4 Horizontally averaged frequency of habits in terms of cross section area at 20 minutes. Thin solid line indicates plates, thin dashed line dendrites, thin dash-dot line columnar crystals, thick solid line planar polycrystals, thick dash-dot line columnar polycrystals, thick dashed line irregular polycrystals.....	236
Figure 5.5 Same as Figure 3.12 except that this is a simulation at 40 minutes.	237
Figure 5.6 Same as Figure 3.13 except that this is at 40 minutes.....	238
Figure 5.7 Spatial distributions of mean and standard deviation of swiping volume (upper panel) and collection rate (lower panel) for ML1 at 40 minutes.	239

Figure 5.8 Same as Figure 3.12 except that the simulated was implemeted with aggregation efficiency model D and at 20 minutes.	240
Figure 5.9 Same as Figure 3.12 except that the simulation was implemented with aggregation efficiency model D and at 40 minutes.	241
Figure 5.10 Concentration of diagnosed habits only including pristine crystals at 40 minutes of simulation for MD1.	242
Figure 5.11 Concentration of diagnosed habits only including aggregates at 40 minutes of simulation for MD1.	243
Figure 5.12 Axis ratio $\varphi = d / a$ of diagnosed habits including all types of ice particles at 40 minutes of simulation for MD1.	244
Figure 5.13 Comparison of trajectories for MP1. All trajectories started at $y=0.5$ km $z=7$ km by 11 km apart each other and at the initial time. Trajectories were numbered 1 to 10 from left to right. The circles on trajectory #1 and #10 indicate approximate locations of PSDs shown in Figure 5.14 and Figure 5.15. The time interval is 20 minutes.	245
Figure 5.14 Evolution of size distribution along the trajectory #1. Size distribution is shown very 20 minutes starting from 20 minutes of simulation. y and z indicates the middle point of grid cells that the contained the trajectory. Ice crystal habits are indicated with markers; circle markers indicate plates, asterisks dendrites, squares columnar crystals, triangles planar polycrystals, crosses columnar polycrystals, and diamonds irregular polycrystals. Ice particle types are indicated with color; blue is pristine crystals, and green is aggregates. Dashed line (dash-dot line) indicates fitted gamma distribution (exponential distribution) using Heymsfield et al. (2002)'s method.	246
Figure 5.15 Same as Figure 5.14 except for trajectory #10.	247
Figure 5.16 Comparison of PSD (left column), and conditional frequencies of types (middle) and habits (right) given maximum dimension at 40 minutes for MD1. They were obtained for vertically grouped samples in the domain. Circle in PSD shows data points, dashed line fitted gamma distribution, and dash-dot lines exponential distribution. For types, circle indicates pristine crystals, asterisks rimed crystals, squares aggregates, crosses rimed aggregates, and triangles graupels. For habits, circle indicates plates, asterisks dendrites, squares columnar crystals, crosses columnar polycrystals, and triangles planar polycrystals, and diamonds irregular polycrystals.	248
Figure 5.17 Comparison of PSD (left column), and conditional frequencies of types (middle) and habits (right) given maximum dimension at 90 minutes of simulation for PCH. They were obtained by grouping samples in section III ($y>276$ km) and according to the temperature. See caption of Figure 5.16 for description of the notation.	249
Figure 5.18 Same as Figure 5.17 except that this is for PCHH.	250
Figure 5.19 Initial concentration of ice particles for each diagnosed type.	251

Figure 5.20 Comparison of horizontally averaged mass content for (a) LS2, (b) LL2, (c) LP2, (d) LC2, and (e) LD2. Solid line indicates the initial condition, dashed line 10 minutes, dash-dot line 20 minutes, dotted line 40 minutes, and thick solid line 60 minutes. The mass content estimated by Woods et al. (2005) is shown by thick gray line with standard deviation.	252
Figure 5.21 Vertical profile of (a) radar reflectivity, (b) mass content, and (c) precipitation rate at 10 minutes for LD2. Solid line denotes horizontal mean and dashed line indicate one standard deviation added or subtracted from the mean. The thick solid line with error bar shows estimates of Woods et al. (2005).	253
Figure 5.22 Spatial distribution of mass content for each diagnosed type of ice particles for LD2 at 10 minutes. The dotted lines indicate contours of 0.01 and 0.05 gm^{-3} , and the solid lines 0.1, 0.3, and 0.5 gm^{-3}	254
Figure 5.23 Concentration of diagnosed type of ice particles for LD2 at 10 minutes.....	255
Figure 5.24 Concentration of diagnosed habits of all ice particles for LD2 at 10 minutes.....	256
Figure 5.25 Comparison of maximum dimension of horizontally averaged PSD in section I ($0 < y < 200\text{km}$). Solid line indicates the initial condition, dashed line 10, dash-dot line 20, dotted line 40, and thick solid line 60 minutes. The values of each layer were plotted in the middle of the layer.	257
Figure 5.26 Same as Figure 5.25 except that this is for number concentration.....	258
Figure 5.27 Comparison of PSD (left column), and conditional frequencies of types (middle) and habits (right) at the initial time in section I. See Figure 5.16 for description of markers.	259
Figure 5.28 Same as Figure 5.27, but at 10 minutes for LL2.....	260
Figure 5.29 Comparison of particle size distribution (left column), concentration tendency of each microphysical process (middle column), and total microphysical tendency and normalized sedimentation flux (right column) for LL2 at 10 minutes of simulation in section I. Circles in PSDs show sample points, and dashed (dash-dotted) line indicates fitted gamma (exponential) distribution. Crosses (circles) in middle and right columns indicate positive (negative) tendency given maximum dimension. In the middle column, blue indicates vapor deposition, green aggregation, magenta breakup, and red riming process. In the right column, green total microphysical tendency, blue sedimentation flux at the upper boundary of the layer, red sedimentation flux at the lower boundary, and black net tendency.	261
Figure 5.30 Same as Figure 5.27, except that this is for LS2 and at 10 minutes.....	262
Figure 5.31 Same as Figure 5.29 except that this is for LS2.....	263
Figure 5.32 Same as Figure 5.27, but for horizontally averaged PSD in section II ($200 < y < 290\text{km}$) at 10 minutes for LL2.....	264

Figure 5.33 Slope parameter of exponential distribution fitted to horizontally averaged PSD over the entire domain ($0 < y < 290\text{km}$). Solid line indicates the initial condition, dashed line 10, dash-dot line 20, dotted line 40, and thick solid line 60 minutes. The values of each layer were plotted in the middle of the layer.....	265
Figure 5.34 Same as Figure 5.33 except that it is the intercept parameter of exponential distribution.....	266
Figure 5.35 Trajectories for LP2 calculated by using constant vertical velocity of 1 m/s.	267
Figure 5.36 Change of slope parameter with temperature fitted the PSDs on the trajectories starting from the initial time. Thick solid curve shows the parameterized slope parameter by Heymsfield et al. (2002) using PSDs from TRMM campaigns, and dotted curves are those fitted to one standard deviation of the data given temperature. Thick dashed curve indicates Houze et al. (1979)'s formula fitted to PSDs taken from frontal clouds.....	268
Figure 5.37 N_0 vs λ for each trajectory of LD2 every 10 minutes. The number in the plot indicates the temperature in Celsius. The trajectory numbers are given from left to right in Figure 5.35. The dashed line indicate gradient of 2.	269
Figure 5.38 N_0 vs λ for trajectories of all simulations every 10 minutes.	270
Figure 5.39 Trajectories for (a) LS2, (b) LL2, and (c) LD2 calculated by using mass-weighted terminal velocity. The vertical motion at two hours is depicted in the background.....	271
Figure 5.40 Comparison of 6 hour accumulation over the domain.	272

LIST OF TABLES

Table 2.1 Summary of prognostic variables advected in the Eulerian dynamic model, UW-NMS and those advected between the mass bins of SHIPS. The unit of variables in SHIPS is listed in the parenthesis. n is the ice parameter number and b bin number.	83
Table 2.2 Parameters to define mass bins for spectra of liquid and solid hydrometeors. The spectrum of liquid (solid) hydrometeors was divided into 21 (20) mass bins. N Nis the number of bins given to each group. The radii calculated with $\rho_w = 1.0$ (g cm ⁻³) for mass boundaries were shown in parenthesis.	84
Table 2.3 Summary of experiment cases to test SHIPS. All the cases simulate ice nucleation, vapor deposition and melting processes.	85
Table 3.1 List of sensitivity experiments. The experiments with “Form Hex” produce hexagonal monocrystals by immersion and homogeneous freezing process. PCHNI and PCLNI do not simulate immersion and homogeneous freezing process.	136
Table 3.2 Moments of average particle size distribution and concentration frequency of habits for 5 temperature ranges. Concentration (Con), mean maximum dimension (M D) and standard deviation of maximum dimension (SD D) are given in L ⁻¹ , mm, and mm, respectively. P denotes plates, D dendrites, C columnar crystals, CP columnar polycrystals, PP planar polycrystals, and IP irregular polycrystals. The frequency is in percentage (%).	137
Table 4.1 Parameters for initialization of ice crystals in box simulations. Axis ratios of ice crystals are defined as $\phi = c / a$, and $\psi = d / a$. α is the aspect ratio of spheroid fitted to the ice crystal.	189
Table 5.1 Experiment design.	273
Table 5.2 Moments of average particle size distribution and concentration frequency of habits for 5 temperature ranges. Concentration (Con), mean maximum dimension (M D) and standard deviation of maximum dimension (SD D) are given in L ⁻¹ , mm, and mm, respectively. P denotes plates, D dendrites, C columnar crystals, CP columnar polycrystals, PP planar polycrystals, and IP irregular polycrystals. The frequency is in percentage (%). Note all types of ice particles are included in the analysis.	274
Table 5.3 Mass content and mass content frequency of types for 5 temperature ranges in the entire domain. Mass content (MC) is given in mg m ⁻³ . PC denotes pristine crystals, RC rimed crystals, AG aggregates, RA rimed aggregates, GR graupels. The frequency is in percentage (%).	275
Table 5.4 Budget of concentration tendency for 8 layers at 10 minutes of simulation for LD2 in section I. The unit is m ⁻³ s ⁻¹ . Concentration flux 1 (2) is located at the top (lower) boundary of a layer and were normalized by the volume of the layer.	276

Table 5.5 Fitted parameters of exponential distributions in section $0 < y < 290$ km. The parameters for all but LS2 are obtained at 10 minutes of simulation; the parameters for LS2 are at 20 minutes.	277
Table 5.6 Estimated gradients between the parameters of exponential distributions for 10 trajectories. The trajectories started from initial time, 2 hours, 4 hours of simulation. r is the correlation coefficient. P is the average precipitation rate (mm hr^{-1}) for 10 trajectories. $\hat{\theta}$ is estimates by Field and Heymsfield (2003)'s empirical equation. The left column indicates the simulation time when the trajectories started.	278
Table 5.7 Domain average 6 hour accumulation.	279

Chapter 1 Introduction

1.1 Studying snow and motivation

According to American Meteorological Society, the term, cloud microphysics, is defined as cloud processes (growth, evaporation, etc.) taking place on the scale of the individual aerosol or precipitation particle as opposed to the scale of the visual cloud. A single hydrometeor takes form of liquid, solid water or mixture of the two phases with soluble or/and insoluble material inside, and it is known that clouds themselves are mixture of these hydrometeors in $T < 0^{\circ}\text{C}$. One can easily imagine that solid hydrometeors (ice particles) play important roles in formation and precipitation of mid and high-latitude clouds by observing snow flakes in winter and possibly hails in summer. In fact even tropical clouds contain ice particles, depending on the cloud top temperature. In the following paragraph, historical view of studying solid hydrometeors and transition of the motivations are briefly listed by extracting the work of Nakaya (1954), Pruppacher and Klett (1997) and Wang (2002).

A Chinese scholar of the Western Han Dynasty, named Han Ying is probably considered to be the first man who documented that snow crystals exhibit a six-fold symmetry in 135 BC. In A. D. 1st century in Asia, a method to protect rice and other crops from frost was already known according to the book written by Fan Sheng-Chih. Chu Hsi, a philosopher of the Sung Dynasty, noted that snow and frost form differently from the moisture above in the air and from the moisture in low levels, respectively in the 13th century. He speculated that snow forms from freezing of raindrops, which is true for riming process. In the 17th century

Johannes Kepler pointed out the six-fold symmetry first in the western history. A dependence of the shape of snow crystals on temperature were noted by Martens (1675) and Scoresby (1789-1857). After the microscope was developed in 17th century, more studies about shapes of snow crystals were published. In Japan Toshitsura Doi published 97 sketches of similar snow crystals in 1839 possibly by using a compound microscope. Bentley published the most complete sets of snow crystal photographs (Bentley and Humphreys, 1931). In 1808 Volta (1745-1827) found that hailstones contain a 'little snowy mass' at their center. Waller and Harting (1853) further supported the idea and pointed out that hailstones also have a shell structure with alternating clear and opaque layers as well. The idea that cloud droplets form on water-soluble nuclei and ice crystals form on insoluble dust was suggested by Wegener (1880-1931). The importance of ice crystals in initiation of precipitation was first pointed out by Renou (1815-1902) in 1866. He suggested a concept similar to feeder-seeder mechanism which requires two cloud layers: lower cloud consisting of supercooled drops and another feeds ice crystals into the lower cloud. Wegener showed supercooled droplets and ice crystals cannot coexist in equilibrium below freezing temperature. Bergeron proposed in 1933 that precipitation is due to the colloidal instability that is caused by the saturation vapor pressure difference between liquid and solid hydrometeors. Modern knowledge of cloud physics started in 1940s during the World War II. The military-related research includes development of radar and icing of aircrafts. Nakaya (1954) is the first one who conducted systematic study of natural and artificial ice crystals under different atmospheric conditions and contributed to understanding of snow crystal morphology. Schaefer and Langmuir (1946) demonstrated weather modification by spraying dry ice in a stratiform cloud and producing precipitation.

Weather modification had promoted all kinds of researches from nucleation to collision-coalescence processes since then.

Recently, new observational technology including radars, lidars, cloud particle imager, etc, and application of remote sensing techniques have revived cloud microphysics. Along with it, aerosols and hydrometeors have been gaining more and more attention in climate change through radiative forcing and modification of water cycle. According to the third assessment report of the Intergovernmental Panel on Climate Change (IPCC), direct and cloud albedo forcing of anthropogenic aerosols remain the dominant uncertainty with cooling effect among other radiative forcing. Cirrus clouds are known to be important in radiative forcing due to their wide coverage and long-lived characteristics. Anthropogenic aerosols can affect nimbo-stratus clouds and orographic clouds (e.g., Borys et al., 2003; Rosenfeld and Givati, 2005). Global warming is predicted to cause more intense precipitation as well as draught in mid latitude. Therefore, better quantitative understanding and modeling of ice microphysics and mixed phase clouds are motivated by short-term quantitative precipitation forecasts and regional water cycle study in context of climate change.

1.2 Challenge in modeling ice microphysics

Variety of ice particles exist in atmospheric clouds. Density of a single ice particle can vary from about 10^{-4} to 10^0 g cm^{-3} , the size can range from 10^{-4} to 10^1 cm and the shape of ice particles is full of variety as shown in Magono and Lee (1966) classification. Hexagonal monocrystals have relatively simple shape. Polycrystals can have non-hexagonal components with complicated crystallographic structure. Aggregates are not only of the fluffy type

composed of dendrites, but can be made of needles and other crystal forms. Chain-like aggregates made of plates were observed in the highly electrified regions of continental thunderstorms (e.g., Connolly et al., 2005). Graupels can take hexagonal, lump, or conelike shapes. Irregular particles can be a result of vapor deposition, breakups, evaporation, melting, or riming and cannot be classified into simple categories other than that they are called “irregular”. The phase of water over the surface of ice particles can change between liquid and solid.

The above variety is the result of cloud microphysical processes, thermodynamics and dynamics that hydrometeors experience. Thus, in order to study evolution of hydrometeors, one needs to understand individual microphysical processes, thermodynamics, radiative heating, and dynamics in which the microphysical processes are embedded, and interaction between these processes. The thermodynamics and dynamics of moist air can be modeled in multi-dimensional Eulerian numerical weather prediction models where hydrometeors interact with those processes through latent heat release or evaporation, and sedimentation. The Eulerian approach is a useful methodology to numerically integrate multivariate evolving continuous atmospheric flow, but poses a challenge to accurately represent evolution of discrete particles contained within. To maintain accuracy, the prognostic scalar variables are cast in scalar tendency equations conserving important integral quantities as the fluid evolves. Such variables, for instances, include number concentration and mass content of hydrometeors. Then, a question rises: how will we maintain and predict the many evolving characteristics of solid hydrometeors in the Eulerian system? Can any method keep track of growth history of ice particles in the Eulerian framework analogous to how a Lagrangian approach can keep the

evolution of each single particle or group? The conventional microphysics framework in the Eulerian models includes bin spectral models, and bulk microphysical parameterization, however, to accomplish some of this. These models use a limited number of categories with predefined properties that pass information through time pertaining to their evolution while to represent the evolution of characteristics.

This study develops a new methodology to shed a light on the prediction problem of habits and types of ice particles in the Eulerian dynamics model. The scheme is called the Spectral Habit Ice Prediction System (SHIPS). The main concept is to predict habits and types of ice particles continuously by retaining their growth history and reflecting current conditions based on physical principles. Chapter 2 describes fundamental concepts of SHIPS in details, and examines simulations of an orographic winter storm with nucleation and vapor deposition processes of hexagonal monocrystals. Chapter 3 formulates polycrystals prediction, and discusses habit frequency observation and importance of immersion freezing process. A scheme to predict density and maximum dimension of ice particles with a stochastic collection model is described in Chapter 4, and it is validated in box simulations. Chapter 5 discusses simulations with aggregation and riming processes for the orographic winter storm. In addition to the validation, sensitivity of predicted distribution of ice particles to aggregation efficiency, ice nuclei, and freezing process is studied. Finally, Chapter 6 summarizes the results obtained and suggests future researches.

References, Chapter 1

- Borys, R. D., D. H. Lowenthal, S. A. Cohn, and W. O. J. Brown, 2003: Mountaintop and radar measurements of anthropogenic aerosol effects on snow growth and snowfall rate. *Geophys. Res. Lett.*, 30, 45-1–45-4.
- Connolly, P. J., C. P. R. Saunders, M. W. Gallagher, K. N. Bower, M. J. Flynn, T. W. Choulaton, J. Whiteway and R. P. Lawson, 2005: Aircraft observations of the influence of electric fields on the aggregation of ice crystals. *Q. J. R. Meteorol. Soc.*, 131, 1695–1712.
- Intergovernmental panel on climate change, 2001: *Climate Change 2001: The Scientific Basis*. http://www.grida.no/climate/ipcc_tar/wg1/index.htm
- Magono, C. and C. W. Lee, 1966: Meteorological classification of natural snow crystals. *J. Frac. Sci. Hokkaido Univ. Ser. 7*, 2, 321–335.
- Nakaya, U., 1954: *Snow crystals, natural and artificial*. Cambridge, Harvard University Press, 510 pp.
- Pruppacher, H. R. and J. D. Klett, 1997: *Microphysics of clouds and precipitation*. Kluwer Academic, 914 pp.
- Rosenfeld, D., and A. Givati, 2006: Evidence of orographic precipitation suppression by air pollution–induced aerosols in the western United States. *J. Appl. Meteor. Climatol.*, 45, 893–911.
- Wang, P. K., 2002: *Ice microdynamics*. Academic Press, 273 pp.

Chapter 2 Model description and simulation of vapor deposition process

2.1 Introduction

Cloud resolving models (CRMs) of the Earth atmosphere have been developed over the past 4 decades to explicitly simulate microphysical processes in order (1) to predict their impact on the modeled thermodynamics and dynamics and (2) to simulate the cloud structure and attendant precipitation. Nevertheless, the underlying microphysical processes are still only partially understood and formulated with a combination of basic theory, empirically derived relationships, and educated approximations to fill the many gaps in knowledge.

Microphysics schemes applied to multidimensional Eulerian CRMs can be classified into two paradigms: (a) bin (or spectral) schemes (e.g., Takahashi (1976); Farley and Orville (1986); Kogan (1991); Ovtchinnikov and Kogan (2000)), and (b) bulk microphysics schemes (e.g., Lin et al. (1983); Thompson et al. (2004)). Both schemes require categorization of solid hydrometeors (or ice particles) to be predicted. The differences arise primarily from methods to approximate size distributions of hydrometeors. Size variations are discretized explicitly into multiple size or mass “bins” with the bin model approach. This approach is the least restrictive on developing arbitrary size distributions, but requires a large number of size bins to represent a complete size spectrum. For this reason, the bin approach has not been feasible for three dimensional CRMs, except when applied to a limited number of categories of hydrometeors. Recently, Lynn et al. (2005) implemented a fast version of spectral (bin)

microphysics model (SBM Fast) in a 3D Eulerian mesoscale model (MM5) to simulate a convective cloud system. They have defined three categories of solid hydrometeors: plate, dendrite, and column category, and used larger mass bins of the categories for aggregates, graupels, and hail particles.

The “bulk” approach to explicit microphysics prediction, first proposed by Kessler (1969), approximates the typically bimodal distribution of liquid hydrometeors by assuming that there are two separate categories of liquid droplets, one precipitating (rain) and one too small to precipitate (cloud droplets). It is further assumed that each category is distributed in a simple statistical distribution characterized by 1-2 moments that can be predicted or assumed based on empirical studies. The bulk technique was extended to the ice phase (e.g., Koenig and Murray (1976); Orville and Kopp (1979); Cotton et al. (1982); Lin et al. (1983)) by also dividing ice particles into several distinct categories including cloud ice category (analogous to cloud droplets) and precipitating ice categories typically called snow, and graupels (analogous to rain). In addition to the classic bulk size distribution assumptions, each category requires the assumption of specific mass-diameter relationship, mass-velocity relationship, bulk density of the ice particles, or diagnosis of geometry of ice particles (or ice crystal habit) to formulate microphysical behavior and tendencies. Therefore, the category to which a particular ice particle belongs is critical to its evolution and movement, how it interacts with other categories, and how it behaves radiatively in a CRM. The properties of ice particles at a given time suggest the past dynamical and microphysical processes experienced by the particles. Inversely, a series of processes or particle history and local environment at a given time determines the properties. In other words, ice particles indicate dynamical and microphysical

memory whereas liquid hydrometeors show little. However, the particle property is predefined in traditional “Bulk” and “Bin” approaches by categories, and the growth history is retained only in form of concentration and mass content of the predefined categories. Thus, the accuracy of the traditional “bulk” or “bin” approaches might be increased by implementing more and more specialized categories, having more predicted parameters for each category. Having more categories leads to more possible routes of mass content and concentration among the categories, and introduces more arbitrary decisions between them. In a practical sense, conventional “Bulk” and “Bin” approaches for solid hydrometeors are a “discrete-property approach”.

In this chapter, the Spectral Ice Habit Prediction System (SHIPS) is developed to evolve property of ice particles by diagnosing particle growth history for each bin of one mass spectrum of ice particles. By introducing the variables that define properties of ice particles for each bin, the categorizations of ice particles are not necessary and so the complicated, arbitrary transfer links among categories are unnecessary. Rather than converting mass between categories, SHIPS mixes properties. Hence through growth and transport, ice crystal habit and structure evolve. SHIPS is a “continuous-property approach” by allowing solid hydrometeors to evolve the properties continuously.

SHIPS is one component of Advanced Microphysics Prediction System (AMPS). The other components of AMPS are Aerosol Prediction System (APS) and Spectral Liquid Prediction System (SLIPS). This study uses University of Wisconsin Nonhydrostatic Modeling System (UW-NMS) (Tripoli 1992) as the CRM. It has been modified to maximize the efficiency of AMPS, but AMPS is built to function with the dynamics of any CRM.

Next section will describe the underlying framework of SHIPS. Section 2.3 will discuss implementation of SHIPS into the Eulerian UW-NMS CRM. Then, in Section 2.4, formulation of vapor deposition process and terminal velocity that reflect crystal habit will be described. Section 2.5 briefly describes setups of UW-NMS and AMPS to simulate a winter orographic storm during the IMPROVE-2 field experiment and also presents experiment design. Results of the model simulations will be evaluated and compared to observations of IMPROVE-2 in section 2.6, and finally, conclusions will be drawn in section 2.7

2.2 Spectral Habit Ice Prediction System (SHIPS)

SHIPS is designed to retain growth history as conserved particle characteristics that can move throughout the cloud and mix with other particles of different characteristics. Rather than assigning ice particles to predefined categories such as cloud ice, pristine crystals or graupel, we define a distinguishable group of hydrometeors contained within an air parcel only by: (1) concentration, (2) mass content, and (3) series of evolved characteristics that reflect the growth history (particle property variables, PPVs hereafter). PPVs can include the amount of mass of a hydrometeor accumulated from a microphysical process, lengths along the crystallographic axes of an ice crystal, circumscribing volume, electric charge, mass of liquid coating and so on. The number of PPVs depends on the complexity of the scheme desired.

In addition to the ability to predict ice particles of differing physical characteristics, SHIPS is designed to predict multi-modal distributions with moderate computation. This research adopted a two-moment bin method with a sub-distribution assumed over a bin.

An important assumption of the SHIPS framework is the implicit mass sorting assumption, which states that different species of solid hydrometeors within a single air parcel, defined by a set of growth parameters, are naturally sorted by mass. Hence, for now, each mass bin can only represent a single set of mean habit characteristics and mean type of solid hydrometeors that are distinguished by mass, number concentration, and PPVs predicted for the bin. The limitation is softened, however, by the fact that the mass-habit relationship for a bin can vary over time and between grid cells as a result of microphysical evolution and transport. The representation of a single habit and single type for a mass bin also means that simulations with SHIPS are somewhat sensitive to the number of bins used. The number of bins corresponds to maximum number of habits and types that can be diagnosed over the mass spectrum, and the range of mass occupied by one bin, therefore one habit, get larger when less number of bins is used. The dependence of growth processes and sedimentation on habits leads to difference in resulting concentration and mass fields of hydrometeors.

2.2.1 Hybrid bin method

The mass bin scheme of SHIPS, which this study uses in an Eulerian dynamic model, is based on the multi-component hybrid bin method proposed and demonstrated in Lagrangian parcel model by Chen and Lamb (1994a, hereafter referred to as CL1). It was adopted for its simplicity and flexibility for defining collision kernels. CL1 described the spectrum of concentration of ice particles by three independent variables: water mass, solute mass and aspect ratio¹ of hydrometeors. The axis of each variable was divided into bins: 45 water mass

¹ This study defines “aspect ratio” as the ratio of semi-minor axis length to semi-major axis length of a spheroid, while “axis ratio” as the ratio of lengths along crystallographic axes of an ice crystal.

bins, 20 solute mass bins and 11 aspect ratio bins. The hybrid bin method conserves two moments of sub-distribution along the axis of each independent variable. In order to reduce computational cost, we simply describe the spectrum as a function of total mass of a hydrometeor. Hence, predicted two moments are number concentration and mass content of a bin.

The sub-distribution in a bin is described by piecewise linear distribution (see CL1 for more detail description):

$$n(m) = n_0 + k(m - m_0) \quad (2.1)$$

where the number of particles per mass and volume of air $n(m)$ is described in terms of mass of the particle m , m_0 is the mid point of mass bin boundaries, and n_0 is the concentration per mass at m_0 . Let m_1^b and m_2^b be the left and right mass boundaries of the b th bin. See appendix C for description of the symbols used in this paper. This study defines the mass boundaries as

$$m_1^b = m_2^{b-1} = k_{bb}^b m_1^{b-1} \quad (2.2)$$

where k_{bb}^b is an arbitrary constant. Then, concentration and mass content predicted for b th bin are defined by

$$N^b = \int_{m_1^b}^{m_2^b} n(m) dm \quad (2.3)$$

$$M^b = \int_{m_1^b}^{m_2^b} mn(m) dm \quad (2.4)$$

The two moments of the sub-distribution of the bin are related to the two parameters of the linear distribution:

$$n_0 = \frac{N^b}{m_2^b - m_1^b} \quad (2.5)$$

$$k = \frac{12(M^b - m_0 N^b)}{(m_2^b - m_1^b)^3} \quad (2.6)$$

The hybrid-bin method of CL1 calculates the increase (or decrease) of concentration and mass content for each bin after the microphysical growth processes are computed. The new concentration $N^{b'}$ and mass content $M^{b'}$ defines a *shifted bin* with the two shifted bin boundaries. The shifted bin boundaries are allowed to be inside of a mass bin in order to ensure the positiveness of $n(m)$ (see CL1 for detail discussion). From the two new moments and shifted bin boundaries, two parameters of the linear distribution in the shifted bin are obtained from Equations (2.5) and (2.6). Then, particles inside the shifted bin are transferred back into the bins defined by original bin boundaries (Equation (2.2)). Finally, tendency of mass content and concentration for b th bin is calculated by subtracting the original mass content and concentration from the newly obtained mass content and concentration.

As the mass content and concentration are moved between bins, PPVs are also mixed weighted by concentration. This results in a mixed structural evolution in a given bin since the flux of mass content and concentration from neighboring bins influence the mean habit evolution in a given bin. The following section describes PPVs that are added to the CL1 hybrid-bin model for the SHIPS application.

2.2.2 Particle property variables (PPVs)

We define the *representative hydrometeor* of a bin as a particle whose mass is equal to the mean mass of the bin \bar{m} :

$$\bar{m} \equiv \frac{M^b}{N^b} \quad (2.7)$$

SHIPS retrieves the properties of the representative hydrometeor in a bin through PPVs that reflect history of dynamical mixing and local microphysical processes. SHIPS considers the following types of PPVs: (a) mass content components, (b) length variable components, (c) volume variable components, and (d) aerosol mass content components. Figure 2.1 shows the schematic of SHIPS where the ice spectrum is divided into five mass bins. Formulation of continuity equations to predict PPVs in the Eulerian dynamic framework of UW-NMS CRM will be given in section 2.3.

2.2.2.1 MASS CONTENT COMPONENTS

Mass of the hydrometeor in a bin consists of four mass components: ice crystal mass component m_I , aggregate mass component m_A , rime mass component m_R , and liquid mass component m_W . The sources of these components are microphysical processes affecting the bin, that is to say, ice crystal mass m_I is produced by vapor deposition process onto ice crystals, aggregate mass m_A by aggregation process, rime mass m_R by riming process, and liquid mass m_W by melting process. The mass components add up to mass of a hydrometeor:

$$m = m_I + m_A + m_R + m_W \quad (2.8)$$

which is valid for any hydrometeor with mass m in a bin as well as for the representative hydrometeor with mass \bar{m} .

It is clear that the mass components m_I , m_A , m_R and m_W are conservative variables as the mass of a hydrometeor. Naturally, quantities of the mass components integrated over the sub-distribution are transferred between bins and between grid cells. The implicit mass sorting assumption implies that the ratio of each mass component to mass of a hydrometeor is fixed over the mass range defined by the bin boundaries; hydrometeors in a bin have the same type. Therefore, the mass content components M_I^b , M_A^b , M_R^b , and M_W^b are proportional to the total mass content M^b . Note that the proportionality of the mass content components change over time, space, and bin number. The mass content components also add up to the total mass content of the bin:

$$M = M_I^b + M_A^b + M_R^b + M_W^b \quad (2.9)$$

In this paper, M_W^b will be ignored, and focus on M^b , M_I^b , and M_R^b . SHIPS predicts M_I^b and M_R^b in addition to M^b , and then M_A^b is diagnosed from the above equation.

2.2.2.2 LENGTH VARIABLE COMPONENTS

This chapter considers six-fold symmetric (hexagonal) ice crystals for representation of ice crystals in simulated clouds. SHIPS retrieves three lengths along two crystallographic

directions of a hexagonal ice crystal for the representative hydrometeor. One can add more lengths if necessary. The conceptual geometry of the hexagonal ice crystal is defined by three independent lengths a , c , and d corresponding to a-axis, c-axis and dendritic arms ((a) of Figure 2.2). Mass of the hexagonal crystal model is related to the lengths as

$$m = 3\sqrt{3}\phi(1-\psi)(1+\psi)a^3\rho_i^h \quad (2.10)$$

where $\phi = c/a$ and $\psi = d/a$ are the axis ratios, and ρ_i^h the bulk density of the hexagonal crystal model. The hexagonal crystal model is used to obtain the geometrical properties of ice crystals defined by Bohm (1992), which are necessary to calculate terminal velocity as discussed later. For each hydrometeor, the bulk crystal density ρ_c is defined through mass-length relationships:

$$m_l = k_s(1+\phi^2)^{3/2}\rho_c a^3 \quad (2.11)$$

$$= k_s(1+\phi^{-2})^{3/2}\rho_c c^3 \quad (2.12)$$

$$= k_s(1+\phi^2)^{3/2}\psi^{-3}\rho_c d^3 \quad (2.13)$$

where the volume of a sphere circumscribing the ice crystal is used ($k_s = 4\pi/3$). The bulk crystal density corresponds to the effective density defined for ice particles in Heymsfield et al. (2002).

Additional PPVs needed to retrieve the geometry of ice crystals include the concentration weighted cubic a-axis length, c-axis length and dendritic arm lengths, ℓ_a^{3b} , ℓ_c^{3b} , and ℓ_d^{3b} (or denoted by ℓ_l^{3b} for l -axis length). To define these PPVs, constant ρ_c , ϕ , and ψ over mass in a bin were assumed, which stems from the implicit mass sorting assumption. Then, the mass-

length relationships, Equations (2.11) to (2.13), are used to integrate cubic lengths weighted by concentration over the mass for each growth axis length. Therefore, ℓ_l^{3b} ($l = a, c, d$) are proportional to the ice crystal mass content component, M_l^b . Each length of the representative hydrometeor of mean mass \bar{m} is retrieved simply by $\bar{l} = \sqrt[3]{\ell_l^{3b} / N^b}$ ($l = a, c, d$).

To retain the growth history of ice crystals along the various crystallographic axes of growth, it was initially considered to predict the mass deposited along each axis instead of the length variables and then use the mass continuity equation to represent mixing of different kind of particles in Eulerian dynamic model. However, it was determined that the mass deposited along each axis alone did not uniquely characterize geometry of a crystal. It was found that axis growth history was better characterized by predicting axis-length variables together with total mass of a particle. The validity of mixing ℓ_l^{3b} between mass bins and grid cells is discussed in appendix A.

2.2.2.3 VOLUME VARIABLE COMPONENTS

In addition to mass content components and length components, solid hydrometeors can be characterized by volume variable components that can be also defined and predicted based on microphysical process. One such volume quantity predicted in this study is the sphere volume that circumscribes one solid hydrometeor, v_{cs} . The volume is related to the total mass of a particle with the bulk sphere density

$$m = \rho_s v_{cs} \quad (2.14)$$

For the case where ice particles are pristine ice crystals or rimed crystals, $\rho_s = \rho_c$.

The volume variable component was determined to be necessary in order to diagnose the bulk sphere density and semi-axis lengths of aggregates and graupels that are categorized based on mass content components. One can also diagnose the sphere volume based on an empirical formula. The circumscribing volume of a nucleated ice crystal is initially calculated with $v_{cs} = k_s (1 + \phi^2)^{3/2} a^3$. Note that v_{cs} is not used to diagnose any property of an ice crystal. The v_{cs} grows by vapor deposition, aggregation and riming processes. Predicting the variable is equivalent to predicting the cubic maximum dimension of a hydrometeor. Instead of v_{cs} , one can also predict length variable components of semi-axis lengths of the spheroid that represent an ice particle.

Similarly to ℓ_l^{3b} , the concentration weighted volume of circumscribing sphere V_{cs}^b for ice particles present in bin b can be obtained by integrating v_{cs} over the bin by multiplying by the concentration. V_{cs}^b is simply proportional to M^b due to the constant ρ_s assumed from implicit mass sorting assumption. The circumscribing volume of the representative hydrometeor is obtained by $\overline{v_{cs}} = V_{cs}^b / N^b$. The validity of mixing V_{cs}^b is further discussed in appendix A.

2.2.2.4 AEROSOL MASS CONTENT COMPONENTS

In the Earth atmosphere solid hydrometeors form on aerosols or form by freezing supercooled liquid hydrometeors that are originally formed on aerosols. SHIPS keeps track of total mass m_{apt} and soluble mass m_{aps} of the aerosols. Insoluble mass of the aerosols m_{api} are diagnosed as $m_{api} = m_{apt} - m_{aps}$. In the same way as the mass content components, the ratio of each aerosol mass content component to the total mass content of the hydrometeors in a bin is

assumed to be constant. Therefore, the aerosol mass content components M_{apt}^b and M_{aps}^b transferred by microphysics processes between bins are easily calculated from the transferred mass content M^b with the ratio in a shifted bin.

2.2.3 Diagnosis of habit and type

From the predicted PPVs one can diagnose the type and habit of solid hydrometeors. This study defines “type” of solid hydrometeors as the category of ice based on physical processes that formed it, e.g., pristine crystal, aggregates or graupels. This study defines “habit” as particular crystallographic feature of an ice crystal (Pruppacher and Klett 1997), e.g., plates, columns, dendrites, etc.. Note that categorization of solid hydrometeors itself is not necessary for SHIPS microphysics simulation. However, categorization aids in verification since observations are often classified into traditional forms found in the Magono-Lee classification (Magono and Lee 1966).

This research diagnoses types of solid hydrometeors based on mass content components as shown in Figure 2.3. Graupels are diagnosed if the bin has more mass content produced by riming process than any other processes. Bins with mass content dominantly produced by aggregation are diagnosed as aggregates. If mass content produced by riming is less than the aggregation mass content in a bin, then the particle type is considered to be rimed aggregates. In the same way, a bin containing mass content largely produced by vapor deposition are diagnosed to certain pristine crystals, and those with some riming mass content but less than mass content by vapor deposition regarded to be rimed crystals.

The diagnosis of solid hydrometeor types is robust because it depends only on microphysical processes that the air parcel experiences. However, in the in-situ observation the mass estimation by each process is somewhat more challenging. Riming mass could be estimated through chemical concentration on solid hydrometeors (Borys et al. 2003; Chen and Lamb 1999). Distinction between rimed aggregates and graupel would be the most difficult among them.

Habit of ice crystals is diagnosed using length variable components as (b) of Figure 2.2. It basically means that crystals with $\phi < 1$ with $\psi \leq 2/3$ ($\psi > 2/3$) are considered as plates (dendrites) and those with $\phi \geq 1$ as columnar crystals.

2.2.4 Outputs and possible applications

The predicted outputs from SHIPS are concentration, mass content, and particle property variables (PPVs) for each bin of the mass spectrum. For ice crystals, the lengths along growth axes are available. Once aggregation starts, those lengths represent the average lengths of ice crystals within the aggregate. This will be described in the subsequent paper. The bulk density, aspect ratio, and maximum dimensions of aggregates, rimed aggregates or graupels are diagnosed from predicted concentration, mass content and circumscribing volume. One can attain a sense of particle history by examining the PPVs formed in each bin. Trajectories of each bin can be formed, providing an estimate of particle origins.

The crystal habit information, maximum dimension, aspect ratio, bulk density, and liquid water mass of solid hydrometeors are useful in the radiative transfer calculation. Employing the distribution of PPVs across mass bins, radiative transfer calculation can explicitly take into

account particle mass, shape or length scales, density, phase structure, and so on. Diagnostic procedure can be used to estimate secondary motions of ice particles such as tumbling behavior as well. Research is currently under way to evaluate the impact of these new available tools.

2.3 Applying hybrid-bin method to the Eulerian dynamics framework

2.3.1 Continuity equation

The SHIPS application of the CL1 hybrid-bin model requires that the system be cast in the Eulerian framework. This requires a continuity equation be formed for each prognostic variable. The general form of the continuity equation, following Tripoli (1992) is given in tensor form as:

$$\begin{aligned} \frac{\partial q_{ice}^{n,b}}{\partial t} = & -\frac{1}{\rho} \frac{\partial \rho (u_i + V_T^{n,b} \delta_{ij}) q_{ice}^{n,b}}{\partial x_j} + \frac{q_{ice}^{n,b}}{\rho} \frac{\partial \rho u_i}{\partial x_i} + \frac{1}{\rho} \frac{\partial}{\partial x_i} \left(\rho K_H \frac{\partial q_{ice}^{n,b}}{\partial x_i} \right) \\ & + \frac{1}{\rho} \frac{\partial^{l_f-1}}{\partial x_i^{l_f-1}} \left(\rho v \frac{\partial q_{ice}^{n,b}}{\partial x_i} \right) + S^{n,b} \end{aligned} \quad (2.15)$$

where $q_{ice}^{n,b}$ is the specific quantity of the ice parameter “ n ” in mass bin “ b ” defined as:

$$q_{ice}^{n,b} = \frac{M_{ice}^{n,b}}{\rho} \quad (2.16)$$

and ρ is the density of the moist air, $M_{ice}^{n,b}$ is the quantity per unit volume of the air of the ice parameter n ($n = 1, 2, \dots, n_i$) in the b th ($b = 1, 2, \dots, N_{BIN}$) mass bin. Equation (2.15) defines

$n_i \times b_i$ separate equations that are added to the UW-NMS CRM. Table 2.1 shows the corresponding prognostic variables defined for UW-NMS and SHIPS. We have $n_i=10$ parameters for solid hydrometeors per bin: concentration, mass content and PPVs explained previous section. The Cartesian grid unit tensor is x_i , and velocity components are u_i . The terminal velocity of the ice parameter n integrated over mass bin b is given by $V_T^{n,b}$, the eddy mixing coefficients for scalars is K_H , the high order numerical mixing coefficient is ν , and the order of the high order filter is l_f .

The source term $S^{n,b}$ is defined by the SHIPS microphysics scheme and involves conversion tendencies between the ice, liquid and vapor water species:

$$S^{n,b} = \frac{\partial q_{ice}^{n,b}}{\partial t} \Big|_{IU} + \frac{\partial q_{ice}^{n,b}}{\partial t} \Big|_{VD} + \frac{\partial q_{ice}^{n,b}}{\partial t} \Big|_{AG} + \frac{\partial q_{ice}^{n,b}}{\partial t} \Big|_{RM} + \frac{\partial q_{ice}^{n,b}}{\partial t} \Big|_{HB} + \frac{\partial q_{ice}^{n,b}}{\partial t} \Big|_{MS} \quad (2.17)$$

where the subscript IU denotes ice nucleation, VD vapor deposition process, AG aggregation process (collection within ice spectrum), RM riming process (collection between ice and liquid spectra), HB hydrodynamic breakup, and MS melting and shedding process. The microphysical computation of SHIPS uses prognostic variables that are defined for unit volume of air, whereas the dynamic part of the model requires specific quantity of the variables. Therefore, tendencies (source and sink) calculated by the microphysics have to be divided by the density of the moist air.

This Eulerian form of the parameterization is cast in a flux conservative form, so that a budget of each parameter leaving and entering a grid cell can be maintained. A small diabatic mass source results from the elastic fluxes of moist air mass into and out of grid cells on a small time step (Tripoli 1992). The associated lapse in conservation due to numerical approximation of the quasi-compressible closure is small and all tests show it to be entirely negligible. The numerical treatment of advection was found to be critical to the performance of the SHIPS system. Whereas Tripoli (1992) reported good results using 6th order Crowley advection scheme, it was found that such a scheme was too diffusive for SHIPS and led to artificial spreading of microphysical habits. Instead, piecewise parabolic method (PPM) described by Colella and Woodward (1984) was adopted as advection scheme. This scheme was found to perform superior to Crowley while maintaining accuracy in the classical nonhydrostatic model tests of mountain wave simulation. The downside of the PPM is the nonlinearity of its operator that has the potential to move PPVs differently. This effect was noticed but seemed to be less significant than the artificially spreading with Crowley.

As mentioned earlier, flux conservative Eulerian transport results in the mass-weighted mixing of bins between grid cells. This results in the PPVs in a given bin reflecting the mean history of the same mass bin of surrounding parcels. This is both a limitation and a benefit of the approach as it does allow a local growth regime to be overwhelmed by a larger mass of ice particles entering the parcel from another location. This makes intuitive sense. On the other hand, if parcels having equal mass contents of differing particles types, the result will be a particle of mixed characteristics. We believe that this is an acceptable compromise in return for the economy of the implicit mass sorting assumption.

2.3.2 Weighted terminal velocity and sedimentation

The sedimentation of hydrometeors in the Eulerian dynamic framework is an important process to sort hydrometeors of different masses into different altitudes. The appropriate terminal velocity for sedimentation of a prognostic variable for a bin is the one weighted according to the corresponding continuity equation. The general formulation of terminal velocity based on boundary layer theory developed by Bohm (1992) is used to obtain the terminal velocity weighted by mass and concentration within a bin. The terminal velocity v_i^b for the representative hydrometeor in b th bin is calculated as:

$$v_i^b = \frac{N_{Re} \eta_a}{l_d \rho} \quad (2.18)$$

where l_d is the characteristic length of the hydrometeor. Bohm (1992) calculates the Davies number X as

$$X = \begin{cases} \frac{8\bar{m}g\rho}{\pi\eta_a^2 \max(\alpha, 1)q_{rat}^{1/4}} & \text{if } q_{rat} \leq 1, \\ \frac{8\bar{m}g\rho}{\pi\eta_a^2 \max(\alpha, 1)q_{rat}} & \text{if } q_{rat} \geq 1 \end{cases} \quad (2.19)$$

where α is the aspect ratio of hydrometeors, and q_{rat} is the area ratio (porosity) defined by the ratio of projected (effective) area of a hydrometeor A_e to that of circumscribing spheroid A_c .

The pressure drag is calculated based on aspect ratio and porosity. Reynolds number N_{Re} is calculated with the pressure drag, the Davis number and aspect ratio, and then modified by correction for transitional flow and one for viscous regime. As done by Mitchell (1996), the

power-law relationships between N_{Re} and X were derived from those calculated with the formula for the hydrometeors considered in Bohm (1992). With the simple relationship and assumption of constant aspect ratio and area ratio over a mass bin, the Bohm's terminal velocity formula can be analytically integrated over each mass bin (see Mitchell and Heymsfield (2005) for theoretical approach).

The sedimentation of prognostic variables, i.e., mass content, concentration and PPVs, with differently weighted terminal velocity can affect the property of representative hydrometeors. Having differently weighted terminal velocity for mass content and concentration leads to sorting of hydrometeors within a bin. This leads to the shift of the mean mass where the representative hydrometeor of a bin is defined. Note that each specific PPV $q_{ice}^{n,b}$ has differently weighted terminal velocity $V_T^{n,b}$ (Table 2.1). All mass content components have the same mass-weighted terminal velocity V_{Tm} as that of the total mass. This is because the ratios of the mass content components to the total mass content are assumed to be constant. Therefore, the type of solid hydrometeors that is diagnosed with the ratios of mass components is not affected by the sedimentation. Length components and volume components are assumed to have concentration-weighted terminal velocity V_{Tc} for each bin because those are related to each particle rather than mass. Similarly, the diagnosed habit is not affected by sedimentation because the axis ratios are assumed to be constant within a bin. Since the mean mass of a bin is affected by the sedimentation, the representative hydrometeor of the bin may have longer or shorter length than before.

2.4 Modeling dependence of depositional growth and terminal velocity on ice crystal habits

This section describes and discusses the methods to simulate vapor depositional growth and terminal velocity for continuously changing geometry (or habit) of ice crystals.

Formulation of ice nucleation and melting-shedding processes used in this study are described in Appendix B. The ice nucleation processes include deposition-condensation nucleation, contact freezing nucleation, and immersion freezing nucleation. The melting-shedding process model estimates melt water mass based on the steady state of the heat budget.

2.4.1 Vapor deposition process

This research uses the parameterization of vapor depositional growth of ice crystals developed by Chen and Lamb (1994b) (hereafter, CL2). It assumes the spheroidal ice crystal to calculate the mass, volume and length growth. The core assumption of the process is the mass distribution hypothesis by CL2:

$$\frac{dc}{da} = \Gamma(T) \frac{c}{a} \quad (2.20)$$

where $\Gamma(T)$ is the inherent growth ratio that reflect current atmospheric condition onto ice crystals. The axis ratio c/a indicates the history of the ice crystal. This hypothesis is important because it gives the ratio of c-axis growth rate to a-axis one, and it can be used in varying ambient temperature. Based on the hypothesis, the changes of a and c axis lengths of a falling ice crystal under ambient temperature T are linked to the change of the mass of ice

particle (see Equations. (41)-(44) of CL2). This study calculates the mass growth of a hydrometeor having mean mass of the bin $\bar{\delta m}$ by

$$\bar{\delta m} = 4\pi C(a, c)G(T, p)f_v f_{kn} s_{vi} \delta t \quad (2.21)$$

where $C(a, c)$ is the capacitance of the spheroid with a and c axis lengths, $G(T, p)$ is the thermodynamic function (see Pruppacher and Klett (1997)), f_v the ventilation coefficient, f_{kn} is the mass-transfer correction factor for kinetic process, s_{vi} is the supersaturation over ice, and δt is the time step.

CL2 gives growth rate of a - and c -axis lengths of spheroidal ice crystal. This study attempts to break the a axis length into length of the inner hexagonal crystal and dendritic length extending from the vertex of the hexagonal crystal as following. We define conditions to grow dendritic arms d as

- The diameter of hexagonal plate is more than $20 \mu\text{m}$: $a_h > 10 \mu\text{m}$, and
 1. $-16 \leq T \leq -12^\circ \text{C}$, and liquid hydrometeors exist or saturated over water.
 2. dendritic arm $d > 10 \mu\text{m}$.

The main condition on the diameter of the hexagonal part is speculated based on ground observation of Auer and Veal (1990), which show the existence of dendritic ice crystals with diameter as small as $50 \mu\text{m}$. The first condition on environmental temperature and moisture is well known in the literature based on laboratory experiments (e.g., Kobayashi (1961)), and this is the dendritic growth regime. However, the second one is a hypothesis: The dendritic arms continue to grow even in plate or column growth region once they are initiated in a dendritic

zone. It is intuitively speculated that the dendritic arms grow due to higher ventilation effect around the tip of arms.

The mass content of a shifted bin for the b th bin $M^{b'} = M^b + \delta M$ is calculated by $\delta M = N^b \delta \bar{m}$. Using the linear distribution corresponding to $N^{b'} = N^b$ and $M^{b'}$, the mass content and concentration are transferred into the bins defined with original mass boundaries as described by CL1. We can calculate the mass content components transferred into original bins using the ratio of each component to the total mass content in the shifted bin. For vapor deposition, the change of mass content δM is added only to the ice crystal mass content component.

The concentration weighted cubic length ℓ_l^{3b} ($l = a, c, d$) transferred to original bins from the shifted bin can be calculated as following. The a-axis and c-axis length in a shifted bin $a' = a + \delta a$ and $c' = c + \delta c$ are calculated, using δa and δc from Equations (41)-(44) of CL2. Only if one of the above conditions for dendritic growth is satisfied, δd is set equal to δa , and the dendritic arm in the shifted bin $d' = d + \delta d$ is obtained. Then, the axis ratios $\phi' = c'/a'$ and $\psi' = d'/a'$ and bulk crystal density $\rho_c' = \bar{m}'/(2\pi\phi'a'^3)$ for the shifted bin are obtained. Since there are mass-length relationships (Equations (2.11)-(2.13), the transferred ℓ_l^{3b} are easily calculated from the axis ratio, bulk crystal density of the shifted bin and the ice crystal mass content transferred from the shifted bin.

In the similar way to the length components, the concentration weighted circumscribing sphere volume V_{cs} can be transferred back to original bins. The volume v_{cs}' in the sifted bin is calculated as

$$v_{cs}' = k_s [(a + \delta a)^2 + (c + \delta c)^2]^{3/2} \quad (2.22)$$

for pristine and rimed crystals. The concentration weighted volume transferred from the shifted bin can be calculated from the bulk sphere density ρ_s' of the shifted bin and transferred total mass content (Equation (2.14)).

As with mass content and concentration, tendency of PPVs per volume of air by vapor deposition process for a bin is calculated by subtracting the original variables from the newly obtained variables.

2.4.2 Terminal velocity

The ice crystal habits can influence not only vapor depositional growth but also terminal velocity, which is especially important in determining the structure and life time of cloud systems with weak vertical motions such as cirrus and stratiform clouds, see e.g., Heymsfield et al. (2002). SHIPS calculates the terminal velocity that corresponds to continuously changing mass and habits by the general formulation of Bohm (1992). As described above, the formula requires aspect ratio, area ratio, and characteristic length of ice particles as well as the mass. Those are calculated from lengths predicted by SHIPS and geometry of the hexagonal crystal model as shown in Figure 2.2. The hexagonal crystal model gives the area ratio of planar crystals with predicted lengths as

$$\begin{aligned} q_{rat} &= \frac{A_e}{A_c} = \frac{(3\sqrt{3}/2)(a-d)(a+d)}{\pi a^2} \\ &= 3\sqrt{3}(1-\psi)(1+\psi)/(2\pi) \end{aligned} \quad (2.23)$$

and $q_{rat} = 4/\pi$ for columnar crystals as defined by Bohm (1992).

To illustrate the effect of changing axis ratios $\phi = c/a$ and $\psi = d/a$ in SHIPS, terminal velocity of a single ice crystal was calculated using Bohm's equation. Given two axis ratios and mass, three axis lengths can be calculated from mass-length relationship, Equation (2.10), with $\rho_i^h = \rho_i$. Mass of the ice crystal was specified by substituting $a = 50 \mu\text{m}$, $\phi = 1.0$ and $\rho_i^h = \rho_i$ into Equation (2.10). As shown in Figure 2.4, the calculated terminal velocity changes continuously with ϕ , and ϕ except for $\phi = 1$. The discontinuity is caused by switching orientation of the crystal to the flow. The terminal velocity is smaller for columnar (planar) crystals with larger (smaller) ϕ and with longer dendritic arms, which is a important feature of habit.

2.5 Model setup and experiment design

A winter orographic snow storm observed on 13-14 December 2001 during IMPROVE-2 campaign was selected as a case study to evaluate SHIPS, following case 3 of 6th International Cloud Modeling Workshop in 2004 (Grabowski 2006). A significant cyclonic storm and vigorous upper-level cold-frontal rainband produced extensive and deep clouds and precipitation over the Oregon Cascades (Woods et al. 2005). The case is ideal for this study because the temperature and moisture distribution cover the whole range of laboratory-known plate growth, column growth, and dendrite growth regimes as well as relatively high predictability of the dynamics forced by topography. A two dimensional idealized (slab-symmetric) simulation is implemented with UW-NMS.

2.5.1 Dynamics

UW-NMS (Tripoli 1992) is implemented as the 2D Eulerian CRM that integrates microphysical variables predicted by SHIPS. UW-NMS features a time split, compressible grid, leapfrog forward model. A 1.5 level turbulence closure is employed. In order to limit the build-up of truncation error, the enstrophy conservative thermodynamic closure described by Tripoli (1992) is used in addition to kinetic energy and potential vorticity conservation. UWNMS adopts a unique height coordinate system called “step topography” that uses a terrain following variable grid spacing near the ground. The ice-liquid water potential temperature (Tripoli and Cotton 1981), specific humidity of total water and other water species except vapor, and pressure are predicted. Vapor specific humidity, potential temperature and temperature are diagnosed based on those predicted variables. Radiative forcing is not calculated in this simulation even though SHIPS produces detail properties of solid hydrometeors. As mentioned in section 2.3, the piecewise parabolic method (PPM) (Colella and Woodward 1984) is implemented for advection of scalar variables. The horizontal resolution is 1 km, and the vertical resolution is 100 m for the lowest 20 points and then increased up to 500 m by the ratio of 1.1. The elevation of terrain along the cross section was provided by the workshop. The numerical filter and diffusion terms in Equation (2.15) are turned off to study the effect of advection and sedimentation.

This study uses a time step of 10 seconds and diagnoses the vapor mass as total water mass subtracted by liquid and ice particle masses. Resolving supersaturation requires the time step of order of 0.1 second, which is computationally expensive for operational use. It is assumed that hydrometeors consume the excess water by vapor deposition to maintain

saturation over water after one time step. The supersaturation is calculated as the value with which the deposited vapor mass on cloud condensation nuclei (CCN) after activation, ice nuclei (IN) after deposition-condensation nucleation, liquid and ice particles within the time step are balanced with supersaturation production by advection from the dynamic model. The supersaturation over ice in the vapor deposition equation for ice particles was capped by the value at water saturation. It is important to note that the supersaturation diagnosis and ice nucleation are one of the most crucial processes to obtain a proper realization of evolution of ice particles in SHIPS. The excess water produced from the dynamic model depends on the time step used. Therefore, the balancing supersaturation and, in turn, the concentration of ice crystals nucleated with Meyers et al. (1992)'s deposition-condensation nucleation parameterization (a function of supersaturation over ice) depend on the time step. The concentration of nucleated ice crystals play an important role in determining the habit and growth of the nucleated ice crystals given temperature and available vapor under vapor competition. Also, it affects subsequent deposition-condensation nucleation through the supersaturation diagnosis.

2.5.2 Microphysics

In the hybrid-bin method, this study uses 21 and 20 bins for liquid and solid mass spectral, respectively. The parameters used to define bins are listed in Table 2.2. The first bin of the liquid spectrum is set up to have mass boundaries that corresponding to 0.2 and 20 μm diameter (activation transition group). The reason for the relatively large mass ratio of the first bin is that this study uses the time step that is larger than one typically required for supersaturation

prediction, and the supersaturation is diagnosed as explained above. Therefore, with the diagnosed supersaturation the size distribution of haze particles (non-activated droplets) and activated small cloud droplets, which range over the first bin or smaller mass, may not be captured accurately even by using fine resolution of the bins. Following Chen and Lamb (1999), the rest of the liquid spectrum (growth group) is divided into bins by mass boundaries defined as Equation (2.2) with varying ratio $k_{bb}^b = a_{bb}k_{bb}^{b+1}$ in order to capture collection process with higher resolution in larger mass. Similarly, in order to capture collection process of ice particles with small number of bins the mass spectrum was divided into three groups with each group having constant bin boundary ratio. Based on the mass range of different types of solid hydrometeors suggested by empirical mass-diameter relationships and the sensitivity test of collection process, we determined three groups, depositional growth group, collection growth group, and riming growth group.

2.5.3 Initial conditions

Two categories of aerosols, cloud condensation nuclei (CCN) and ice nuclei (IN), are set up as follows. Totally soluble sea salts are assumed for initial CCN, and the modal radius (0.133 μm) and standard deviation (0.210 in log of μm) of lognormal distribution are taken from the accumulation mode of the maritime distribution by Jaenicke (1993). The measured droplet concentration between 4 and 6 km in the altostratus cloud deck during the case study is 10-30 cm^{-3} , according to Woods et al. (2005). Therefore, the CCN vertical concentration was initialized in such a way that it decreases exponentially with height from 25 cm^{-3} at 5 km to 0.5 cm^{-3} at 10.5 km. This gives 876 cm^{-3} at the sea level. The IN vertical concentration was

initialized with 230 L^{-1} throughout the domain as done by CL1, and the radius of the uniform distribution was set to $1.0 \text{ }\mu\text{m}$ radius. UW-NMS was homogeneously initialized with the sounding data at 12Z of December 13th 2001 derived from a rawinsonde launched near Creswell, OR.

2.5.4 Experiment design

Three experiments are designed to demonstrate the habit simulation of SHIPS, to discuss resulting advection of length PPVs, current state of knowledge challenged by mixing of the habit in space, and upper level growth mode of ice crystal with sedimentation effect. Table 2.3 lists the three experiments. They are set up with or without advection and sedimentation of solid hydrometeors and with two different growth regimes of ice crystals in temperature $T = -20^\circ\text{C}$. The ice microphysical processes simulated in these experiments include ice nucleation, vapor deposition and melting processes. Note that aggregation and riming processes are not simulated in this study. The simulations with aggregation and riming processes are described and discussed in chapter 4.

The orographic storm simulation is spun up only with liquid microphysics first and after 12 hours of simulation it reached the quasi-steady state. All the experiments were implemented by turning on ice microphysics from the quasi-steady state obtained with liquid microphysics only. The atmospheric conditions at the quasi-steady state are shown in Figure 2.5. Figure 2.5 (a) shows that the upward vertical motion has developed over the windward slope of the Cascades due to mountain waves indicated by potential temperature. The atmosphere is dried out through subsidence just downwind of the highest peak, but the strong

lee-side mountain wave formation causes clouds developing at high levels. Production of strong rain bands is shifted downwind, while the cloud droplets are nucleated in location of the upward vertical motion. These distributions of liquid hydrometeors correspond to the distribution of 0 % supersaturation over water as shown in Figure 5 (c). As soon as ice microphysics is turned on, ice crystals will take vapor from the moist air and liquid species above 2km which is about $T = 0^{\circ}\text{C}$ (Figure 2.5 (b)).

2.6 Results

2.6.1 Vapor deposition process and advection

For the first test of SHIPS, advection and sedimentation of hydrometeors were turned off and only vapor deposition process was left on in order to isolate the nucleation and growth effects from subsequent mixing (EXP1). Figure 2.6 shows the horizontally averaged a-axis, c-axis and dendritic arm lengths after 20 minutes of vapor deposition process. The peaks of a-axis and c-axis lengths are the order of $10^2\ \mu\text{m}$, and the dendritic arms only exists in the thin layer at 5 km where the ambient temperature satisfies the condition for dendritic arm growth. The Lagrangian simulation of a falling ice crystal under water saturation at 700hPa was performed for comparison (Figure 2.7). The simulated lengths and their spatial distributions in the Eulerian dynamical model closely follow the Lagrangian one except below 2.5 km. The variability of the lengths in the lower level come from the contact freezing nucleation of evaporatively cooled liquid hydrometeors.

For the second test, advection and sedimentation between grid cells in the Eulerian dynamical model were turned on, and the UW-NMS was run with vapor deposition and melting process (EXP2). For diagnostic purpose, the concentration-weighted lengths of three growth axes over the spectrum at each grid cell were calculated as shown in Figure 2.8. After 20 minutes from the quasi-steady state, EXP2 produces a more spread region of dendritic arms than without advection (EXP1). This is because the dendritic arms were produced originally between 4 and 5 km, and then advected upward and downward. Once the radius of hexagonal part and the advected dendritic arm reaches the threshold of $10\ \mu\text{m}$, it begins growing in any condition of temperature and supersaturation over ice.

The ice crystals were diagnosed by length variable components for each mass bin as shown in Figure 2.2 (b). Figure 2.9 shows the concentration of diagnosed habits at each grid cell at 20 minutes of EXP2. The columnar crystals are dominant above 6 km because of (1) high nucleation tendency by deposition-condensation nucleation, and (2) columnar growth mode in $T < -20^\circ\text{C}$. In EXP1 and EXP2 the temperature range between -30 and -20°C is defined as columnar growth mode, and $\Gamma = 1$ below -30°C was assumed for growth of solid columns whose existence was known under low supersaturation (see Pruppacher and Klett (1997)). The vertical distribution of low concentration of plates (order of $10^{-4}\ \text{L}^{-1}$) corresponds to the vertical motion $>1\ \text{m s}^{-1}$ and area of active immersion freezing nucleation. Both of deposition-condensation nucleation and immersion freezing nucleation contributed to the plates and dendrites in levels between 3 and 6 km.

For each diagnosed habit, the concentration-weighted lengths over the spectrum were calculated at each grid cell. Figure 2.10 shows the axis ratios calculated with the average

lengths at 20 minutes of EXP2. The lhs of the figure shows that the flatness of predicted ice crystals ($\phi = c/a$) follows the temperature dependence of growth regime. The flat plates in the locations of height >8km and distance 150 km and 210 km, and of height 3 to 6 km and distance 330 km were produced by evaporating c-axis length more than a-axis length, although they have very small concentration. The dendrites have the minimum horizontally averaged ϕ of 0.25 at 4 km, while the maximum horizontally averaged ϕ of the columnar crystals is about $\phi = 2$ at 2.5 km and 5.5 km. The axis ratio ϕ of dendrites (columns) is larger (smaller) than Takahashi et al. (1991)'s observation at 20 minutes of ice crystal growth. This lack of sharpness in axis ratio was found to come mainly from the large time step used. The right panel of Figure 2.10 shows the axis ratio $\psi = d/a$ at 20 minutes. The simulation produced the broad-branched crystal and dendrites shown by (b) and (d) below 6 km, which roughly matches with the habits observed during the aircraft observation shown in Figure 8 of Woods et al. (2005). (f) of the figure indicate that even some columns have dendritic arms. In SHIPS the conceptual geometry of the capped column is assumed to be the columnar crystal with dendritic arms growing at the a-axis. The aircraft observation shows capped columns, CP1a in 3 to 5 km, above and below of dendritic growth region (Woods et al. 2005). It is known that capped columns grow from columns after they go through plate growth region (Hallett 1984) and Ono (1969) observed them around dendritic growth region. However, quantitative conditions of temperature and moisture necessary for the growth of capped columns have not been investigated yet in laboratory. There are at least 7 known habits that have columnar components, plates, and dendritic feature together as shown in the Magono-Lee diagram. Therefore, at this point the SHIPS uses just simple conditions for dendritic arm growth

described in section 2.4. Quantitative laboratory study of ice crystals have to be done to validate the main and second condition of dendritic arms and the condition of capped column growth, in order to model the transitional growth of habit properly.

2.6.2 Sensitivity of upper level growth mode

In the previous section the 20 minutes simulation of vapor deposition and melting simulation (EXP2) featured a wider vertical area of dendrites and capped column due to advection. This section explores the sensitivity of the habit prediction to the growth mode in the upper level through the sedimentation effect. Figure 2.11 (a) shows the concentration of ice crystals after 90 minutes of vapor deposition and melting processes (EXP2). It increases with height and reaches horizontal mean of $\sim 400 \text{ L}^{-1}$ at 9 km. Compared with the magnitude of the concentration, the concentration tendency of all the ice nucleation processes shown in Figure 2.11 (b) are almost negligible except for the lower levels, left boundary and locations of strong vertical motion. This indicates that high concentration of ice crystals were horizontally and vertically advected, and falling into lower levels. In fact, most of the ice crystals were nucleated during the first 20 minutes of simulation by deposition-condensation nucleation process. After 20 minutes, the process was relatively insignificant due to depletion of available IN inside of the domain and moisture competition with growing ice crystals. On the other hand, immersion freezing and contact freezing processes kept their strength at the locations of strong vertical motion and lower levels.

As shown in Figure 2.12, columnar crystals including capped columns are more abundant than plates and dendrites in terms of mass content. The reason for the dominance can be

explained by inherent growth ratio defined for $T < -20^\circ\text{C}$ along with the high concentration of ice crystals in the upper level. Figure 2.13 shows the inherent growth ratio Γ defined in Equation (2.20). EXP1 and EXP2 assume the inherent growth ratio $\Gamma(T)=1$ for $T < -30^\circ\text{C}$ and columnar growth regime for $-30 < T < -20^\circ\text{C}$. The nucleated ice crystals fell through the columnar growth region and grew to columns as they traveled downwind. Then, the high concentration of falling columns from above overwhelmed planar crystals nucleated and grown in dendritic growth regime ($-16 < T < -12^\circ\text{C}$) and dendritic arms grew on the columnar crystals.

In order to clarify the sensitivity of low and middle level habit distribution to the upper level growth mode and sedimentation, we perform a simple sensitivity test (EXP3), where the planar inherent growth rate at $T = -3.5^\circ\text{C}$ assigned to $T < -20^\circ\text{C}$ (Figure 2.13). As shown in Figure 2.14, the ice crystals in the domain are mostly planar at 90 minutes of the vapor deposition and melting simulation. Note that concentration and mass content of dendrites were increased between 2 and 5 km over the crests of the Cascade. This is because more planar crystals in the upper level above 5.5 km or -20°C were produced and then dendritic arms grew onto the plates falling from the above into the dendritic growth region. Figure 2.15 shows the simulated mass spectrum at horizontal distance of 194 km at three neighboring grid cells in vertical, (a) 4.4 km, (b) 4.0 km and (c) 3.7 km. Plates are further diagnosed into broad-branched crystal if they have $1/3 \leq \psi < 2/3$, and columns are named as capped columns if they have $1/3 \leq \psi$. Five points indicate the linear distribution of a bin, and the vertical line shows that the linear distribution can take on zero concentration ($\text{cm}^{-3}\text{g}^{-1}$) on bin boundaries. The figure suggests that the ice crystals experience the transition of diagnosed habit at 4 km from

broach-branched crystals to dendrites due to the growth of axis ratio to $\psi > 2/3$. The similar dispersion and mode of mass spectra among the three indicate that the ice crystals have similar growth history and lack of crystals with nucleation-size mass implies that they fell from the higher altitude.

The mass content estimated by Woods et al. (2005) based on the crystal habit and particle size distribution measurements along the flight legs ranges from 0.12 to 0.26 gm^{-3} between 4.2 and 6.0 km (see Figure 13 of Woods et al., 2005). Similarly, EXP2 and EXP3 showed increase of mass content below 6 km over the peaks of the Cascade where water-saturated condition was simulated in the model (Figure 2.5). Also, both of EXP2 and EXP3 predicted the same order of mass content with the estimates for the altitude above 4 km where the active vapor deposition process was suggested in the observation. Note that EXP3 shows faster sedimentation of ice crystal mass than EXP2 due to the difference in calculated terminal velocity for the dominant habit. Dendritic ice crystals are associated with a second snow flake diameter maximum at -12 and -17°C , and known to be important to the initiation of an aggregation process through mechanical locking mechanism (p. 608 of Pruppacher and Klett (1997)). Therefore, in addition to the effect on sedimentation, the dominant distribution of broad-branched crystals and dendrites in EXP3 would lead to more efficient aggregation and riming processes than that of columns and capped columns in EXP2.

Figure 2.16 shows the size spectra of solid hydrometeors constructed from linear distributions over bins at horizontal distance of 240 km and six altitudes from (a) 5.8 km to (f) 1.55 km. The spectra become narrow toward lower altitude and the mode shifts to larger mass, which possibly indicates sedimentation effect of larger particles and vapor depositional growth.

Figure 2.16 (b) and (c) show that dendrites, broad-branched crystals, plates and columns co-exist in one spectrum from small mass below dendrite growth area. Comparison with the leg-averaged size spectra shown in Figure 12 of Woods et al. (2005) indicates that the predicted spectra have less concentration of ice particles in size larger than 0.25 mm. The discrepancy may stem from the initialization of ice crystal fields, neglect of aggregation and riming processes and less available moisture. In reality the upper-level front brought ice crystals to the domain, which are missing in our initialization. The observation shows aggregates of dendrites below 4 km. As Woods et al. (2005) noted that the most significant increases of large size particles were associated with dendrites and their aggregates, aggregation process is certainly an important factor in order to predict the spectrum. Also, the 2D simulation does not have the advection of IN and ice crystals, moisture convergence in the direction perpendicular to the cross-section and vertical component of vorticity.

As shown above, the growth mode in $T < -20^{\circ}\text{C}$ can play an important role in simulation of orographic storms due to its high nucleation rate and subsequent sedimentation into altitude of active vapor deposition growth with dendritic growth mode. The sedimentation effect of the upper level crystals simulated by the SHIPS favors the plate growth mode for $T < -20^{\circ}\text{C}$, compared with the aircraft observation. Then, it can be asked: is the columnar growth regime at $T < -20^{\circ}\text{C}$ real? Bailey and Hallett (2004a, 2002) show that between -20 and -40°C plates and plate-like polycrystals dominate the habit, and generally columns appear with low frequency. They pointed out that the use of silver or lead iodide for nucleation in past laboratory experiments resulted in the dominance of columns and thin and thick plates in the temperature range. The aircraft observation of IMPROVE-2 (Woods et al., 2005) also

indicates existence of assemblages of sectors, sideplanes and plates above 4 km colder than -15°C . As for $T < -40^{\circ}\text{C}$, Bailey and Hallett (2004a) show the higher frequency of observation of long columns and formation of bullet rosettes with increase of moisture, but also show plate growth for smaller ice supersaturation. Therefore, in order for the SHIPS to provide further insights on the upper level growth mode, representation of the polycrystal growth modes appears necessary. Research is currently under way to include these effects and will be presented in the next chapter.

2.7 Conclusions

SHIPS is a framework to explicitly evolve mass spectrum of solid hydrometeors, ice crystal habit, and shape and density of solid hydrometeors in a multidimensional CRM by using basic physical principles. Mass spectrum of solid hydrometeors is divided into bins defined by mass boundaries and each bin has a linear distribution. The particle characteristics in a bin is expressed by a set of prognostic variables called particle property variables (PPVs). This study considers the mass content components, length variable components, volume variable components, and aerosol mass content components for the PPVs. PPVs are predicted based on the current atmospheric conditions and the growth history embedded in PPVs. SHIPS eliminates needs to assume the analytical distribution for the whole spectrum, particle properties, idealized category of ice particles, and conversion between those categories. The use of PPVs allows ice particles together with complex 2D or 3D flow fields to build realistic crystal habits and ice types.

This study focused on formulation and test of the simulation of ice nucleation and vapor deposition processes. Explicit simulation of habit by length components showed not only the high potentials of this approach but also missing quantitative knowledge of growth conditions of ice crystals. The notable results are the followings:

- The size and vertical distribution predicted by SHIPS correspond well to Lagrangian simulations at twenty minutes of the simulation where advection and sedimentation of ice crystals were turned off.
- The advection process in the Eulerian dynamics model made growth region of dendrites wider than local atmospheric condition would predict, and revealed the importance of growth conditions of dendritic arms outside of the dendritic regime. The columnar crystals with dendritic arms were diagnosed as capped columns, but the quantitative growth condition of capped columns is not investigated yet in the literature.
- A sensitivity test of upper level growth mode of ice crystal habit in $T < -20^{\circ}\text{C}$ indicated that proper simulation of habit of this range of temperature is crucial in orographic storms due to possible high ice crystal concentration at the level (>6km) and subsequent sedimentation into altitude of active vapor deposition with dendritic growth mode. Comparison of sensitivity tests with the aircraft observation cast doubt on the role of columnar growth regime of hexagonal crystals defined for $-30 < T < -20^{\circ}\text{C}$ in the past literature and the definition of a single growth mode given ambient temperature and moisture in $T < -20^{\circ}\text{C}$.

Because dendrites are a key for aggregation and hence, for physical chain of precipitation process, more quantitative studies of growth condition of dendrites and capped columns must be done while varying temperature and humidity. Prediction of growth of the a-axis and c-axis lengths in SHIPS relies on the mass distribution hypothesis by CL2. Even though the transition of aspect ratio of ice crystals from colder to warmer temperature are observed by Korolev and Isaac (2003); Bailey and Hallett (2004b), the core assumption has to be verified quantitatively in laboratory under realistic scenarios of transitioning pressure, temperature and humidity. For further realistic simulation of ice crystals in $T < -20^{\circ}\text{C}$, length scales representing bullet rosettes and other polycrystalline habits have to be incorporated into SHIPS. Chapter 3 will report on the development of a general model for vapor deposition growth that incorporates the effects of polycrystals in $T < -20^{\circ}\text{C}$.

Ice nucleation processes through homogeneous and heterogeneous nucleation and the super saturation diagnosis with a time step that does not resolve vapor-aerosol interaction can be considered the weakest links of the model. The spatial distribution and concentration of IN and supersaturation determine the habit of ice crystals and their concentration. Even if SHIPS is proved to be useful to predict habit and its evolution in multidimension Eulerian models, the inappropriate ice nucleation process and supersaturation could lead the simulation to the different realization of solid hydrometeors.

SHIPS is the first proposed scheme for multidimensional CRMs to explicitly evolve arbitrary ice crystal habit. The simulations with SHIPS including aggregation and riming processes will be validated and improved over time with direct and indirect observations of solid hydrometeors. This paradigm of microphysics treatment, a continuous-property

approach, offers great potential to atmospheric modeling and data assimilation. In the future, the most likely source of high resolution of microphysical observations will be from our spaceborne remote sensing platforms. The usefulness of their observations, particularly of clouds, lies in our ability to physically model what they observe and so the physical connection with traditional atmospheric state variables. SHIPS is a step in the direction of being able to explicitly model microphysical process and ultimately the attendant radiative effects satellites can observe. In the short term, SHIPS provides new insights and understandings of the complex interactions between ice crystal habit, aerosols and cloud dynamics.

Currently, SHIPS is computationally more expensive than bulk microphysics parameterization. As computational power continues to double every 1.5-2 years, we may be able to afford more integrity on cloud microphysics in CRMs.

Appendix A Mixing PPVs between bins and grid cells

PPVs defined in section 2 have to be advected between mass bins in a physical and statistical manner that preserves the history of a mean particle. This requires that (1) the predicted variable is conserved under mass or concentration weighted mixing, and (2) it produces a mean property of the bin that physically corresponds to the hydrometeor having mass equal to the mean mass of the bin. As the mass content components and aerosol mass content components are proportional to the total mass content of hydrometeors, they automatically satisfy the continuity equation for the total mass content.

A.1 Length variable components

An important numerical challenge is how to transfer the information on lengths of a particle between bins in Eulerian microphysics scheme or between grid cells in the Eulerian dynamics framework. In both cases, a flux conservative numerical formulation represents the transfer as a conservative mixing between the bins in a grid cell or between the same mass bins of surrounding grid cells. For mixing two groups of ice particles, one can write the conservation statement on the length variable component. Then, the mean length of a particle after the mixing must be retrieved. A requirement is that the length of a mean particle resulting from a mixture of particles contained in the two groups must correspond to the length for the mean mass of the mixture. Since the axis ratio and bulk crystal density of ice crystals are also constant within a bin from the implicit mass sorting assumption, ℓ_i^{3b} must be proportional to M_i^b , while cubic of concentration weighted length ℓ_i^{1b} is not. Therefore,

$\bar{l} = \sqrt[3]{\ell_l^{3b} / N^b}$ ($l = a, c, d$) and $\bar{m} = M^b / N^b$ are consistent with the mass-length relationship defined by Equations (2.11) to (2.13). Furthermore, if original and resulting particles have the same bulk crystal density and axis ratios, the conservation statement of ℓ_l^{3b} is equivalent to the mass continuity equation.

In order to show that ℓ_l^{3b} is better than ℓ_l^{1b} with regard to the requirement (2), the lengths of the representative hydrometeors were simulated with the two concentration-weighted variables by the hybrid bin method. These were compared with the lengths of a single ice crystal simulated in a Lagrangian model. Vapor deposition process was simulated under water saturation at -15°C and 700hPa, employing five bins in the hybrid bin method. According to (a) of Figure A 1, the simulation with ℓ_l^{1b} tends to overestimate the maximum dimension, compared to the Lagrangian simulation. As the relative humidity increases, the prediction with ℓ_l^{1b} gives increasingly larger errors (not shown). On the other hand, (b) of Figure A 1 indicates that the simulation with ℓ_l^{3b} gives a solution closer to the Lagrangian model than one with ℓ_l^{1b} . In order to further validate use of ℓ_l^{1b} , property of bulk crystal density and axis ratio of mixed particles is discussed using the example of mixing two groups of particles. By substituting mass-length relationships for each particles group into conservation equations

$N_3 \bar{a}^{-3} = N_1 a_1^3 + N_2 a_2^3$ and $N_3 \bar{c}^{-3} = N_1 c_1^3 + N_2 c_2^3$, one can obtain

$$\bar{\phi}_3 = \left(\frac{W_1 (1 + \phi_2^2)^{3/2} \rho_{c2} \phi_1^3 + W_2 (1 + \phi_1^2)^{3/2} \rho_{c1} \phi_2^3}{W_1 (1 + \phi_2^2)^{3/2} \rho_{c2} + W_2 (1 + \phi_1^2)^{3/2} \rho_{c1}} \right)^{1/3} \quad (\text{A.1})$$

$$\bar{\rho}_{c3} = \frac{(1 + \phi_3^2)^{-3/2}}{W_1(1 + \phi_1^2)^{-3/2} \rho_{c1}^{-1} + W_2(1 + \phi_2^2)^{-3/2} \rho_{c2}^{-1}} \quad (\text{A.2})$$

where $W_1 = M_1 / M_3$ and $W_2 = M_2 / M_3$ ($W_1 + W_2 = 1$). As Equation (A.1) indicates, $\bar{\phi}_3$ is bounded by the original axis ratio ϕ_1 and ϕ_2 , and monotonically changes with W_1 and W_2 as well as ϕ_1 and ϕ_2 . Also, simple calculations show that the quality of boundedness and monotonicity holds for the bulk crystal density $\bar{\rho}_{c3}$.

Examples of the axis ratio and bulk density after mixing the two bins containing planar crystals (group 1) and columnar crystals (group 2) are shown in Figure A 2. From Equation (2.10), the following relationship between the bulk crystal density and axis ratios for the hexagonal crystal model can be derived,

$$\rho_c = \frac{3\sqrt{3}\phi\rho_i^h(1-\psi)(1+\psi)}{k_s(1+\phi^2)^{3/2}} \quad (\text{A.3})$$

If $\rho_i^h = \rho_i$ is assumed, the bulk crystal density ρ_c takes maximum of 0.437 at $\phi = 0.707$ and $\psi = 0$. All particle groups in the cases 1 to 4 except for group 1 of case 3 satisfy the density-axis ratio relationship. For instance, case 1 shows that the case of mixing planar crystals of $\phi_1 = 0.1$, $\rho_{c1} = 0.112$ and columnar crystals of $\phi_2 = 10.0$, $\rho_{c2} = 0.0112$ by about equal amount of mass content gives a representative ice crystal with $\phi_3 = 2.15$, and about $\rho_{c3} = 0.0169$.

Comparison of curves 2 and 5 or 4 and 6 of Figure A 2 (b) indicate that the mixing gives a smaller bulk crystal density ρ_{c3} than one obtained by substituting the resulting axis ratio ϕ_3 into Equation (A.3). This suggests that the mixed particles can satisfy the mass-length

relationship of the hexagonal crystal model only with smaller bulk density ρ_i^h . The discrepancy in the bulk crystal density decreases as the difference of axis ratios between original particle groups decreases.

In conclusion, advection of ℓ_i^{3b} is better than ℓ_i^{1b} or other powered length because it is consistent with mass-length relationship and implicit mass sorting assumption. The resulting average properties after mixing are bounded by properties of original particles and monotonically increase or decrease with mixed amounts.

A.2 Volume variable components

The conservation statement for the concentration weighted volume V_{cs} is equivalent to that for mass conservation only if bins of the original and resulting particles have the same density ρ_s . One can easily show that the bulk sphere density of the representative hydrometeor after mixing should be a bounded and monotonic function of the ρ_s of the original particle groups. The use of V_{cs} as the predicted PPV will result in an estimate of the mean property of the mixed particles in the Eulerian framework.

Appendix B Description of microphysical process models

The development of equations simulating the underlying liquid and ice microphysical processes follows Chen (1992) and CL1. It was modified to integrate the PPVs based on microphysical processes and suited to multidimensional CRMs. In the following, the current version of aerosol microphysics package (Aerosol Prediction System, APS) and liquid-phase

microphysics package (Spectral LIquid Prediction System, SLIPS) of AMPS are described briefly, and then ice phase microphysics package (SHIPS) is described.

B.1 Aerosol microphysics (APS)

Two types of aerosols are predicted: cloud condensation nuclei (CCN) and ice nuclei (IN). This research defines the partially soluble and insoluble aerosols as CCN, while pure insoluble aerosols as IN. Therefore, for each grid cell there are two categories of internally mixed particles. In addition to the concentration and mass content, the soluble mass content is predicted as the PPV for each category. Currently the CCN and IN are predicted with bulk approach due to computational cost associated with bin approach. The accumulation mode of CCN is modeled with log-normal distribution with a fixed standard deviation, and the geometric mean size is diagnosed. IN is assumed to have one uniform size.

The sources and sinks considered are evaporation of hydrometeors and nucleation scavenging. If a hydrometeor evaporates and loses the water mass of the hydrometeor, the aerosol total and soluble mass contents are transferred back into CCN or IN category, depending on the solubility. Once hydrometeors are nucleated, the total mass and soluble mass contents of CCN or IN are transferred into the bin of the nucleated hydrometeors. The deposition-condensation nucleation and contact freezing nucleation are the sink for IN, while CCN is only deprived by cloud droplet activation. The fraction of activated cloud droplets is calculated with use of the dry critical radius formulated by Abdul-Razzak et al. (1998) based on Kohler curve for mixed aerosols .

B.2 Liquid-phase microphysics (SLIPS)

The liquid-phase mass spectrum is divided into bins that are defined with mass boundaries. The prognostic variables are concentration, mass content, and also aerosol mass content and soluble aerosol mass content are predicted as PPVs. The hybrid bin method is also applied to the liquid phase.

The processes simulated for the liquid spectrum is vapor deposition process, collision-coalescence process, and collision-breakup process. The vapor deposition onto the activated droplets is calculated to compensate the time step. The CCN whose radius are between the critical radius and 99.5 percentile of the lognormal size distribution are activated and condensed into multiple liquid bins. This enables the collision process among liquid bins to start. The autoconversion process within a bin is not considered in this research. The collision processes are modeled by quasi-stochastic approach, and coalescence and breakup processes are modeled based on Low and List (1982). There is no prediction of chemical reactions, which is different from CL1.

B.3 Ice-phase microphysics (SHIPS)

B.3.1 ICE NUCLEATION

The ice nucleation process assigns the produced mass only to ice crystal mass content component M_I . Meyers et al. (1992)'s parameterization is used to estimate the number of pristine ice crystals due to deposition and condensation freezing nucleation. The concentration tendency (cm^{-3}) is given as

$$\frac{\partial N}{\partial t} = \frac{\min(10^{-3} \exp(a_1 + b_1 100s_{vi}), N_{IN})}{\delta t} \quad (\text{B.1})$$

where $a_1 = -0.639$, $b_1 = 0.1296$, and s_{vi} is the supersaturation over ice. It is bounded by concentration of IN, N_{IN} , predicted in the model. Similarly to Thompson et al. (2004), the conditions to turn on the nucleation are determined based on Schaller and Fukuta (1979): temperature is less than -5°C and it is supersaturated over water, or it is more than 5% supersaturation over ice. The deposition and condensation freezing nucleation is a sink for IN. Initially, the radius and mass of the nucleated ice particle are set to those diagnosed from the uniform distribution of IN category predicted at the grid cell. This research calculates the growth of nucleated ice crystals by vapor deposition during the time step of nucleation with use of s_{vi} , which is obtained from saturation adjustment described in section 2.5. The length and mass growth of the nucleated crystals are calculated according to the local temperature and moisture as explained in section 2.4. The tendency of ice crystal mass content component is calculated by multiplying the mass change due to the IN and vapor deposition onto it by concentration tendency. The tendencies of length and volume components are formed by multiplying the cubic lengths and volume by concentration tendency. The tendencies of the nucleated mass content and concentration as well as PPVs are given to the mass bin that encompasses the resulting mean mass.

Contact nucleation is modeled using the model of Young (1974) that considers contacts by Brownian diffusion, thermophoresis and diffusiophoresis, following Cotton et al. (1986)'s treatment. Contact nucleation represents a sink to both the liquid hydrometeors and IN. The

ice crystal created by contact nucleation process have mass corresponding to the freezing liquid hydrometeor, and conserve the axis ratio of semi-major and semi-minor length of the freezing liquid hydrometeor which is diagnosed by empirical formula of Chuang and Beard (1990).

The lengths are obtained from mass-length relation of hexagonal crystal $m = 3\sqrt{3}\phi\alpha^3\rho_i$.

Therefore, contact nucleation can produce relatively large planar crystals from drizzles in warm temperature.

Immersion freezing is modeled based on Bigg (1953)'s stochastic hypothesis, following Reisin et al. (1996):

$$N_{fl}^b = N_l^b \left\langle 1 - \exp \left\{ - \frac{\bar{m}_l^b}{\rho_w} \bar{A} \exp[\bar{B}(T_0 - T)] \delta t \right\} \right\rangle \quad (\text{B.2})$$

where N_{fl}^b is the number of frozen drops of the b th bin in the mass spectrum of liquid hydrometeors, the parameters are $\bar{A} = 10^{-4} \text{ cm}^{-3} \text{ s}^{-1}$ and $\bar{B} = 0.66 \text{ deg}^{-1}$, \bar{m}_l^b is the mean mass of b th bin. The axis lengths and axis ratio of the nucleated ice crystal are calculated in the same way as contact nucleation. Then, concentration and mass content of frozen liquid hydrometeors as well as PPVs are transferred to mass spectrum of solid hydrometeors, using the sub distributions obtained with the two moments. Tendencies by immersion freezing are given by newly transferred prognostic variables divided by time step. The immersion freezing is a sink for liquid hydrometeors.

The secondary nucleation known as Hallett-Mossop mechanism is not considered in this study since we do not consider riming process. Finally, the tendency by ice nucleation process of SHIPS is given by adding tendencies of the three processes.

B.3.2 MELTING-SHEDDING PROCESS

For this paper the melt-water mass content component is not predicted. Heat tendency by melting is estimated based on the steady state of the heat budget:

$$\left(\frac{\partial q}{\partial t}\right)_{melting} = \left(\frac{\partial q}{\partial t}\right)_{diff,h} + \left(\frac{\partial q}{\partial t}\right)_{others} \quad (\text{B.3})$$

where the term on the lhs is the heat tendency by melting, the first term on the right hand side is the tendency by diffusion of heat through air, and the second term is the heat tendency by other processes. This research considers only the heating rate due to vapor deposition for “other” processes, but it may include freezing by riming process and heat extracted for lowering temperature of rimed ice to temperature of parent ice surface. If the ambient temperature is above freezing ($T > T_0$), then it is reasonably assumed that the surface of solid hydrometeor is coated by at least thin layer of liquid water. Substituting

$$\left(\frac{\partial q}{\partial t}\right)_{diff,h} = 4\pi Ck_a f_h (T - T_s) \quad (\text{B.4})$$

$$\left(\frac{\partial q}{\partial t}\right)_{diff,m} = 4\pi CL_e G(T, p) f_v s_{vw} \quad (\text{B.5})$$

into Equation (B.3) with surface temperature $T_s = T_0$ gives the melting tendency for the representative hydrometeor in a bin:

$$\frac{dm_w}{dt} = \left(\frac{dq}{L_f dt} \right)_{melting} \quad (\text{B.6})$$

If the mass component m_w is predicted, and it exists, then the same approach can be used to obtain the tendency.

In cases where it is subfreezing condition ($T < T_0$) and melting water does not exist, the melting tendency can be estimated by assuming it is 0 first in Equation (B.3). Then, T_s can be calculated from the heat balance. If $T_s > T_0$, the hydrometeor is melting and it is assumed that $T_s = T_0$. Then, the melting tendency is obtained by the method discussed above.

Otherwise, the tendency is zero.

The melt water m_w on the ice crystal over the time step is obtained by Equation (B.6). Knowing the mass of dry core of an ice crystal $m_{icore} = m - m_w$, the a-axis and c-axis lengths of the core are calculated from Equations (2.11) to (2.13) with assumption of the same bulk crystal density and axis ratios as before melting. The shedding condition, shedded mass m_{shed} , and size distribution of shedded drops are treated as done by Chen (1992) and CL1. The circumscribing sphere volume after melting and shedding is estimated as

$$V_{cs}' = \max[(m_w - m_{shed}) / \rho_w + m_{icore} / \rho_i, m_{icore} / \rho_c].$$

If the shedding occurs, the tendency of mass content can be given by multiplying $-m_{shed} / \delta t$ by concentration of ice particles. The concentration tendency is 0, unless all mass of the representative hydrometeor is melted.

Appendix C List of Symbols

a	a-axis length of hexagonal crystal
a_{bb}	ratio of mass ratios of adjacent boundaries
a_h	diameter of hexagonal part of crystal without dendritic arm lengths
A_e, A_c	area defined by the ratio of projected area of a hydrometeor, and that of circumscribing spheroid, respectively
c	c-axis length of hexagonal crystal
$C, C(a, c)$	capacitance of an ice particle, capacitance model of a spheroid with a and c axis lengths
d	dendritic arm length of hexagonal crystal
f_h, f_v	mean ventilation coefficient for heat diffusion and vapor diffusion
f_{kn}	mass-transfer correction factor for kinetic process
$G(T, p)$	thermodynamic function
k	slope of linear distribution within a mass bin
k_a	heat conductivity of air
k_{bb}^b	arbitrary mass ratio of adjacent boundaries
k_s	coefficient associated with sphere volume
K_H	eddy mixing coefficients for scalars
l_d	characteristic length of the hydrometeor

l_f	order of the high order filter
L_e, L_f	latent heat of evaporation of water, and melting of ice per unit mass
ℓ_l^{1b}, ℓ_l^{3b}	general symbol for concentration weighted length and concentration weighted cubic length for b th bin, respectively
$\ell_a^{3b}, \ell_c^{3b}, \ell_d^{3b}$	concentration weighted cubic a-axis length, cubic c-axis length, cubic dendritic arm length for b th bin, respectively
n_0	$n(m)$ evaluated at m_0
$n(m)$	number of particles per unit volume and mass
N^b	concentration of particles (number of particles per unit volume of air) in b th mass bin
N_{BIN}	total number of mass bin
N_i	concentration of particle group i
N_l^b	concentration of b th bin in the liquid spectrum
N_{IN}	number concentration of IN
N_{Re}	Reynolds number
m	mass of a hydrometeor
$m_{apt}, m_{aps}, m_{api}$	total, soluble, and insoluble mass of aerosols within a solid hydrometeor
m_{icore}	mass of dry core of an ice crystal after melting
m_{shed}	mass of shedded water from an ice particle
m_l	mass component produced by vapor deposition process onto an ice

	crystal
m_R	mass component produced by riming process for a solid hydrometeor
m_A	mass component produced by aggregation process for a solid hydrometeor
m_W	mass component produced by melting on a solid hydrometeor
\bar{m}	mean mass defined by M^b / N^b
m_0	mean of left and right mass boundaries
m_1^b, m_2^b	left and right mass boundaries of b th bin
p	atmospheric pressure
q	heat
$q_{ice}^{n,b}$	specific quantity of the ice parameter n in mass bin b
q_{rat}	area ratio A_e / A_c
s_{vw}, s_{vi}	supersaturation over water and ice
$S^{n,b}$	source term by microphysics processes
T	temperature of ambient atmosphere
T_s	surface temperature of a hydrometeor
T_0	melting temperature of ice
u_i	velocity components
V_{cs}	volume of the spheroid circumscribing a hydrometeor

U_i^b	terminal velocity of the representative hydrometeor in b th bin
V_{cs}^b	concentration weighted circumscribing volume
W_i	weights defined by mass content for group i
x_i	the Cartesian grid unit tensor
X	Davis number
α	aspect ratio defined as ratio of semi-minor axis length to semi-major axis length of a spheroid circumscribing a hydrometeor
$\Gamma(T)$	inherent growth ratio
δt	time step for microphysical processes
η_a	dynamic viscosity
ν	high order numerical mixing coefficient
ρ	density of moist air
ρ_c	bulk crystal density (mass of an ice crystal per volume of a sphere circumscribing the crystal)
ρ_i, ρ_w	density of ice and water
ρ_i^h	bulk density of the hexagonal crystal model
ρ_s	bulk sphere density (mass of particle per volume of a sphere circumscribing the particle)
M_{apt}^b, M_{aps}^b	total and soluble mass content (mass of particles per unit volume of air) of aerosols within solid hydrometeors in b th mass bin

M_i	mass content of particle group i
$M_{ice}^{n,b}$	quantity per unit volume of air of the ice parameter n in mass bin b
M^b	mass content of b th mass bin
$M_I^b, M_R^b, M_A^b,$	mass content components (integrated mass components over mass for a
M_W^b	bin)
ϕ, ψ	axis ratios of hexagonal ice crystal, c/a and d/a ; axis ratios are defined as the ratio of lengths along crystallographic axes of an ice crystal
–	property of the representative hydrometeor at mean mass of the bin or group such as \bar{a} , \bar{c} , $\bar{\rho}_c$, and $\bar{\phi}$

References, Chapter 2

- Abdul-Razzak, H., S. J. Ghan, and C. Rivera-Carpio, 1998: A parameterization of aerosol activation 1. single aerosol type. *J. Geophys. Res.*, 103, 6123–6131.
- Auer, A. H. and D. L. Veal, 1990: The dimension of ice crystals in natural clouds. *J. Atmos. Sci.*, 27, 919–926.
- Bailey, M. and J. Hallett, 2002: Nucleation effects on the habit of vapour grown ice crystals from -18 to -42°C . *Q. J. R. Meteorol. Soc.*, 128, 1461–1483.
- , and ———, 2004a: Growth rates and habits of ice crystals between -20° and -70°C . *J. Atmos. Sci.*, 61, 514–543.
- , and ———, 2004b: A new habit diagram and mass parameters for atmospheric ice crystals from -20° and -70°C . *14th International Conference on Clouds and Precipitation*, Bologna, Italy, International Commission on Clouds and Precipitation, 1, 703–706.
- Bigg, E. K., 1953: The formation of atmospheric ice crystals by the freezing of droplets. *Quart. J. Roy. Meteor. Soc.*, 79, 510–519.
- Bohm, H. P., 1992: A general hydrodynamic theory for mixed-phase microphysics. Part I: Drag and fall speed of hydrometeors. *Atmos. Res.*, 27, 253–274.
- Borys, R., D. Lowenthal, S. Cohn, and W. Brown, 2003: Mountaintop and radar measurements of anthropogenic aerosol effects on snow growth and snowfall rate. *Geophys. Res. Lett.*, 30, 45–1–45–4.
- Chen, J.-P., 1992: Numerical simulation of the redistribution of atmospheric trace chemicals through cloud processes. Ph.D. thesis, The Pennsylvania State University, 343 pp.
- , and D. Lamb, 1994a: Simulation of cloud microphysical and chemical processes using a multicomponent framework. Part I: Description of the microphysical model. *J. Atmos. Sci.*, 51, 2613–2630.
- , and ———, 1994b: The theoretical basis for the parameterization of ice crystal habits: Growth by vapor deposition. *J. Atmos. Sci.*, 51, 1206–1221.
- , and ———, 1999: Simulation of cloud microphysical and chemical processes using a multicomponent framework. Part II: Microphysical evolution of a wintertime orographic cloud. *J. Atmos. Sci.*, 56, 2293–2312.

- Chuang, C. C. and K. V. Beard, 1990: A numerical model for the equilibrium shape of electrified raindrops. *J. Atmos. Sci.*, 47, 1374–1389.
- Colella, P. and P. R. Woodward, 1984: The piecewise parabolic method (PPM) for gas-dynamical simulations. *J. Comput. Phys.*, 87, 171–200.
- Cotton, W. R., M. S. Stephens, T. Nehr Korn, and G. J. Tripoli, 1982: The Colorado state university cloud/mesoscale model-1982. Part II—an ice phase parameterization. *J. Rech. Atmos.*, 16, 295–320.
- , G. J. Tripoli, R. M. Rauber, and E. A. Mulvihill, 1986: Numerical simulation of the effects of varying ice crystal nucleation rates and aggregation processes on orographic snowfall. *J. Clim. and Appl. Meteor.*, 25, 1658–1680.
- Farley, R. and H. Orville, 1986: Numerical modeling of hailstorms and hailstone growth. Part I: Preliminary model verification and sensitivity tests. *J. Appl. Meteor.*, 25, 2014–2035.
- Grabowski, W. W., 2006: Sixth WMO international cloud modeling workshop. *Bull. Amer. Meteor. Soc.*, 87, 639–642.
- Hallett, J., 1984: How snow crystals grow. *Amer. Sci.*, 72, 582–589.
- Heymsfield, A. J., S. Lewis, A. Bansemer, J. Iaquinta, L. M. Miloshevich, M. Kajikawa, C. Twohy, and M. R. Poellot, 2002: A general approach for deriving the properties of cirrus and stratiform ice cloud particles. *J. Atmos. Sci.*, 59, 3–29.
- Jaenicke, R., 1993: Tropospheric aerosols. *Aerosol-Cloud-Climate Interactions*, P. V. Hobbs, ed., Academic Press, 1–31.
- Kessler, E., 1969: *On the Distribution and Continuity of Water Substance in Atmospheric Circulations*, *Meteor. Monogr.*, No. 32, Amer. Meteor. Soc., 84 pp.
- Kobayashi, T., 1961: The growth of snow crystals at low supersaturations. *Phil. Mag.*, 6, 1363–1370.
- Koenig, L. R. and F. W. Murray, 1976: Ice-bearing cumulus cloud evolution: Numerical simulation and general comparison against observations. *J. Appl. Meteor.*, 15, 747–762.
- Kogan, Y. L., 1991: The simulation of a convective cloud in a 3-D model with explicit microphysics. Part I: Model description and sensitivity experiments. *J. Atmos. Sci.*, 48, 1160–1189.
- Korolev, A. and G. Isaac, 2003: Roundness and aspect ratio of particles in ice clouds. *J. Atmos. Sci.*, 60, 1795–1808.

- Lin, Y.-L., R. D. Farley, and H. D. Orville, 1983: Bulk parameterization of the snow field in a cloud model. *J. Appl. Meteor.*, 22, 1065–1092.
- Low, T. and R. List, 1982: Collision, coalescence and breakup of raindrops. Part II: Parameterization of fragment size distributions. *J. Atmos. Sci.*, 39, 1607–1619.
- Lynn, B. H., A. P. Khain, J. Dudhia, D. Rosenfeld, A. Pokrovsky, and A. Seifert, 2005: Spectral (bin) microphysics coupled with a mesoscale model (MM5). Part I: Model description and first results. *Mon. Wea. Rev.*, 133, 44–58.
- Magono, C. and C. W. Lee, 1966: Meteorological classification of natural snow crystals. *J. Frac. Sci. Hokkaido Univ. Ser. 7, 2*, 321–335.
- Meyers, M. P., P. J. Demott, and W. R. Cotton, 1992: New primary ice-nucleation parameterizations in an explicit cloud model. *J. Appl. Meteor.*, 31, 708–721.
- Mitchell, D. L., 1996: Use of mass- and area- dimensional power laws for determining precipitation particle terminal velocities. *J. Atmos. Sci.*, 53, 1710–1723.
- , and A. J. Heymsfield, 2005: Refinements in the treatment of ice particle terminal velocities, highlighting aggregates. *J. Atmos. Sci.*, 62, 1637–1644.
- Ono, A., 1969: The shape and riming properties of ice crystals in natural clouds. *J. Atmos. Sci.*, 26, 138–147.
- Orville, H. D. and F. J. Kopp, 1979: Numerical simulation of the life history of a hailstorm. *J. Atmos. Sci.*, 34, 1596–1618.
- Ovtchinnikov, M. and Y. L. Kogan, 2000: An investigation of ice production mechanisms in small cumuliform clouds using a 3D model with explicit microphysics. Part I: Model description. *J. Atmos. Sci.*, 57, 2989–3003.
- Pruppacher, H. R. and J. D. Klett, 1997: *Microphysics of Clouds and Precipitation*. Kluwer Academic, 914 pp.
- Reisin, T., Z. Levin, and S. Tzivion, 1996: Rain production in convective clouds as simulated in an axisymmetric model with detailed microphysics. Part I : Description of the model. *J. Atmos. Sci.*, 53, 497–519.
- Schaller, R. and N. Fukuta, 1979: Ice nucleation by aerosol particles: Experimental studies using a wedge-shaped ice thermal diffusion chamber. *J. Atmos. Sci.*, 36, 1788–1802.
- Takahashi, T., 1976: Hail in an axisymmetric cloud model. *J. Atmos. Sci.*, 33, 1579–1601.

- Takahashi, T., T. Endoh, G. Wakahama, and N. Fukuta, 1991: Vapor diffusional growth of free-falling snow crystals between -3 and -23°C . *J. Meteor. Soc. Japan*, 69, 15–30.
- Thompson, G., R. M. Rasmussen, and K. Manning, 2004: Explicit forecasts of winter precipitation using an improved bulk microphysics scheme. Part I: Description and sensitivity analysis. *Mon. Wea. Rev.*, 132, 519–542.
- Tripoli, G. J., 1992: A nonhydrostatic mesoscale model designed to simulate scale interaction. *Mon. Wea. Rev.*, 120, 1342–1359.
- , and W. R. Cotton, 1981: The use of ice-liquid water potential temperature as a thermodynamic variable in deep atmospheric models. *Mon. Wea. Rev.*, 109, 1094–1102.
- Woods, C. P., M. T. Stoelinga, J. D. Locatelli, and P. V. Hobbs, 2005: Microphysical processes and synergistic interaction between frontal and orographic forcing of precipitation during the December 13, 2001 IMPROVE-2 event over the Oregon cascades. *J. Atmos. Sci.*, 62, 3493–3519.
- Young, K. C., 1974: A numerical simulation of wintertime, orographic precipitation: Part I. description of model microphysics and numerical techniques. *J. Atmos. Sci.*, 31, 1735–1748.

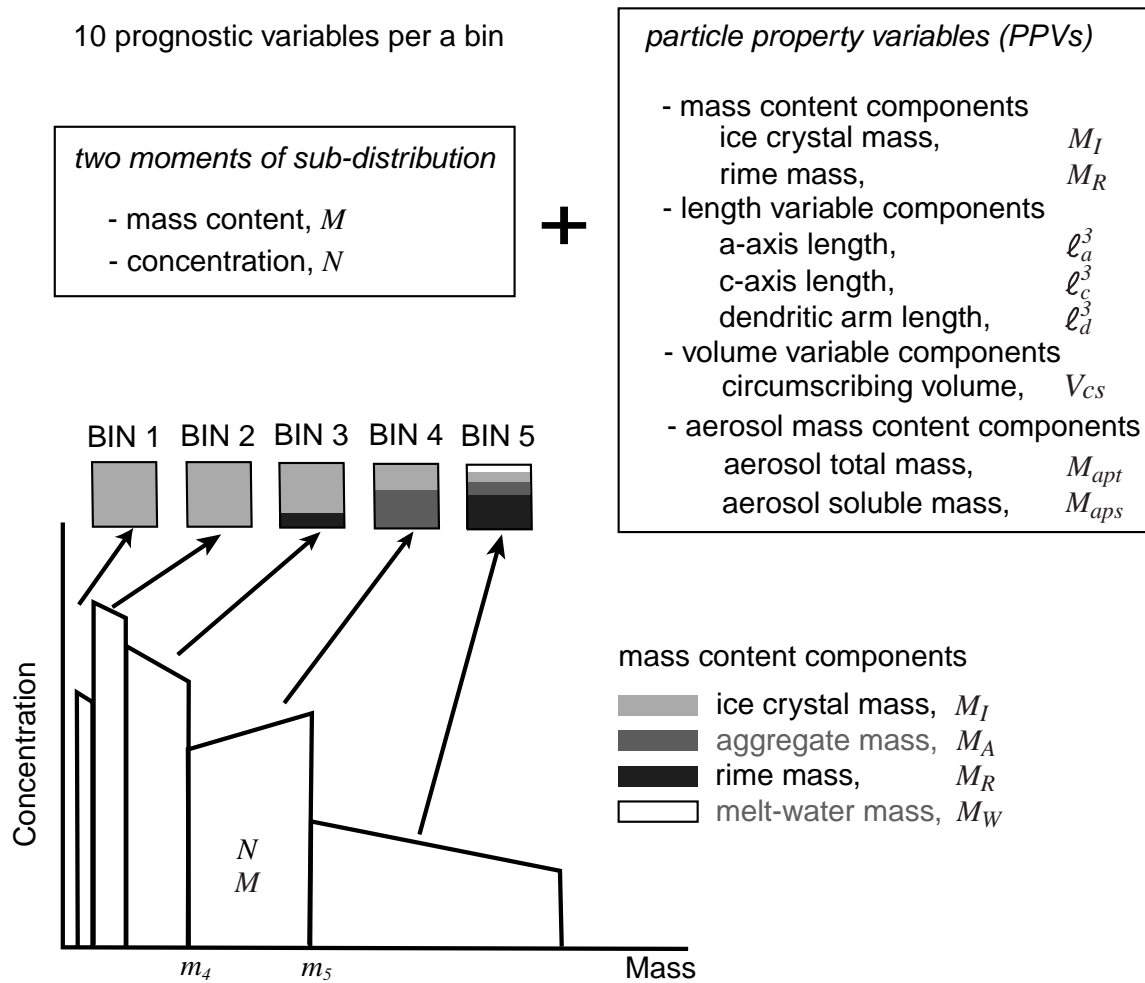


Figure 2.1 Schematic of SHIPS. In this example, the mass spectrum of ice particles is divided into five mass bins. The mass content M of each bin consists of four mass content components, M_I , M_A , M_R , and M_W , shown by the square boxes with BIN number above the mass spectrum. From the mass content components, one can diagnose the type of solid hydrometeor for a bin. The largest bin may be diagnosed as graupel because of the dominant rime mass component. The variables in the top two boxes are prognostic variables. Length variable components are used to diagnose the geometry of an ice crystal or habit in an ice particle. Volume variable component is used to diagnose the density and maximum dimension of ice particles. Aerosol mass content components gives solubility of aerosols within an ice particle. Two moments of sub-distribution, concentration N and mass content M define the sub distribution within a bin.

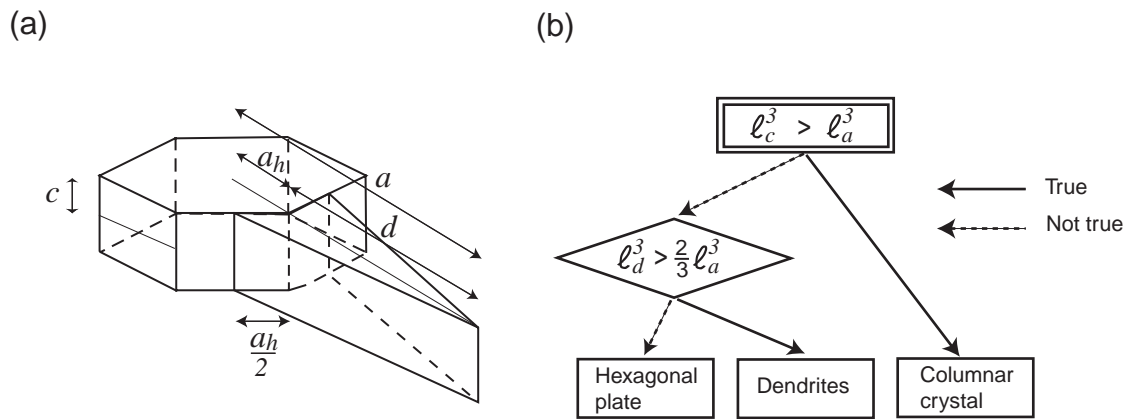


Figure 2.2 Diagnosis of habit of the representative hydrometeor for a bin. (a) is the dimension of the hexagonal crystal model, and (b) is the diagnosis flow chart.

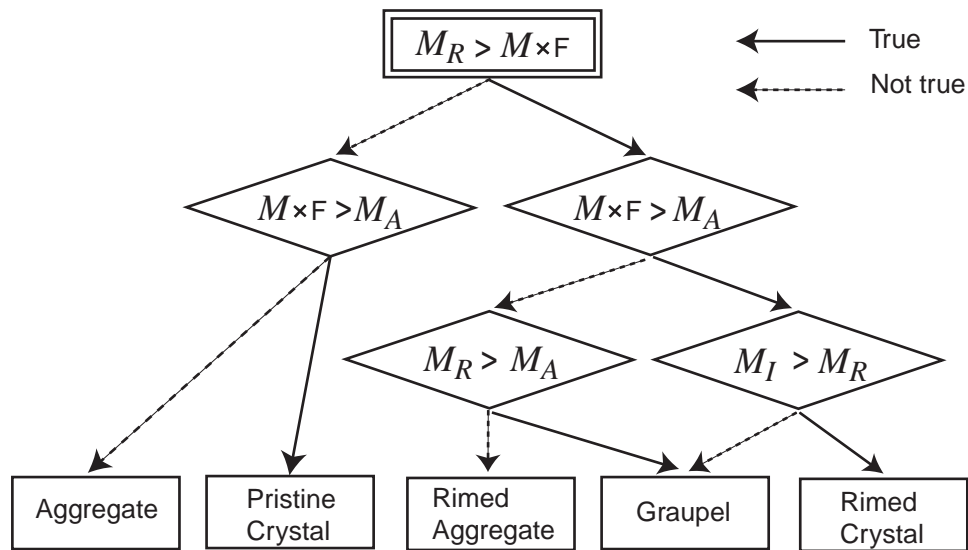


Figure 2.3 Diagnosis of type of the representative hydrometeor for a bin. F is set to 0.1 for this study.

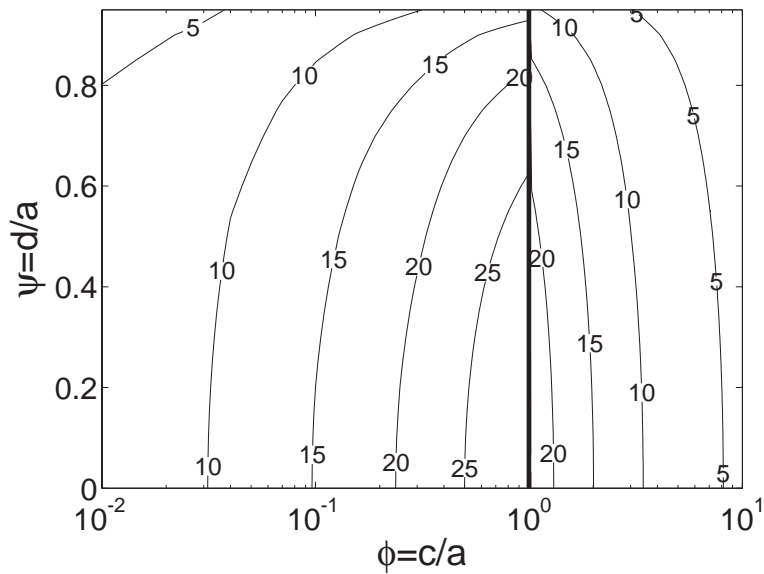


Figure 2.4 Example of terminal velocity that is a continuous function of axis ratios $\phi = c / a$ and $\varphi = d / a$ with use of the hexagonal crystal model. The mass of the crystal used for the calculation has the mass of the hexagonal crystal model with a-axis length $50 \mu\text{m}$ and axis ratio $\phi = 1.0$. The unit of velocity is cm s^{-1} .

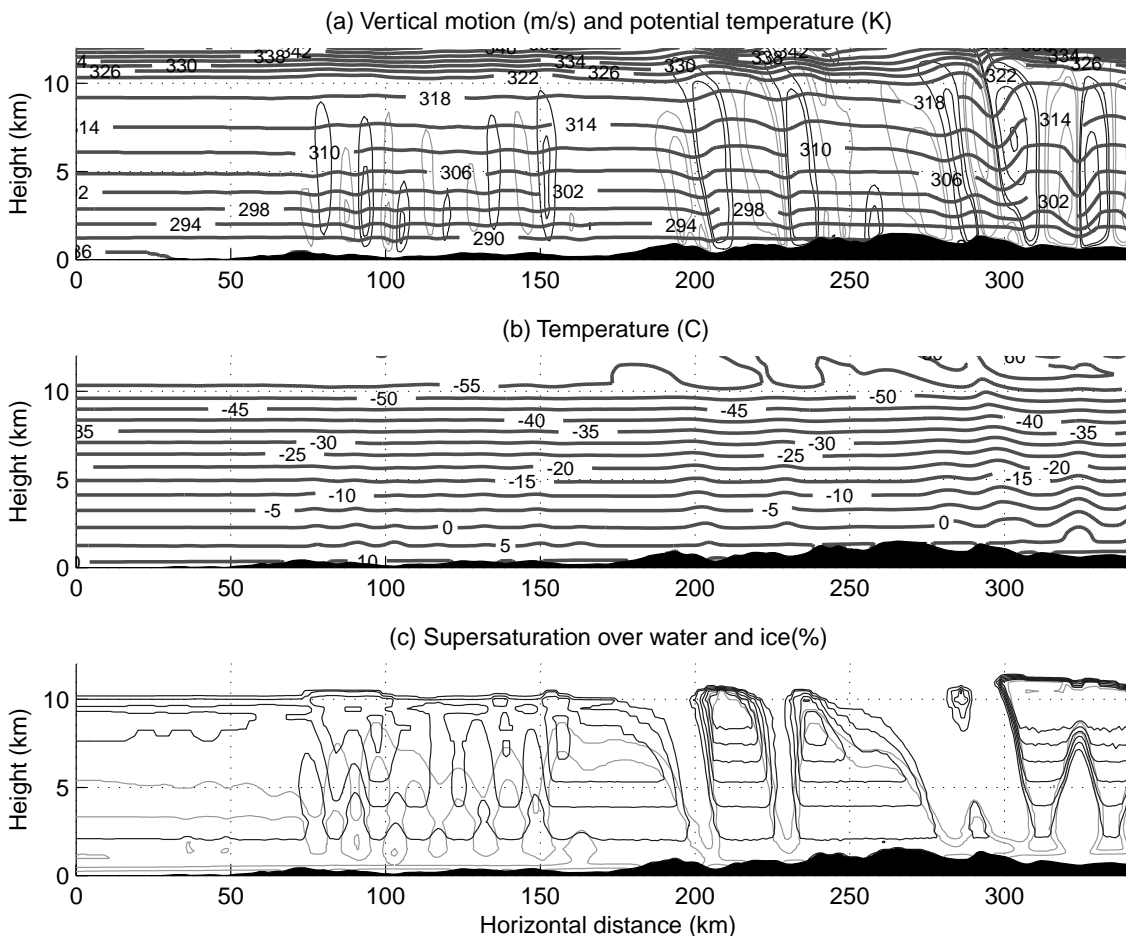


Figure 2.5 Quasi-steady state after 12 hours of run only with liquid species. Vertical motion (m s^{-1}) and potential temperature (K) are shown in the panel (a). Dark (light) thin line is upward (downward) vertical motion. The contours are given at 0.5, 1, 3, 5 and -0.5, -1, -3, -5. Temperature is shown in the panel (b). Supersaturations over ice and water are shown in the panel (c). Light (dark) thin line is supersaturation over water (ice) with contours of -10 and 0% (0 to 50%) by 10% increment.

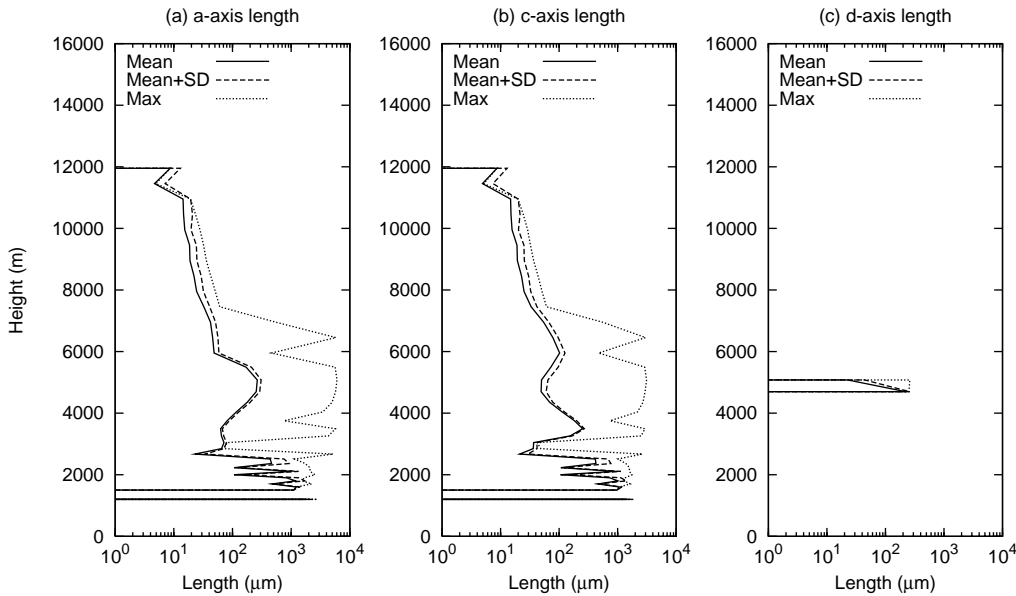


Figure 2.6 Horizontally averaged axis lengths of ice crystals at 20 minutes of vapor deposition simulation without advection and sedimentation (EXP1). “Mean” is the horizontally averaged value, “SD” is the standard deviation, and “Max” is the maximum value.

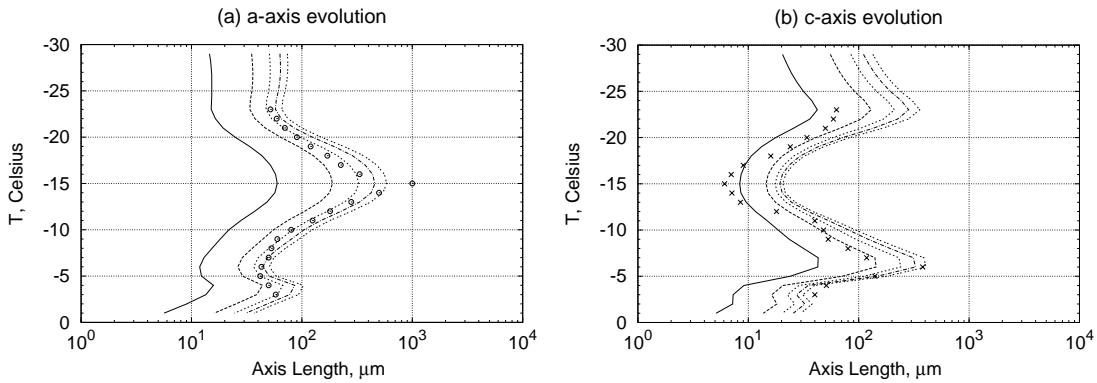


Figure 2.7 Lagrangian simulation of a-axis and c-axis length under water saturation. Time is 1, 5, 10, 15, and 20 minutes from the left, and circle and cross are observation by Takahashi et al.(1991).

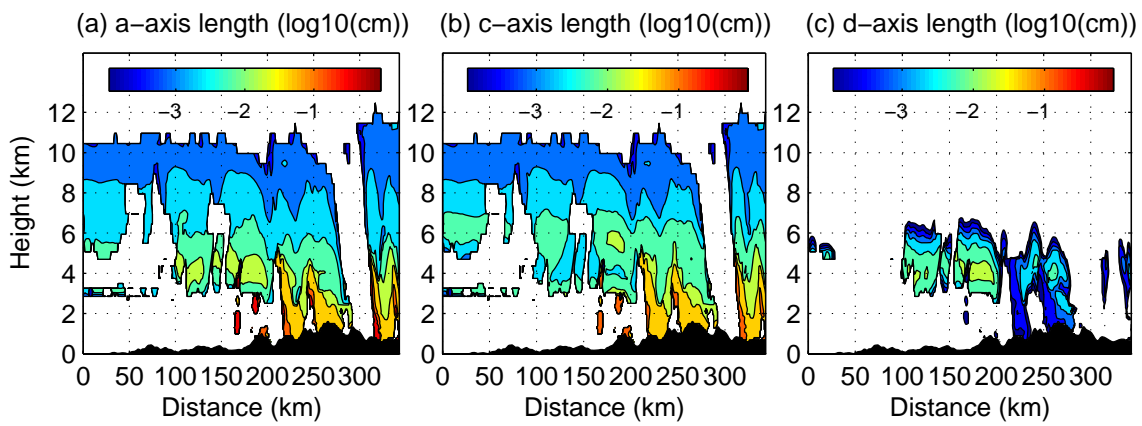


Figure 2.8 Comparison of average axis lengths at 20 minutes of vapor deposition simulation with advection and sedimentation (EXP2). The length is given in logarithm of cm.

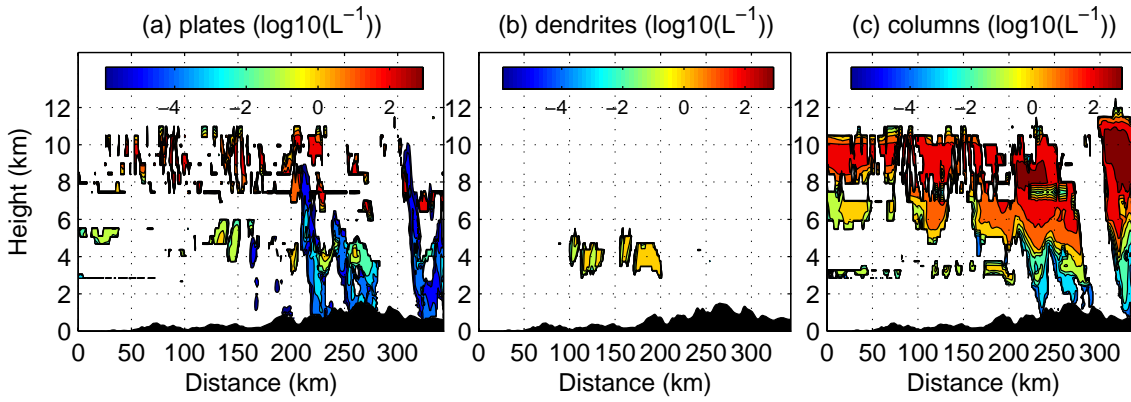


Figure 2.9 Comparison of concentrations at 20 minutes of vapor deposition simulation with advection and sedimentation (EXP2). The concentration is given in logarithm of L^{-1} .

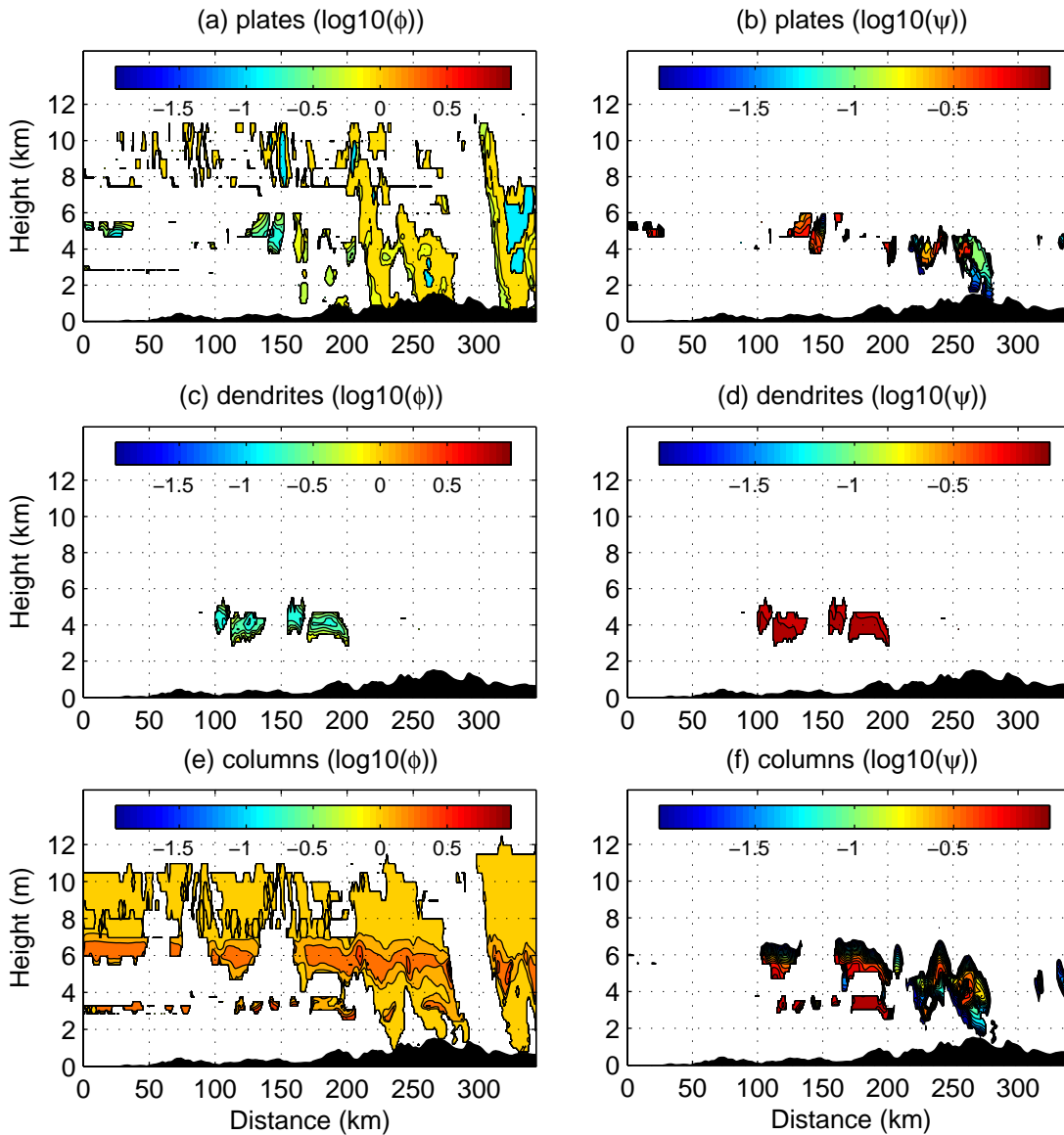


Figure 2.10 Comparison of average axis ratios at 20 minutes of vapor deposition simulation with advection and sedimentation (EXP2). The left-hand side shows logarithm of $\phi = c/a$ and the right-hand side $\phi = d/a$.

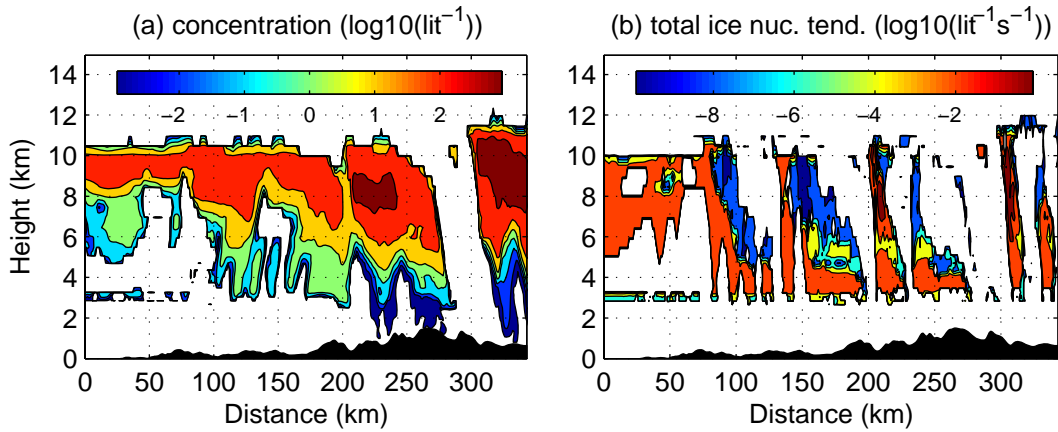


Figure 2.11 Comparison of (a) concentration of ice crystals ($\log_{10}(L^{-1})$) and (b) concentration tendency by all the ice nucleation processes ($\log_{10}(L^{-1} s^{-1})$) after 90 minutes of vapor deposition simulation (EXP2).

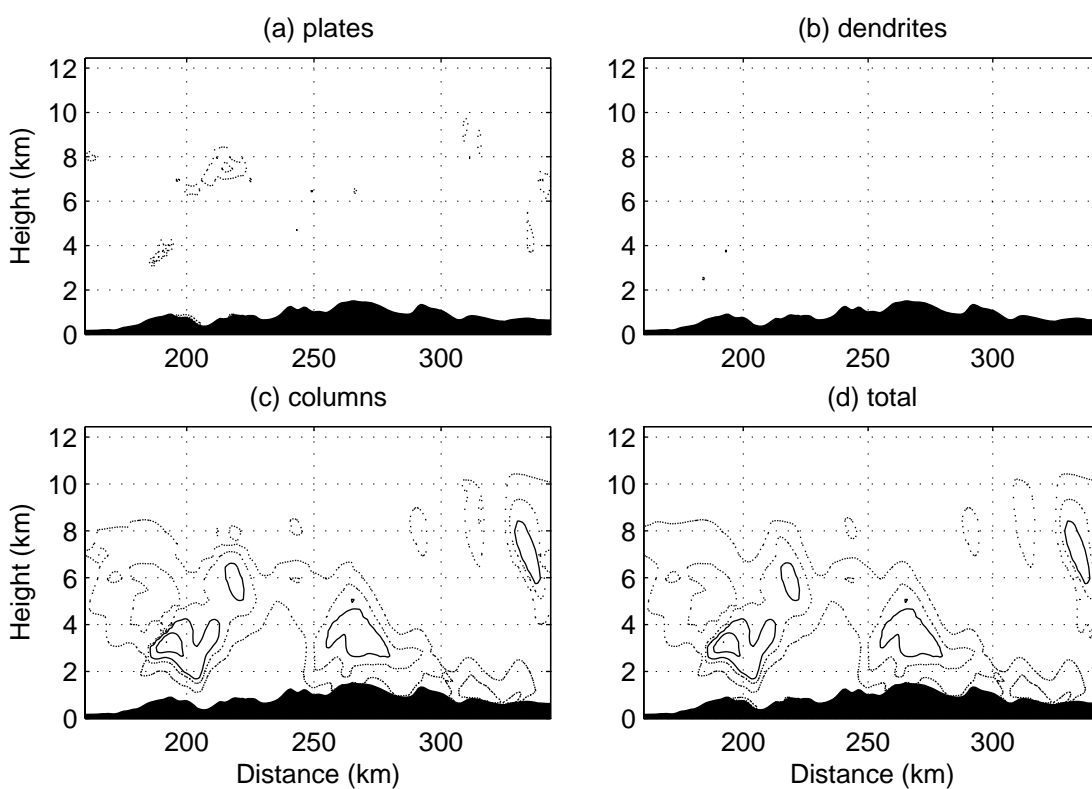


Figure 2.12 Comparison of mass contents for diagnosed habits after 90 minutes of vapor deposition simulation (EXP2). The dots contours are 0.01, and 0.05 (g m^{-3}) and the solid contours 0.1, 0.2, and 0.3 (g m^{-3}).

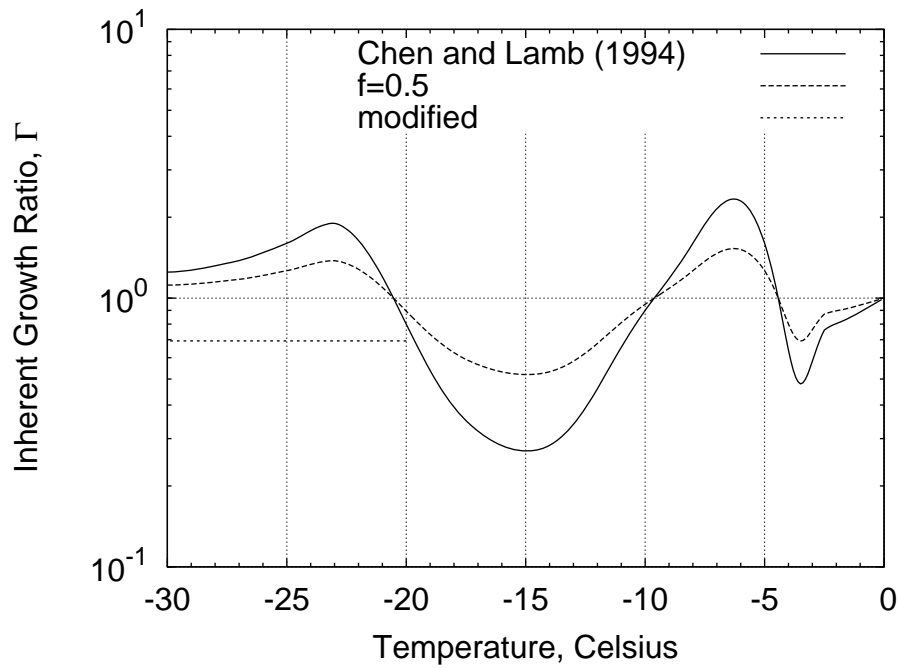


Figure 2.13 Inherent growth ratio. Solid line is Chen and Lamb (1994b), broken line is our parameterization to obtain convergence solution with smaller time step, and thin broken line is defined for sensitivity test EXP3.

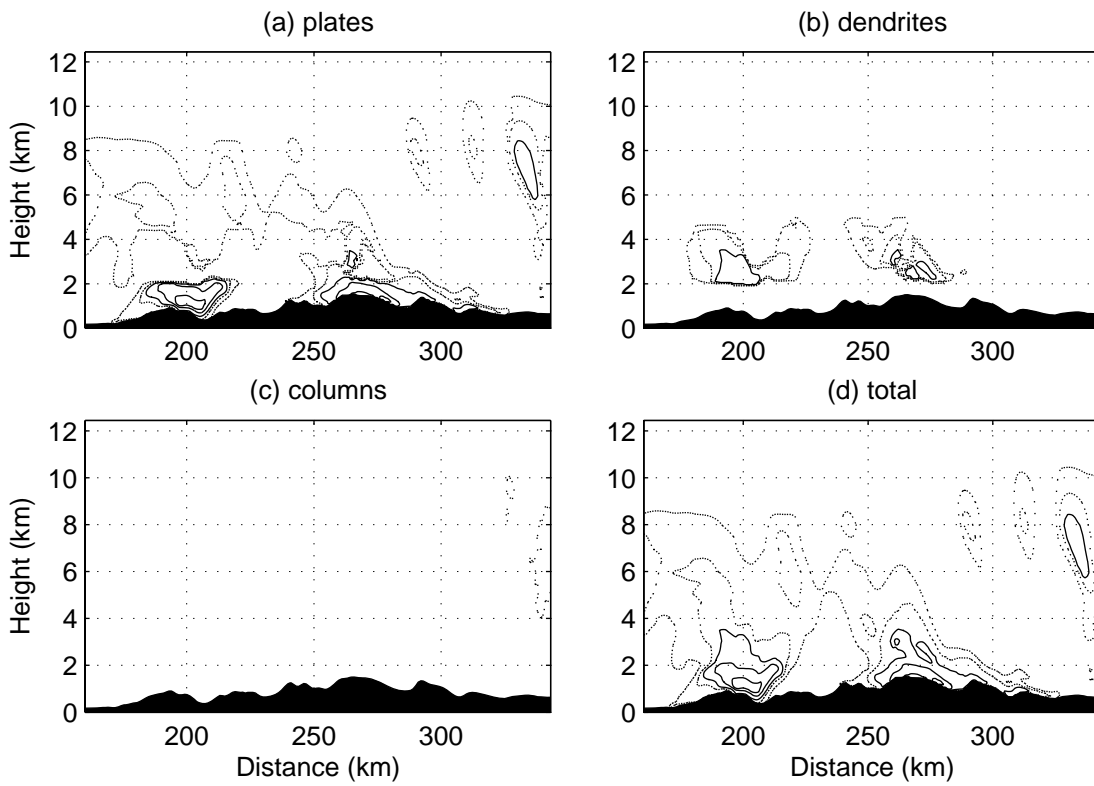


Figure 2.14 Same as Figure 12 except that this is a vapor deposition simulation with plate growth at upper level (EXP3).

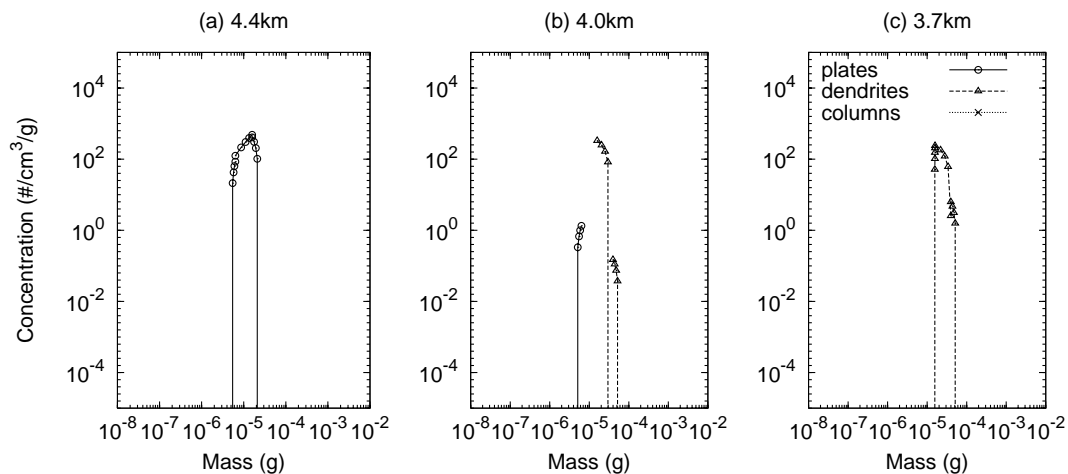


Figure 2.15 Mass spectra of solid hydrometeors at horizontal distance of 194 km from EXP3. (a) is at altitude of 4.4 km, (b) 4.0 km, and (c) 3.7 km. The linear distribution of a mass bin is indicated with 5 points. The circles indicate plates, the squares broad-branched crystals, the triangles dendrites, the crosses columns, and plus symbols capped columns.

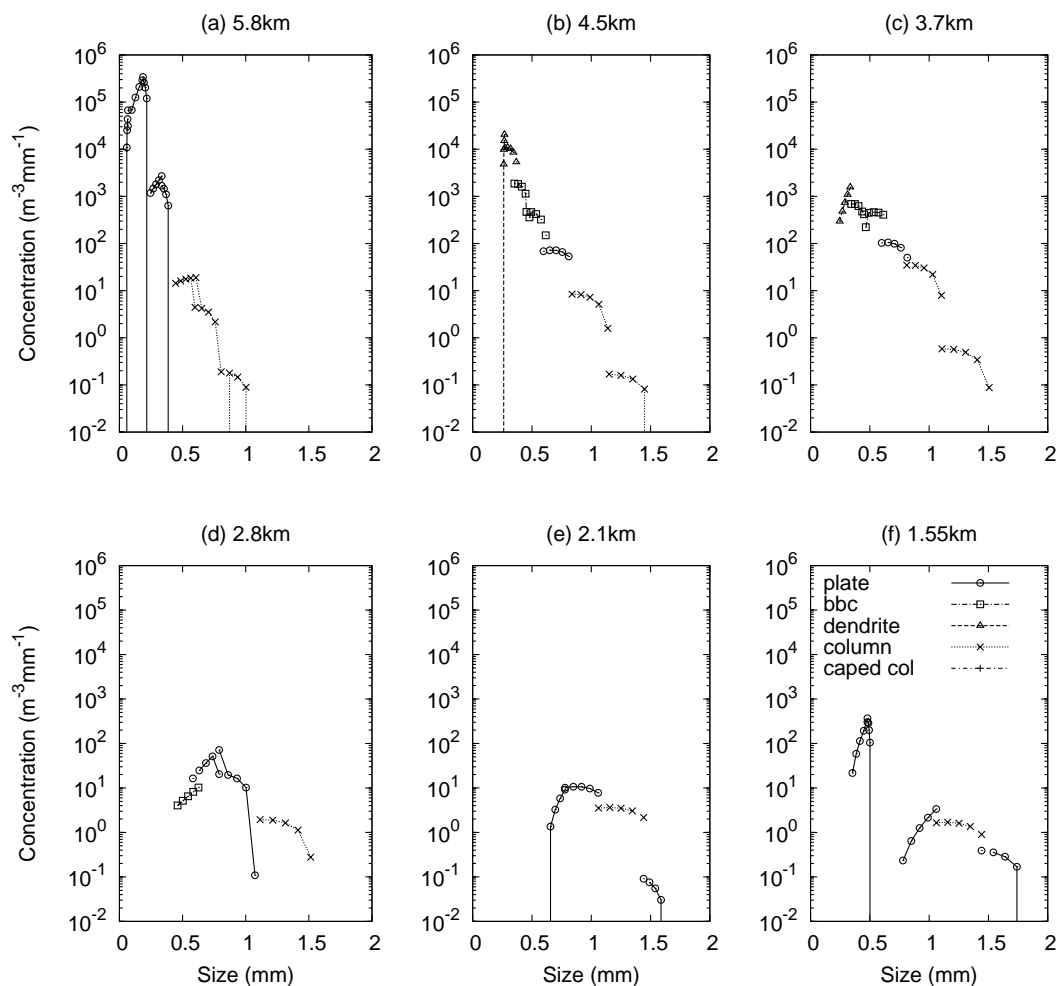


Figure 2.16 Size spectra of solid hydrometeors at horizontal distance of 240 km from EXP3, and at from altitude of (a) 5.8 km to (f) 1.55 km. The linear distribution of a mass bin is indicated with 5 points. The circles indicate plates, the squares broad-branched crystals, the triangles dendrites, the crosses columns, and plus symbols capped columns.

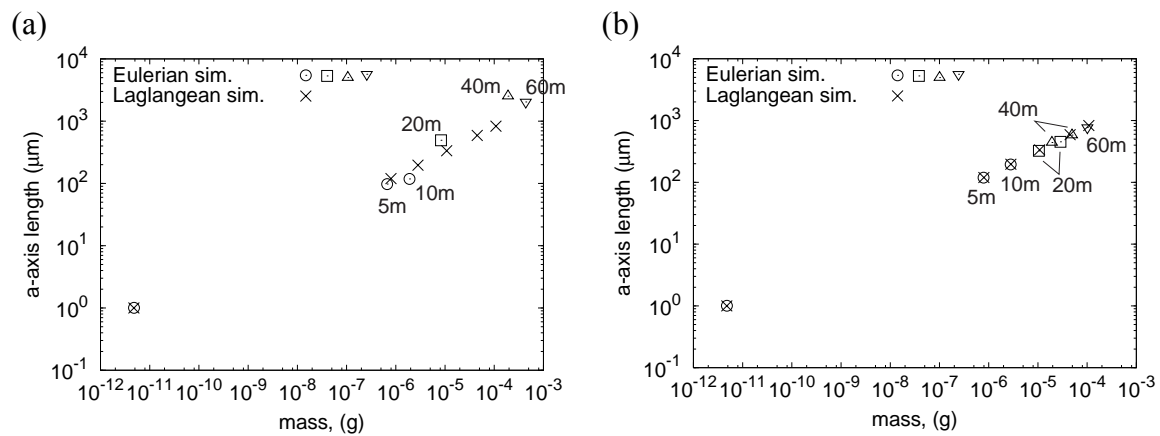


Figure A 1 Comparison of Eulerian and Lagrangian simulation of length under water saturation and -15°C . (a) concentration-weighted length and (b) concentration-weighted cubic length were used as a prognostic variable in the hybrid bin model with 5 bins. For Eulerian simulation, the simulated length corresponds to the hydrometeor having mass equal to mean mass of the bin.

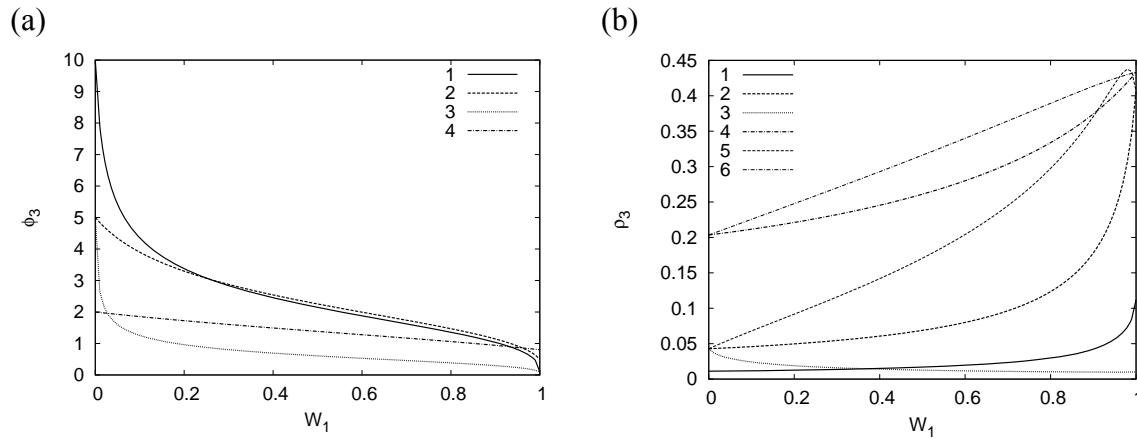


Figure A 2 Example of mixing planar (group 1) and columnar (group 2) crystals. The subscripts of variables indicate group number. The axis ratio and bulk crystal density of the average particle after mixing are shown in (a) and (b) as a function of mass ratio of group 1 $W_1 = M_1 / M_3$. The shown curves are 1 $\phi_1 = 0.1$, $\rho_1 = 0.112$, $\phi_2 = 10.0$, $\rho_2 = 0.0112$, 2 $\phi_1 = 0.5$, $\rho_1 = 0.407$, $\phi_2 = 5.0$, $\rho_2 = 0.0429$, 3 $\phi_1 = 0.1$, $\rho_1 = 0.01$, $\phi_2 = 5.0$, $\rho_2 = 0.0429$, 4 $\phi_1 = 0.8$, $\rho_1 = 0.433$, $\phi_2 = 2.0$, $\rho_2 = 0.203$, 5 ϕ_i and ρ_i ($i = 1, 2$) are the same as case 2, but ρ_3 calculated with the density-axis ratio relationship of hexagonal ice crystal model, Equation (A3), and 6 same as case 5 but for the axis ratios of case 4.

Table 2.1 Summary of prognostic variables advected in the Eulerian dynamic model, UW-NMS and those advected between the mass bins of SHIPS. The unit of variables in SHIPS is listed in the parenthesis. n is the ice parameter number and b bin number. $c(m)$ is number concentration (mass) weighted terminal velocity.

Ice par. n	Meaning per particle	UW-NMS $q_{ice}^{n,b}$	SHIPS $M_{ice}^{n,b}$	Weighting for $V_T^{n,b}$
1	Mass of a solid hydrometeor	M^b / ρ	M^b (g cm ⁻³)	m
2		N^b / ρ	N^b (cm ⁻³)	c
3	Circumscribing volume	V_{cs}^b / ρ	V_{cs}^b (cm ³ cm ⁻³)	c
4	a-axis length	ℓ_a^{3b} / ρ	ℓ_a^{3b} (cm ³ cm ⁻³)	c
5	c-axis length	ℓ_c^{3b} / ρ	ℓ_c^{3b} (cm ³ cm ⁻³)	c
6	Dendritic arm length	ℓ_d^{3b} / ρ	ℓ_d^{3b} (cm ³ cm ⁻³)	c
7	Mass produced by riming	M_R^b / ρ	M_R^b (g cm ⁻³)	m
8	Mass produced by vapor dep. onto an ice crystal	M_i^b / ρ	M_i^b (g cm ⁻³)	m
9	Total mass of aerosols	M_{apt}^b / ρ	M_{apt}^b (g cm ⁻³)	m
10	Soluble mass of aerosols	M_{aps}^b / ρ	M_{aps}^b (g cm ⁻³)	m

Table 2.2 Parameters to define mass bins for spectra of liquid and solid hydrometeors. The spectrum of liquid (solid) hydrometeors was divided into 21 (20) mass bins. N is the number of bins given to each group. The radii calculated with $\rho_w = 1.0 \text{ (g cm}^{-3}\text{)}$ for mass boundaries were shown in parenthesis.

phase	group	N	k_{bb}^b	a_{bb}	Smallest mass	Largest mass
liquid	Activation transition group	1	1.0×10^3	1.0	4.19×10^{-15} (0.1 μm)	4.19×10^{-9} (10 μm)
	Growth group	20	varying	1.02	4.19×10^{-9} (10 μm)	5.24×10^{-1} (5mm)
solid	Deposition growth group	4	22.1	1.0	4.19×10^{-12} (1 μm)	1.0×10^{-6} (62 μm)
	Collection growth group	10	2.51	1.0	1.0×10^{-6} (62 μm)	1.0×10^{-3} (620 μm)
	Riming growth group	6	3.16	1.0	1.0×10^{-3} (620 μm)	$1.0 \times 10^{+1}$ (1.34cm)

Table 2.3 Summary of experiment cases to test SHIPS. All the cases simulate ice nucleation, vapor deposition and melting processes.

phase	Advection and sedimentation of ice particles	Inherent growth rate $\Gamma(T)$
EXP1	off	Chen and Lamb (1994b)'s columnar growth in $-30 < T < -20^\circ \text{C}$ and $\Gamma(T) = 1$ for $T \leq -30^\circ \text{C}$
EXP2	on	Same as EXP1
EXP3	on	Planar growth of $\Gamma(-3.5)$ used for $T < -20^\circ \text{C}$

Chapter 3 Simulation of nucleation and depositional growth of polycrystals

3.1 Introduction

Polycrystals and irregular crystals alongside hexagonal crystals have been recognized in the literature since the modern observation of ice crystals began about 50 years ago (e.g., Nakaya, 1954). It is known that orographic wave clouds and cirrus clouds mainly consist of bullet rosettes and other polycrystals. Baker et al. (2006) used cloud particle imager (CPI) to analyze 17 orographic wave clouds and reported that the dominant crystal type by mass in most wave clouds is the rosette shape that includes pristine bullet rosettes, mixed-habit rosettes, rosettes with sideplane, and platelike polycrystals. Similarly, Lawson et al. (2006a) showed mixed-habit rosettes and platelike polycrystals constitute over 50% of the surface area and mass of ice particles $D > 50 \mu\text{m}$ and infer that homogeneous and heterogeneous freezing processes similar to wave clouds occur in cirrus clouds. The irregular particles including polycrystals in altostratus clouds associated with winter orographic storms were also reported. Rauber (1987) studied 17 wintertime storm systems over the mountains of northwestern Colorado and found that irregular particles (I1, I2, I4, S1, S2, S3) accounted 70% of the number concentration on the ground while dendrites for 20% even though 72~77% of samples were rimed. Rauber (1987) noted that the dominant habits (irregular particles) observed on the ground for the cloud top temperature colder than -20°C are different from those (pristine crystals) in the cloud due to the wide range of ambient conditions that ice crystals would

experience. During a snow storm over Cascade Mountain Woods et al. (2005) reported the assemblage of plates at $T < -20^{\circ}\text{C}$.

Korolev et al. (2000) diagnosed ice crystal habits of the cloud particle images taken during flights through stratiform clouds whose temperature ranges from -45 to 0°C . According to Korolev et al., the frequency of irregular particles is more than 50% over the temperature range, and it tends to increase with decreasing temperature. The high frequency of irregular crystals at $T < -20^{\circ}\text{C}$ is supported by the laboratory experiments of Bailey and Hallett (2004a) (hereafter, BH04a). Aircraft measurements of the boundary layer, multi-layer and cirrus clouds over the Arctic by Korolev and Isaac (1999) had approximately 3% pristine crystals with irregular shaped crystals prevailing. In the Antarctic the frequency of blowing snow on the ground is higher in the Antarctic winter due to the stronger wind speed (Lawson et al., 2006b). However, if one excludes the blowing snow and irregular crystals associated with it, the habits observed on the ground appears to be diamond dusts with frequency $\sim 95\%$ in the winter and up to 60% in the summer with rosette shaped polycrystals or precipitating snow grain accounting for the rest of the frequency (Walden et al., 2003; Lawson et al., 2006b).

Ice crystal habits affect both short and long wave radiative transfer directly and indirectly. The radiative forcing of clouds is one of the largest uncertainties in the global climate model. Macke et al. (1998) analyzed size distributions taken from cirrus clouds, and showed that the different assumptions of crystal habits led to as significant variability of scattering properties as those from the sampled size distributions themselves. Liu et al. (2003) simulated cirrus clouds with a cloud resolving model and radiative transfer model for warm and cold soundings. They showed that the IR heating rate is more sensitive to habits than the solar heating rate because

habits affect capacitance for the vapor deposition process and resulting microphysical properties of the cloud.

In addition to the larger capacitance, the polycrystals are potentially important due to the interaction with other hydrometeors. Rauber (1987) suggested that the spatial dendrites with rimed core and large planar dendrites were responsible for aggregation initiation due to the large differential fall speed between them and horizontal fluctuations in the large dendrites' motion.

One way to study radiative impacts of clouds and precipitation or to improve remote sensing application is to simulate realistic ice crystal habits and types of ice particles with the framework where dynamics, radiative response, and microphysical processes can interact. One of such framework is cloud resolving model (CRM). However, none of CRMs has simulated monocrystals and polycrystals together with all ice microphysical processes. Prediction is at most limited to the hexagonal habits, namely plates, dendrites, and columns (e.g., Lynn et al., 2005; Straka and Mansell, 2005). Liu et al. (2003) simulated bullet rosettes as a pristine crystal category with two-moment bulk water parameterization.

In order to reflect the complexity of ice crystal habits in the real atmosphere, this study demonstrates the simulation of nucleation and vapor deposition processes of polycrystals based on current knowledge of habit location and frequency. This study hopes to shed light on roles of immersion and homogeneous freezing processes, concentration of ice nuclei (IN) for the formation and growth of monocrystals and polycrystals and sedimentation effects on habit frequency observed at local points. The next section gives a brief description of the framework to simulate polycrystals with Spectral Habit Prediction System, SHIPS. In section

3.3 the experiment design and model setup are described. The results are discussed in section 3.4. The methodology and parameterizations used are discussed in section 3.5. The conclusions and future prospects are given in section 3.6.

3.2 Framework to simulate polycrystals with SHIPS

3.2.1 Brief description of SHIPS

The main concept of SHIPS is to evolve properties of ice particles in the Eulerian dynamic model continuously in such a way that the ambient conditions along the trajectory of ice particles are reflected in the evolving particle properties. The distribution of ice particles are divided into mass bins where each mass bin represents average habit and type of ice particles given the mass range. SHIPS introduces Particle Property Variables (PPVs) that contain information on the property of particles in a bin. Currently, mass content components, length variable components and volume variable components are considered. Mass content components include rime mass, aggregation mass, ice crystal mass, and melt mass. They are integrated based on the respective physical processes that ice particles are experiencing. Length variable components include lengths along a-axis, c-axis and dendritic arm. The maximum dimension of ice particles is predicted as volume variable components. Readers are referred to Chapter 2 for more detail explanation of the scheme.

The main philosophy for simulation of vapor deposition process is to grow the lengths of ice crystals along the crystallographic directions based on a physical model. Chapter 2 demonstrated simulation of the three axis lengths of hexagonal mono-crystals using the

inherent growth ratio approach of Chen and Lambs (1994), hereafter CL94, with a CRM, University of Wisconsin Nonhydrostatic Modeling System (UWNMS) (Tripoli, 1992). It showed that the advection and sedimentation of ice crystals affect distribution of habits significantly. The following describes a methodology to include prediction of polycrystals into SHIPS.

3.2.2 Habit diagram and frequency

The habit diagram has been constructed by many authors (e.g., Magono and Lee, 1966) for $T \leq -40^\circ\text{C}$. However, the frequency of the habits given temperature and moisture is limited in the literature. BH04a constructed the habit diagram for $-70 \leq T \leq -20^\circ\text{C}$ along with the frequency of occurrence. As shown by Kumai (1982) and BH04a the occurrence of multiple habits are common in $T \leq -20^\circ\text{C}$, while one habit tends to dominate in $T > -20^\circ\text{C}$.

Because the mechanisms for formation of polycrystalline structures of ice crystals are only qualitatively known in literature, this study uses habit frequency constructed by laboratory experiments in order to generate polycrystals and also to allow formation of multiple habits given temperature ($T \leq -20^\circ\text{C}$) and moisture. Figure 3.1 shows the habit frequency constructed by using BH04a's data. The frequencies of plates, columns, and polycrystals in the figure (a), (b), and (c), respectively, add up to 1. The hexagonal plates have moderate frequency in low supersaturation over ice ($s_i < 20\%$) over the wide temperature range, while columnar crystals were often observed below $T \leq -40^\circ\text{C}$ with moderate and high s_i . The polycrystals are associated with high excess vapor density, and they appear to prevail in $-45 \leq T \leq -20^\circ\text{C}$. The frequency for columnar polycrystals (bullet rosettes) and planar

polycrystals (side planes, over-lapping parallel plates, and crossed plates are included from BH04a's data) given the occurrence of polycrystals are shown in (d) and (e). The columnar polycrystals and planar polycrystals appear to be separated by the boundary $T \approx -40^\circ \text{C}$.

The habit frequency actually depends on the property of ice nuclei (Bailey and Hallett, 2002). This study only uses the frequency data for sodalime glass whose composition is close to the most prevalent IN (BH04a). If one wants to simulate ice formation by artificial precipitation, one would need the habit frequency for the IN that are present or sprayed in the volume.

3.2.3 Prognostic variables and diagnosis

This study introduces three PPVs to identify polycrystalline habits in addition to hexagonal monocrystals (Figure 3.2). New predicted variables added to SHIPS are the coordinates of center of gravity of a polycrystal and number of extra crystalline structures added to a hexagonal monocrystal. The coordinates of center of gravity are defined from the center of a monocrystal. The underlying assumption is that components are hexagonal monocrystals themselves and they are all identical and symmetric. Some examples of the possible assemblages are shown in Figure 3.3; (a) is the conceptual model of a bullet rosette with four branches (C2a), (b) a side plane (S1), (c) radiating assemblage of plates (P7a), (d) overlapping parallel plates (opp in BH04a), (e) crossed plates (cp in BH04a) and (f) is the scalelike side plane (S2). This study categorizes (a) as the columnar polycrystals, and (b), (c), (d) and (e) as the planar polycrystals. The crossed plates would have the same center of gravity as a monocrystal, but this study categorizes the habit into the planar polycrystals. The

scalelike side plane (f) is one example where the coordinates of the center of gravity cannot be defined uniquely from the hexagonal crystal. Those having characteristics between the columnar and planar polycrystals are called irregular polycrystals.

During the nucleation period where the maximum dimension of an ice crystal D is less than $20 \mu\text{m}$, all polycrystals are initialized to have a characteristic a_g and c_g , and non-zero number of extra crystalline structures, n_{exice} . The columnar and planar polycrystals are assumed to have $(a_g/a, c_g/c, n_{exice}) = (0,1,1)$, a square in Figure 3.2 and $(a_g/a, c_g/c, n_{exice}) = (1,0,1)$, a triangle, respectively, so that they show the distinct characteristic in the parameter space. The irregular polycrystals are assumed to be in the middle of those two crystals indicated with a cross: $(a_g/a, c_g/c, n_{exice}) = (0.5,0.5,1)$. The monocrystals are initialized with $(a_g/a, c_g/c, n_{exice}) = (0,0,0)$, shown by a circle.

After advecting PPVs between mass bins and spatial grid cells, $(a_g/a, c_g/c, n_{exice})$ of a mass bin changes with time and take any combination of values in the parameter space. This study simply assumes the ice particle is a monocrystal if $n_{exice} < 0.5$, and otherwise polycrystals. The particles are diagnosed as planar (columnar) polycrystals if $a_g/a \geq c_g/c + 0.5$ ($c_g/c \geq a_g/a + 0.5$) (Figure 3.2). Then, the region between those boundaries is taken to be irregular polycrystals. As a result, this study identifies 10 crystal habits from six PPVs: two monocrystal habits, three polycrystalline habits, and each with dendritic feature.

For now we assume the number of extra crystalline structure $n_{exice} = 1$ for the polycrystals because n_{exice} is not quantitatively known in literature. The bullet rosettes tend to have three or

four bullets in observation (literature needed), and the number of different crystalline structure for planar polycrystals are in general not known. Furthermore, it is not clear that n_{exice} is a continuous function of temperature and moisture. In this study $n_{exice} = 1$ is treated as an indication of polycrystals rather than as the actual number of extra crystalline structures. No geometrical length for polycrystals is predicted due to lack of information on the growth along the crystallographic directions. Instead, we diagnose the maximum dimension by using empirical mass-diameter relationships. The planar polycrystals are diagnosed by side planes (S1) of Mitchell et al. (1990), the columnar polycrystals by bullet rosettes model of Chiruta and Wang (2003), and other irregular polycrystals by combination of bullet, columns, plates (S3) of Mitchell et al. (1990).

The mass variable for an ice crystal is still only one: mass component of ice crystal, m_I . The mass growth is calculated based on the diagnosed habit. Three axis lengths of a hexagonal crystal are always changed according to mass growth whether or not the diagnosed habit is polycrystalline. This way the mass component of ice crystal, and a-axis, c-axis and d-axis (dendritic arm) lengths are continuous and consistent with the predicted mass component of the ice crystal.

3.2.4 Growth rate calculation

This study uses capacitance approach to simulate mass growth of hexagonal monocrystals and polycrystals. The capacitance of hexagonal monocrystals is modeled as a spheroid following CL94's treatment, and Chiruta and Wang (2003) is used for columnar polycrystals. Other polycrystals' capacitances are modeled with spheroid assuming semi-axis ratio of 0.25.

As for the growth rate of length of hexagonal monocrystals the inherent growth approach of CL94 is extended to $T \leq -20^\circ \text{C}$. Figure 3.4 shows extended inherent growth ratio Γ for $T \leq -20^\circ \text{C}$, in which two curves divert at $T = -20^\circ \text{C}$ for columnar and planar growth regimes. BH04a shows axis ratio of about 20 at $T = -50^\circ \text{C}$. Thus, the inherent growth ratio for the columnar regime was tuned so that the axis ratio of simulated single particle reaches the order of 10 under in water saturation. Otherwise, there is no other measurement of growth along a and c axes or $c = \eta a^\beta$ ($\Gamma = \beta$) in $T \leq -30^\circ \text{C}$ at this moment. The ventilation coefficients are calculated with a formula for idealized ice crystals in Pruppacher and Klett (1997) except that the one for bullet rosettes is calculated by the Liu et al. (2003)'s formula.

If $D < 20 \mu\text{m}$ and $T \leq -20^\circ \text{C}$, the growth regime that the ice crystal takes at given temperature and moisture is determined by using the corresponding cumulative relative frequency of habits and random number generator. First, the growth regime is chosen from polycrystalline regime, columnar and planar hexagonal regimes, and then if it is polycrystalline, another random number determines if it is columnar or planar polycrystalline. Furthermore, if it is polycrystalline, another drawing of random number determines growth regime for hexagonal monocrystal. In other words, small ice crystals can grow with different growth mode from the habit diagnosed at the beginning of time step. In $T > -20^\circ \text{C}$ polycrystals are assumed not to form. Once the maximum dimension is greater than $20 \mu\text{m}$, the ice crystal is assumed to follow the growth of the diagnosed habit at the beginning of a time step.

3.2.5 Bin shifting of polycrystal variables

After calculating mass growth and growth of axis length for the representative hydrometeor in a bin (see section 2.4 for details), the polycrystalline property of ice particles in the *shifted bin* is calculated as follows. As explained above, the three parameters (a_g', c_g', n_{exice}') for the ice crystals in a shifted bin are only initialized when ice crystals are small ($D < 20 \mu\text{m}$) based on the growth regime: $(a_g', c_g', n_{exice}') = (0, c', 1)$ for columnar polycrystals, $(a_g', c_g', n_{exice}') = (a', 0, 1)$ for planar polycrystals, $(a_g', c_g', n_{exice}') = (0.5a', 0.5c', 1)$ for irregular polycrystals, and $(a_g', c_g', n_{exice}') = (0, 0, 0)$ for monocrystals. The variables a' and c' are the a-axis and c-axis length of a hexagonal monocrystal in a shifted bin and calculated with δa and δc obtained from Eqs. (41)-(44) of CL94. For $D \geq 20 \mu\text{m}$,

$$a_g' = a_g + r_a \delta a \quad (3.1)$$

$$c_g' = c_g + r_c \delta c \quad (3.2)$$

where $r_a = 1.0$, $r_c = 0.0$ for planar polycrystals, $r_a = 0.0$, $r_c = 1.0$ for columnar polycrystals, $r_a = 0.5$, $r_c = 0.5$ for irregular polycrystals, and $r_a = 0.0$, $r_c = 0.0$ for monocrystals.

The number of extra crystalline structures in a shifted bin, n_{exice}' is also initialized according to the growth regime if $D < 20 \mu\text{m}$. For $D \geq 20 \mu\text{m}$, it stays the same as the dynamically advected number, i.e. $n_{exice}' = n_{exice}$.

The coordinates of center of gravity are transferred between mass bins as concentration-weighted cubic lengths in the same way as other length variable components. The number of extra crystalline structures is weighted by concentration.

3.2.6 Terminal velocity

The general formula of Bohm (1992) is used in this study as done in Chapter 2. For polycrystals, the aspect ratio α is assumed to be 0.25. The area ratio q_{rat} for bullet rosettes is calculated with Chiruta and Wang (2003)'s geometric model, and those for other polycrystals are calculated by substituting predicted bulk crystal density into Heymsfield et al. (2002)'s formula for S1.

3.3 Model setup and experiment design

As described in Chapter 2, SHIPS has been installed into a cloud resolving model, UWNMS. The case study that SHIPS is validated against is a winter orographic snow storm observed on 13-14 December 2001 during IMPROVE-2 campaign (see Woods et al., 2005, for synoptic and microphysical observations). Most of the model setups for the two dimensional idealized simulation are the same as Chapter 2 except the following few points. CCN are fixed to the initial concentration and mass content at each level, but concentration and mass content of IN are predicted. In the dynamics model the threshold mass content for each mass bin can be defined to remove insignificant mass content and so to avoid consuming computational time on the advection of insignificant mass content in the model. Chapter 2 set the threshold mass

content to 10^{-6} of the mixing ratio of water species. By eliminating slow growing small ice particles in the low and middle levels (especially those nucleated by depositional nucleation), effects of sedimentation of ice crystals nucleated at the initial stage showed up more clearly. This study uses the threshold of 10^{-12} to keep track of those small crystals in the dynamics model in order to see the effect of vapor competition.

Eight experiments are carried out as listed in Table 3.1. S-HCH simulates only monocrystals with CL94's inherent growth parameterization extended to $T \leq -20^\circ \text{C}$ and habit frequency approach, while S-PCH simulates polycrystals in addition to the monocrystals. Those are implemented with the threshold for mass contents as done in Chapter 2 to investigate the sedimentation effect of polycrystals. In addition to deposition-condensation freezing, immersion freezing and contact freezing processes the homogeneous freezing process was simulated in PCH, PCHH, PCL, and PCLH. The parameterization of Heymsfield and Miloshevich (1993) for pure water was used in this study. PCH and PCL are assumed to form polycrystals through the four nucleation processes based on the habit frequency, whereas PCHH and PCLH only form hexagonal monocrystals from the contact, immersion and homogeneous freezing processes. The sensitivity of polycrystal formation to the freezing nucleation processes is discussed by comparison between them. PCH and PCL (PCHH and PCLH) have IN concentration of 230 L^{-1} (1 L^{-1}) to investigate the sensitivity of habit distribution and vapor depositional growth to concentration of IN. PCHNI and PCLNI do not simulate immersion and homogeneous freezing process.

First, a quasi-steady state was obtained only with liquid microphysics on as was done in Chapter 2. Then, the above experiments were started by using the quasi-steady state as initial

conditions and by turning on the ice microphysics processes including ice nucleation, vapor deposition and melting processes. Note that the time of simulation mentioned is the time after the ice microphysics processes were turned on. In the following, the horizontal distance from the west boundary in the domain is denoted with y , and the altitude with z .

3.4 Results

3.4.1 Habit distributions with and without polycrystals

Concentration of ice crystals was horizontally averaged for each habit and also average axis ratio was calculated by using concentration-weighted axis lengths. The average concentration and axis ratios for S-HCH and S-PCH at 20 minutes of simulation are shown in Figure 3.5. The concentration for HCEP, (a), shows that columnar crystals dominate above $z \sim 7$ km and then plates between $z = 4$ and 6 km. As shown in Figure 3.6, the supersaturation over ice stays around 0.2 above $z = 7$ km and temperature decreases with height at the initial time. The habit frequency (Figure 3.1) shows that the habit of larger frequency between hexagonal monocrystals shifts from plates to columns across $T \sim -40^\circ \text{C}$ at supersaturation over ice $s_i \sim 0.2$. According to (d), prediction of polycrystals (S-PCH) introduced the highest concentration of irregular polycrystals above $z = 4$ km, which can be expected from the frequency map given the vertical profile of supersaturation. Also, high concentrations of planar and columnar polycrystals were predicted in the region $6 < z < 8$ km and $9 < z < 11$ km, respectively. Concentration of the plates was reduced by order of 2, while concentration of columnar crystals is as high as the polycrystals above $z = 8$ km. The dominance of habits can

be mainly understood from the habit frequency (Figure 3.1) at 20 minutes of simulation. However, the effect of advection is noticeable. The dendrites were advected downward to 3 km according to (a) and (d). The axis ratio, $\phi = c/a$, is similar between S-HCH and S-PCH ((b) and (e)). The irregular polycrystals already show growth of the axis ratio, $\psi = d/a$ at this time.

The SHIPS produces the known dependence of dimension and terminal velocity on the axis ratio. The mass-dimensional and mass-terminal velocity relationships at 20 minutes of simulation are shown in Figure 3.7. The data points were plotted for mean mass of all mass bins and grid cells in the domain. A few empirical power laws are also plotted for quick reality check. It can be seen that the maximum dimension (terminal velocity) becomes large (small) with decrease of axis ratio ϕ given mass for planar crystals, which is expected. The opposite is true for columnar crystals. The maximum dimension predicted for plates turned out to be less than P1a of Mitchell (1996) and Heymsfield and Kajikawa (1987) in the mass greater than 10^{-4} mg. This is true for dendrites against P1e of Heymsfield and Kajikawa. Most of data points have axis ratios ϕ between 0.1 and 1 as seen in Figure 3.5. As noted in Chapter 1, underestimation of the thinning of planar crystals has to be resolved in the future. Some are related to ice particles formed from supercooled liquid drops and planar growth ratio Γ in $T \leq -20^\circ\text{C}$ with ϕ close to 1. In turn, this resulted in a larger terminal velocity than the empirical formulas would predict. The columnar crystals show a wide range of axis ratio from 1.0 to more than 30.0. It shows the columnar crystals with $\phi > 10$ that exist above $z = 10$ km hardly falls. The columnar crystals with $1 < \phi < 10$ cover the range of hexagonal columns and

N1a by Mitchell (1996) and Mitchell et al. (1990), which seems to be reasonable. Polycrystals follow the mass-dimensional relationships specified with empirical equations and the terminal velocities calculated with Bohm's general formula agree with empirical relationships well.

Sedimentation of ice crystals can be clearly seen by comparing 20 minutes and 60 minutes of simulation (Figure 3.5 and Figure 3.8). S-HCH predicts sedimentation of the plates to the low levels ($2 < z < 4$ km), while S-PCH shows sedimentation of the irregular polycrystals to the levels (see (a) and (d) of the figures). At this time irregular polycrystals in the low levels have significant growth of dendritic arms indicated by $\psi = d/a$ in (f). It is because the polycrystals fell through the dendritic growth region ($-16 < T < -12^\circ \text{C}$). Vertical profiles of the axis ratio $\phi = c/a$ in (b) and (e) also indicate downward shifts, but the change at a level is combination of growth and sedimentation.

The mass content of diagnosed habits at 90 minutes for S-HCH is shown in Figure 3.9. The spatial distribution appears to be a combination of EXP2 and EXP3 of Chapter 2 at this time. The planar crystals are dominant in lower levels ($2 < z < 4$ km) and columnar crystals have high mass content in middle levels ($3 < z < 6$ km and $y=270$ km) and upper levels. On the other hand, S-PCH indicates dominance of irregular polycrystals in low and middle levels (Figure 3.10). These resulted from the horizontal advection and sedimentation from the earlier spatial distribution explained by the habit frequency map (Figure 3.5). The maximums of mass content for S-PCH are larger than S-HCH. It is speculated that the capacitance model assumed for irregular polycrystals is larger than that of plates and columns predicted for S-HCH on average, which gave larger mass growth to irregular polycrystals. Also, terminal velocity of irregular polycrystals is somewhat smaller than hexagonal monocrystals, which

allowed irregular polycrystals to have longer time for depositional growth. The experiments, S-HCH and S-PCH, clearly showed the potential importance of the habits in middle and upper levels due to habit-dependent sedimentation, and growth rate.

3.4.2 Effect of formation of polycrystals through freezing

Different nucleation processes show distinct characteristics in creating spatial and size distributions of ice particles. The ice nucleation rates in concentration and nucleated mass per a single particle are shown for each process in Figure 3.11 and Figure 3.12, using 20-minute simulation from PCH as an example. These show that the deposition nucleation process has large impact in terms of concentration, while the immersion and homogeneous freezing processes nucleate large ice crystals as well as high concentration. Concentration tendency by the contact nucleation is much smaller than the others by two or more order. As to the spatial distribution, the freezing processes produce high concentration (mass content) tendency of more than $1 \text{ L}^{-1} \text{ s}^{-1}$ ($10^{-7} \text{ g m}^{-3} \text{ s}^{-1}$) at $y \sim 210 \text{ km}$ and 310 km above 6 km . These are associated with the strong vertical motion in the regions (2 to 5 m s^{-1}). The contact freezing nucleation process is active between 3 and 5 km . The depositional nucleation occupies wider area of stratiform clouds where the vapor is saturated over ice. Note that in Bailey and Hallett's frequency map (Figure 3.1) temperature range of active immersion freezing process ($-35 < T \leq -20^\circ \text{C}$) corresponds to the high frequency of planar polycrystals, whereas that of homogeneous freezing process ($T \leq -35^\circ \text{C}$) to the high frequency of irregular and columnar polycrystals.

The formation of polycrystals through the immersion and homogeneous freezing has large impact on spatial distribution of polycrystalline habits. Concentration of diagnosed habits for PCL and PCLH are shown in Figure 3.13 and Figure 3.14. It can be seen that the concentration of ice crystals is closer to the concentration of IN in these simulations due to the lower threshold in the dynamic model. Comparison of PCL and PCLH indicates that the area with different dominant habits clearly correspond to the area of active immersion and homogeneous freezing nucleation processes (horizontal distance of 200 to 250 km and 300 to 350 km and above 6 km). PCLH assumes that all the ice crystals form hexagonal monocrystals after the freezing nucleation processes, while PCL generates polycrystals by using habit frequency tables. Therefore, PCLH shows more hexagonal monocrystals and less polycrystals in the areas than PCL. The habit distributions of PCL and PCLH in $y < 200$ km are almost identical due to no active freezing process. PCH and PCHH show similar differences but with higher concentration (order of 100 L^{-1}) in the regions where the deposition nucleation process is active.

The frequency of diagnosed habits was calculated for five temperature ranges in the entire domain and over the first three hours of simulation (Table 3.2). The temperature ranges are $T \leq -40^\circ \text{C}$ ($z > 8.1$ km), $-40 \leq T < -30^\circ \text{C}$ ($6.8 < z < 8.1$ km), $-30 \leq T < -20^\circ \text{C}$ ($5.5 < z < 6.8$ km), $-20 \leq T < -10^\circ \text{C}$ ($4 < z < 5.5$ km) and $-10 \leq T < 0^\circ \text{C}$ ($2.2 < z < 4$ km). Note that this analysis includes the sedimentation effects of ice crystals. Therefore, the habit frequency is not only function of the temperature and moisture at the local grid cell. With the formation of polycrystals by the freezing processes (PCH and PCL), irregular polycrystals are the most dominant habit in $T \leq -20^\circ \text{C}$. For $T \leq -40^\circ \text{C}$, if the freezing is not the mechanism to produce

polycrystals (PCHH and PCLH), columnar crystals prevail with frequency of more than 80 %. For $T \leq -20^\circ \text{C}$ the fraction of irregular polycrystals increases with temperature for PCH and PCHH. Furthermore, the formation of polycrystals by freezing processes has a large impact on planar monocrystals in $-20 < T \leq -30^\circ \text{C}$. When the polycrystals are formed with the freezing, planar monocrystals take on less than 1 % of the concentration. However, when the monocrystals are formed with the freezing, they show the frequency of 24 % (PCHH) and 79 % (PCLH). In the region $T > -20^\circ \text{C}$ the plates and dendrites prevail except for PCL where the irregular polycrystals have the largest frequency due to sedimentation. The frequency of columnar crystals increases in the layer $-10 < T \leq 0^\circ \text{C}$ from the above layer due to the columnar growth region ($T \sim -6^\circ \text{C}$).

Next, the simulated frequency is compared with an observed habit frequency in stratiform clouds by Korolev et al. (2000). The observed frequency of irregular particles ranged from 70 to 90 % for $D > 125 \mu\text{m}$ (see their Figure 6). PCH and PCL show similar high frequency of irregular polycrystals. The observed frequency of irregular particles increases with a decrease of temperature and the peak shift from $T \sim -37^\circ \text{C}$ to $T \sim -30^\circ \text{C}$ with size possibly due to sedimentation. However, the peak frequency of irregular polycrystals for PCH or PCL is shifted warmer temperature. PCH and PCL show increase in frequency of columnar crystals in $T < -30^\circ \text{C}$ with decrease of temperature, which agrees with the peak in frequency of needles observed in $T < -35^\circ \text{C}$. The increase of frequency of columnar crystals in $T > -10^\circ \text{C}$ also qualitatively agrees with the observation as well as the peak frequency of dendrites in $T > -10^\circ \text{C}$. Note that Korolev et al. included heavily rimed particles, graupels, and others with characteristics that do not fall into the categories of needles, dendrites or spheres, whereas

this study only simulates nucleation, vapor deposition, and melting. Simulations with aggregation and riming processes must be carried out in order to compare with the observation more rigorously.

It is important to mention that the simulations without the immersion and homogeneous freezing processes (PCHNI and PCLNI) still produce the highest frequency of irregular polycrystals in temperature ranges $-40 < T < -10^{\circ}\text{C}$, which are comparable to cases with immersion freezing of polycrystals. However, frequencies of the planar and columnar polycrystals turned out to be less than PCH and PCL. This is simply because the concentration nucleated by immersion and homogeneous freezing processes was removed, so the relative contribution of crystals which form in high saturation was reduced. PCHNI and PCLNI maintained higher supersaturation over the area $y > 210\text{ km}$ than PCH and PCL. The supercooled liquid hydrometeors act as the source of moisture through vapor deposition process in PCHNI and PCLNI rather than source of concentration and mass of ice crystals through the freezing nucleation processes.

The assumed habits for the freezing nucleation processes can affect the habit frequency given a size significantly. The particle size distribution (PSD) of ice particles were averaged for five temperature ranges in the domain as defined above for analysis of habit frequency. Along with it, conditional frequency of diagnosed habits given a maximum dimension was calculated. The results for PCL and PCLH at 90 minutes of simulation are shown in Figure 3.15 and Figure 3.16. The average PSDs for PCH and PCHH or PCL and PCLH are very similar, and the difference in conditional frequency of habits shows the effect of polycrystal formation by the freezing processes. Comparison of conditional frequencies for PCL and

PCLH clearly shows that hexagonal monocrystals of PCLH reached much higher concentration in 10 to 100 μm in $T \leq -20^\circ\text{C}$ than those of PCL, and it corresponds to the size produced by the freezing nucleation. Note that the immersion and homogeneous freezing process are potentially quite important because the potential concentration of liquid hydrometeors nucleated from CCN is much higher than that of solid hydrometeors nucleated from IN by order of 10^2 to 10^3 and also because the process nucleates large initial size and mass. (a) of Figure 3.17 shows concentration of supercooled liquid hydrometeors by using ambient temperature and diameter of liquid hydrometeors at 20 minutes for PCL. The concentration decreases with decrease of temperature and with increase of size. In $T \leq -20^\circ\text{C}$ size of the supercooled liquid hydrometeor ranges between 10 to 100 μm . The nucleation rate by the immersion and homogeneous freezing processes are shown in (b) and (c) of Figure 3.17, respectively. Even though the Bigg's formula (see Appendix B.3.1) in $-40 < T < -20^\circ\text{C}$ and $5 < D < 100 \mu\text{m}$ indicates low probability of freezing (about 0.0001 to 0.1), the concentration is high enough to produce the rate of more than $1.0 \text{ L}^{-1} \text{ s}^{-1}$. The rate is significant compared to the IN concentration available for PCL and PCLH.

In the literature, rapid freezing of large liquid hydrometeor is considered to be one of the key formation processes of polycrystals (Pruppacher and Klett, 1997). Baker and Lawson (2006) and Lawson et al. (2006a) show that polycrystals of rosette shapes dominate the population of crystals with a large maximum dimension (above 100 μm) while spheroids occupy the size range of 10 to 20 μm in wave and cirrus clouds. This study simulates columnar crystals to dominate the largest size for temperature $T \leq -40^\circ\text{C}$. The discrepancy

may be due to the fact that this study does not include breakup of long needles, and aggregation processes. Also, no parameter to describe spheroids was predicted. Better understanding of growth of supercooled droplets to polycrystals is necessary to improve the prediction.

The effect of nucleating hexagonal monocrystals instead of polycrystals appears in the mean maximum dimension and standard deviation of PSD for $T \leq -20^\circ \text{C}$ (Table 3.2). Since polycrystals tend to be more compact than hexagonal monocrystals given a mass, the mean and standard deviation of PCH (PCL) is smaller than those of PCHH (PCLH).

After all, experiments with polycrystal formation based on BH04a habit frequency data (PCH and PCL) produced the habit frequency that moderately agrees with observations in stratiform clouds, and wave and cirrus clouds.

3.4.3 Effect of ice nucleation concentration

The distributions of supersaturation over ice for PCH and PCL at 20 minutes are shown in Figure 3.18. It shows that PCL has higher supersaturation ($s_i \approx 25$ to 30 %) at 6 to 8 km due to less concentration of ice crystals than PCH. This is the direct effect of difference in concentration of ice crystals due to IN concentration. The same thing is true for PCLH and PCHH. As a result, PCL indicates higher frequency of planar polycrystals than PCH in $-30 < T < -20^\circ \text{C}$ (Table 3.2). Columnar polycrystals are also found to have higher frequency for the same reason in $T < -40^\circ \text{C}$. Thus, IN concentration indeed affects habit frequency observed at a given level through supersaturation during nucleation period of ice crystals.

Another effect of IN concentration to habit frequency at a level is through the sedimentation of ice crystals. The difference in IN concentration can lead to the difference in

maximum dimension of ice crystals. Comparison of the mean maximum dimensions for PCH and PCL shown in Table 3.2 indicates that PCL has larger dimension of ice crystals in $T > -20^{\circ}\text{C}$ ($z < 6\text{ km}$) as well as standard deviation. However, the mean maximum dimension over the domain decreases by increasing IN concentration in $T < -20^{\circ}\text{C}$. Spatial distributions of the mean maximum dimension are shown for PCH and PCL in Figure 3.19 and Figure 3.20. PCL simulates columnar crystals as large as 1mm in the upper levels whereas PCH does 100 μm in the levels. The maximum dimension of irregular polycrystals in PCL is one order larger than those in PCH at $y < 200\text{ km}$, but it decreases in the active nucleation area of $y > 200\text{ km}$ due to the high concentration. As a result of the faster growth rate, one can see the clearer sedimentation of large irregular polycrystals into dendritic growth regime $-20 < T \leq 0^{\circ}\text{C}$ in PCL than PCH. Thus, IN concentration can change habit frequency through vapor deposition growth rate and subsequent sedimentation.

3.5 Discussions

The SHIPS framework to predict polycrystals shows some potential but falls short from complete verification due to the many unknowns. More validations must be done before it proves its usefulness. The following discussion addresses major concerns and points necessary to improve the prediction of polycrystals as well as hexagonal crystals in cold temperature.

The quantitative conditions to form polycrystals from nucleation processes and also from riming process are still not fully understood. This study assumed one frequency map constructed by BH04a for all the nucleation processes. According to Bacon et al. (2003),

crystals grown from frozen droplets exhibit isometric compact habits at $T > -22^{\circ}\text{C}$ and polycrystals at lower temperature, whereas frost ‘seeds’ develop into pristine hexagonal prism. Connolly et al. (2004) simulated ice crystals in cloud chamber from Arizona test dust aerosol at $T \leq -20^{\circ}\text{C}$. They showed that columnar crystals and bullet rosettes were dominant in low relative humidity cases, whereas budding rosettes were dominant at water saturation possibly due to immersion freezing process. As they discuss, it is possible that soda lime threads used in BH04a affected the nucleation mode with a preference for immersion freezing nucleation.

This study used two inherent growth ratios for $T \leq -20^{\circ}\text{C}$, namely columnar and planar inherent growth ratios in order to take into account the comparable frequency of plates and columns. According to CL94, the inherent growth ratio $\Gamma(T)$ is a parameter related to surface kinetic processes occurring on basal and prism faces of hexagonal ice crystal and is a function of temperature. The ambient moisture is reflected in the parameterization of deposition (apparent) density, which is used to calculate the growth of axis lengths. This assumes that the habit does not change with moisture. No information on the deposition density is available in $T \leq -20^{\circ}\text{C}$, but the known hollowness of columnar crystals can be represented by low apparent density. Aircraft observations and laboratory experiments showed that pristine bullet rosettes can grow into more complex shape with sideplanes and irregular shapes as they experience warmer temperature (Bailey and Hallett, 2004b; Baker and Lawson, 2006). It may be possible to model such transitions with SHIPS by referring to axis lengths of hexagonal crystals in polycrystals if the transition is reflected in the inherent growth ratio.

Diagnosing a-axis and c-axis lengths of polycrystals may not be possible if only one mass component for an ice crystal is used. For a given mass, the maximum dimension of

polycrystals and monocrystals are similar, which means that a and c-axis lengths of a monocrystal and those of the monocrystal in a polycrystal can be quite different. Thus, mixing of those lengths may produce unrealistic mass-length relationships if they are diagnosed as monocrystals.

Even in a Lagrangian simulation of an ice particle, the prediction of geometry of polycrystals is challenging due to the fact that the growth data along crystalline axis for polycrystals is limited and that the geometry itself is difficult to describe by only a few parameters. This study used the coordinates of gravity and number of extra crystalline structure to “categorize” the types of polycrystals (Figure 3.2). The frequency of crystals diagnosed to be polycrystals in the model actually depends on the assigned volume in the parameter space to habits as well as the frequency of formation observed by BH04a. If one knows the 3D geometry of a polycrystal, it is possible to vigorously calculate the coordinates and number of crystalline structure from it. However, at this moment it is not clear that what kind of habit can be identified from the space defined with coordinates of gravity and number of extra crystalline structures. BH04a shows a variety of polycrystals such as crossed plates, gohei twins, scrolls, spearheads, overlapping parallel plates in $-40 < T \leq -20^\circ \text{C}$. They describe a family of sideplanes in terms of a twin boundary structure (TBS). Therefore, the length and number of TBSs may be used as PPVs. The challenging problem on the geometry can be also found in the automatic diagnosis of habits from given an ice particle. Baker and Lawson (2006) and Lawson et al. (2006a, b) developed the software using “focus”, “cutoff”, “Crystal”, “Length”, “Width”, “Perimeter”, and “h1-h6 from radial harmonics”. The parameters, “h1-h6” are the first six harmonic frequencies. Similar methodology may be

applied to the prognostic variables of polycrystals in SHIPS. Construction of a database with minimum characteristic physical parameters that define spaces for each habit is necessary to improve prediction of polycrystals in the numerical model and the automatic habit diagnosis for instruments as well as the database of growth rates along crystallographic directions for polycrystals.

3.6 Conclusions

This paper proposed a framework to predict growth of polycrystals by vapor deposition in a consistent way with simulation of monocrystals based on history of ice crystals and current atmospheric conditions. The inherent growth ratio approach of Chen and Lamb (1994) for hexagonal monocrystals was extended into $T < -20^{\circ}\text{C}$. In $T < -20^{\circ}\text{C}$ during nucleation period ($D < 20\ \mu\text{m}$) crystal habits given one combination of temperature and moisture were determined using a simple stochastic approach based on the habit frequency constructed by Bailey and Hallett (2004). The major findings are the followings:

- During the early stage of growth, prediction of only hexagonal monocrystals with extended inherent ratio led to domination of columns in upper levels and plates in middle levels below temperature $T = -20^{\circ}\text{C}$. Prediction of polycrystals introduced the highest concentration of irregular polycrystals above $z = 4\ \text{km}$ ($T = -10^{\circ}\text{C}$), which can be expected from the frequency map given the vertical profile of supersaturation. Also, high concentrations of planar and columnar polycrystals were predicted in the region $6 < z < 8\ \text{km}$ ($-40 < T < -20^{\circ}\text{C}$) and $9 < z < 11\ \text{km}$ ($T < -50^{\circ}\text{C}$), respectively.

Concentration of the plates was reduced by order of 2 in the altitudes compared to the case with only hexagonal monocrystals. Concentration of the columnar crystals remained as high as the polycrystals above $z = 8$ km ($T < -50^\circ$ C). The difference in the spatial distribution of habits was found even more significant at 90 minutes of simulation due to the sedimentation and mass growth of ice crystals. It is clear that understanding the frequency of habit formation as well as the growth rate and terminal velocity of habits in middle and upper levels are necessary to understand spatial distribution of ice crystals.

- Differences of each nucleation process in spatial patterns, and concentration tendency and nucleated particle mass were discussed. The immersion (homogeneous) freezing process appears to be a key process to create planar (columnar and irregular) polycrystals because temperature and moisture of the active freezing process corresponds to high frequency of planar (columnar and irregular) polycrystals in the frequency map. The assumed habits for the freezing processes were shown to change the conditional frequency of habits in $10 < D < 100$ μ m significantly. Since concentration of CCN is generally much higher than IN, the freezing nucleation processes can affect habit frequency. Simulations with the formation of polycrystals through the freezing based on Bailey and Hallett (2004a) showed similar frequency of habits to observations in stratiform clouds, and wave and cirrus clouds.
- Vapor competition and effect of moisture on habits due to concentration of IN were demonstrated. IN concentration may modulate supersaturation by changing concentration of ice crystals, and in turn may change preferable habits given the

temperature. In the case study, the effect appeared in area of strong vertical motion with supercooled liquid hydrometeors. Planar and columnar polycrystals indicated higher frequency with lower concentration of IN. Also, IN concentration was able to change the habit frequency analyzed at a given altitude through vapor deposition growth rate and subsequent sedimentation.

In order to improve simulation and diagnosis of polycrystals, it is necessary to construct a database in laboratory experiments that provides relationships between characteristic physical parameters and habits as well as the growth rate along the characteristic parameters. It is not clear if the deposition-condensation nucleation process and freezing processes make any difference in habit frequency. More researches have to be done on the quantitative conditions to form polycrystals.

Future study includes simulation of cirrus and orographic wave clouds with homogeneous and heterogeneous freezing nucleation process with solution effects and all microphysical processes turned on in high spatial and temporal resolutions. Chapter 4 will discuss simulations of aggregation and riming processes with SHIPS.

References, Chapter 3

- Bacon, N. J., M. B. Baker, and B. D. Swanson, 2003: Initial stages in the morphological evolution of vapour-grown ice crystals. *Quart. J. Roy. Meteor. Soc.*, 129, 1903-1927.
- Baker, B. A. and R. P. Lawson, 2006: In situ observations of the microphysical properties of wave, cirrus, and anvil clouds. Part I: wave clouds. *J. Atmos. Sci.*, 63, 3160–3185.
- Bailey, M. and J. Hallett, 2002: Nucleation effects on the habit of vapour grown ice crystals from -18°C to -42°C . *Quart. J. Roy. Meteor. Soc.*, 128, 1461-1484.
- , and ———, 2004a: Growth rates and habits of ice crystals between -20° and -70°C . *J. Atmos. Sci.*, 61, 514–543.
- , and ———, 2004b: A new habit diagram and mass parameters for atmospheric ice crystals from -20° and -70°C . *14th International Conference on Clouds and Precipitation*, Bologna, Italy, International Commission on Clouds and Precipitation, 1, 703–706.
- Bohm, H. P., 1992: A general hydrodynamic theory for mixed-phase microphysics. Part I: Drag and fall speed of hydrometeors. *Atmos. Res.*, 27, 253–274.
- Chen, J.-P. and D. Lamb, 1994a: The theoretical basis for the parameterization of ice crystal habits: Growth by vapor deposition. *J. Atmos. Sci.*, 51, 1206–1221.
- Chiruta M., and P. K. Wang, 2003: The capacitance of rosette ice crystals. *J. Atmos. Sci.*, 60, 836–846.
- Connolly, P. J., P. R. Field, O. Moehler, S. Buttner, H. Saathoff, A. J. Heymsfield, M. W. Gallagher, T. W. Chouarton 2004: Simulations of ice crystal nucleation and growth: results from the AIDA cloud expansion chamber. *14th International Conference on Clouds and Precipitation*, Bologna, Italy, International Commission on Clouds and Precipitation.
- Heymsfield, A. J., M. Kajikawa, 1987: An improved approach to calculating terminal velocities of plate-like crystals and graupel. *J. Atmos. Sci.*, 44, 1088–1099.
- , S. Lewis, A. Bansemer, J. Iaquinta, L. M. Miloshevich, M. Kajikawa, C. Twohy, and M. R. Poellot, 2002: A general approach for deriving the properties of cirrus and stratiform ice cloud particles. *J. Atmos. Sci.*, 59, 3–29.
- , and L. M. Miloshevich, 1993: Homogeneous ice nucleation and supercooled liquid water in orographic wave clouds. *J. Atmos. Sci.*, 50, 2335–2353.

- Kajikawa, M., 1982: Observations of the falling motion of early snowflakes. Part I: Relationship between the free-fall pattern and the number and shape of component snow crystals. *J. Meteor. Soc. Japan*, 60, 797-803.
- Korolev, A., and G. A. Isaac, 1999: Ice particle habits in arctic clouds. *Geophys. Res. Lett.*, 26, 1299–1302.
- , ——— and J. Hallett, 2000: Ice particle habits in stratiform clouds. *Quart. J. Roy. Meteor. Soc.*, 126, 2873–2902.
- Kumai, M., 1982: Formation of ice crystals and dissipation of supercooled fog by artificial nucleation, and variations of crystal habit at early growth stages. *J. Atmos. Sci.*, 21, 579–587.
- Lawson, R. P., B. A. Baker, B. Pilson, and, Q. Mo, 2006a: In Situ Observations of the Microphysical Properties of Wave, Cirrus, and Anvil Clouds. Part II: Cirrus Clouds. *J. Atmos. Sci.*, 63, 3186–3203.
- , B. A. Baker, P. Zmarzly, D. O’Connor, Q. Mo, J.-F. Gayet, and V. Shcherbakov, 2006b: Microphysical and optical properties of atmospheric ice crystals at South Pole station. *J. App. Meter. and Clim.*, 45, 1505–1524.
- Liu, H. C., P. K. Wang and R. E. Schlesinger, 2003: A numerical study of cirrus clouds. Part I: Model Description. *J. Atmos. Sci.*, 60, 1075-1084.
- Locatelli, J. D., and P. V. Hobbs, 1974: Fall speeds and masses of solid precipitation particles. *J. Geophys. Res.*, 79, 2185-2197.
- Lynn, B. H., A. P. Khain, J. Dudhia, D. Rosenfeld, A. Pokrovsky, and A. Seifert, 2005: Spectral (bin) microphysics coupled with a Mesoscale Model (MM5). Part I: model description and first results. *Mon. Wea. Rev.*, 133, 44–58.
- Macke, A., P. N. Francis, G. M. McFarquhar, and S. Kinne, 1998: The role of ice particle shapes and size distributions in the single scattering properties of cirrus clouds. *J. Atmos. Sci.*, 55, 2874–2883.
- Mitchell, D. L., 1996: Use of mass- and area-dimensional power laws for determining precipitation particle terminal velocities. *J. Atmos. Sci.*, 53, 1710–1723.
- , R. Zhang, and R. L. Pitter, 1990: Mass-dimensional relationships for ice particles and the influence of riming on snowfall rates. *J. Appl. Meteor.*, 29, 153–163.

- Nakaya, U., 1954: *Snow crystals, natural and artificial*. Cambridge, Harvard University Press, 510 pp.
- Pruppacher, H. R. and J. D. Klett, 1997: *Microphysics of Clouds and Precipitation*. Kluwer Academic, 914 pp.
- Rauber, R. M., 1987: Characteristics of cloud ice and precipitation during wintertime storms over the mountains of northern Colorado. *J. Appl. Meteor.*, 26, 488-524.
- Straka, J. M., and E. R. Mansell, 2005: A bulk microphysics parameterization with multiple ice precipitation categories. *J. Appl. Meteor.*, 44, 445–466.
- Walden, V. P., S. G. Warren, and E. Tuttle, 2003: Atmospheric ice crystals over the Antarctic Plateau in winter. *J. Appl. Meteor.*, 42, 1391-1405.
- Woods, C. P., M. T. Stoelinga, J. D. Locatelli, and P. V. Hobbs, 2005: Microphysical processes and synergistic interaction between frontal and orographic forcing of precipitation during the 13 December 2001 IMPROVE-2 event over the Oregon Cascades. *J. Atmos. Sci.*, 62, 3493–3519.

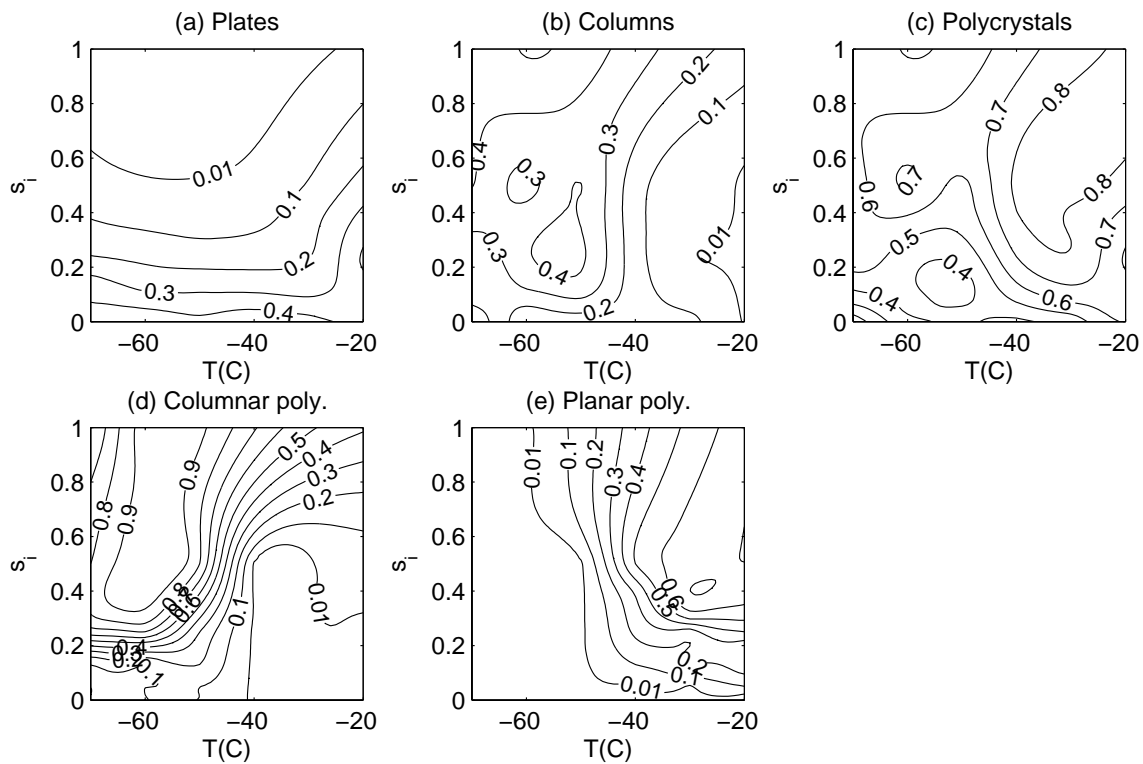


Figure 3.1 Habit frequency given temperature T and supersaturation over ice s_i . They were constructed from Bailey and Hallett (2004). (a) plates, (b) columnar crystals, (c) polycrystals, (d) columnar polycrystals and (e) planar polycrystals. The frequency of (d) and (e) is conditional frequency given the occurrence of polycrystals, while the frequencies of (a), (b) and (c) add up to unity.

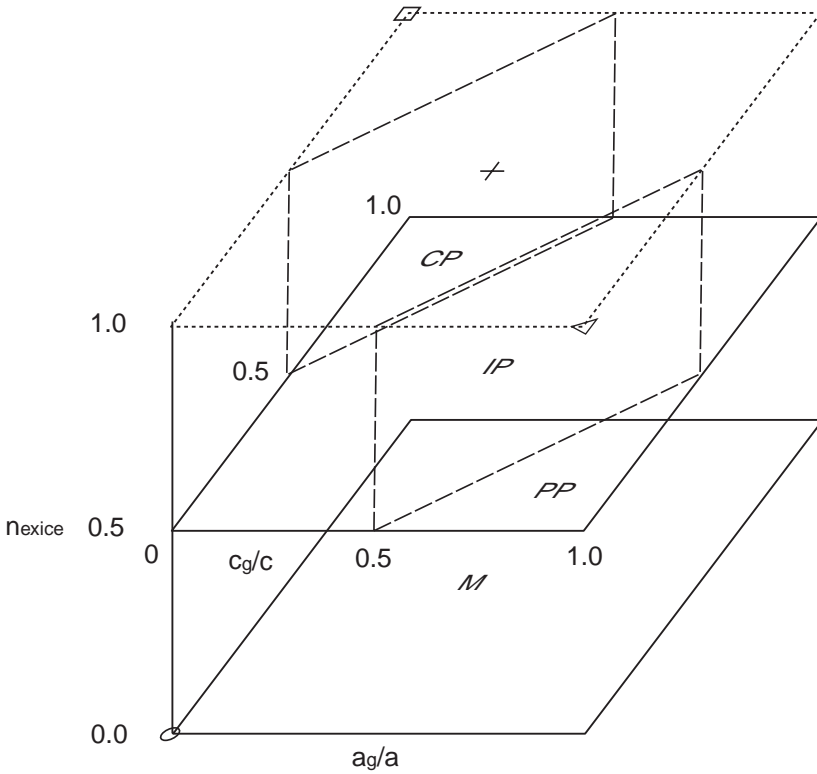


Figure 3.2 Diagnosis of ice crystal habits including polycrystals. n_{exice} is the number of extra crystalline structure, and a_g and c_g are the coordinates of center of gravity of a polycrystal. “M” indicates monocrystals defined in $n_{exice} < 0.5$. Polycrystals are defined in $n_{exice} \geq 0.5$. “PP” (“CP”) indicates planar (columnar) polycrystals defined by $a_g/a \geq c_g/c + 0.5$ ($c_g/c \geq a_g/a + 0.5$). “IP” indicates irregular polycrystals defined between “PP” and “CP”.

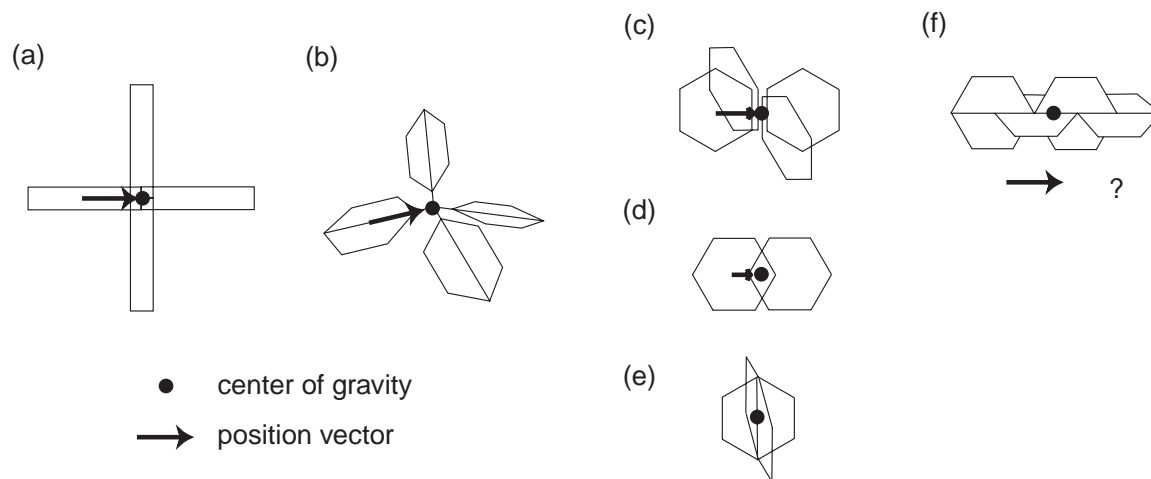


Figure 3.3 Conceptual models of center of gravity for polycrystals. (a) is bullet rosette, (b) side plane, (c) assemblage of plates, (d) overlapping parallel plates, (e) crossed plates, and (f) scalelike side plane.

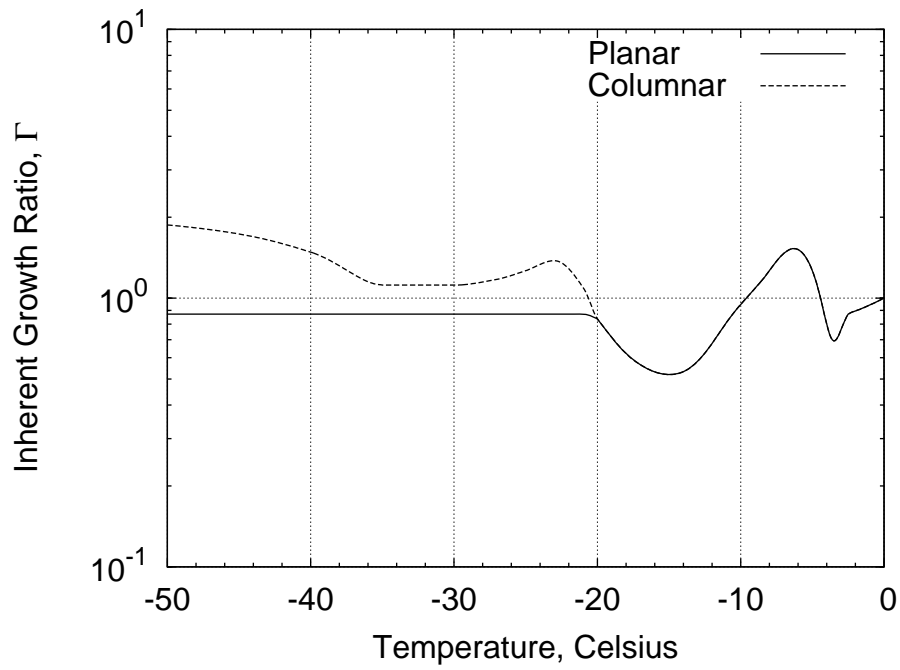


Figure 3.4 Extended inherent growth ratios for columnar and planar growth in $T \leq -20^\circ\text{C}$.

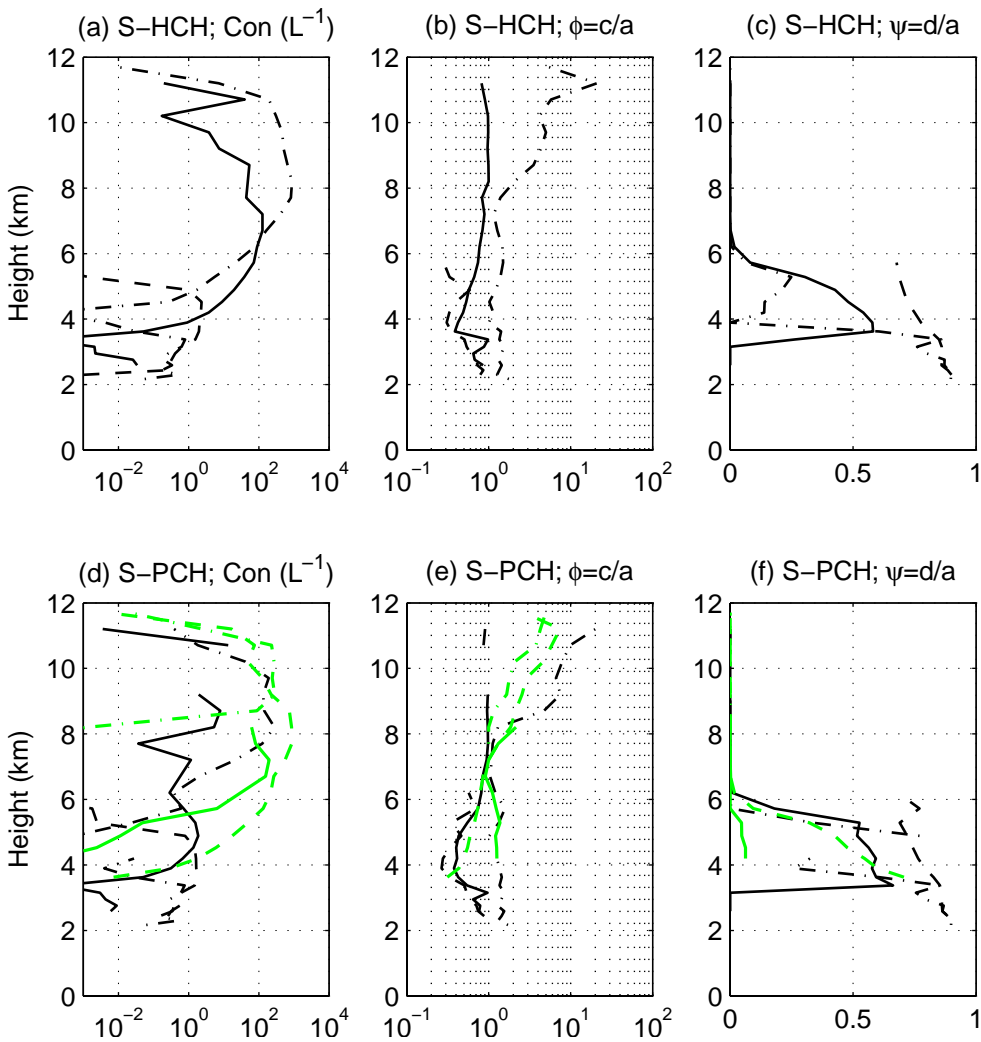


Figure 3.5 Vertical profile of horizontally averaged concentration and axis ratios for each habit at 20 minutes of simulation. The upper figures show results from S-HCH, and the lower from S-PCH. The solid line indicates plates, dashed dendrites, dash-dotted columns, gray solid planar polycrystals, gray dash-dotted columnar polycrystals, and gray dashed irregular polycrystals.

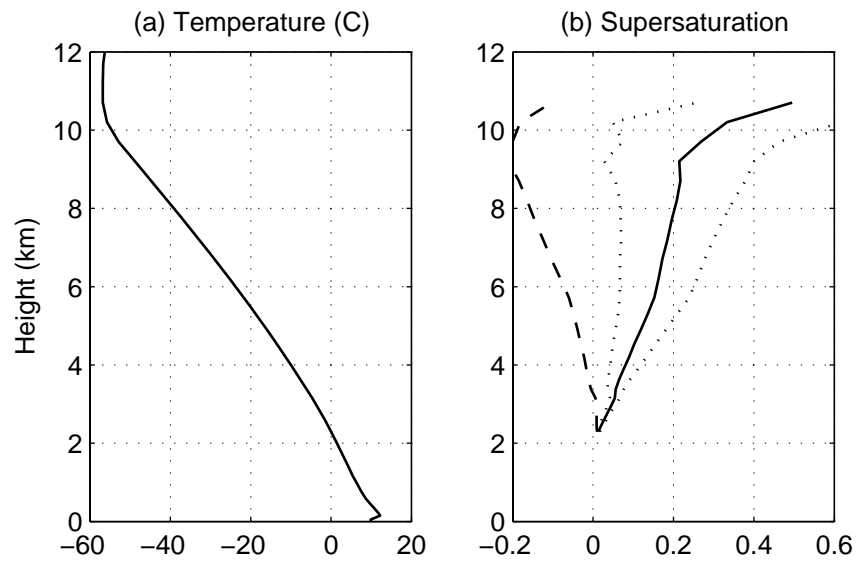


Figure 3.6 Vertical profile of temperature and supersaturation. Solid line in (b) indicates supersaturation over ice averaged only for positive values. Dotted lines indicate one standard deviation added or subtracted from the mean, and dashed line supersaturation over water corresponding to the one over ice.

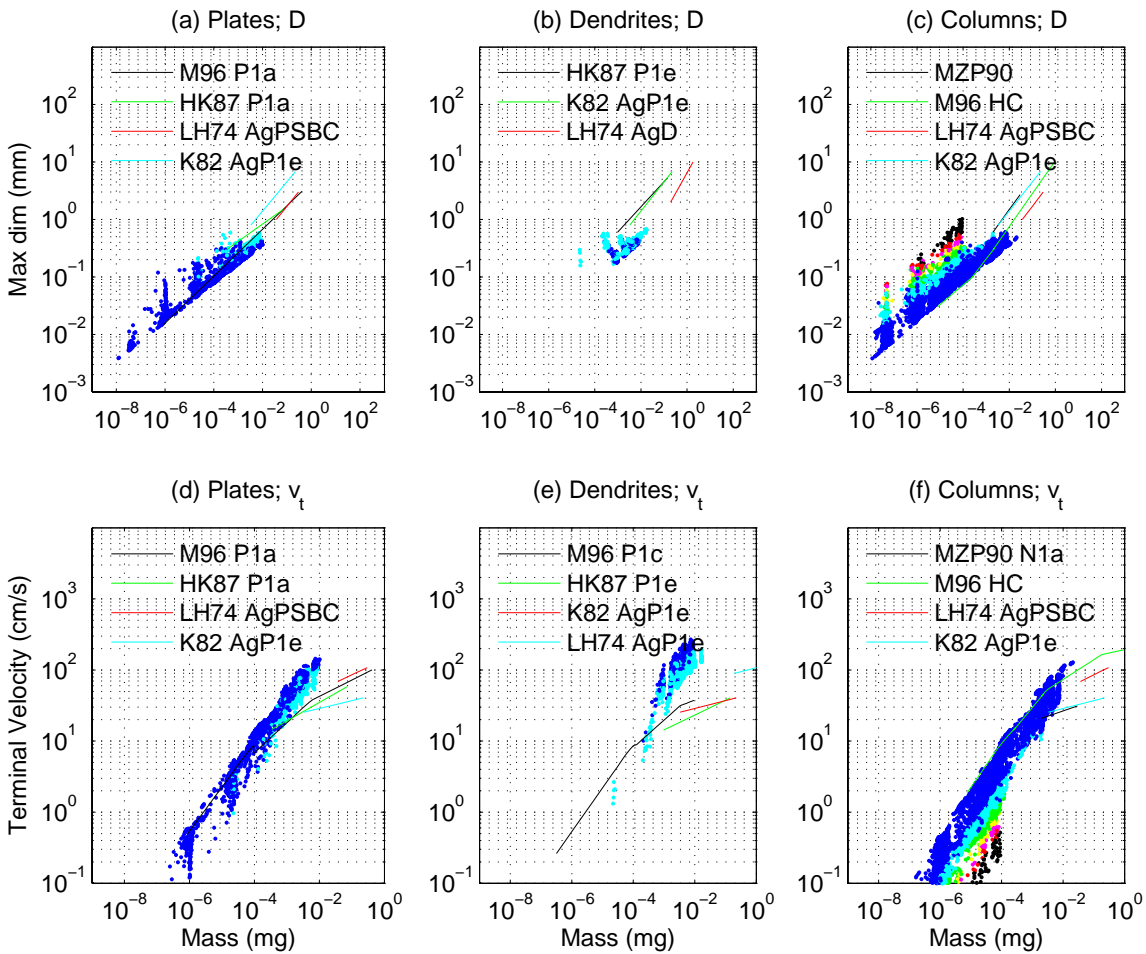


Figure 3.7 Mass-dimensional and mass-terminal velocity relationships at 20 minutes of simulation for S-HCH. The color points for plates and dendrites indicate axis ratio, $\phi = c/a$; $0.5 < \phi$: blue, $0.1 < \phi \leq 0.5$: cyan, and $0.05 < \phi \leq 0.1$: green. Those for columnar crystals $1 \leq \phi < 5$: blue, $5 \leq \phi < 10$: cyan, $10 \leq \phi < 15$: green, $15 \leq \phi < 20$: yellow, $20 \leq \phi < 25$: magenta, $25 \leq \phi < 30$: red, and $30 \leq \phi$: black. HK87 denotes Heymsfield and Kajikawa (1987), K82 Kajikawa (1982), LH74 Locatelli and Hobbs (1974), MZP90 Mitchell et al. (1990), and M96 Mitchell (1996). “Ag” indicates “aggregates of” the habit.

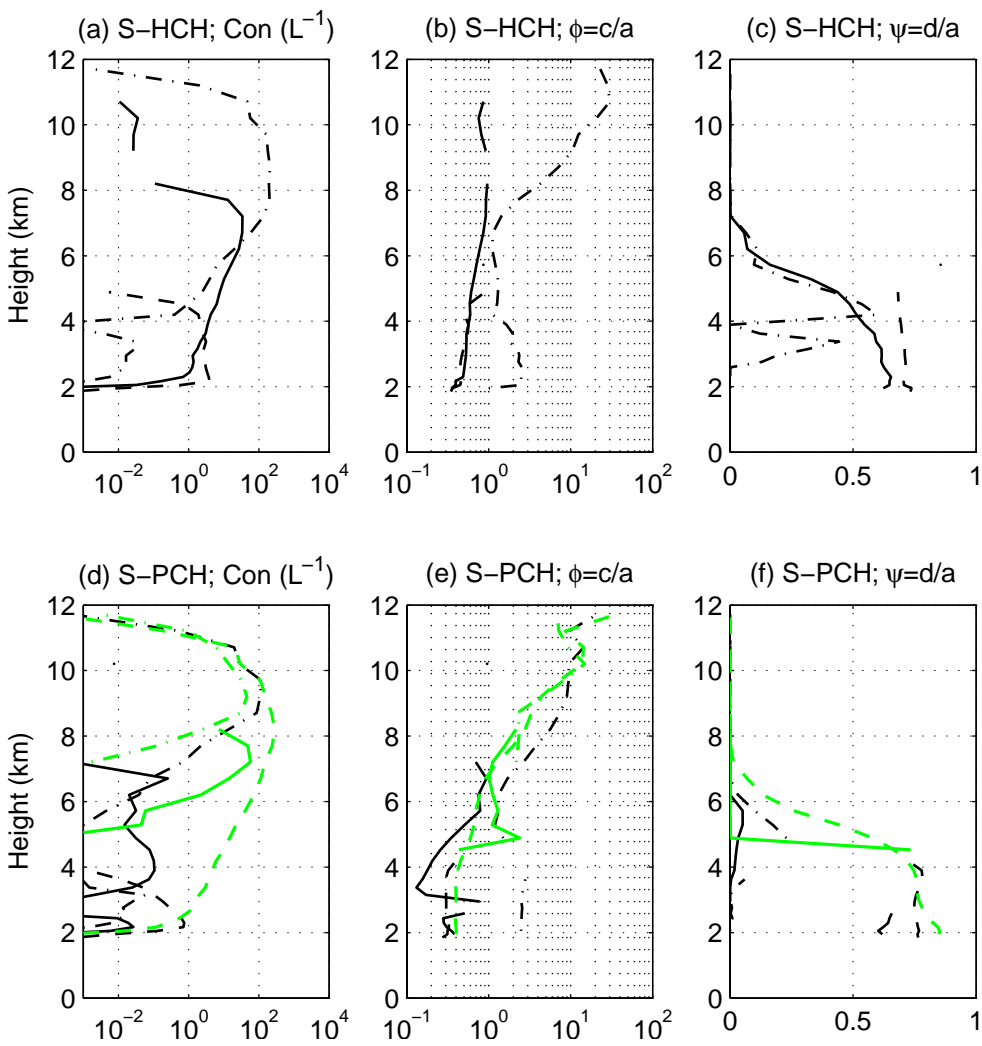


Figure 3.8 Same as Figure 3.5 except that this is at 60 minutes of simulation.

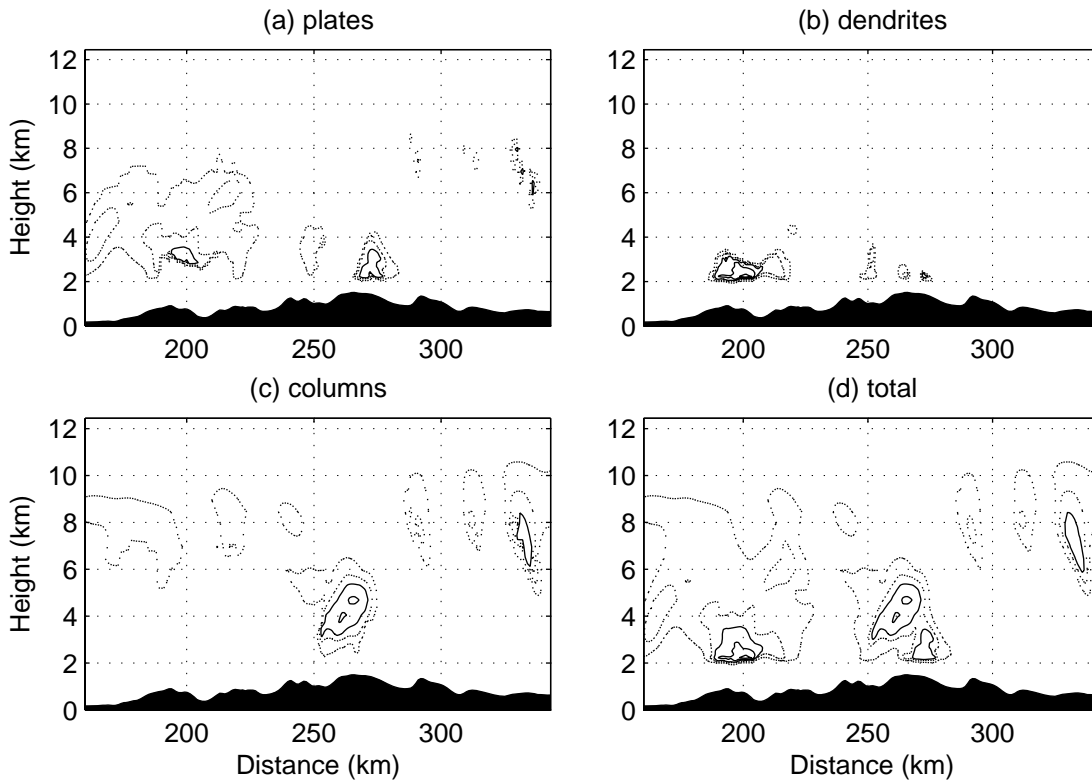


Figure 3.9 Comparison of mass contents for diagnosed habits after 90 minutes of vapor deposition simulation (S-HCH). The dots contours are 0.01, and 0.05 (g/m^3), and the solid contours 0.1, 0.2, and 0.3 (g/m^3).

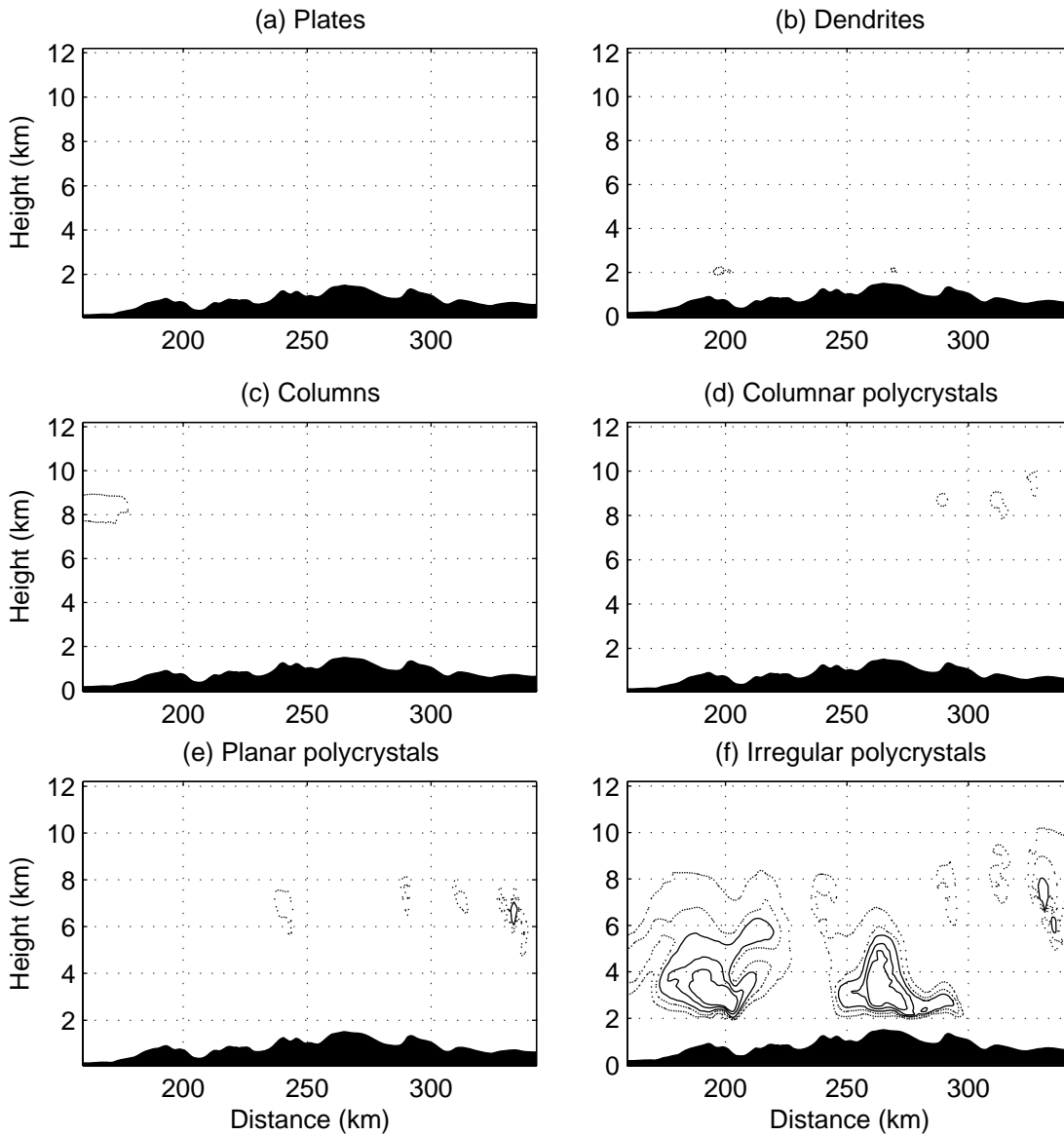


Figure 3.10 Comparison of mass contents for diagnosed habits after 90 minutes of vapor deposition simulation (S-PCH). The dots contours are 0.01, and 0.05 (g/m^3), and the solid contours 0.1, 0.2, and 0.3 (g/m^3).

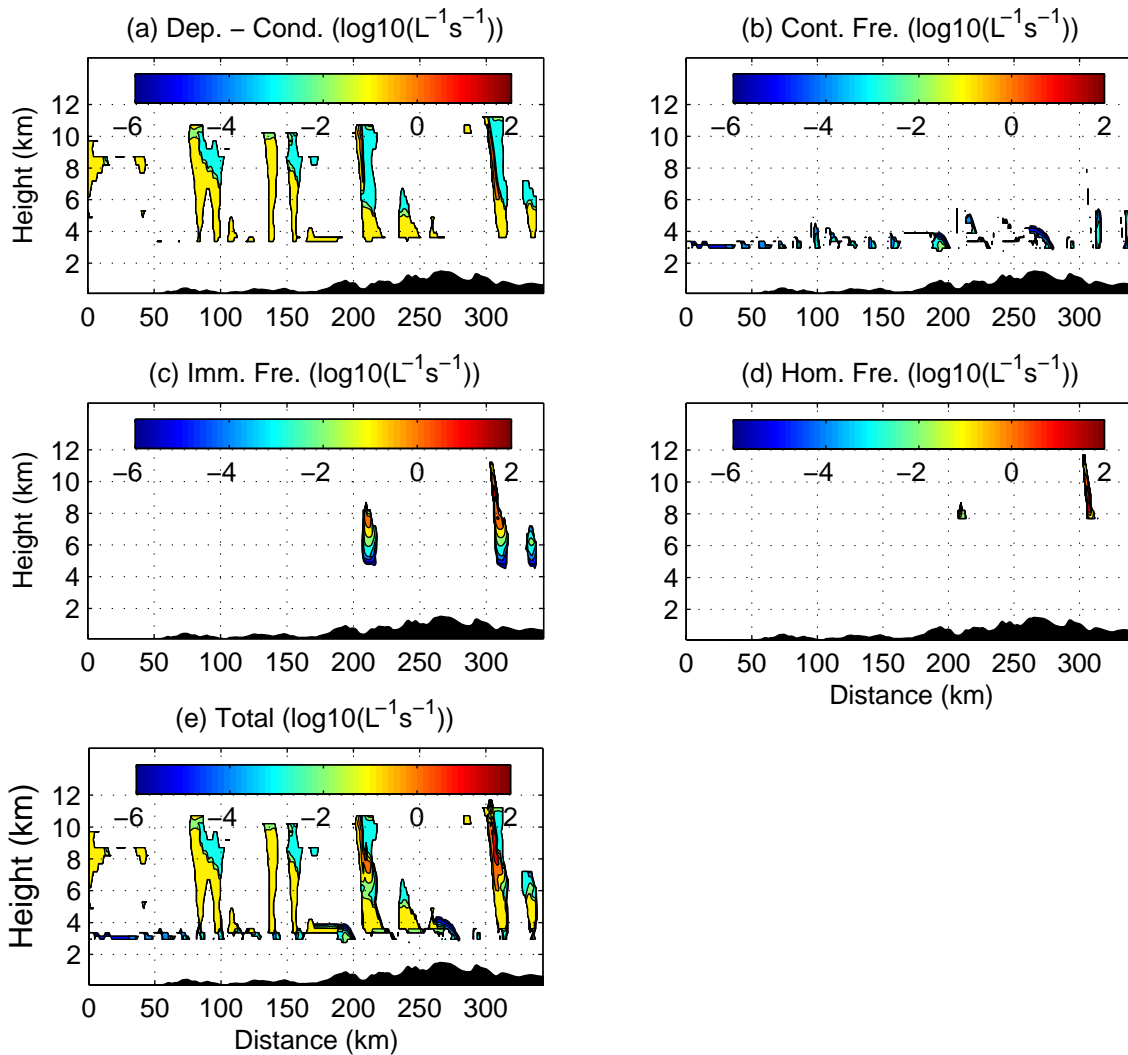


Figure 3.11 Concentration tendency of ice nucleation processes for PCH at 20 minutes; (a) deposition-condensation nucleation, (b) contact freezing nucleation, (c) immersion freezing nucleation (d) homogeneous freezing nucleation and (e) total.

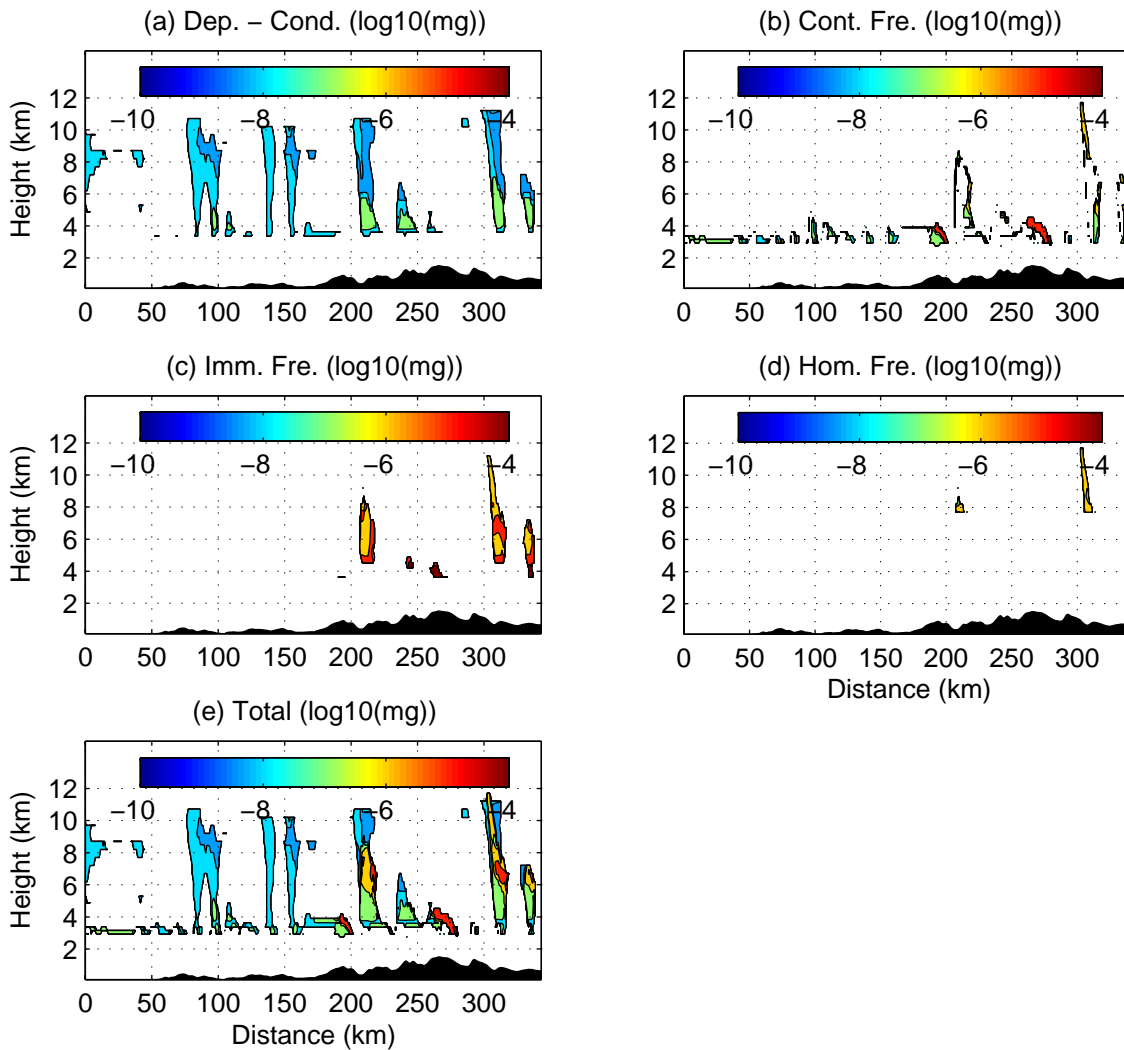


Figure 3.12 Initial mass per a single particle produced by ice nucleation processes for PCH at 20 minutes; (a) deposition-condensation nucleation, (b) contact freezing nucleation, (c) immersion freezing nucleation (d) homogeneous freezing nucleation and (e) total.

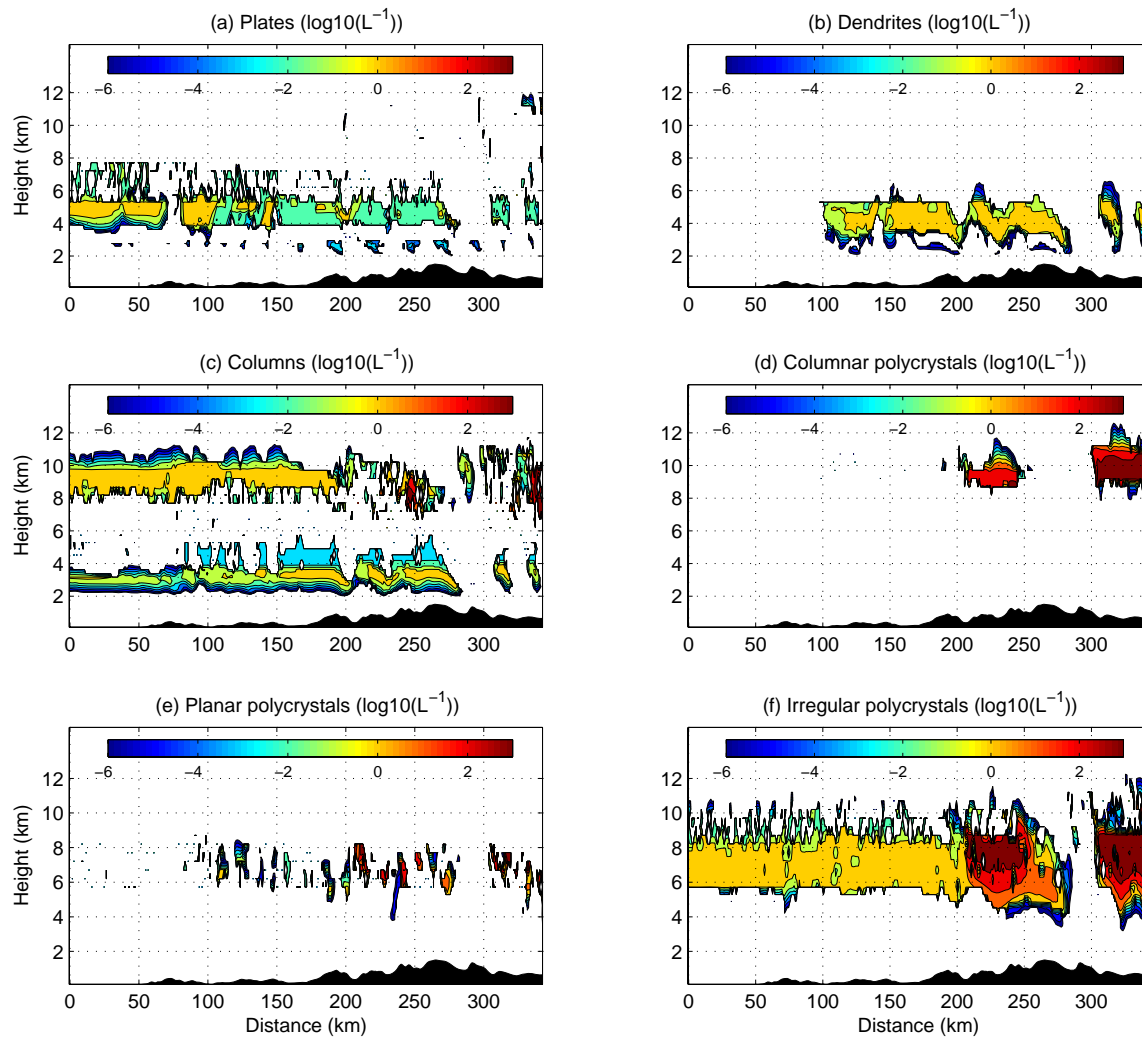


Figure 3.13 Concentration for diagnosed habits for PCL at 20 minutes.

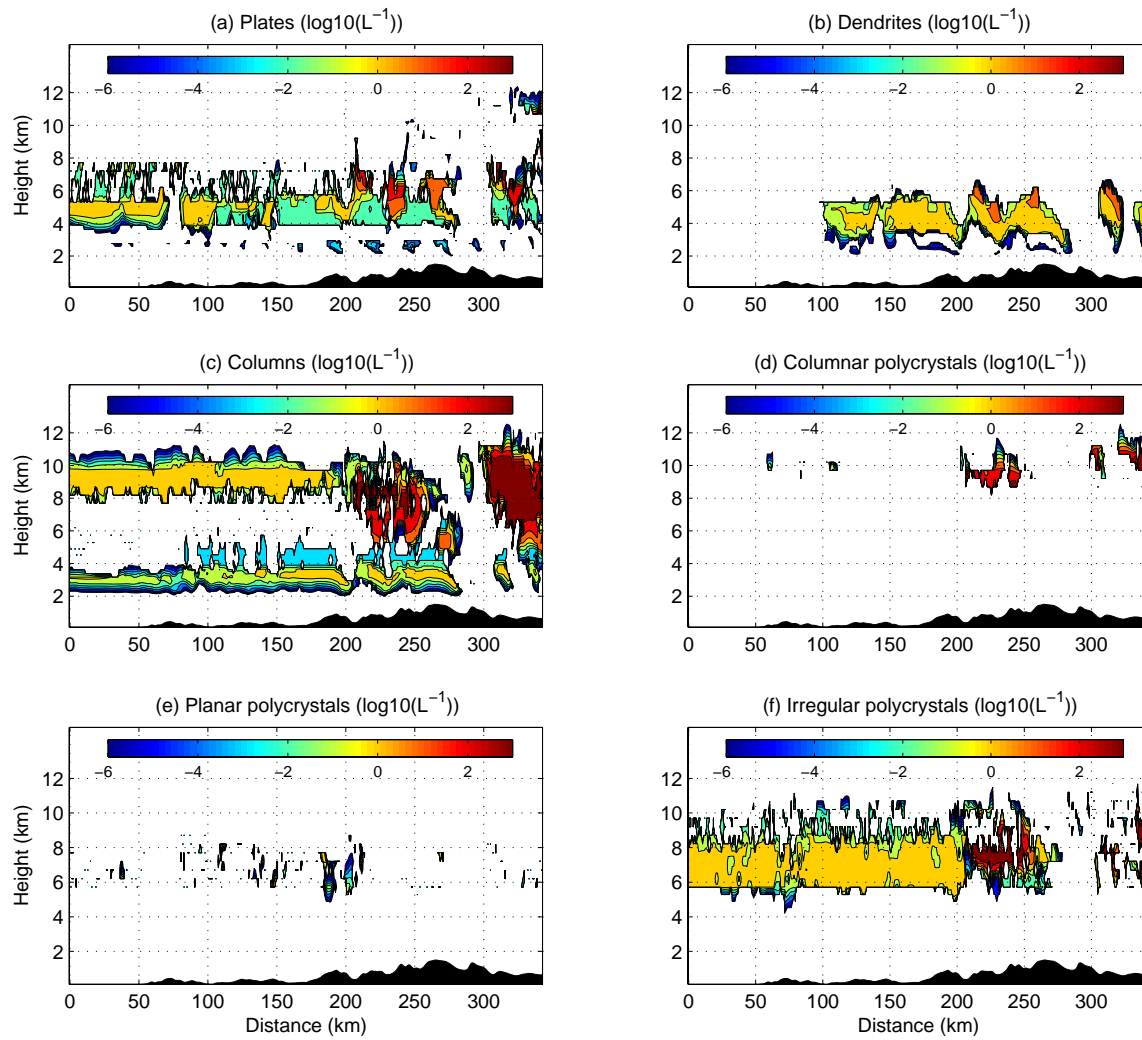


Figure 3.14 Concentration for diagnosed habits for PCLH at 20 minutes of simulation.

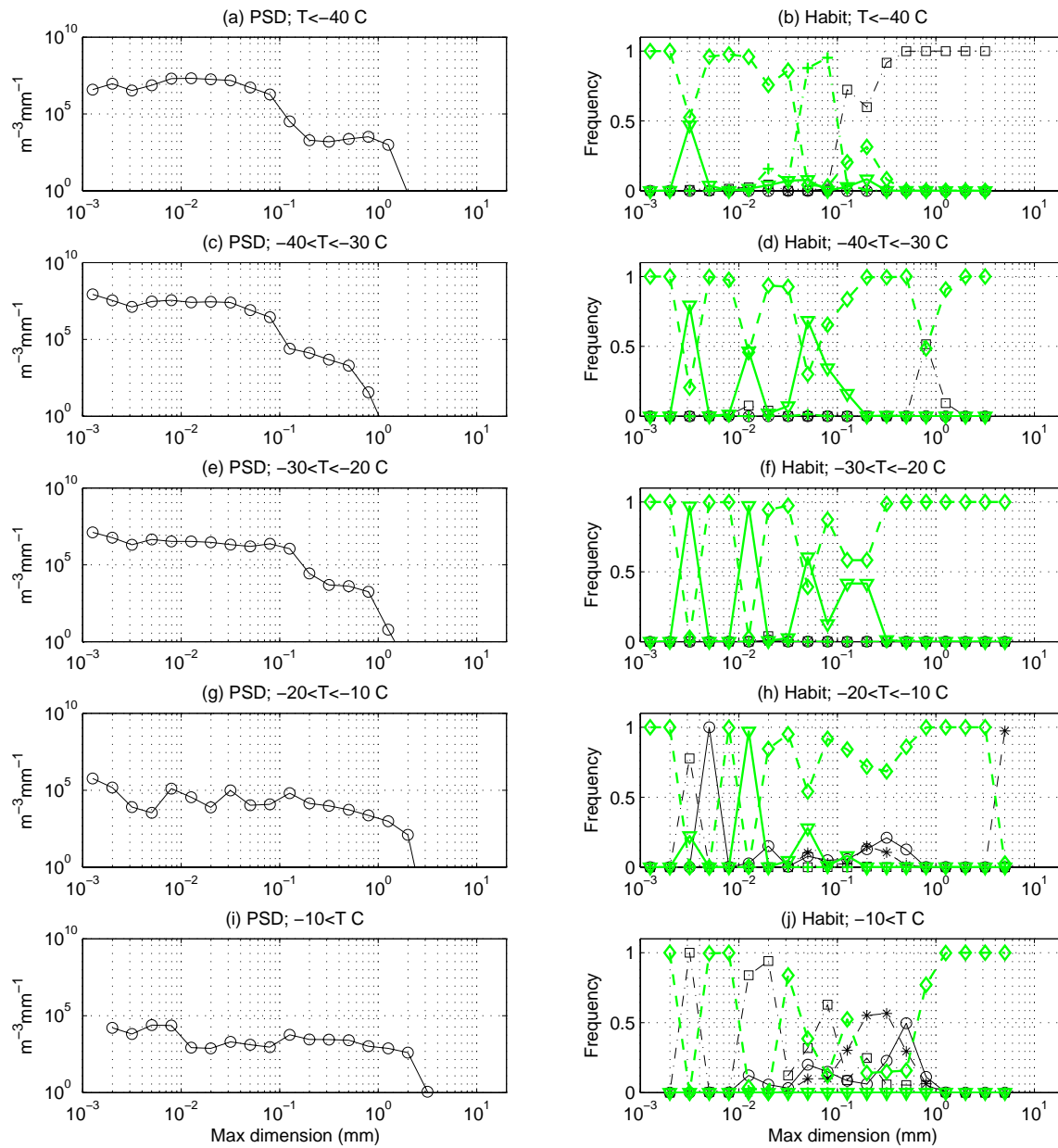


Figure 3.15 Average particle size distribution (left column) and conditional frequency (right column) of habits in the five temperature ranges for PCL at 90 minutes. Open circles in the left column indicate samples. In the right plates, dendrites, and columns are indicated by circles, asterisks, and squares, respectively. Columnar, planar, and irregular polycrystals are indicated by crosses, triangles, and diamonds, respectively.

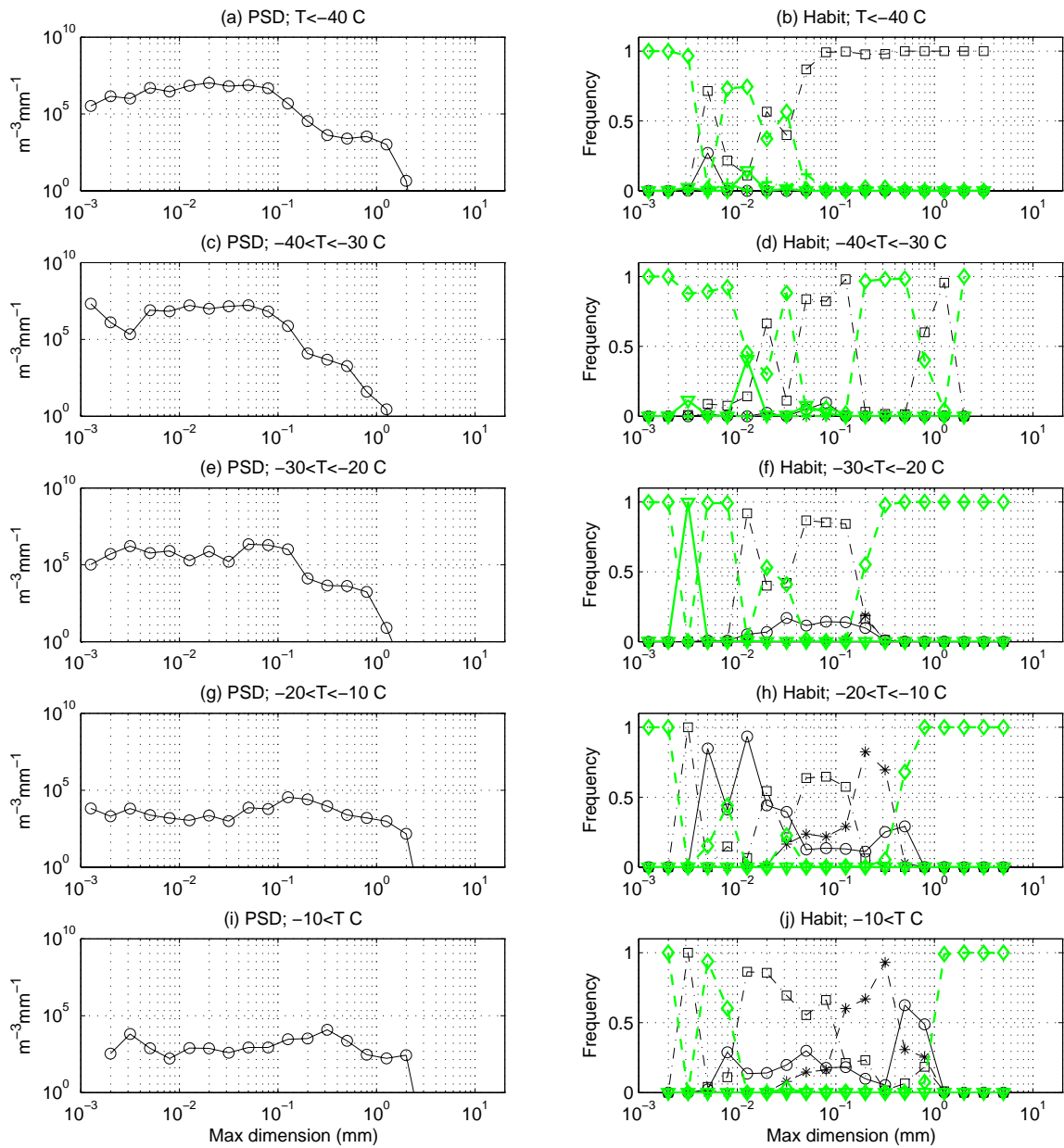


Figure 3.16 Same as Figure 3.15 except that this is for PCLH at 90 minutes.

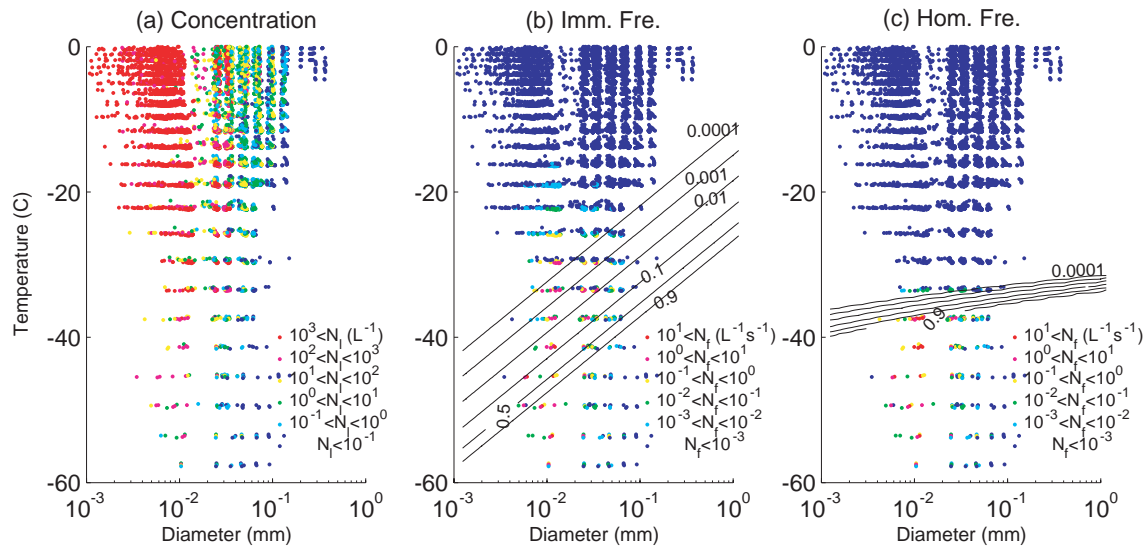


Figure 3.17 Comparison of concentration of supercooled liquid hydrometeors (a) and immersion freezing nucleation rate calculated with Bigg's formula (b) at 20 minutes for PCL. The solid line in (b) indicates the freezing probability of a particle per second.

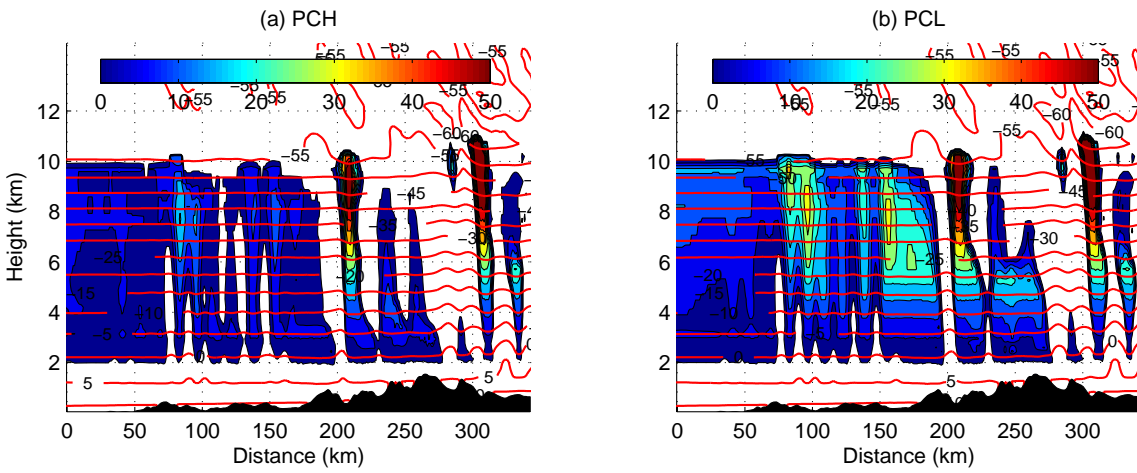


Figure 3.18 Comparison of supersaturation over ice for (a) PCH, and (b) PCL. Color-filled contour indicates supersaturation over ice in %, and the red solid lines temperature in Celsius. PCH and PCHH or PCL and PCLH have similar distributions.

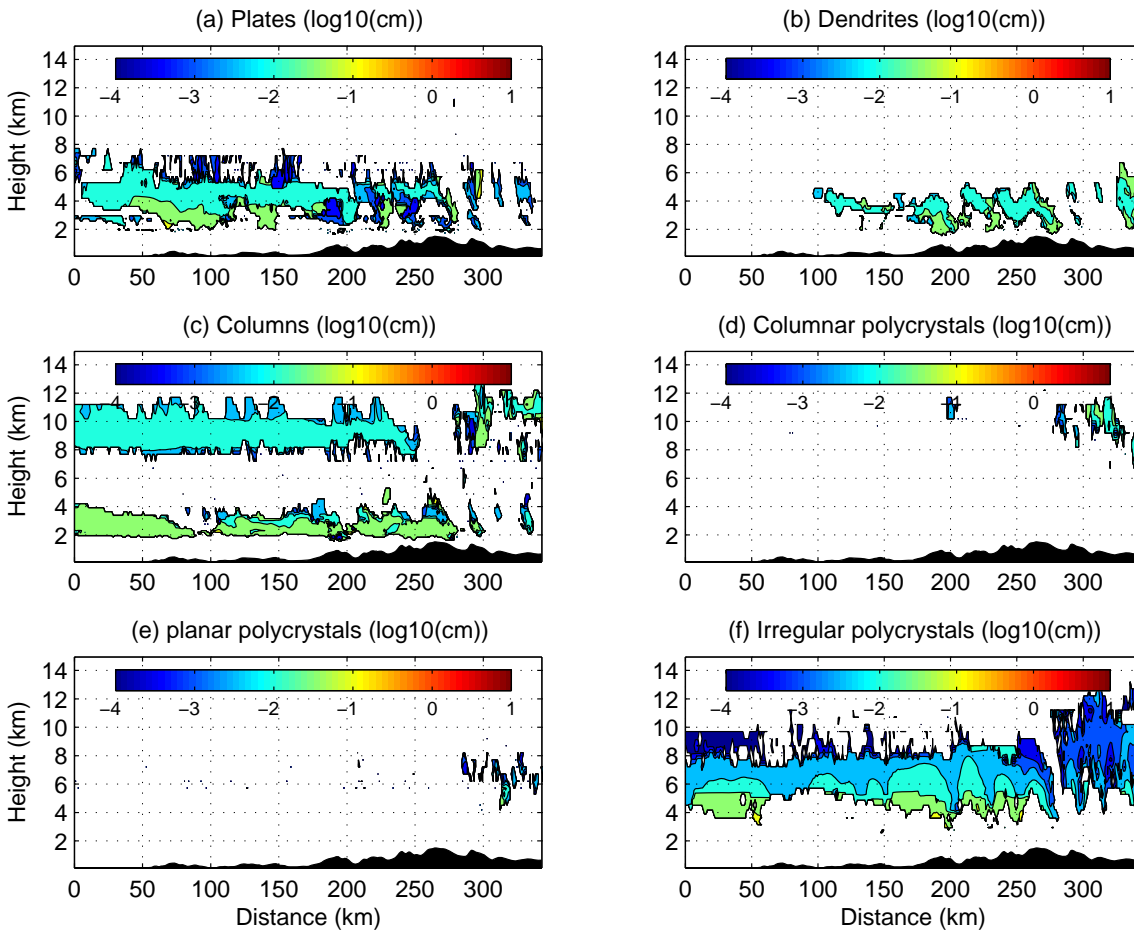


Figure 3.19 Comparison of maximum dimension averaged for each diagnosed habit at 90 minutes for PCH.

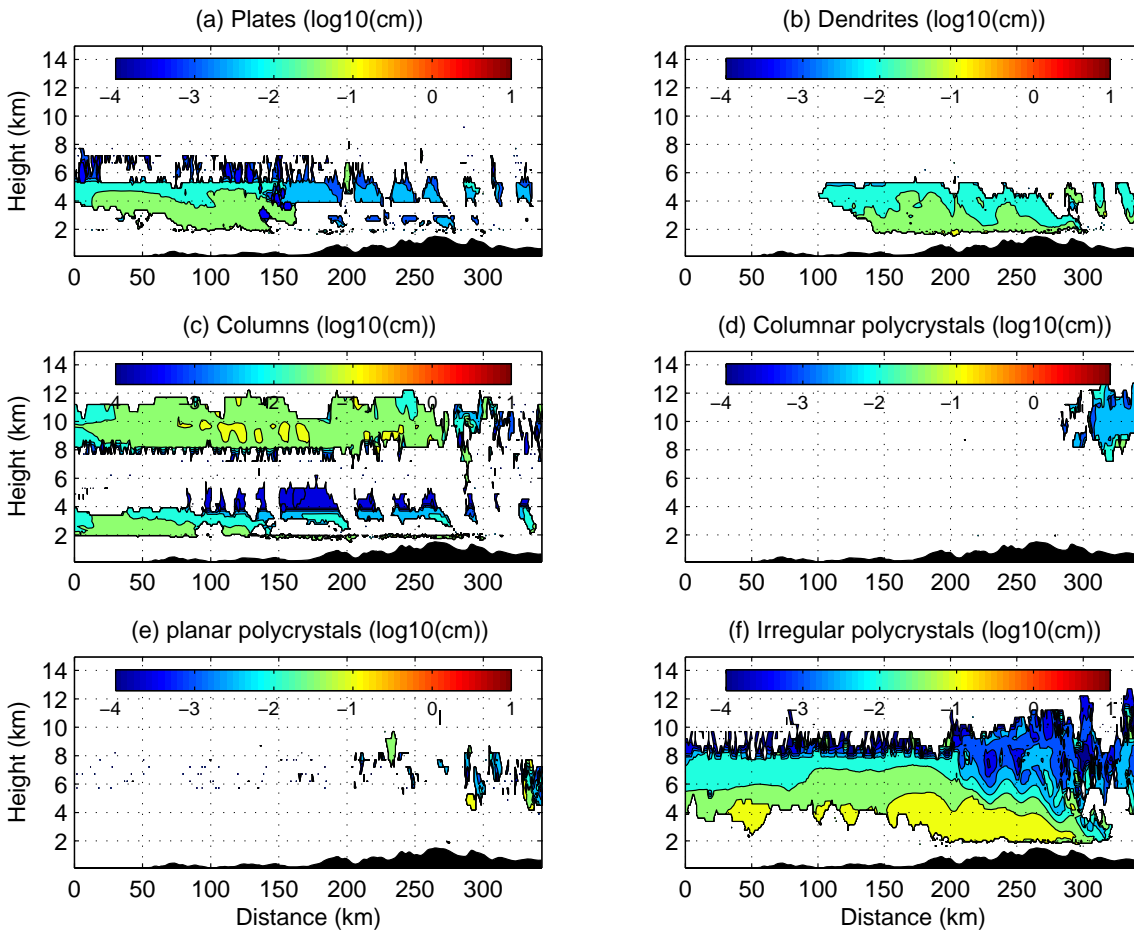


Figure 3.20 Same as Figure 3.19 except that this is for PCL.

Table 3.1 List of sensitivity experiments. The experiments with “Form Hex” produce hexagonal monocrystals by immersion and homogeneous freezing process. PCHNI and PCLNI do not simulate immersion and homogeneous freezing process.

Experiment #	Formation of polycrystals by freezing	IN concentration (L^{-1})	Mass limit	Polycrystals prediction
S-HCH	Form Hex	230	H	NO
S-PCH	Yes	230	H	YES
PCH	Yes	230	L	YES
PCHH	Form Hex	230	L	YES
PCL	Yes	1	L	YES
PCLH	Form Hex	1	L	YES
PCHNI	No Imm. Hom.	230	L	YES
PCLNI	No Imm. Hom.	1	L	YES

Table 3.2 Moments of average particle size distribution and concentration frequency of habits for 5 temperature ranges. Concentration (Con), mean maximum dimension (M D) and standard deviation of maximum dimension (SD D) are given in L^{-1} , mm, and mm, respectively. P denotes plates, D dendrites, C columnar crystals, CP columnar polycrystals, PP planar polycrystals, and IP irregular polycrystals. The frequency is in percentage (%).

	Con	M D	SD D	P	D	C	CP	PP	IP	
T<-40	PCH	304	0.059	0.061	0	0	25	10	2	64
	PCHH	227	0.098	0.067	0	0	87	3	0	10
	PCL	204	0.041	0.062	0	0	4	33	2	61
	PCLH	181	0.059	0.066	1	0	82	7	0	10
	PCHNI	100	0.139	0.088	0	0	74	3	1	21
	PCLNI	2	0.665	0.479	0	0	84	1	1	15
-40<T<-30	PCH	570	0.042	0.031	1	0	7	0	17	74
	PCHH	479	0.051	0.026	4	0	38	0	2	56
	PCL	519	0.034	0.025	0	0	3	0	20	77
	PCLH	433	0.047	0.029	2	0	55	0	3	40
	PCHNI	146	0.079	0.049	2	0	8	0	6	83
	PCLNI	2	0.234	0.221	1	0	6	0	2	92
-30<T<-20	PCH	183	0.099	0.148	1	0	0	0	8	91
	PCHH	176	0.093	0.047	16	0	8	0	1	75
	PCL	85	0.073	0.072	0	0	1	0	23	76
	PCLH	67	0.086	0.070	25	1	53	0	0	20
	PCHNI	134	0.109	0.053	1	0	0	0	2	96
	PCLNI	3	0.340	0.208	1	1	0	0	1	97
-20<T<-10	PCH	65	0.212	0.363	60	19	0	0	0	21
	PCHH	65	0.173	0.090	54	25	1	0	0	20
	PCL	5	0.348	0.289	10	7	0	0	3	80
	PCLH	5	0.324	0.267	31	34	15	0	0	20
	PCHNI	70	0.181	0.185	53	27	0	0	0	20
	PCLNI	2	0.523	0.362	28	20	2	0	0	51
-10<T	PCH	35	0.369	0.671	17	40	44	0	0	0
	PCHH	38	0.291	0.118	11	49	39	0	0	0
	PCL	2	0.622	0.496	18	33	10	0	0	38
	PCLH	2	0.517	0.421	16	59	10	0	0	15
	PCHNI	37	0.348	0.599	12	47	41	0	0	0
	PCLNI	1	0.615	0.522	23	40	14	0	0	24

Chapter 4 Description and box model simulations of habit-dependence aggregation and riming process

4.1 Introduction

Proper description of three dimensional spatial distributions and particle size distributions (PSDs) of habits and types of solid hydrometeors (ice particles) are necessary to understand precipitation and radiative forcing of ice clouds, and to improve remote sensing application. Aggregation of ice particles occurs in most of clouds with ice particles, and it changes spatial distribution of bulk property such as number concentration or Ice Water Content and also PSD. The single-scattering cloud albedo is determined by extinction coefficient and shape-dependent asymmetry parameter. The aggregation process produces particles with higher area ratios than single particles of the same diameter (Heymsfield and Miloshevich, 2003), while it can reduce the concentration of small particles. Mitchell et al. (1996) shows that aggregation decreased optical depth by 10% to 20 % because less projected area is available given an Ice Water Content. Also, aggregation makes sedimentation of ice particles faster, so that the life time of cirrus can be modulated by aggregation. The large particles including aggregates tend to have less influence on the single-scattering properties in the visible and near-infrared bands than do the more numerous small particles, but they are important for inferring the ice water content (Baum et al., 2005).

Aggregation is a key process leading to precipitation in stratiform clouds. Stratus, nimbostratus and altostratus clouds cover 14% of land and 23% of ocean (Warren and Eastman,

2007). Even within ice clouds in the tropics the aggregation process has been shown to be most important process leading to precipitation (e.g., McFarquhar and Heymsfield, 1996; Stith et al., 2002).

Modeling aggregation process is a challenging subject due to variety of shapes and density of ice particles. In general, there are two kinds of approach to simulate aggregation processes. One is Lagrangian approach that keeps track of each single particle; another is Eulerian approach of solving stochastic collection equation for a group of particles defined by mass (cf., Pruppacher and Klett, 1997, hereafter PK97). Maruyama and Fujiyoshi (2005), hereafter MF05, developed a Lagrangian stochastic aggregation model with a Monte Carlo method to study evolution of PSDs and structure of snowflakes. MF05 used spheres to represent ice crystals, but successfully simulated the mass-geometrical relationships of aggregates and fractal dimension that are similar to observations. Chen and Lamb (1994), hereafter CL94, simulated aggregation process by solving stochastic collection equation in a way that aspect ratio of spheroidal ice particles was evolved according to aggregation. Direct effects of different shapes of ice crystals on growth rate of aggregates are still not known.

This study attempts to simulate the habit dependency of PSD evolution by the Eulerian stochastic approach for use in a cloud resolving model. The purpose of this paper is to describe a quasi-stochastic collection model with prediction of ice particle property, and validate simulations with currently available data. The next section describes the quasi-stochastic collection model to simulate aggregation and riming processes. The model is developed in the framework of Spectral Habit Ice Prediction System (SHIPS). In section 4.3

box model simulations are implemented and validated against available theoretical and empirical results. The conclusions and future researches are given in section 4.4.

4.2 Modeling aggregation and riming processes with SHIPS

4.2.1 SHIPS and quasi-stochastic collection equation

The main concept of SHIPS is to evolve properties of ice particles in the Eulerian dynamic model continuously in such a way that the ambient conditions along the trajectory of ice particles are reflected in the particle properties. The distribution of ice particles are divided into mass bins where each mass bin represents average habit and type of ice particles given the mass range. SHIPS introduces Particle Property Variables (PPVs) that contain information on the property of particles in a bin. The current version of SHIPS includes mass content components, length variable components, volume variable components, and concentration variable components as PPVs. Mass content components include rime mass, aggregation mass, ice crystal mass, and melt mass. They are integrated based on the respective physical processes that ice particles are experiencing. Length variable components include lengths along a-axis, c-axis, and dendritic arm for hexagonal ice crystals. Chapter 3 introduced the coordinates of center of gravity into length variable components, and number of extra crystalline structure to a hexagonal monocrystal as a concentration variable component in order to predict polycrystals. The maximum dimension of ice particles is predicted as volume variable components, which is used to predict the density of ice particles. Readers are referred to Chapter 2 and Chapter 3 for more detail explanation of the scheme.

The primary aim of SHIPS in modeling collision-coalescence processes among ice particles and between liquid and solid hydrometeors is to reflect characteristics of habits by using predicted habit information and simple parameterizations to simulate the evolution of PSDs in a computationally efficient way. SHIPS formulates aggregation and riming processes in the quasi-stochastic collection equations (SCE). Calculation of tendencies of two moments, concentration and mass content of a bin are conducted by the hybrid bin method proposed in CL94. The interaction kernel of two representative hydrometeors² in mass bins i and j is defined as:

$$K_{i,j} = E_{collection}(i, j) \cdot |v_t^i - v_t^j| (A_i + A_j) \quad (4.1)$$

where v_t^i and A_i are the terminal velocity and cross-section area of the representative hydrometeor in a mass bin i . The collection efficiency is defined as the product of collision and coalescence efficiencies; $E_{collection} = E_{col} \cdot E_{coal}$. In the quasi-stochastic approach it is assumed that particles in a bin collect particles in other bins once, but with all possible pairs during one time step. The scheme of CL94 divides particles contained in a mass bin i into groups called “fortunate” and “unfortunate groups” based on the number of collected particles, $K_{i,j} N^j \delta t$ ($j = 1, \dots, N_{BIN}$) where N^j is concentration of mass bin j , and N_{BIN} is the total number of mass bin. Particles in all groups possess the same property as the representative hydrometeor of the bin. Then, each group forms a shifted bin with mass content incremented with those collected, and bin boundaries of the shifted bin is incremented based on the collection rates. The concentration and mass content of all shifted bins are transferred back to

² The representative hydrometeor of a mass bin is a hydrometeor defined having mean mass of the bin.

the bins defined by the original bin boundaries. In the following, modifications of the scheme to predict and diagnose shapes and density of ice particles with PPVs will be described.

4.2.2 Diagnosis of semi-axis lengths, aspect ratio, and porosity

This study predicts the circumscribing sphere volume (or maximum dimension) of the representative hydrometeor in each mass bin, while the semi-axis lengths or aspect ratio of the hydrometeor are not predicted. Semi-axis lengths are necessary for calculation of cross sections, coalescence efficiency, and terminal velocity. Another parameter necessary for calculation of terminal velocity with a general equation by Bohm (1992) is porosity. First, the aspect ratio α of ice particles is parameterized with total mass of the ice particle and mass of an ice crystal in the particle. If $m_{lmt} > m_t$, $\alpha = 10^\Phi$ where

$$\Phi = \frac{\log 10(\phi_{lmt}) - \log 10(\phi_{ic})}{\log 10(m_{lmt}) - \log 10(m_t)} (\log 10(m_t) - \log 10(m_{lmt})) + \log 10(\phi_{lmt}). \quad (4.2)$$

Otherwise, $\alpha = \phi_{lmt}$. For aggregates and rimed aggregates (graupels) ϕ_{lmt} and m_{lmt} are set to 0.25 (0.7) and 10^{-4} (10^{-3}) g, respectively. The shape of aggregates is assumed to be a cylinder, while rimed aggregates and graupels are assumed to be a spheroid. From the aspect ratio, predicted circumscribing sphere volume and diagnosed type, the semi-axis lengths are calculated. The porosity of ice particles are parameterized in similar way as the aspect ratio, by replacing α , ϕ_{lmt} , and ϕ_{ic} with q_{rat} , q_{lmt} , and q_{ic} where q_{lmt} is given as

$$q_{lmt} = \frac{m_t}{\rho_i V_{cs}}. \quad (4.3)$$

A discontinuity in terminal velocity can lead to the discontinuity in the size distribution through the collection kernel. The above formulations allow the terminal velocity to have continuous transition from ice crystals over the typical mass range for aggregates $m < m_{lim}$. However, if aggregates are forming over $m > m_{lim}$, the transition will be discontinuous.

4.2.3 Aggregation process

4.2.3.1 EFFICIENCY

Collision, coalescence, and breakup between ice particles are poorly understood in the literature. There is no theoretical estimation of collision efficiency between ice crystals because flow fields around crystals were not available till recent years and collision criteria are difficult to define (PK97). There are a few laboratory experiments that address the collection efficiency. For instance, Keith and Saunders (1989) estimated the efficiency by investigating collisions between planar crystals and a fixed cylindrical target. Also, the efficiency has been estimated by using theoretical collection models and aircraft observations together. The estimated efficiency ranges typically from 0.1 to 1 with 0.3 being typical for deep stratiform cloud layers (e.g., Mitchell, 1988; Field and Heymsfield, 2003). Passarelli (1978) estimated 1.4 using his analytical collection model with observed PSDs. By using a stochastic collection equation Field et al. (2006) estimated aggregation efficiency of 0.09 for cirrus cloud and sub-300 μm particles were speculated to have efficiency greater than unity for geometric sweep-out kernel. This study also assumes that the collision efficiency is 1 for aggregation process. The coalescence efficiency for ice particles are assumed to consists of two mechanisms; ‘interlocking mechanism’ and ‘sticking mechanism’ (PK97).

This study defines the coalescence efficiency as sum of the two efficiencies:

$$E_{coal} = \min(1.0, E_{int} + E_{stick}) \quad (4.4)$$

Three models for the interlocking efficiency are studied. Similarly to CL94, the first model (P) is based on bulk sphere density and circumscribing sphere volume of the colliding two particles,

$$E_{int} = \max(E_{int}^{min}, 1.0 - \frac{v_{cs}^i \rho_s^i / \rho_c^{i,h} + v_{cs}^j \rho_s^j / \rho_c^{j,h}}{v_{cs}^i + v_{cs}^j}) \quad (4.5)$$

where ρ_s^i is the bulk sphere density calculated by $\rho_s^i = m_i^i / v_{cs}^i$, $\rho_c^{i,h}$ is the reference crystal density of a hexagonal crystal assuming the same aspect ratio as the ice particle,

$$\rho_c^{i,h} = c_\rho \rho_i \alpha / (1 + \alpha^2)^{1.5} \quad (c_\rho = 1.24049). \quad \text{It is assumed that } \alpha = \phi \text{ for pristine and rimed}$$

hexagonal monocrystals whereas $\alpha = 0.25$ for pristine and rimed polycrystals. E_{int}^{min} is the minimum interlocking efficiency and assumed to be 0.1. Note that this model utilizes the density of each ice particle, which means that the efficiency increases with growth of aggregates because aggregates tend to have less density with growth. The second model (C) is similar to the first one except for use of bulk crystal density within an ice particle:

$$E_{int} = \max(E_{int}^{min}, 1.0 - \frac{v_{cs}^i \rho_c^i / \rho_c^{i,h} + v_{cs}^j \rho_c^j / \rho_c^{j,h}}{v_{cs}^i + v_{cs}^j}) \quad (4.6)$$

where $\rho_c^{i,h}$ is calculated with the above assumed aspect ratio of ice crystals for all types of ice particles. ρ_c^i is calculated by the mass of an ice crystal within the ice particle, m_i^i , divided by the volume of sphere circumscribing the crystal, v_i^i . v_i^i is calculated with a and c-axis lengths for monocrystals and with empirical maximum dimension for polycrystals (see section 3.2.3).

This formulation means that the efficiency is mainly function of the composing crystal habit. Then, the third model (D) formulates the efficiency based on the assumption that dendritic feature enhances the efficiency:

$$E_{\text{int}} = \max(E_{\text{int}}^{\text{min}}, \psi_i / 0.9, \psi_j / 0.9) \quad (4.7)$$

where $E_{\text{int}}^{\text{min}}$ is set to 0.7 if it is a columnar polycrystal (bullet rosettes), otherwise set to 0.1.

The axis ratio is divided by 0.9 because the value is assumed to be the maximum axis ratio of dendritic crystals. Since lengths of hexagonal monocrystals within polycrystals are predicted, dendritic growths on polycrystals are also reflected by the model. One example of such polycrystals is planar polycrystals with dendritic arms (spatial dendrites).

The sticking efficiency is modeled based on Hallgren and Hosler (1960)'s data,

$$E_{\text{stick}} = 10^{0.05(\max(T_i, T_j) - 273.15) - 0.5457} \quad (4.8)$$

When the ice particles are embedded in liquid water, the coalescence efficiency is set to 0.

This study assumes that graupels have negligible growth by aggregation. Once ice particles in a bin are diagnosed to be graupels, the coalescence efficiency is assumed to be 0.

4.2.3.2 GROWTH OF PPVs

CL94 parameterized the growth of major and minor semi-axis lengths by considering a relationship between growth of mass and maximum dimension obtained from known mass-dimension relationships of aggregates, a relationship of growth of maximum dimension and the separation ratio S for similar two crystals, and arbitrary crossing angle between two crystals.

This study predicts the growth of the circumscribing sphere volume or maximum dimension of

ice particles. The growth is parameterized based on a simple geometrical consideration of colliding two particles as illustrated in Figure 4.1. The variables in the figure have the following relationships:

$$D_f = \frac{D_1^L + D_2^L}{2}(1.0 - S) \quad (4.9)$$

$$L_1^2 = D_1^{S^2} + (D_1^L - D_f)^2 \quad (4.10)$$

$$L_2^2 = D_2^{S^2} + D_2^{L^2} \quad (4.11)$$

$$\theta = a \cos((D_1^L - D_f) / L_1) - a \cos(D_2^L / L_2) + \pi - \theta_0 \quad (4.12)$$

$$L_3 = \sqrt{L_1^2 + L_2^2 - 2L_1L_2 \cos \theta} \quad (4.13)$$

There are two parameters in the formulation: the separation ratio S and angle between two particles θ_0 . Kajikawa and Heymsfield (1989) showed that the separation ratio S between two crystals has the highest frequency at about 0.6 in the observed cirrus clouds. Thus, S is set to 0.6 in this study. The angle between two particle θ_0 is parameterized by using the similar approach to the interlocking efficiency:

$$\theta_0 = \theta_{0\max} \left(1.0 - \frac{V_{cs}^i \rho_s^i / \rho_c^{i,h} + V_{cs}^j \rho_s^j / \rho_c^{j,h}}{V_{cs}^i + V_{cs}^j} \right) \quad (4.14)$$

where the largest angle between two particles $\theta_{0\max}$ is assumed to be 45° as done in CL94.

Kajikawa et al. (2002) and Maruyama and Fujiyoshi (2005) suggest that aggregates grow in

two dimensional way for early stage and three dimensional way for later stage. The parameterization of θ_0 leads to larger θ_0 and therefore smaller L_3 for particles of smaller density when other variables kept constant. To some extent, it implies the transition from two to three dimensional growth. Finally, the growth of the circumscribing sphere volume of a group k in mass bin i is given by

$$v_{cs}^{k,i} = v_{cs}^k + \sum_j^{N_G^k} \left(\frac{\pi}{6} L_3^3 - v_{cs}^i \right) N_p^{k,j} \quad (4.15)$$

where $N_p^{k,j}$ is the number of particles in mass bin j collected by a group k of mass bin i , and N_G^k is the total number of mass bin collected by a group k in mass bin i . In SHIPS the PPVs for ice crystals are averaged during the aggregation process, so that the PPVs indicate the average habit of the components of aggregates within mass bin. The a-axis length of the representative hydrometeor of a group k in the shifted bin is calculated as

$$a^{k,i} = \left\{ \left(a^k{}^3 + \sum_j^{N_G^k} a^j{}^3 N_p^{k,j} \right) / \left(1.0 + \sum_j^{N_G^k} N_p^{k,j} \right) \right\}^{1/3} \quad (4.16)$$

Similarly, other length variables such as c^k , d^k , a_g^k , c_g^k in the shifted bin are averaged with cubic power weighted by number of particles, and number of extra crystalline n_{exice}^k weighted by number of collected particles. During aggregation, except for ice crystal mass component all the mass content components of a shifted bin of a group are increased by the mass components collected by the group. The ice crystal mass component is calculated by

averaging the ice crystal mass components of collected and collecting ice particles so as to match with the length variable components in the shifted bin.

4.2.4 Riming process

4.2.4.1 EFFICIENCY

The coalescence efficiency of ice particles colliding with liquid hydrometeors is assumed to be 1. SHIPS contains habit information of ice particles, so it should be reflected as much as possible into the collision efficiency. It is known that planar and columnar crystals have different thresholds of size for riming. Wang and Ji (2000) calculated the collision efficiency of ice crystals catching liquid hydrometeors for plates, broad-branched crystals, and columns. Lew and Pruppacher (1983) and Lew et al. (1985) calculated the efficiency of large liquid hydrometeors catching columnar and planar crystals, respectively. By using those data, lookup tables of the efficiency for plates, broad-branched crystals, and columns were built as a function of Reynolds numbers of collecting and collected hydrometeors. There is no data available in the region where large liquid hydrometeors catch ice crystals in $N_{Reliq} < 100$. Therefore, the efficiency was interpolated in the region with a line of riming cutoff where liquid and solid hydrometeors have similar terminal velocity. The lookup tables are used for pristine crystals, and rimed crystals. However, no efficiency for polycrystals is available, so those for plates (broad-branched crystals) are used for planar and irregular polycrystals (columnar polycrystals). Collision efficiency between graupels of density at 0.1, 0.4, and 0.8 g cm⁻³ and liquid hydrometeors were calculated by Khain et al (2001) using the superposition method. In the same way, from them lookup tables for the densities were constructed as a

function of the Reynolds number of ice particle and ratio of maximum dimensions. They are used for aggregates, rimed aggregates, and graupels.

4.2.4.2 GROWTH OF PPVs

The growth of circumscribing sphere volume is modeled by following the treatment of CL94. All droplets are assumed to accrete on the short semi-axis length of an ice particle with the density calculated with Heymsfield and Pflaum (1985)'s formula. If $T < 0^{\circ}\text{C}$, the mass content collected by ice particles in the group is added to the rime mass content component of the shifted bin of the group. For $T \geq 0^{\circ}\text{C}$, it is added to the melt mass content component. The ice crystal mass component of the shifted bin stays the same as the one of the original bin of the group. Furthermore, the aerosol total and soluble mass content components in collected liquid hydrometeors are added to those of the shifted bin.

4.2.5 Hydrodynamic breakup

As shown later, the aggregation process alone modeled in this study can produce unrealistically large ice particles in less than one hour. Hobbs and Farber (1972) reported that in their aircraft observations the arms of stellar crystals, the tips of needles and sheaths, dendrites and capped columns were particularly susceptible to break up, and especially collisions of comparatively large water drops or graupels were quantitatively shown to be capable to break ice crystals due to its large kinetic energy. Griggs and Choulaton (1986) studied fragmentation of ice crystals and rime against fast air flow and collision breakup with glass beads in laboratory, leading qualitatively to the same conclusions as Hobbs and Farber

(1972). Nevertheless, very little else is known about the fragmentation of aggregates by collision or turbulence.

This study assumes that the large ice particles diagnosed as aggregates, rimed aggregates, and graupels with bulk sphere density less than 0.8 g cm^{-3} break up spontaneously due to interaction with the flow. This study does not include breakup process caused by collisions. The probability of break up is modeled based on Komabayashi et al (1964)'s exponential function for a drop. The coefficient within the exponential function was modified, so that ice particles with maximum dimension of 2 cm break up with a probability of one. It is assumed that the ice particles produced by fragmentation follow the power-law mass-density relationship $\rho = a_1 D^b$. The constant b for hexagonal monocrystals was obtained from Kajikawa (1982), and planar and irregular (columnar) polycrystals were set to side planes (CPI rosettes) in Table 1 of Heymsfield et al. (2002). Another constant a_1 was determined by substituting b , the bulk sphere density and maximum dimension of the parent ice particle. Sizes of the fragments are assumed to range from the size of the average ice crystal within the parent ice particle to the parent ice particle. The size distribution of fragmentation ($\text{cm}^{-3} \text{ cm}^{-1}$) is assumed to be a uniform distribution, which means that the fragmentation produces ice particles of different sizes between the size limits with equal possibility.

4.3 Box model simulations

Box model simulations are conducted in order to validate the growth of ice particles by collection processes. In the setup, all particles stay in a box, so that there is no effect of sedimentation on PSD and only microphysical process changes PSD. The collection processes

depend on habits directly through the cross-section area, terminal velocity, and collision and coalescence efficiencies. However, there are very few in-situ observations or theoretical calculations available for evolution of PSD by collection processes with a specific ice crystal habit. Therefore, this study attempts to validate the collection process of SHIPS against empirical relationships between property of ice particles and against a theoretical study, and sensitivity of habits to the processes is discussed.

4.3.1 Aggregation process

MF05 simulated PSDs, and property of ice particles including fractal feature of the aggregate shape by implementing a pure stochastic model of aggregation with a Monte Carlo simulation. This study uses MF05's results to validate the evolution of PSD simulated by SHIPS. Following MF05, the mass distributions of solid hydrometeors in all the simulations are initialized with exponential distribution in terms of mass:

$$n(m) = \frac{N}{\bar{m}} \exp\left(-\frac{m}{\bar{m}}\right), \quad (4.17)$$

where $N = M / \bar{m}$ and $\bar{m} = (4\pi/3)\rho_s \bar{r}^3$, the total mass content M is set to $10^{-7} \text{ g cm}^{-3}$, and the bulk sphere density ρ_s to 0.3 g cm^{-3} . The initial distributions are set up with six habits (plates, dendrites, columns, columnar polycrystals, planar polycrystals, and irregular polycrystals) with characteristic axis ratios and aspect ratios as shown in Table 4.1. The mass bins with the representative hydrometeor of a or c axis lengths less than $1 \text{ }\mu\text{m}$ are removed. For the initialization of dendrites, small crystals are assumed to be hexagonal plates, and dendrites are

formed in a mass bin when the hexagonal part of the crystal is larger than $10 \mu\text{m}$ given the axis ratios and mass. In addition to the six habits, a sphere shaped particle of $\rho_s = 0.3 \text{ g cm}^{-3}$ is simulated as reference. For the box simulations total of 80 mass bins is defined with bin boundary ratio $k_{bb}^b = \sqrt{2}$ starting from the minimum mass of $4.19 \times 10^{-9} \text{ g}$. The pressure and ambient temperature were set to 1000 hPa and -5°C .

Firstly, simulations only with aggregation process are discussed. Different habits of ice crystals can have different terminal velocity and cross section area due to the different geometrical representation. By setting unit collection efficiency ($E_{collection} = 1$) in Equation (4.1), differences in evolution of PSDs due to the difference in sweeping volume, namely difference in terminal velocity and cross sections are discussed. The simulations are started from the initial distribution with mean radius \bar{r} of 10^{-2} cm . Mass distributions at 60 minutes are shown in (a) of Figure 4.2. Dendrites show the fastest evolution, followed by columns. The first mode exists at 0.2 mm and/or 2 mm. The collection rate (collection kernel), cross section and velocity difference for an ice particle collecting another particle with the half of its mass at 60-minute simulation are shown in Figure 4.3. It is clear that dendrites have the largest collection rate due to the largest cross section. It is interesting to note that the increase of cross section with mass is larger than the increase of velocity difference by factor of 10. Moreover, the velocity difference gets smaller with mass because the increase in terminal velocity declines with mass. Difference in habit may lead to difference in cross section and velocity difference by factor of 10 at a given mass. The difference in the resulting collection rate may vary by factor of 10 to 100, depending on mass. It is interesting to note that columnar

crystals show the smallest velocity difference in $m < 1.5 \times 10^{-3}$ mg, therefore the collection rate becomes the smallest. Compared with aggregates of sphere, the other habits compensate smaller velocity difference by having larger cross sections. This is the consequence of allowing density of ice particles to decrease with mass for the non-spherical habits. MF05 shows that the maximum difference of terminal velocities do not vary too much with time for their aggregation models, and emphasizes the importance of collision cross section in estimating snowflake growth rates. Therefore, the stochastic collection model of SHIPS is qualitatively similar to the pure stochastic models of MF05. It is important to note that vapor depositional growth is the process that produces crystals $m < 1 \times 10^{-3}$ mg and it also depends on the habit through capacitance.

The dip in velocity difference of columnar crystals at $m = 2 \times 10^{-2}$ mg corresponds to the switch of aspect ratio from a prolate spheroid to an oblate spheroid where the calculation of terminal velocity is changed. The hump in cross section area of columnar crystals is also associated with the shift. This can be unrealistic. The three peaks in velocity difference for all habits are reflected onto collection kernel due to the smooth transition of cross section. Those peaks then corresponded to each mode in the size distribution of melt particles (or mass distribution) with combination of given concentration of collecting and collected particles. This is due to the monotonously decreasing initial mass distribution, and in case of initial mass distributions with multiple modes the peaks of terminal velocity may or may not correspond to peaks of mass distribution in such a simple way. Evolution of size distribution for plates is shown in Figure 4.4 as an example. The initial mode seen in size distribution keeps itself with time. This is because the first peak in the collection kernel associated with velocity difference

happened to be very close to the initial mode (Figure 4.3). The second larger mode appears around 30 minutes, and eventually the concentration becomes larger than the smaller mode. This peak corresponds to the second peak in the collection kernel. In this particular case, it can be seen that exponential distribution may fit larger part of the distribution, which is true for most of observed PSDs.

The size distribution of melt ice particles for the interlocking efficiency model P, C, and D are shown in (b), (c), and (d) of Figure 4.2. The main difference in the size distributions from that of unit efficiency is that aggregates, except for those of dendrites, have more surviving small ice crystals ($D < 10^{-1}$ mm). This is due to smaller modeled efficiencies as shown in (d) of Figure 4.5, Figure 4.6, and Figure 4.7. Note that these ice particles were diagnosed to be aggregates, starting from $10^{-2} < m < 10^{-1}$ mg. As formulated, the model P shows strong dependence on the diagnosis of aggregates such that the coalescence efficiency becomes unit for aggregates for all the habits. On the other hand, model D shows just constant efficiency over the mass. Model C gives constant and variable efficiency, depending on mass-dimension relationship chosen for each habit. The empirical formula used for planar and irregular polycrystals gives less density for larger mass, while the formulas for the others give constant bulk crystal densities. Although the efficiency model is different among the four cases, still the same multiple modes appear at similar masses in the PSDs (Figure 4.2). Note that basically terminal velocity difference and cross section are not affected by the difference in efficiency model, which imply that *predicted property of particles given mass stay the same in case of aggregation process only*. The efficiency model changes habit dependency of growth rate as can be seen in Figure 4.2. Use of bulk crystal density (model C) resulted in the 2nd

fastest growth of planar polycrystals whereas columnar crystals showed the 2nd fastest growth in case of using bulk sphere density (model P). Model D showed the smallest growth of ice crystals due to lack of dendritic arms except for dendrites. As shown later with simulations in an Eulerian dynamic model, predicted polycrystals can have dendritic arms growing. But the mass-dimension relationships used for polycrystals do not reflect any growth of dendritic arm. Therefore, model P and C cannot reflect such growth.

The maximum dimension, terminal velocity, and bulk sphere density predicted with the efficiency model P at 60 minutes are shown in Figure 4.8, Figure 4.9, and Figure 4.10, respectively. The simulated maximum dimensions show moderate agreements with the empirical formula. Especially, dendrites and plates capture the change of the slope as the ice particles evolve from pristine crystals to aggregates. Columns show a bump $10^{-2} < m < 10^0$ mg due to the above mentioned change in the diagnosed aspect ratio. The left side of the bump is associated with aggregates with aspect ratio larger than one, while the right side is related to aspect ratio less than one. This can be just an artifact by the diagnosis of aspect ratio. However, it is not possible to verify the behavior since there are only few empirical relationships for aggregates of needles and columns. The simulated terminal velocity is also in moderate agreements with empirical formula. The discontinuity in dendrites is caused by habit change from plates to dendrites and the discontinuity in columns is caused by the aspect ratio change. It is quite surprising to see such good agreements in the maximum dimension-density relationships (Figure 4.10). Especially, the inflection point of density agrees with the change of diagnosed type from pristine crystal to aggregate. Actually, the inflection points for three relationships turned out to depend on the initial distribution. Starting with larger mean mass

moved the points to larger mass. It is interesting to note that dimension-density relationships of columns shift from one of planar to one of columnar polycrystals with the increase in dimension.

Thirdly, aggregation simulations are started from the initial distribution with mean radius \bar{r} of 5×10^{-2} cm, which is the same as the control experiment in MF05. The mass density distributions at 90 minutes of simulation for the efficiency model P in terms of maximum radius are shown in Figure 4.11. Please note that initial size distributions for those cases are different because each habit has different mass-dimensional relationships, but that initial mass (or melt size) distributions are identical. All aggregates in this study show faster evolution in maximum dimension, compared to the distribution with the ice sphere and those simulated with the Monte Carlo method of MF05 (see their Fig. 3). Modes of the aggregates of dendrites, planar and irregular polycrystals reached unrealistically large maximum radius in 90 minutes. Also, the distributions simulated for all the six habits showed two modes in mass density distribution at certain times, while MF05 shows one mode. MF05 uses ice spheres as components of aggregates. Therefore, direct comparison for each habit is not available. The simulation with dendrites and the initial distribution with mean radius \bar{r} of 10^{-2} cm led to larger melt diameter of mean mass than the one starting from the initial distribution of mean radius \bar{r} of 5×10^{-2} cm at 60 minutes (Figure 4.12). It is mainly due to the higher concentration of collected ice particles in the former case and not due to collection kernels. Efficiency model C and D predict slower evolution of the mean mass of PSD except for dendrites than efficiency model P as shown in Figure 4.13. (a) of Figure 4.13 indicates that use of non-spherical habit and density prediction can lead to faster growth of aggregates than

constant density sphere aggregates. Also, comparison of the (a) and Fig. 4 of MF05 shows that all but columnar polycrystals grow faster than MF05's Lagrangian aggregation models. MF05 conducted sensitivity tests where density of ice sphere components ($\rho_s = 0.1, 0.5 \text{ g cm}^{-3}$) and standard deviation were changed. They showed that the use of lower density sphere and wider dispersion led to faster growth as expected, reaching 1 cm of the melt diameter of mean mass at 120 minutes (Fig. 13 of MF05). Some habits in P, C, and D show quantitatively similar melt diameter growth to the MF05's aggregation models. This indicates that efficiency model is as important as mass-dimensional relation of each habit in this model in terms of prediction of mean mass of spectra. Mass-terminal velocity experience discontinuity at $1 \times 10^{-1} \text{ mg}$ because the ice particles with mass smaller than the mass were not diagnosed as aggregates. This suggests that the thresholds for the parameterization of aspect ratio, and porosity should be improved.

As shown in Figure 4.11, Figure 4.12 and Figure 4.13, aggregates simulated in SHIPS can become unrealistically large. Therefore, hydrodynamic (spontaneous) breakup process is modeled as described in the subsection 0. As an example, aggregation and breakup processes were simulated with the same initial condition of mean radius 0.05 cm and efficiency model P (Figure 4.14). It indicates that all habits growing aggregates larger than breaking size (2 cm diameter) reached similar equilibrium mass density distribution. Mass-dimension, mass-terminal velocity, and diameter-density relationships are very similar to those without breakup process. Size distributions for dendrites without and with breakup scheme are compared in Figure 4.15. The first mode appears due to the discontinuity in mass-terminal velocity relationship. The balance between aggregation and breakup processes created the main mode

around 7.5mm. The breakup process produced aggregates that are larger than the component ice crystal (about 3 mm diameter) and smaller than the breaking aggregate. The formulated breakup scheme is valid in that it gives equilibrium distribution, and the probability of breakup increases with size. In aircraft observations of cirrus and deep stratiform cloud layers where aggregation process is active, PSDs appear to have two modes (e.g., McFarquhar and Heymsfield, 1996; Field and Heymsfield, 2003). Ability of SHIPS to produce these modes has to be tested with vapor deposition and ice nucleation processes turned on as well as sensitivity of the equilibrium distribution to fragment distribution. In reality the collision breakup is probably occurring before ice particles reach the size where their structure is hydrodynamically unstable. It is the case for liquid hydrometeors. The hydrodynamic breakup for liquid hydrometeors is shown to be negligible compared to collision breakup and the equilibrium distribution between hydrodynamic breakup and coalescence appear to be too flat (cf. PK97). But no information is available on the fragment distribution and probability of occurrence for ice particles. The distributions of aggregate fragments as well as fragments of ice crystals created by collisions and the hydrodynamic effect have to be studied in the laboratory.

4.3.2 Riming process

The liquid hydrometeors are initialized with Marshall-Palmer size distribution of rain rate 1 mm hr^{-1} (cf. PK97). The initial distribution with mean radius of 0.01 cm is used for ice particles, as defined in the previous section. The pressure and ambient temperature were set to 1000 hPa and -15°C to simulate dry growth of rimed particles. For the sake of simplicity, no

microphysical processes for liquid hydrometeors are simulated, while aggregation, hydrodynamic breakup, and riming processes are simulated.

Simulated mass distributions for the six habits at 60 minutes are shown in Figure 4.16. The interlocking efficiency mode P was used. All the habits but columns show similar, rather complicated distributions with multiple modes. A clear difference can be seen in the concentration of mass range $m < 1 \times 10^{-3}$ mg, which is probably associated with difference in the collection rate in that range (see (a) of Figure 4.5). In case of dendrites the distribution is in equilibrium and each mode is related to the diagnosed type as shown in (c) of Figure 4.17, namely graupel, rimed aggregate, and graupel from smaller mode. The rimed aggregates between $1.9 \times 10^{-1} < m < 7.8 \times 10^{-1}$ mg break up and transfer their rimed mass and aggregate mass components to $1.1 \times 10^{-3} < m < 1.9 \times 10^{-1}$ mg. It caused the flatness of rimed mass fraction and formation of graupels in the mode of the smallest mass. This is an example where the hydrodynamic breakup process in SHIPS can create aggregates, rimed aggregates, and graupels, depending on the mass components of a parent ice particle and ice particles in the smaller mass range. This is one of drawbacks that stem from diagnosing an average single habit and type for a single mass bin based on the mass components all together. Simulated property of ice particles at 60 minutes is shown in Figure 4.18. The simulated rimed aggregates show the mass-dimensional relationship similar to the aggregates of P1e by K89, and then the simulated graupels indicates similarity to R4b and R4c by HK87. Terminal velocity of the rimed aggregates also shows good agreements with the empirical formula of the aggregates of P1e by K89, R1d and R4b by HK87. The simulated graupels follows the empirical formula of hail by M96, which is suggested by the high density shown in (c) of the

figure. The evolution of PSDs by aggregation and riming processes remains challenging in observations, modeling and its validation. Some of the complexities stem from multiple secondary nucleation processes, phase change over the surface of ice particles, and dramatic change of density and shape due to collision.

4.3.3 Effect of implicit mass sorting assumption

It is concluded that aggregation and riming processes of SHIPS can predict at least properties of ice particles that are quantitatively similar to observed empirical relationships. The predicted PSDs for different ice crystal habits qualitatively agree with MF05's results. One of major differences from MF05's model is that SHIPS diagnoses each mass bin as a group of single habit and type of ice particles (implicit mass sorting assumption). This framework allows mass-dimension and mass-terminal velocity relationships to change over mass. Passarelli and Srivastava (1979) included terminal velocity and diameter of particles as independent variables for number concentration in addition to mass, and showed that the including the spectrum of terminal velocity significantly enhance aggregation process. Sasyo and Matsuo (1985) also included observed variation of fall velocity into a new kernel and showed that it reduced the time required to reach specified snowfall intensity, but did not increase snowfall intensity. MF05 explicitly simulated the variation of those variables with their Monte Carlo method along with PSD. Their aggregation simulation did not show the secondary mode in the predicted mass density, but SHIPS did. It may be an artifact produced by assigning mean terminal velocity and diameter to a mass bin. Introduction of another independent variable to SHIPS can solve the problem, but it would consume more

computational power. Further validation of the evolution of PSD predicted by SHIPS for each ice crystal habit, has to wait for a Lagrangian stochastic model with realistic ice crystal shape or laboratory experiments. The hybrid-bin method used in this study does not consider collection process within a bin. The consideration could be as important as the variation of property given mass when small number of mass bins is used to reduce computational cost.

4.4 Summary and conclusions

SHIPS solves the stochastic collection equation with prediction of habit and types of ice particles. It was made possible by integrating Particle Property Variables (PPVs) based on simple parameterization of growth of maximum dimension, and diagnosis of aspect ratio and porosity of ice particles. Validation of the scheme was conducted in box model simulations. The major conclusions are the following:

1. Simulations with unit efficiency showed that collection kernel was largely a function of cross section area, and having different habits can lead to difference in collection rate by factor of 10 to 100 at a given mass. Dendrites show the fastest collection rate due to the largest cross section among habits. The stochastic collection model of SHIPS is qualitatively similar to the pure stochastic models of MF05 in that the cross section is more important to determine the growth rate of snowflakes than terminal velocity difference. This is the consequence of predicting density of aggregates to decrease with mass.

2. Three interlocking efficiency models were formulated based on bulk crystal density, bulk sphere density, and dendritic arm lengths. They showed significant differences in evolution of PSD due to nonlinear feedback, even though it ranges between 0 and 1.
3. Mass-dimension, mass-terminal velocity, and diameter-density relationships are not sensitive to aggregation efficiency if only aggregation processes are considered, but sensitive to the initial PSD.
4. Aggregation and riming processes of SHIPS can reproduce mass-dimension, mass-terminal velocity and diameter-density relationships that moderately agree with empirically-derived relationships.
5. The non-spherical habits predicted by SHIPS show faster growth by aggregation than constant-density sphere aggregates, and also than Monte Carlo model with ice sphere components of MF05 if the same initial mass distribution is used for different habits. The aggregation process in SHIPS shows sensitivity to efficiency models as well as mass-dimensional relationship of each habit.
6. The aggregation simulation with breakup process led to an equilibrium size distribution that is similar in terms of mass density among the habits. The resulting relationships between particle properties are similar to those without breakup process.

This research raised questions regarding to fundamental understanding of aggregation process and possibility of simulating habit-dependent aggregation process with Eulerian stochastic approach. The parameterization of growth of maximum dimension, and diagnosis of aspect ratio and porosity should be validated by direct observations of aggregation and riming processes. Currently, SHIPS assume a single habit and type for a given mass and for an

entire mass bin. The effect of the variation of property of ice particles in a bin should be investigated in SHIPS as well as the self-collection of particles within a mass bin. Further validation of the evolution of PSD predicted by SHIPS for each ice crystal habit, has to wait for a Lagrangian stochastic model with realistic ice crystal shape or laboratory experiments. The distributions of aggregate fragments as well as fragments of ice crystals created by collisions and the hydrodynamic effect also have to be studied more in laboratory settings.

If the aggregation process of SHIPS is proved adequately, it can be used to understand impacts of assumed fragmentation distribution by breakup on the evolution of PSDs in a box model setup. Also, relationships between ice nuclei concentration, precipitation rate and habit through vapor deposition and aggregation processes can be studied efficiently.

The evolution of single graupel, and hail stone has been studied in the past. The evolution of PSDs by aggregation and riming processes is not studied enough in literature. More investigations from theoretical and observational aspects are necessary.

Appendix D Description of microphysical process models

D.1 Surface temperature diagnosis

This study predicts melt water mass on ice particles. Thus, adequate calculation of surface temperature is necessary, depending on the environment, microphysical processes and property of ice particles. When $T < 0^\circ\text{C}$, heat balance is assumed (cf., p.681 of PK97):

$$A \left(\frac{e_\infty}{T_\infty} - \frac{e_s(T_s)}{T_s} \right) + \{L_f + c_w(T_\infty - T_s)\} \frac{dm}{dt} \Big|_{rim} - L_f \frac{dm}{dt} \Big|_{melting} = B(T_s - T_\infty), \quad (\text{D.1})$$

where $A = L_x \frac{4\pi C D_v M_w}{R}$ and $B = 4\pi C k_a f_h$. The surface temperature T_s can be obtained by

solving the above implicit equation. The first term is vapor deposition tendency, the second is the heat associated with riming process, and the third is melting tendency. Right hand side is the heat diffusion term. In the calculation, the melting tendency is assumed to be 0, first.

Substituting back the calculated temperature to Equation (D.1) gives melting tendency if the surface temperature is warmer than the freezing temperature. Depending on the surface

condition of ice particle, that is dry or wet, the proper latent heat and saturation vapor pressure have to be used in the vapor deposition term. The criterion used in this study is the ratio of

melt water to total mass of ice particle, m_w / m . Assumed threshold is $m_w / m = 0.05$, which

has the thickness corresponding to 1.6% of total radius of ice sphere with liquid coating. The riming tendency is calculated by collision-coalescence scheme which assumes that all liquid

hydrometeors colliding are frozen right after collision in $T < 0^\circ\text{C}$. After all, the above

formulation allows the surface temperature to rise according to riming process. For instance, if

riming rate is high enough to increase surface temperature greater than ambient temperature, the saturation pressure in terms of ambient temperature can be sub-saturated in terms of the surface temperature.

When $T \geq 0^\circ\text{C}$, the surface temperature is assumed to be freezing temperature. If a graupel particle has $D > 5$ mm, the internal circulation in the melt water can be laminar (cf. p.694 of PK97). Therefore, for particles with $m_w / m \geq 0.5$, the surface temperature is obtained based on the steady state where the heat transfer through the water layer to the ice core is balanced with the transfer from air to the surface of the melting particle and vapor deposition process at the surface. Equation (16-78) of PK97 is solved by assuming spherical ice particle.

D.2 Melting and shedding process

As described in the previous subsection, when the ambient temperature is below freezing and surface of the ice particle is dry, Equation (D.1) is used to calculate the melting tendency. In case of above-freezing ambient temperature, the latent heat of evaporation and saturation pressure over water are used in Equation (D.1). In addition, since the riming process assumes that the collided liquid hydrometeors stay as liquid in the above-freezing temperature (add deposited mass to melt mass component directly, and not to rime mass component), the latent heat of freezing in the second term is removed from the equation. When an ice particle has liquid coating in sub-freezing temperature, the liquid surface is assumed in the first term and the latent heat of freezing is kept in the equation.

If the melt tendency is positive, mass is transferred from aggregation, rime and ice crystal mass components to melt mass component. The largest mass component among the three is decreased first, and then second largest one is decreased if the first transfer is not large enough to provide the melt water mass, and so on. In case of freezing (negative melt tendency), the melt mass component is transferred to riming mass component. The shedding process was formulated as described in Chapter 2. This study assumes that pristine and rimed crystals do not change length and concentration variable components due to melting. For aggregates, rimed aggregates, and graupels, melting may change the maximum dimension. First, volume of dry core of the ice particle v_{core} is calculated according to the type (aggregates are cylinder; rimed aggregates, and graupels are spheroid) by using mass of dry core ($m_{core} = m - m_W$), diagnosed aspect ratio and bulk sphere density of the ice particle. Then, the empty volume in the ice particle is calculated as $v_{space} = \max(0, v_{core} - m_{core} / \rho_i)$. If the empty volume is more than volume of melt water, then no shedding occurs and no change is made on the length, volume, and concentration variable components. Otherwise, shedding may occur, depending on mass of melt water on the particle as formulated in Chapter 2.

D.3 Secondary nucleation process

The ice splinter mechanism (Hallett and Mossop, 1974) is implemented in SHIPS. The concentration tendency nucleated by riming process in b th mass bin ($b = 1, \dots, N_{BIN}$) is modeled by following the treatment of Cotton et al. (1986):

$$\frac{\partial N^1}{\partial t} = 3.5 \times 10^5 \left. \frac{dm}{dt} \right|_{rim}^b f_1(T_s) N^b, \quad (\text{D.2})$$

$$f_1(T_s) = \begin{cases} 0, & T_s > 270.16 \\ \frac{T_s - 268.16}{2}, & 270.16 \geq T_s > 268.16 \\ \frac{T_s - 268.16}{3}, & 268.16 \geq T_s > 265.16 \\ 0, & 265.16 \geq T_s \end{cases}, \quad (\text{D.3})$$

The nucleated ice crystals are assumed to be a columnar crystal with $a = 1 \mu\text{m}$, and $c = 3 \mu\text{m}$.

The nucleated concentration and mass as well as PPVs are transferred to the smallest bin of ice mass spectrum.

References, Chapter 4

- Baum, B.A., A.J. Heymsfield, P. Yang, and S.T. Bedka, 2005: Bulk Scattering Properties for the Remote Sensing of Ice Clouds. Part I: Microphysical Data and Models. *J. Appl. Meteor.*, 44, 1885–1895.
- Bohm, H. P., 1992: A general hydrodynamic theory for mixed-phase microphysics. Part I: Drag and fall speed of hydrometeors. *Atmos. Res.*, 27, 253–274.
- Chen, J.-P. and D. Lamb, 1994: Simulation of cloud microphysical and chemical processes using a multicomponent framework. Part I: description of the microphysical model. *J. Atmos. Sci.*, 51, 2613–2630.
- Cotton, W. R., G. J. Tripoli, R. M. Rauber, and E. A. Mulvihill, 1986: Numerical simulation of the effects of varying ice crystal nucleation rates and aggregation processes on orographic snowfall. *J. Climate Appl. Meteor.*, 25, 1658–1680.
- Field, P. R., and A. J. Heymsfield, 2003: Aggregation and scaling of ice crystal size distribution. *J. Atmos. Sci.*, 60, 544–560.
- , A.J. Heymsfield, and A. Bansemer, 2006: A test of ice self-collection kernels using aircraft data. *J. Atmos. Sci.*, 63, 651–666.
- Griggs, D. J. and T. W. Choullarton, 1986: A laboratory study of secondary ice particle production by the fragmentation of rime and vapor-grown ice crystals. *Quart. J. R. Met. Soc.*, 112, 149–163.
- Hallett, J. and S. C. Mossop, 1974: Production of secondary ice particles during the riming process. *Nature*, 249, 26–28.
- Hallgren, R. E. and C. L. Hosler, 1960: Ice crystal aggregation. *Geophys. Monogr.*, 5, 251–260.
- Heymsfield, A. J., and J. Iaquinta, 2000: Cirrus crystal terminal velocities. *J. Atmos. Sci.*, 57, 916–938.
- , and L.M. Miloshevich, 2003: Parameterizations for the Cross-Sectional Area and Extinction of Cirrus and Stratiform Ice Cloud Particles. *J. Atmos. Sci.*, 60, 936–956.
- , and M. Kajikawa, 1987: An improved approach to calculating terminal velocities of plate-like crystals and graupel. *J. Atmos. Sci.*, 44, 1088–1099.

- , S. Lewis, A. Bansemer, J. Jaquinta, L. M. Miloshevich, M. Kajikawa, C. Twohy, and M. R. Poellot, 2002b: A general approach for deriving the properties of cirrus and stratiform ice cloud particles. *J. Atmos. Sci.*, 59, 3–29.
- , and J. C. Pflaum, 1985: A quantitative assessment of the accuracy of techniques for calculating graupel growth. *J. Atmos. Sci.*, 42, 2264–2274.
- Hobbs, P. V. and R. J. Farber, 1972: Fragmentation of ice particles in clouds. *J. Rech. Atmos.*, 6, 245-258.
- Kajikawa, M., 1982: Observations of the falling motion of early snowflakes. Part I: Relationship between the free-fall pattern and the number and shape of component snow crystals. *J. Meteor. Soc. Japan*, 60, 797-803.
- , and A. J. Heymsfield, 1989: Aggregation of ice crystals in cirrus. *J. Atmos. Sci.*, 46, 3108–3121.
- , E. Narita, K. Ichinoseki, S. Kudo, and R. Sasaki, 2002: Observation of composition factors of snowflakes (in Japanese). *Seppyō*, 64, 69-76.
- Keith, W. D., and C. P. R. Saunders, 1989: The collection efficiency of a cylindrical target for ice crystals. *Atmos. Res.*, 23, 83–95.
- Khain A., M. Pinsky, M. Shapiro, and A. Pokrovsky, 2001: Collision rate of small graupel and water drops. *J. Atmos. Sci.*, 58, 2571–2595.
- Lew, J. K., and H. R. Pruppacher, 1983: A theoretical determination of the capture efficiency of small columnar ice crystals by large cloud drops. *J. Atmos. Sci.*, 40, 139–145.
- , D. E. Kingsmill, and D. C. Montague, 1985: A theoretical study of the collision efficiency of small planar ice crystals colliding with large supercooled water drops. *J. Atmos. Sci.*, 42, 857–862.
- Locatelli, J. D., and P. V. Hobbs, 1974: Fall speeds and masses of solid precipitation particles. *J. Geophys. Res.*, 79, 2185-2197.
- Magono, C., and T. Nakamura, 1965: Aerodynamic studies of falling snowflakes. *J. Meteor. Soc. Japan*, 43, 139-147.
- Maruyama, K. and Y. Fujiyoshi, 2005: Monte Carlo simulation of the formation of snowflakes. *J. Atmos. Sci.*, 62, 1529–1544.
- Mitchell, D.L., 1988: Evolution of Snow-Size Spectra in Cyclonic Storms. Part I: Snow Growth by Vapor Deposition and Aggregation. *J. Atmos. Sci.*, 45, 3431–3451

- , 1996: Use of mass- and area-dimensional power laws for determining precipitation particle terminal velocities. *J. Atmos. Sci.*, 53, 1710–1723.
- , S. K. Chai, Y. Liu, A. J. Heymsfield, and Y. Dong, 1996: Modeling cirrus clouds. Part I: treatment of bimodal size spectra and case study analysis. *J. Atmos. Sci.*, 53, 2952–2966.
- , R. Zhang, and R. L. Pitter, 1990: Mass-dimensional relationships for ice particles and the influence of riming on snowfall rates. *J. Appl. Meteor.*, 29, 153–163.
- McFarquhar, G. M., and A. J. Heymsfield, 1996: Microphysical characteristics of three anvils sampled during the Central Equatorial Pacific Experiment (CEPEX). *J. Atmos. Sci.*, 53, 2401–2423.
- Passarelli, R. E., Jr., and R. C. Srivastava, 1979: A new aspect of snowflake aggregation theory. *J. Atmos. Sci.*, 36, 484–493.
- Pruppacher, H. R. and J. D. Klett, 1997: *Microphysics of Clouds and Precipitation*. Kluwer Academic, 914 pp.
- Sasyo, Y., and T. Matsuno, 1985: Effects of the variations of falling velocities of snowflakes on their aggregation. *J. Meteor. Soc. Japan*, 63, 249–261.
- Stith, J.L., J.E. Dye, A. Bansemer, A.J. Heymsfield, C.A. Grainger, W.A. Petersen, and R. Cifelli, 2002: Microphysical observations of tropical clouds. *J. Appl. Meteor.*, 41, 97–117.
- Wang, P. K., W. Ji, 2000: Collision efficiencies of ice crystals at low–intermediate reynolds numbers colliding with supercooled cloud droplets: a numerical study. *J. Atmos. Sci.*, 55, 1001–1009.

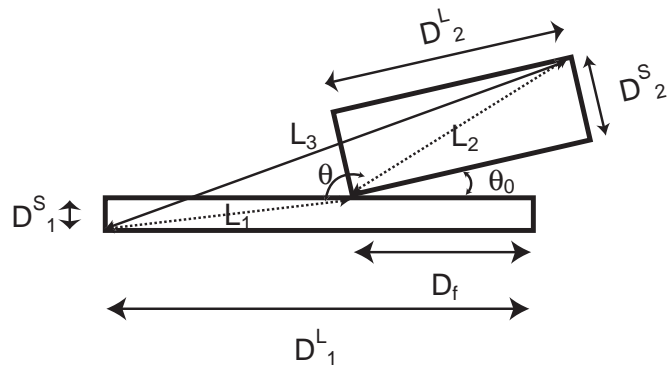


Figure 4.1 growth model of maximum dimension for colliding two plates.

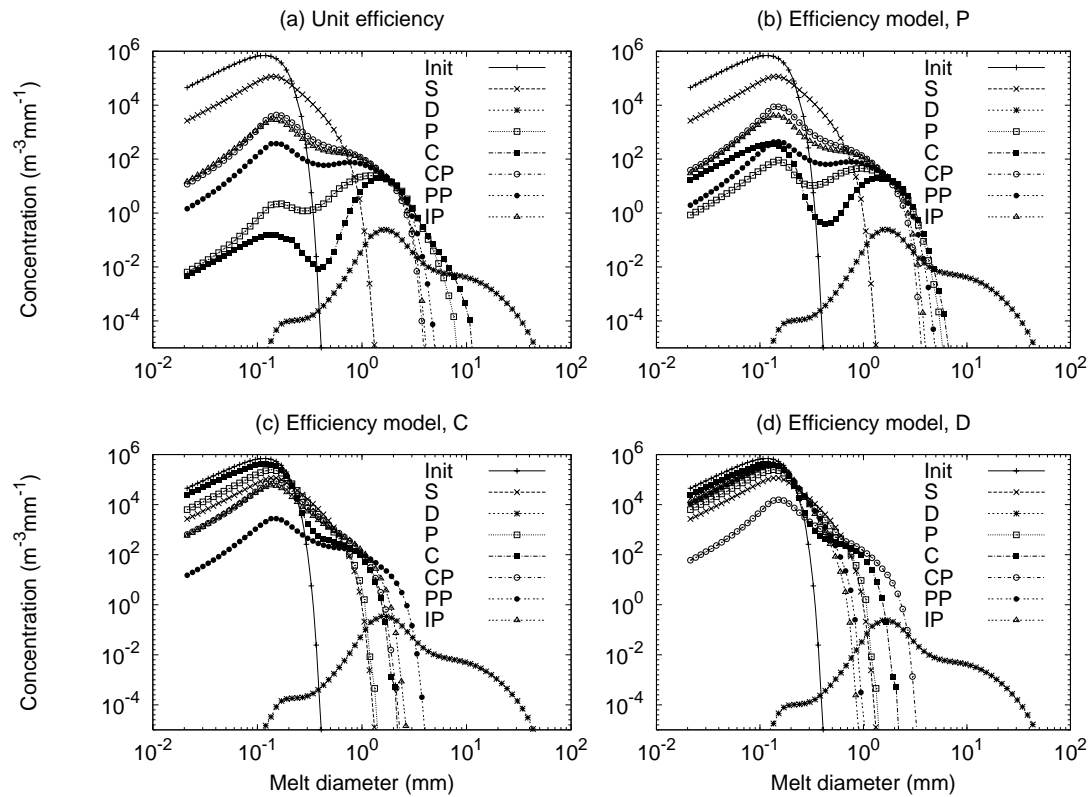


Figure 4.2 Comparison of mass distributions at 60-minute simulation for six different ice crystal habits, namely sphere (S), dendrites (D), plates (P), columns (C), columnar polycrystals (CP), planar polycrystals (PP), and irregular polycrystals (IP). (a) shows the simulation with unit collection efficiency, (b) with efficiency model P, (c) with efficiency model C, and (d) with efficiency model D.

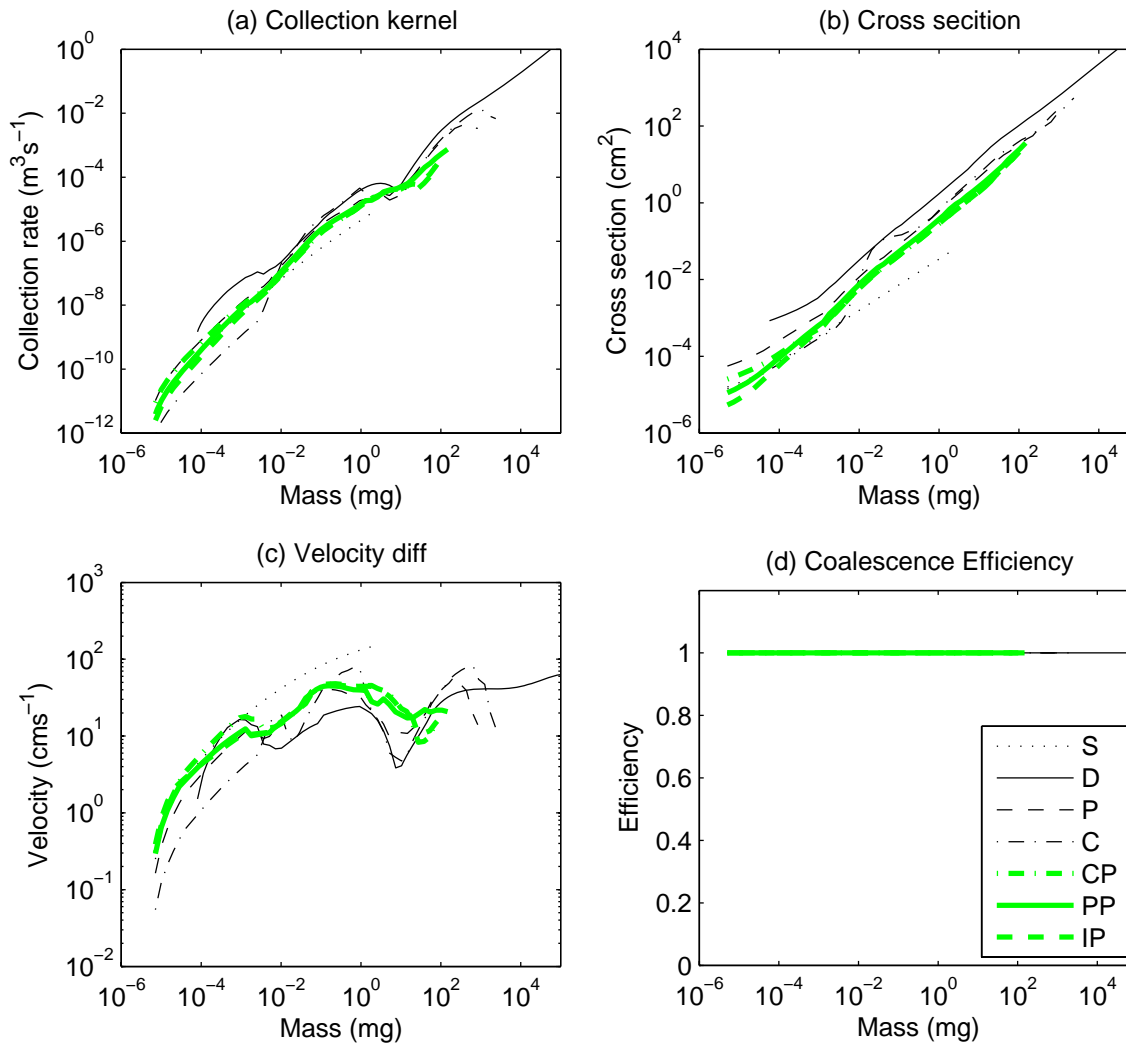


Figure 4.3 Comparison of (a) collection rate, (b) cross section, (c) terminal velocity difference, and (d) coalescence efficiency with the unit collection efficiency.

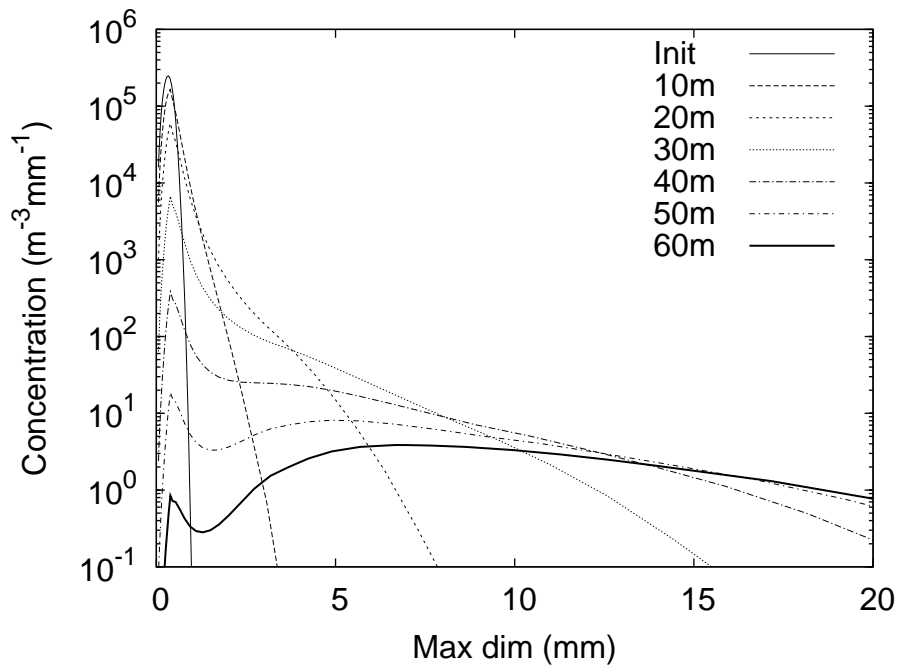


Figure 4.4 Evolution of size distribution for plates with unit efficiency.

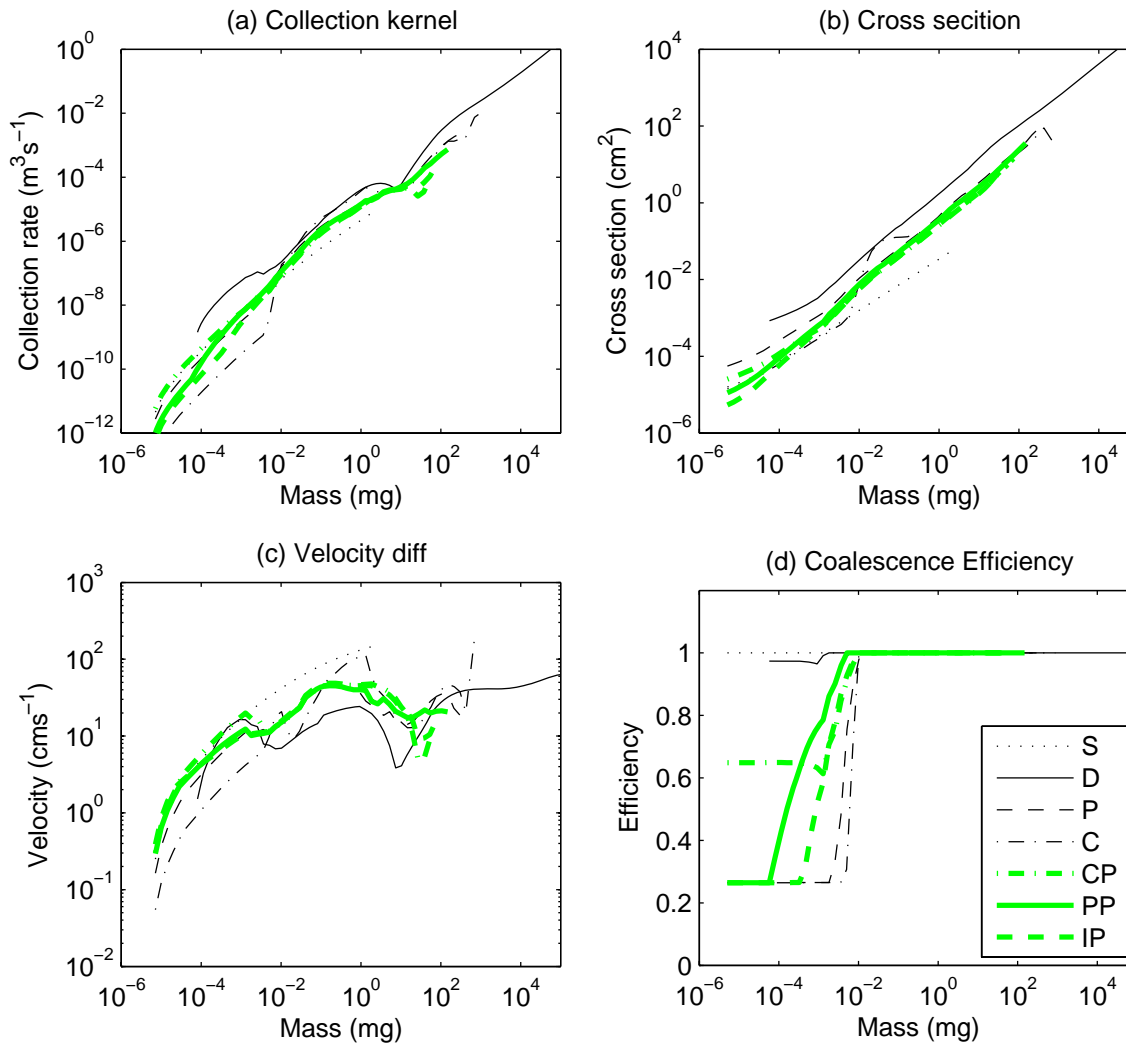


Figure 4.5 Comparison of (a) collection rate, (b) cross section, (c) terminal velocity difference, and (d) coalescence efficiency with interlocking efficiency model P.

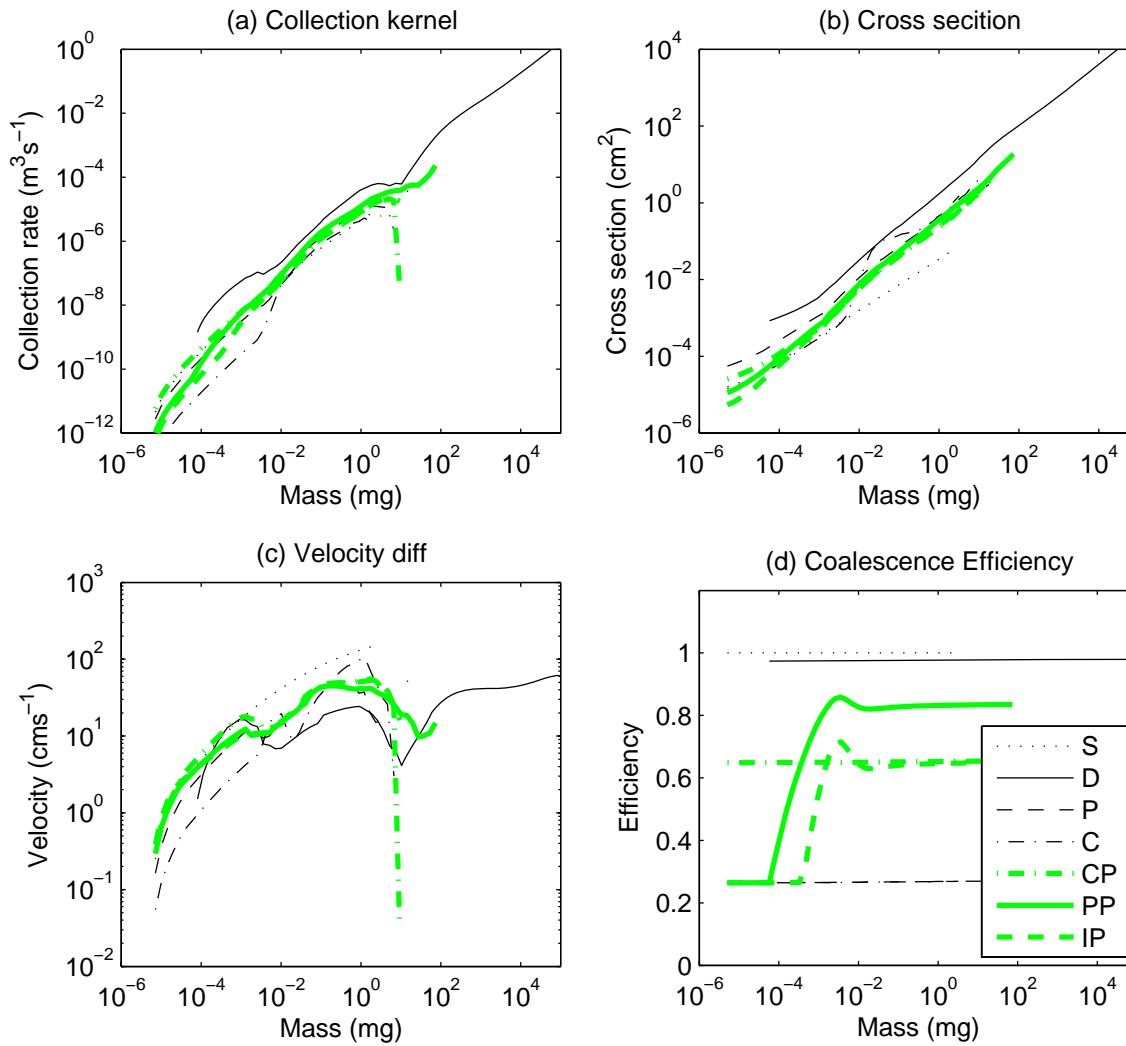


Figure 4.6 Comparison of (a) collection rate, (b) cross section, (c) terminal velocity difference, and (d) coalescence efficiency with interlocking efficiency model C.

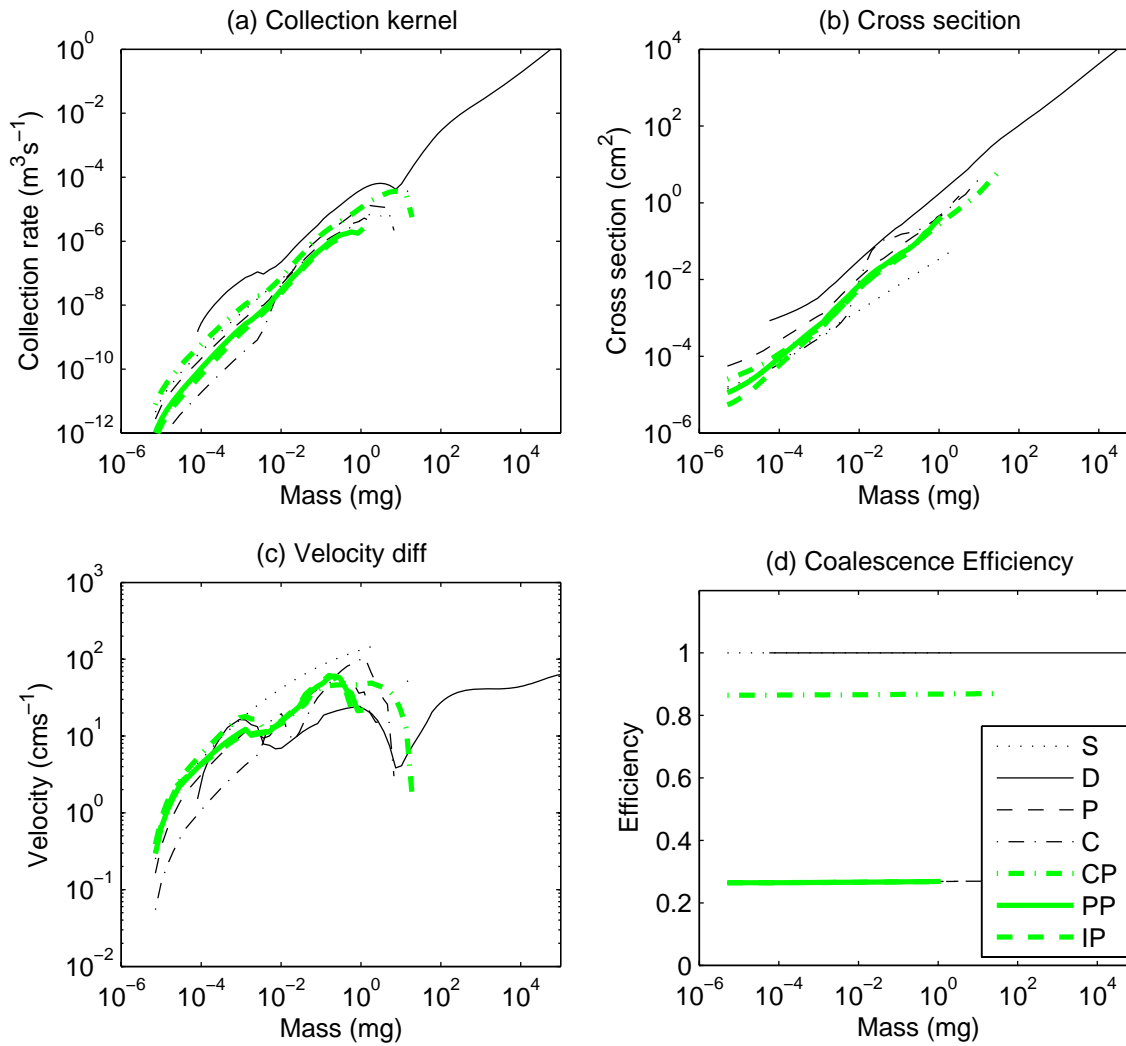


Figure 4.7 Comparison of (a) collection rate, (b) cross section, (c) terminal velocity difference, and (d) coalescence efficiency with interlocking efficiency model D.

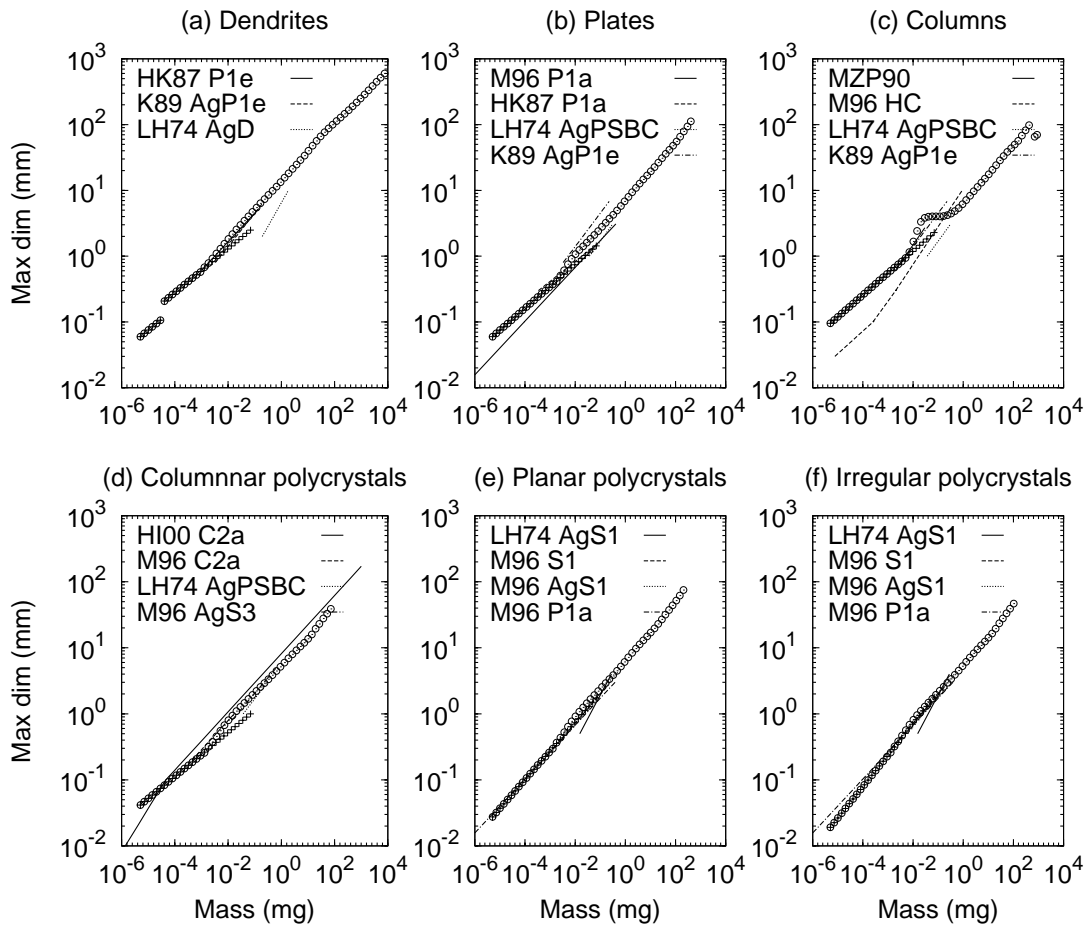


Figure 4.8 Comparison of simulated mass-dimensional relationship with the efficiency model P at 60 minutes. Cross indicates the initial condition, and circle predicted at 60 minutes. HK87 denotes Heymsfield and Kajikawa (1987), K82 Kajikawa (1982), LH74 Locatelli and Hobbs (1974), MZP90 Mitchell et al. (1990), M96 Mitchell (1996), and HI00 Heymsfield and Iaquina (2000). “Ag” indicates “aggregates of” the habit.

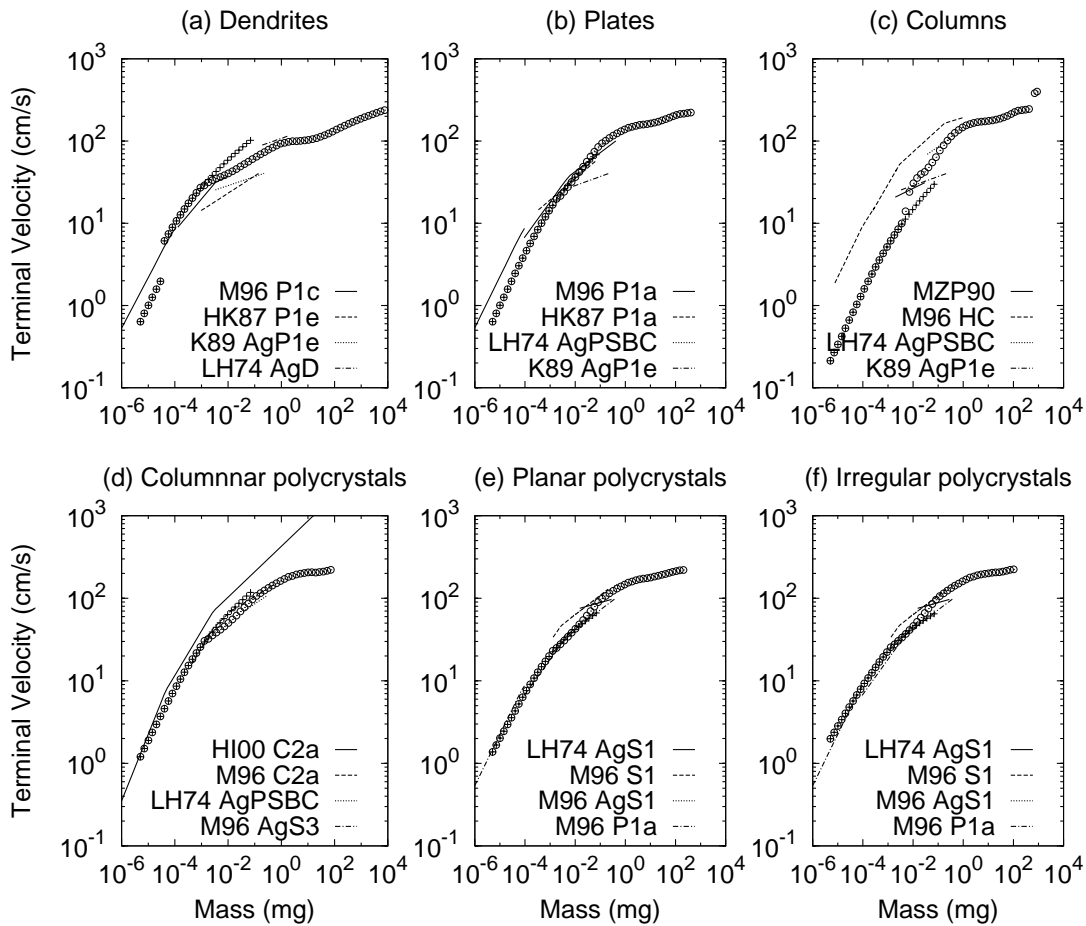


Figure 4.9 Comparison of simulated mass-terminal velocity relationships with the efficiency model P at 60 minutes. Cross indicates the initial condition, and circle predicted at 60 minutes. The reference that empirical formula was taken from is shown in the caption of Figure 4.8.

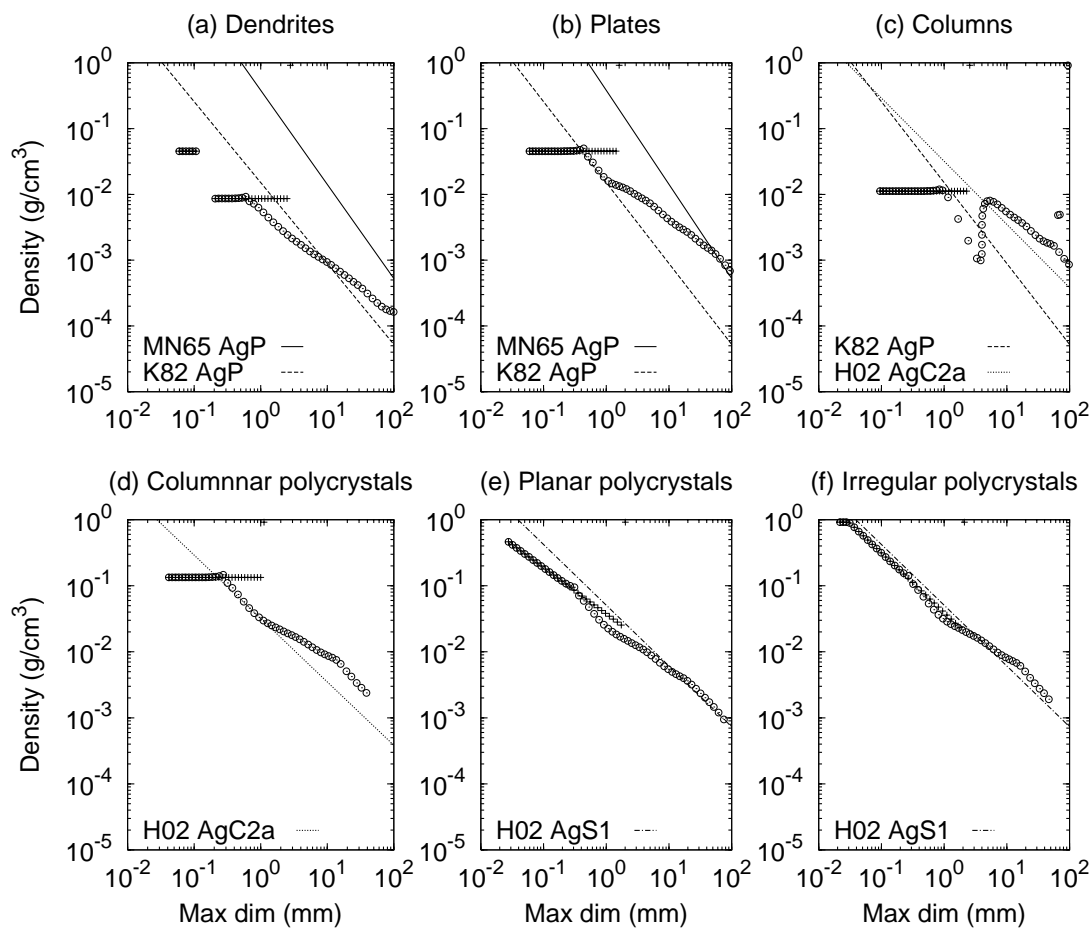


Figure 4.10 Comparison of simulated max dimension-density relationships with the efficiency model P at 60 minutes. Cross indicates the initial condition, and circle predicted at 60 minutes. Solid line in the figure is aggregates of planar crystals from Magono and Nakamura (1965), long dashed line is aggregates of planar crystals Kajikawa (1982), short dashed line is aggregates of rosettes obtained by Heymsfield et al. (2002), and dash-dotted line is aggregates of S1-S3 by Heymsfield et al. (2002).

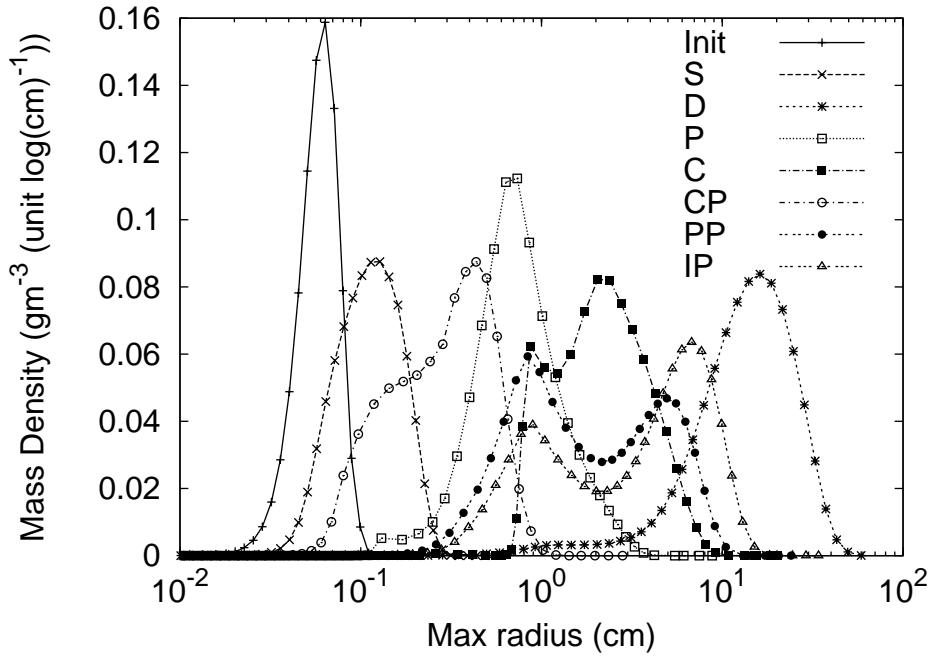


Figure 4.11 Mass densities as a function of maximum radius at 90 minutes of simulation with efficiency model P. Ice sphere is denoted by S, dendrites D, plates P, columns C, columnar polycrystals CP, planar polycrystals PP, and irregular polycrystals IP.

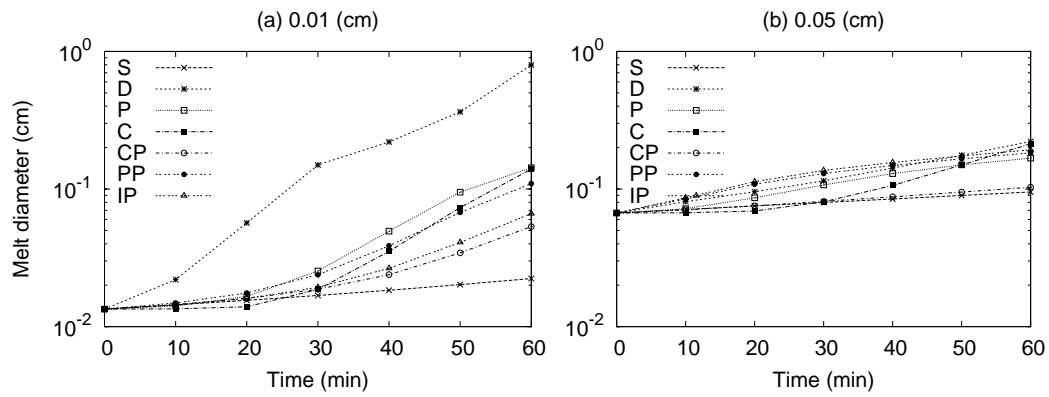


Figure 4.12 Comparison of time series of melt diameter of mean mass for (a) initial distribution with mean radius of 0.01 cm and (b) one of 0.05 cm. The efficiency model is P.

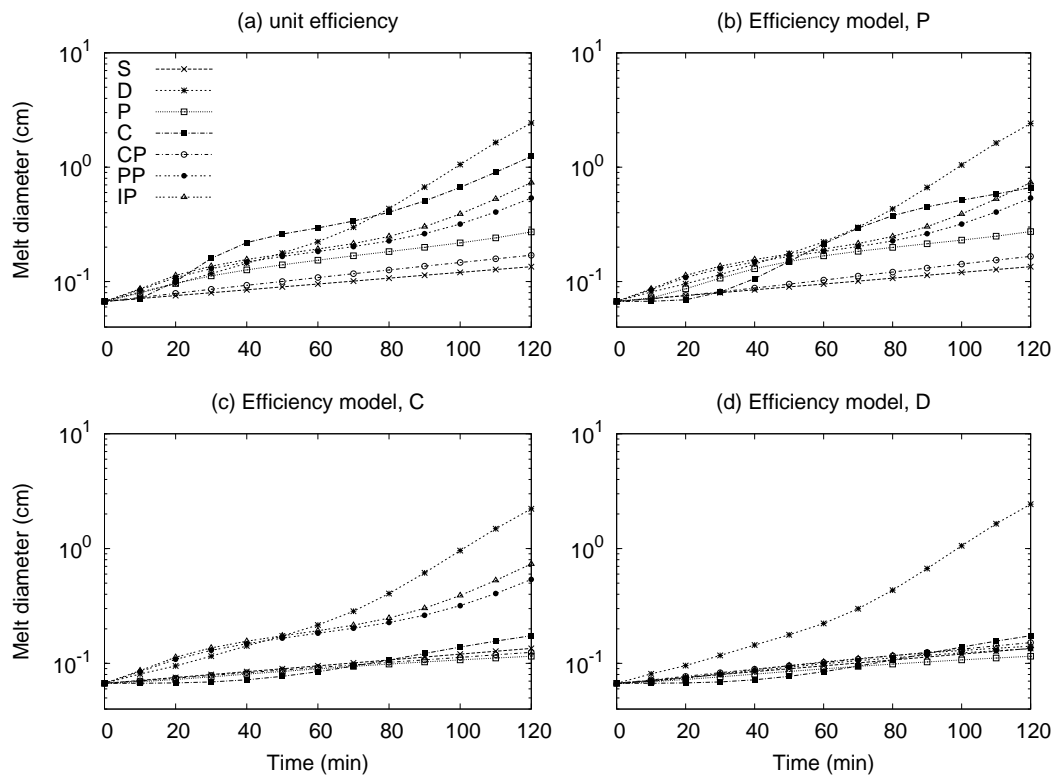


Figure 4.13 Comparison of melt diameter of mean mass with initial distribution of mean radius \bar{r} of 5×10^{-2} cm.

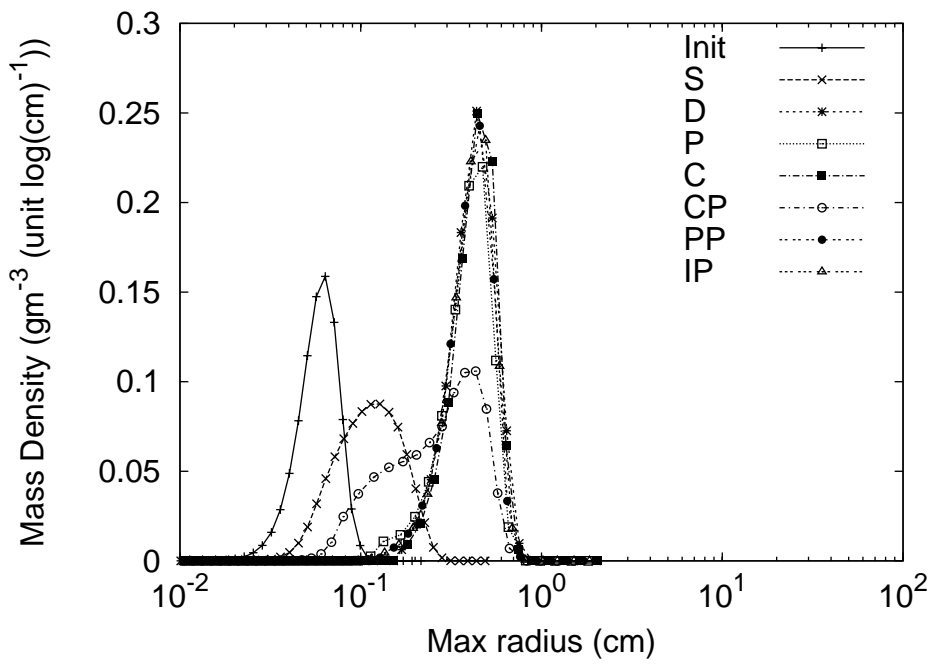


Figure 4.14 Same as Figure 8, except that these simulations are with the breakup process.

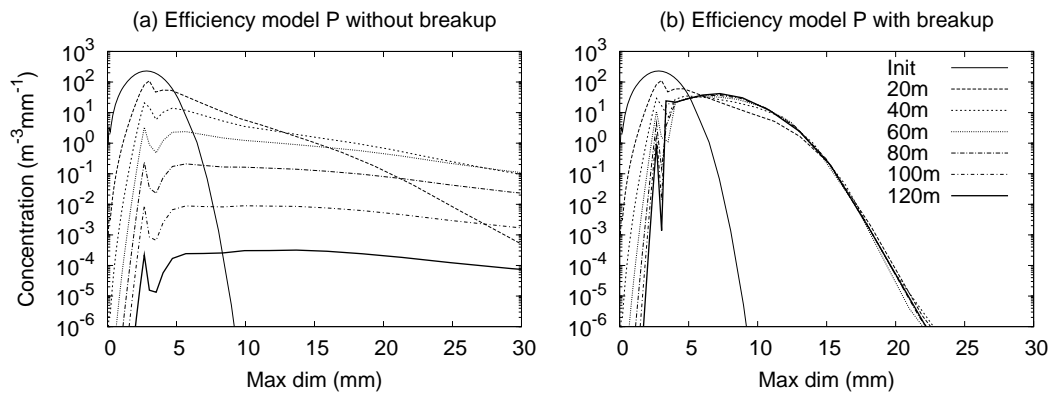


Figure 4.15 Comparison of size distribution for efficiency model P with (a) and without (b) breakup scheme.

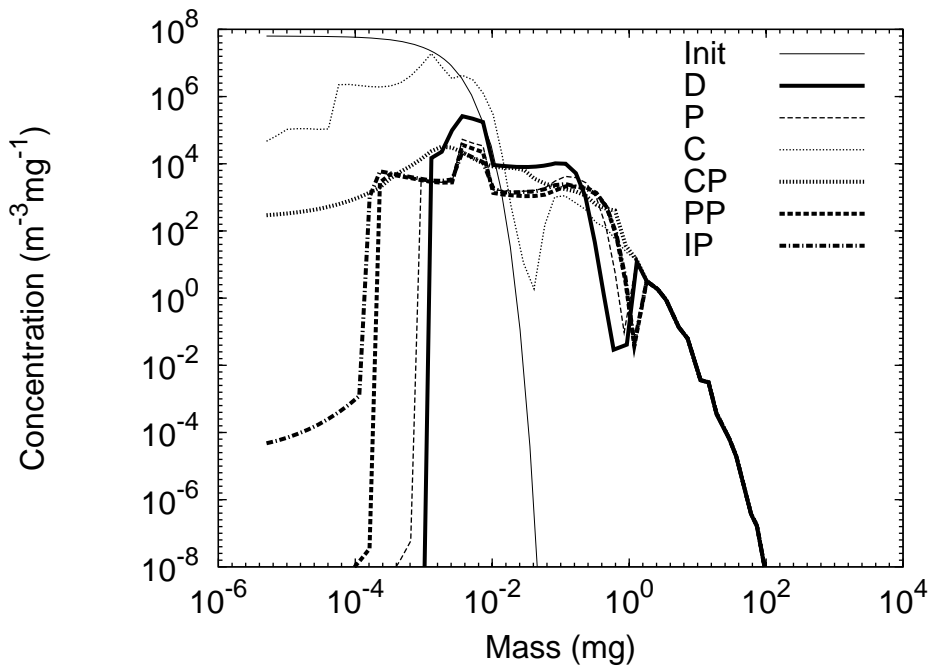


Figure 4.16 Comparison of mass distributions among six habits with aggregation, breakup and riming processes at 60 minutes of simulation.

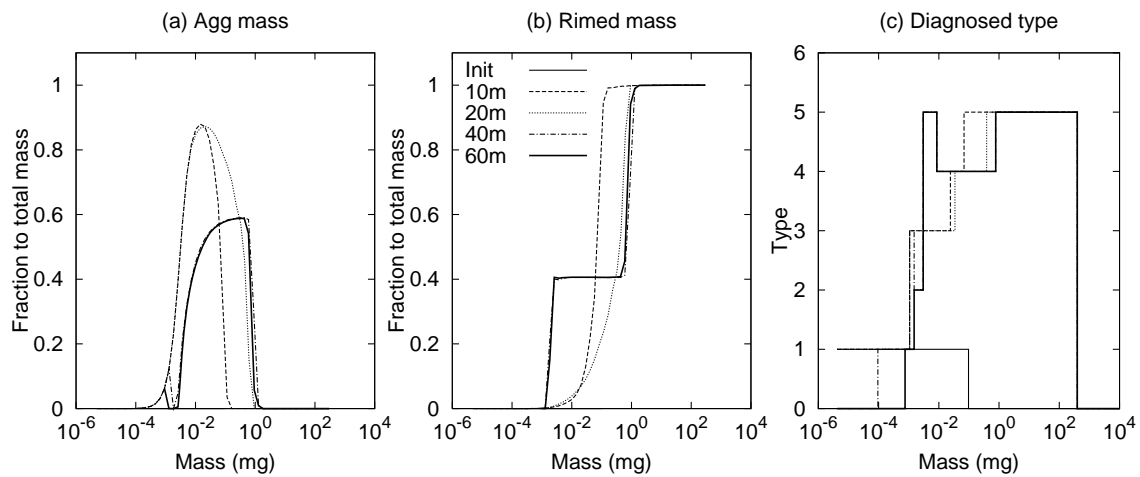


Figure 4.17 Mass components and diagnosed type of ice particles. (a) is the fraction of the aggregation mass component to the total mass for the representative hydrometeor, (b) the fraction of the rimed mass component, and (c) is the diagnosed type of ice particles. In (c), “1” indicates pristine crystals, “2” rimed crystals, “3” aggregates, “4” rimed aggregates, and “5” graupels.

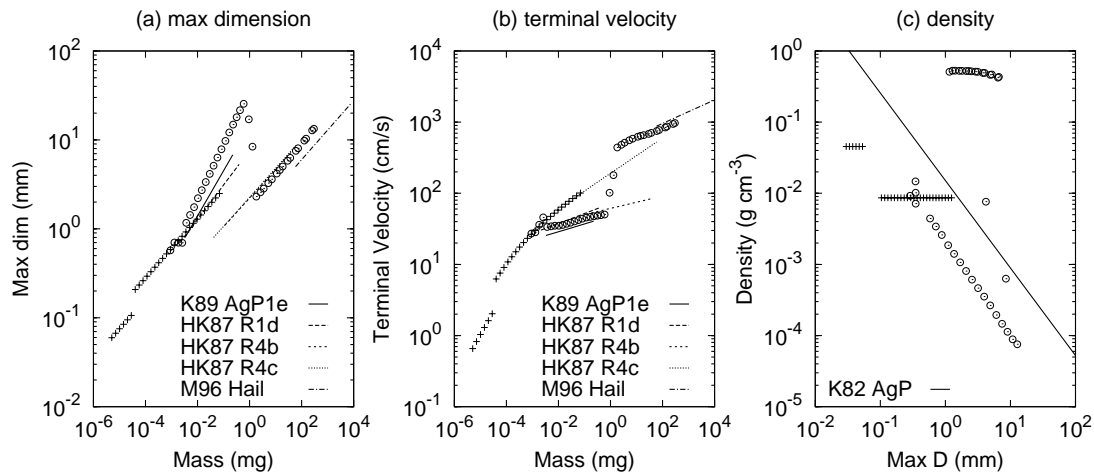


Figure 4.18 Property of ice particles simulated with aggregation, breakup, and riming processes at 60 minutes of simulation. (a) is mass-dimensional relationship, (b) is mass-terminal velocity relationship, and (c) is dimension-density relationship.

Table 4.1 Parameters for initialization of ice crystals in box simulations. Axis ratios of ice crystals are defined as $\phi = c/a$, and $\psi = d/a$. α is the aspect ratio of spheroid fitted to the ice crystal.

<i>Habit</i>	ϕ	ψ	α
Plates	0.04	0.0	ϕ
Dendrites	0.04	0.9	ϕ
Columns	10.0	0.0	ϕ
Columnar polycrystals	10.0	0.0	0.25
Planar polycrystals	0.04	0.0	0.25
Irregular polycrystals	0.04	0.0	0.25

Chapter 5 Aggregation process and explicit prediction of ice crystal habits in a two dimensional orographic storm

5.1 Introduction

Sedimentation and habit (shape) of ice particles are important factors in evolution of PSDs. The former modifies the PSD through flux difference over the size (or mass), and also it can enhance or reduce aggregation process by increasing or decreasing collecting or collected particles for further aggregation at a given level. Habits of ice particles are known to control mass-dimensional relationships, which has implication on cross-section area involved in the aggregation process. Therefore, it is crucial to study the aggregation process in the framework that both effects are included. Eulerian numerical weather prediction models have been suffering from habit-dependency of mass-dimensional relationship in addition to the lack of knowledge on parameters of PSD. Garvert et al. (2005a, b) simulated an orographic winter storm during IMPROVE-2 campaign with the fifth-generation Pennsylvania State University-National Center for Atmospheric Research (PSU-NCAR) Mesoscale Model (MM5). The simulation with the bulk microphysics parameterization correctly produced the extent of the snow field and the growth of snow particles by vapor deposition, but overpredicted mass content of snow. The PSD of snow category predicted showed larger slope of exponential size distribution. They concluded that it was caused by inappropriate parameterization of intercept which depends on density of snow, mixing ratio, and temperature. Also, the importance of

mass-diameter relationships was noted to properly simulate PSDs, which in turn affect growth of snow by deposition, riming, and fall speed.

The observation of PSDs of ice particles has been challenging due to limited area that aircrafts can fly at a given time, and the limitation of instruments. Lo and Passarelli (1982) proposed a sampling method called the advecting spiral descent (ASD) where a single aircraft makes loops downward at approximately the mean terminal velocity of ice particles and drift horizontally with the wind. It is better than horizontal flight legs because it follows ice particles that were produced by presumably the same nucleation process, and the evolution of PSD is mainly due to microphysical processes in one (vertical) dimension and not due to horizontal variation of ambient conditions. ASD has been widely used in sampling ice particles of stratiform cloud layers associated with fronts. The PSDs obtained by ASD can be compared with PSDs predicted in microphysical models by implementing trajectory analysis.

As shown in Chapter 4 with box simulations, aggregation and riming processes of SHIPS can produce observed relationships of ice particles, and have dependence on the ice crystal habits. The purpose of this study is to validate these processes of SHIPS in a cloud resolving model, where atmospheric conditions vary spatially and sedimentation modifies PSDs. In addition to the validation, this paper investigates the sensitivity of concentration of IN and ice crystal habit to aggregation initiation, studies the effect of aggregation process and freezing nucleation processes on habit frequency analysis, and investigates the sensitivity of efficiency model and prediction of lengths to precipitation on the ground. The next section describes the model setups and experiment designs. Two types of simulations which use different initial and

upstream boundary conditions are discussed in sections 5.3 and 5.4. The results are summarized in section 5.5.

5.2 Model setup and experiment design

5.2.1 Case study and model set up

On 13-14 December 2001 during IMPROVE-2 campaign a winter orographic snow storm produced heavy precipitation over the Cascade Mountains as a vigorous cyclonic storm passed over the Pacific Northwest (see Woods et al., 2005, for synoptic and microphysical observations). The orographic winter storm was chosen as the test case due to relatively predictable dynamics and existence of stratiform cloud layers with wide range of temperature. SHIPS has been installed into a cloud resolving model, University of Wisconsin - Nonhydrostatic Modeling System (UW-NMS). The model was set up for the two dimensional idealized simulation as described in section 2.5.

A degraded version of SHIPS (hereafter, referred to as D-SHIPS) was prepared, in which PPVs necessary for predicting ice crystal habits, namely lengths of ice crystals, number of extra crystallographic structures, and coordinates of center of gravity are not advected in the dynamic model. Instead, the habits of ice crystals are diagnosed based on local temperature and moisture as follows. First, depositional growth of hexagonal ice crystals was simulated under water saturation in a box model, $-50 < T < -1^{\circ} \text{C}$ and corresponding international standard pressure. From that, lookup tables of crystal density and axis ratio were constructed to retrieve a-axis and c-axis lengths given temperature and mass of ice crystal. The dendritic arm length

is assumed to be 90% of a-axis length in $-16 < T < -12^\circ\text{C}$ and water saturated environment.

In $T < -20^\circ\text{C}$ the habit frequency of Bailey and Hallett (2004) is utilized to obtain the habit of ice crystals given temperature and supersaturation in a grid cell. Then, the maximum dimension of polycrystals is calculated from empirical mass-dimensional relationships as used in SHIPS (see the subsection 3.2.3). The other PPVs are predicted and microphysical processes are identical to SHIPS.

5.2.2 Experiment design

Firstly, a simulation with only liquid microphysics was run for 12 hours (43200 s) to reach quasi-steady state as done in Chapter 2 and Chapter 3. The liquid microphysical processes include Cloud Condensate Nuclei (CCN) activation, vapor deposition, collision-coalescence, and collision-breakup processes. All the experiments are started from the quasi-steady state with ice microphysics processes on. Therefore, simulation time referred in the following starts from the time when ice microphysics processes are turned on.

Nineteen experiments are conducted as shown in Table 5.1. Experiments are set up by changing IN concentration, aggregation efficiency model, microphysical processes, formation of polycrystals through freezing processes, initial condition of ice distributions, and habit prediction. IN concentration takes on 1, 10, and 230 L^{-1} . Two constant aggregation efficiencies among all habits and types are used; $E_{coal} = 0.1$ and 1. $E_{coal} = 0.1$ is suggested to be the probable minimum value in the literature (ex., Field and Heymsfield, 2003), while $E_{coal} = 1.0$ is the upper limit that is plausible in $-20 < T < -10^\circ\text{C}$ associated with dendritic crystals. In addition to these constant efficiencies, three interlocking efficiency models, P, C,

and D, defined in the subsection 4.2.3.1 are explored. Some experiments are simulated without riming process in order to see the effect of aggregation more closely. As implemented in Chapter 3, two simulations, PCHH and PCLH are assumed to form hexagonal monocrystals through contact, immersion, and homogeneous freezing processes based on the frequency database. PCH-HCCN is run with high concentration of CCN by setting a lower limit of 250 cm^{-3} to the vertical profile of CCN. Note that PCH, PCL, PCLH, PCLH and PCH-HCCN simulate homogeneous freezing nucleation, while others do not.

It turned out that simulations starting without any ice particles cannot produce the magnitude of observation-based estimates of mass content profiles. As suggested by Sixth WMO international cloud modeling workshop (Grabowski 2006) the horizontally uniform distribution of ice particles is used to mimic the upper-level front coming from the west of the Cascade for some of the experiments. The initial mixing ratio of snow was given in 2500 < z < 8000 m by the equation:

$$q_s = \max(0.0, -0.047z_{ref}^4 + 0.0625z_{ref}^3 + 0.0242z_{ref}^2 - 0.1657z_{ref} + 0.2215) \quad (5.1)$$

where $z_{ref} = (z - 5000.0)/1947.2$, and in $220.15 < T < 273.15^\circ\text{C}$ concentration of cloud ice was given by $C_i = 5.0 \exp(0.304(273.15 - \max(T, 238.))) / \rho_a$. The snow is assumed to be aggregates, and the mixing ratio is distributed with the exponential size distribution. The slope parameter λ was specified by using Heymsfield et al. (2002)'s fit to the observed PSD from precipitating stratiform clouds: $\lambda = 12.5 \exp(-0.066T)$. The concentration of cloud ice was given to the first bin of mass distribution. The mass component of ice crystals within aggregates was assumed to be one-tenth of mass of the ice particle. Habit of ice crystals was

specified to the one with maximum frequency given temperature and moisture based on Bailey and Hallett (2004)'s frequency data. The lengths of hexagonal crystals were diagnosed from the mass and temperature by using the lookup table explained in the previous subsection.

Throughout the text, z and y are used to denote the altitude and horizontal distance in km.

5.3 Eulerian simulation without initial ice distribution

This section studies 1) the dependency of aggregation initiation on ice nuclei concentration and crystal habits, 2) the ability of SHIPS to form realistic PSDs from ice nucleation process, and 3) the habit frequency obtained at a given temperature range. The first two are investigated with the simulations that include all but riming process: ice nucleation, vapor deposition, aggregation, hydrodynamic breakup, and melting-shedding processes. They are indicated by the letter "1" at the end of experiment names in Table 5.1. The third is discussed with the simulations with all the microphysical processes on. Note that the difference between PCH and PCHH (PCL and PCLH) is that PCH (PCL) forms ice crystals based on a habit frequency database whereas PCHH (PCLH) does only hexagonal monocrystals.

5.3.1 Aggregation initiation and ice nuclei concentration

First, the sensitivity of aggregation initiation to ice nucleation (IN) concentration is discussed. The distribution of predicted habits for MS1 at 20 minutes is shown in Figure 5.1. Dendrites exist over the higher topography at $3 < z < 5$ km associated with high concentration of supercooled liquid hydrometeors due to the stronger vertical motion. Columnar crystals prevail in high ($z=10$ km) and low ($z=3$ km) altitude. Planar polycrystals (side planes, over-

lapping parallel plates, and crossed plates) exist in $6 < z < 8$ km. Irregular polycrystals prevail in $z > 6$ km. Columnar polycrystals (bullet rosettes) have high concentration in area of strong vertical motion. As discussed in Chapter 3, the change in IN concentration resulted in the difference in supersaturation fields. The difference in the predicted habits was found especially in the area of strong vertical motion with supercooled liquid hydrometeors. Planar and columnar polycrystals were more found in the case with lower IN concentration. Simulated distributions of pristine crystals and aggregates at 20 minutes are compared among the different IN concentrations and constant efficiency of 0.1 (HS1, MS1, and LS1) (Figure 5.2). It can be seen that locations of high concentration of aggregates exist at $z=4$ km for HS1, at $z=6$ and $y=240$ for MS1 and LS1, and at $3 < z < 10$ km and $y > 320$ km for all the three cases. The first thing noticed from the figure is that the concentration of aggregates in $100 < y < 275$ km and $2 < z < 8$ km is correlated with concentration of pristine crystals. This is clear from the fact that the rate of a parent particle collecting is proportional to the available concentration of collected particles.

The collection rate is also proportional to cross section area, difference of terminal velocity and efficiency. However, the difference of former two caused by difference in IN concentration turned out to be secondary importance in the initiation of aggregates. Horizontal average of mean and standard deviation of terminal velocity and cross section area of a particle for a grid cell is plotted at 20 minutes of simulation (Figure 5.3). Peaks in terminal velocity and cross section area at $z=4$ km and 2 km are related to the maximum growth rate of dendrites and melting layer, respectively. The frequency of crystal habit in terms of cross section area in a grid cell was calculated and horizontal average of the frequency is shown in Figure 5.4.

Three cases have similar vertical distribution of contribution of habits in terms of cross section area, which corresponds to the concentration distribution shown in Figure 5.1. The peaks of mean and standard deviation of cross section area shown in Figure 5.3 are related to the vertical distribution of contribution from each habit. As IN concentration is increased, the contribution of plates decreases and one of dendrites increases in $4 < z < 6$ km. The peak of dendrites corresponds to the maximum mean cross section in vertical. Comparison between (b) and (f) of Figure 5.3 clearly indicate that case of small concentration of ice particles (LS1) has larger cross section area on average than that of large concentration (HS1), which implies potentially large cross section area of two colliding particles. The standard deviation of terminal velocity over a PSD can give some idea about the spread of terminal velocity of two colliding particles. According to horizontal average of the standard deviation shown in Figure 5.3, LS1 has larger spread above 4 km than the other two cases, but all cases show similar magnitude at 4 km. The differences between those three cases stems from competition of vapor through depositional growth. Even though larger cross sections and larger variance in terminal velocity with smaller IN, they turned out to be not large enough to counter concentrations. For instance, consider the following cases. Case I has a collector particle and 10 L^{-1} of available particles for collection, and Case II has 100 L^{-1} of available particles for collection. And both cases have similar terminal velocity differences. In order to achieve the same collection rate, the collector particle of case I need 10 times larger swiping volume than the collector of case II. The rate of aggregate production is product of collection rate and the concentration of collector particles. Thus, the swiping volume of collectors of 10 L^{-1} need to be 100 times larger than particles of 100 L^{-1} . This was not the case in these experiments. Other mechanisms to

enhance aggregation are turbulence, and electrostatic force. It is conceivable that larger crystals may induce stronger local turbulence and enhance the collection rate. Also, the electric dipole induction might be larger for crystals having larger dimensions. The relation between IN concentration, habit, and precipitation rate through vapor deposition and aggregation processes should be investigated in a box model setup.

The local maximum of concentration at $z=6$ and $y=240$ km that can be seen clearly for MS1 and LS1 is produced by combination of high concentration of ice particles from the same level or above due to immersion freezing nucleation and large swiping volume associated with fast growth of planar crystals upwind at the level. This is the case of feeder-seeder mechanism for ice collection process.

Secondly, results from HS1, MS1, and LS1 at 40 minutes are discussed. At this time the immersion freezing nucleation process is still as active as 20 minutes ago. Comparison of concentration of aggregates between 20 and 40 minutes (Figure 5.2 and Figure 5.5) indicates that the aggregates of $3 < z < 4$ km at 20 minutes fell to just above melting level and also advected to down stream. The high concentration at $z=6$ and $y=240$ km at 20 minutes was also advected downwind. The main features are the new areas of aggregation initiation $6 < z < 8$ km and $0 < y < 200$ km, and ongoing active initiation in $5 < z < 8$ and $210 < y < 240$ km. The broadening of aggregation initiation to 8 km is associated with growth of cross section area and variance of terminal velocity (Figure 5.6); MS1 and LS1 have mean cross section area of 5×10^{-5} to 5×10^{-4} cm² between 6 and 8 km, whereas HS1 has that of 2×10^{-5} to 1×10^{-4} cm². However, the difference between the low concentration of aggregates extending to 8 km and aggregates at $z=8$ km and $y=210$ km is that the latter has continuous source of pristine crystals that can be

collected by other crystals. The spatial distribution of mean and standard deviation of swiping volume and collection rate at a grid cell is shown in Figure 5.7. The increase of mean collection rate at $z=8$ km from $210 < y < 225$ km corresponds to the decrease of mean swiping volume (see (a) and (c)). The horizontal gradient is caused by the significant concentration of ice crystals nucleated through the immersion freezing process that are active at 40 minutes for MS1 and LS1. The standard deviation of swiping volume (b) and collection rate (d) over the area $6 < z < 8$ km and $210 < y < 230$ km is higher than $2 < z < 5$ km and $100 < y < 225$ km, even though both area have high mean collection rates. It suggests that more variance exists in the PSD over just below the area of the active immersion freezing nucleation. It is speculated that the relatively large ice particles ($\sim 100 \mu\text{m}$) from the upwind of $y=210$ km arrived to the source region and triggered the aggregation process over the source as mentioned previously. This is why at 20 minutes the two cases had similar active freezing processes, but aggregation was not initiated yet. Higher concentration of ice particles in HS1 had consumed the liquid droplets by vapor deposition of ice particles, and the immersion freezing process had little production at the level and at the simulation time. Also, the mean size of ice crystals upwind is 30 to 50 μm . Therefore, the strong aggregation initiation that occurred for LS1 and MS1 cannot be seen in HS1 (Figure 5.5).

Since the simulations were started from quasi-steady state with liquid hydrometeors only, the immersion freezing process may have produced much higher concentration of ice particles from high concentration of super-cooled liquid hydrometeors. In these experiments riming process was turned off. Therefore, the above results elucidate the potential importance of the immersion freezing. In reality three processes, vapor deposition, freezing nucleation and

riming processes are modulated by IN concentration. The interaction between these processes has to be quantitatively investigated.

5.3.2 Aggregation initiation and habit dependency

The previous section examined experiments with constant efficiency for all habits and types. This section discusses the role of habit in terms of interlocking efficiency. Simulations with the aggregation efficiency model D were conducted for each concentration of IN (HD1, MD1, and LD1). Comparison of predicted concentration of aggregates (Figure 5.2 and Figure 5.8) indicates that higher concentration of aggregates was produced in the area of dendritic crystals ($z \sim 5$ km) and in columnar polycrystals ($9 < z < 10$ km and $230 < y < 250$ km). This results from the assumption on the interlocking mechanisms of the two habits. Again, the concentration of aggregates shows dependence on IN concentrations because the efficiency model still varies between 0.1 and 1 and not large enough to counter the concentration of collected particles. The aggregation distribution at 40 minutes of the simulation for MD1 and LD1 shows similar local maximums at $6 < z < 8$ km and $y = 210$ km as seen for those with the constant efficiency due to the immersion freezing nucleation and advection of large ice crystals to the area (Figure 5.9). In addition to the area, another high concentration of aggregates can be found in $4 < z < 6$ km and $240 < y < 275$ km. The area is in the edge of high concentration of ice crystals and dendritic growth regime.

Concentration of diagnosed habits only including pristine crystals at 40 minutes for MD1 is shown in Figure 5.10. The one only including aggregates is shown in Figure 5.11. Plates and columnar crystals generally remain as pristine crystals. Dendrites take form of pristine

crystals and aggregates in $2 < z < 4$ km and they are the result of sedimentation from $4 < z < 5$ km. The aggregates in $4 < z < 8$ km are associated with irregular polycrystals. It is clear that irregular polycrystals in $4 < z < 6$ km and $240 < y < 275$ km fell from the above into the dendritic growth temperature ($-16 < T < -12$ C) because irregular polycrystals are not generated in $z < 6$ km ($T > -20$ C). Average axis ratios were calculated by using concentration-weighted a-axis and d-axis lengths given a diagnosed habit as shown in Figure 5.12. The irregular polycrystals indeed have the dendritic extension in $4 < z < 6$ km and this corresponds to the high concentration of aggregates. This implies that high concentration of irregular crystal fell down to the dendritic growth zone and became “spatial dendrites”, and then they may have triggered the aggregation in the area with its high concentration. Rauber (1987) suggests the riming near cloud top in the vicinity of the dendritic growth region may promote the development of spatial dendritic crystals based on Kikuchi and Uyeda (1979)’s study on spatial crystallographic directions caused by rimed particle. This case study had deep cloud top and the sedimentation of polycrystals into dendritic zone was modeled to form spatial dendrites without considering riming process. This pathway to spatial dendrites should be investigated in the laboratory because the habit may play an important role in the initiation of aggregation with large planar dendrites as pointed by Rauber (1987). It can be also seen that some of the columnar crystals have dendritic growth (kinds of capped columns) and some of them are diagnosed as aggregates. Therefore, the habit dependence of the efficiency is able to enhance initiation of the aggregates if enough concentration of ice crystals exists nearby. Spatial relation of active immersion freezing nucleation and dendritic growth zone can be a key for aggregation process in orographic snow storms.

5.3.3 Evolution of particle size distribution from ice nucleation process

This subsection examines the particle size distributions (PSDs) predicted along trajectories of ice particles and attempts to assess the ability of SHIPS to produce the observed feature of PSDs from ice nucleation processes. The evolution of PSDs has been studied in clouds with a sampling method called the advecting spiral descent (ASD) or Lagrangian spiral descent of aircrafts (ex., Lo and Passarelli, 1982; Field, 1999; Heymsfield et al., 2002). In the ASD, it is conventional to descend an aircraft with a constant bank angle ($\sim 15^\circ$) and constant rate (~ 1 to 2 m s^{-1}) in order to follow certain population of particles with background air motion. The velocity corresponds to ice particle of order of 1 mm diameter. Therefore, the trajectory mainly follows large particles produced by aggregation or riming processes. Note that given PSD on the trajectories the large particles can be locally produced or fell from upper levels. By using wind fields and mass weighted terminal velocity of ice particles 10 trajectories were calculated for MD1. The 10 trajectories start from $y=0.5 \text{ km}$ and $z=7 \text{ km}$ by 11 km apart at 150 s as shown in Figure 5.13.

Evolution of PSDs in each grid cell along the trajectory #1 is plotted every 20 minutes in Figure 5.14. The circle on the trajectory in Figure 5.13 indicates approximate locations of PSD shown in Figure 5.14. At 20 minutes of simulation, ice particles consist of pristine crystals of plates and irregular polycrystals. Then, aggregates of irregular polycrystals begin to form in the largest size. The habits diagnosed are similar until the trajectory reaches -16° C at 120 minutes. Dendrites begin appearing at this time, but the mean habit of ice crystals within aggregates stay as irregular polycrystals. Then, at 160 minutes columnar crystals appear on

the smallest of the mass spectrum due to columnar growth regime in $-9 < T < -5^{\circ}\text{C}$. It can be seen that in this trajectory the mode made of pristine crystals grow to larger size with time, also that the aggregates get larger with time and its concentration increases. Aggregates of irregular polycrystals can be seen throughout in the large end of PSD. This is because the mass weighted terminal velocity used for trajectory analysis mainly represents velocity of the large particles. The small end of PSD shows the habits that reflect local growth regime of ice crystals given temperature and moisture. It is interesting that the ice particles less than the mode are pristine crystals, which imply that those particles are grown by vapor deposition, not by aggregation process.

PSDs along the trajectory #10 are shown in Figure 5.15. It started with ice particles consisting of pristine crystals of plates, irregular, and planar polycrystals. Then, aggregates of planar and irregular polycrystals begin to form in the largest size. At 100 minutes pristine crystals of dendrites appear in size of less than $100\ \mu\text{m}$. This trajectory experiences more upward and downward motion than #1. The mode of PSDs are diagnosed as pristine crystals, so the concentration distribution is mainly created by vapor deposition process. Whether or not particles at the mode are locally produced, the mode does not show clear increase due to evaporation and condensation associated with the vertical motion. At 120 minutes aggregates of plates and dendrites appear in $D \sim 100\ \mu\text{m}$. It is speculated that they are formed by dendrites from previous time. Then, at 140 minutes, aggregates of irregular polycrystals stay in the large size, while the aggregates of dendrites and plates that existed in previous time disappeared. It implies the mass-weighted terminal velocity followed the aggregates of

irregular polycrystals. As seen in the above analysis, habits and types of ice particles can be used as marker of growth history or origin of particle to study the evolution of PSDs.

The domain was divided into vertical sections $2 < z < 4$, $4 < z < 6$, $6 < z < 8$ and $z > 8$ km, and samples for each section were put together to calculate average PSD, conditional frequency of type and habit of ice particles given size. Such analysis for MD1 at 40 minutes of simulation is shown in Figure 5.16. The PSDs show exponential-like distribution and the slope and intercept of fitted exponential distribution decreases with height. This behavior of the parameters with height qualitatively agrees with PSDs generally observed in deep stratiform cloud layers. Compared with Figure 12 of Woods et al. (2005), the fitted PSDs in $2 < z < 4$ and $4 < z < 6$ have similar order of intercept and slopes to observed PSDs. However, the PSD in $2 < z < 4$ km misses very small particles ($D < 250 \mu\text{m}$). As the height decreases, conditional frequency of aggregates increases toward smaller size. The conditional habit frequency shows that most of millimeter size particles are irregular polycrystals and dendrites appear in $2 < z < 4$ km at this time. Those characteristics can be seen from Figure 5.10 and Figure 5.11. From the ice nucleation process, SHIPS was able to reproduce sub-exponential distribution that consists of pristine crystals and aggregates. The simulations without ice particles at the initial time turned out to underestimate the mass content compared with observations since altostratus seeder clouds associated with upper-level front came into the domain in the observation. More detailed comparisons with observed fields are given in the following section where simulations are started with initial ice distribution to mimic the incoming altostratus clouds.

5.3.4 Habit frequency analysis

This subsection discusses the habit frequency at a given temperature range and the importance of freezing nucleation processes for polycrystal formation. Section 3.4 discussed the habit frequency for simulations of polycrystals with only vapor deposition process on. This is a follow-up of the discussion with all microphysical processes on. Five simulations were implemented: PCH, PCHH, PCL, PCLH and PCH-HCCN. The setups are identical to those in section 3.4 except for the simulated microphysical processes. PCHH and PCLH nucleate only hexagonal monocrystals from freezing nucleation processes whereas PCH, PCL, and PCH-HCCN nucleate polycrystals based on the frequency database. PCH, PCHH and PCH-HCCN predict 230 L^{-1} of IN, whereas PCL and PCLH 1 L^{-1} .

The habit frequencies and moments of average PSDs were calculated by grouping samples in five temperature ranges, $T < -40^\circ \text{C}$, $-40 < T \leq -30^\circ \text{C}$, $-30 < T < -20^\circ \text{C}$, $-20 < T < -10^\circ \text{C}$, and $T > -10^\circ \text{C}$, and in the entire domain during the first three hours of simulation (Table 5.2). The analysis includes all types of ice particles. Comparison of the habit frequencies shown in Table 3.2 and Table 5.2 indicates that the habit frequencies including all the microphysical processes are qualitatively similar to those only with nucleation and vapor deposition processes except for $T > -10^\circ \text{C}$. Note that SHIPS predicts a single average habit of ice crystals within an aggregate, rimed aggregate, or graupel. Bulk properties of PSDs, however, show some differences. The number concentration in Table 5.2 is smaller than in Table 3.2, and mean and standard deviation of maximum dimension are larger. This is due to the aggregation processes simulated in this section. In $T > -10^\circ \text{C}$, plates have larger

frequency for PCH and PCHH with all processes on, whereas frequency of columnar crystals is larger for PCL and PCLH. Faster sedimentation of aggregates of plates may have resulted in the increase for PCH and PCHH. As shown later, PCL and PCLH simulate more active riming process than PCH and PCHH due to larger size and less depletion of supercooled droplets used for vapor deposition. Thus, the accompanying active secondary nucleation process (Hallett and Mossop mechanism) for PCL and PCLH can explain the higher frequency of columnar crystals in the temperature.

The case with high concentration of CCN (PCH-HCCN) shows high concentration of columnar crystals in $T < -30^{\circ}\text{C}$, even though the freezing processes determine growth mode based on BH04a's frequency map. The high concentration of CCN led to high concentration of small supercooled droplets ($D < 10\ \mu\text{m}$). The nucleated size by freezing processes is less than assumed threshold for nucleation period. Even if the droplets freeze as polycrystals, they can still change the growth mode based on the environment. Therefore, it is speculated that the nucleated crystals became columnar crystals by following the ambient moisture condition. This suggests importance of studying the dependency of growth mode of frozen hydrometeors on the size and environmental conditions.

Similarly, mass content and its frequency for type of ice particles were calculated in the domain and the five temperature ranges (Table 5.3). For all cases, the mass content increases with increase of temperature as well as the frequency of rimed aggregates and graupels. The cases with less IN concentration (PCL and PCLH) have more fractions of rimed particles than PCH and PCHH, which indicates that riming process is relatively more active to produce the mass on ice particles. Comparing PCH and PCHH, the different assumption of habit formed

by freezing processes resulted in the only difference in mass content frequency of aggregates in $T < -30^{\circ}\text{C}$. The small frequency of aggregates for PCHH can be associated with high concentration of small columnar crystals in the wave cloud area ($y > 276\text{ km}$). As discussed in section 3.5, it is not known if ice crystals produced by freezing processes follows similar habit frequency for the crystals nucleated by deposition nucleation or not. The above experiments indicated a sensitivity of the nucleated habit to the resulting microphysical processes and spatial distribution of ice particles.

In order to study effects of the immersion and homogeneous freezing nucleation processes on PSDs, the domain is divided into three sections. Section I ($0 < y < 200\text{ km}$) is a stratiform cloud area with small vertical motion, section II ($201 < y < 275\text{ km}$) is a seeder-feeder area with vertical motion created by the topography, and section III ($y > 276\text{ km}$) is an orographic wave cloud area. As expected, no significant difference in distribution of ice particles can be found among the experiments in section I because supercooled liquid hydrometeors are not available in the section. As shown in Figure 3.13 and Figure 3.14, in section II and III the immersion and homogeneous freezing processes are active, and columnar and planar polycrystals were found abundant. Average PSDs were constructed by grouping the samples for the five temperature ranges in section III. Along with PSDs, conditional frequency of type and habit given maximum dimension were calculated. Figure 5.17 and Figure 5.18 show the results at 20 minutes of simulation for PCH and PCHH, respectively. The simulated PSDs show multiple modes as the PSDs observed in wave and cirrus clouds normally exhibit. It is interesting to note that the inflection points of PSDs are associated with the change of dominant type of ice particles from pristine crystals to aggregates. Furthermore,

it was found that PCH has the inflection points in smaller size than PCL. It is probably because PCH has high concentration to obtain sufficient collection rate whereas ice crystals in PCL have to reach enough size to obtain comparable collection rate. Mitchell et al. (1996) modeled bimodal distributions observed in cirrus clouds by combining two size distribution functions, and advanced a hypothesis that the smaller part of distribution is a result of a balancing act between the production and removal of ice particles. Mechanisms to produce the modes are something to be explored as future research with SHIPS.

Comparison of habit frequency in Figure 5.17 and Figure 5.18 clearly indicate the assumption on the habit nucleated by the freezing processes affects the frequency in size larger than 10 μm . The size corresponds to the one of supercooled droplets. As discussed in section 3.4.2, the habit frequency given maximum dimension agree with observation by Baker and Lawson (2006) in that rosette-shape and irregular shape crystals are dominant in the size larger than 100 μm . The discrepancies with the observed habit frequency are the existence of long needles and lack of spheroid representation in SHIPS.

In conclusion, simulations with the formation of polycrystals through the freezing processes based on Bailey and Hallett (2004a) was able to produce habit frequency similar to observations. Formation of hexagonal monocrystals by the freezing appeared to be unrealistic in $T \leq -30^\circ\text{C}$ and high saturated condition. The immersion and homogeneous freezing processes can potentially affect habit frequency significantly due to much higher concentration of CCN than IN.

5.4 Eulerian simulations with initial ice distribution

In order to reflect observed altostratus clouds coming into the domain, simulations are initialized with the horizontally uniform distribution of ice particles and constant boundary conditions of ice particles at the upstream boundary. The initial distribution of type of ice particles is shown in Figure 5.19. Setups of the simulations are shown in Table 5.1 and indicated by the letter “2” at the end of experiment names. The simulations include all the ice microphysical processes: ice nucleation, vapor deposition, aggregation, riming, hydrodynamic breakup, and melting-shedding processes. Quantitative comparison of predicted fields with observations, and sensitivity to the aggregation efficiency models and IN concentration are discussed.

5.4.1 Comparison of simulated bulk property

Horizontally averaged mass contents for LS2, LL2, LP2, LC2, and LD2 are shown in Figure 5.20. It is clear that after 1 hour the maximum of mass content at initial time moves down just above the melting layer ($\sim 2\text{km}$) and the average is much lower than observed. Note that the average profiles generated by the simulation are obtained for the entire domain, while the estimates by Woods et al. (2005) are calculated along the flight legs. The lower flights were taken over the upslope near the crest ($200 < y < 260$ km of Figure 5.19) where production of supercooled liquid hydrometeors was active. It is difficult to compare directly from this figure. All the simulations show average profiles similar to Woods et al. between 10 to 20 minutes of simulation. Also, even though starting from the same initial distribution of ice particles, one can see clear differences among the efficiency models. The average mass content for LP2 and

LL2 are very similar because LP2's efficiency model gives unit efficiency once ice particles become aggregates. In contrast to those two cases, LS2 shows two maximums from 10 minutes with slower downward shift of these peaks. LC2 and LD2 show the second peak around 5 km because of the smaller modeled efficiencies at the level compared to LL2 and LP2, while aggregation process below 4 km is as active as those.

The equivalent radar reflectivity of each grid cell was calculated by following the procedure of Woods et al. (2005) with use of simulated linear distribution for each mass bin. Vertical profiles of the horizontally averaged radar reflectivity, mass content, and precipitation rate are plotted along with standard deviation for LD2 at 10 minutes (Figure 5.21). Woods et al. (2005) reported that the upper peak is associated with vapor deposition growth of the cold-type crystals in the upper cold-frontal band, while the second peak was due to the production of dendrites and to the riming of both the dendrites formed immediately above the flight leg and the cold-type ice crystals that fell from aloft over the upslope ($200 < y < 260$ km). At this time reflectivity, mass content, and precipitation rate predicted by LD2 show the observed variability. Spatial distribution of mass content at 10 minutes is shown in Figure 5.22. The definition of diagnosed categories is based on the mass produced by the physical process (see the subsection 2.2.3). Therefore, it is easy to have sense of dominant process given location. Pristine crystals have significant mass above 6 km, leading to aggregates (aggregation) becoming significant below 6 km. Riming occurs below 6 km over crests due to the supercooled liquid hydrometeors, which make aggregates be rimed. The rimed ice particles with mass mostly produced by aggregation are indicated by rimed aggregates. The ice particles formed primarily by riming are called graupel. It can be seen that graupels reach the

two mountain crests. Since it is just 10 minutes into simulation, the predicted fields are mainly results of local microphysical processes rather than sedimentation effects. This result does not prove that SHIPS can reproduce the observed habit distribution yet. However, it suggests that aggregation and riming processes of SHIPS may be able to predict the third and six moments of PSD and mass flux in a realistically consistent way.

Concentration of diagnosed types of ice particles for LD2 at 10 minutes is shown in Figure 5.23. Compared with Figure 5.19, concentration of pristine crystals below $z=4$ km decreased. It is because they have been collected by other pristine crystals or aggregates. Concentration of the aggregates at $z=4$ km decreases from 10 L^{-1} to 1 L^{-1} by collecting aggregates each other, while more aggregates were formed in $6 < z < 8$ km from collision between pristine crystals. The high concentration of pristine crystals at $y=210$ km and $z=8$ km, and $y>300$ km and $z > 8$ km is associated with the immersion freezing nucleation process as discussed in the previous section. Concentration of diagnosed habits including all types of ice particles are shown in Figure 5.24. From Figure 5.22 and Figure 5.24 the peak of mass content at $z\sim 3$ (5) km shown in Figure 5.21 can be associated with rimed aggregates of columns (aggregates of dendrites). This is different from Woods et al. (2005)'s report. It is speculated that observed ice particles may have experienced larger sedimentation with traveling upper front or the ambient temperature associated with the front may have been colder than the sounding.

5.4.2 Comparison of simulated particle size distribution

In order to investigate simulated PSDs, the domain is divided into two sections, I: $0 < y < 200$ km, and II: $200 < y < 270$ km. Section I has less vertical motion, riming process is not active, and habit and concentration of ice particles are also horizontally uniform, whereas section II are strongly affected by vertical motion, nucleation, and riming process (see Figure 5.23 and Figure 5.24). Then, samples were taken for eight layers of 1 km depth in each section to construct PSDs. From the PSDs, vertical profiles of mean maximum dimension D_m and concentration of ice particles were calculated. Evolution of those variables for section I is shown in Figure 5.25 and Figure 5.26. Both of LP2 and LL2 show rapid increase in D_m within 20 minutes from the initial condition, while LS2 shows much smaller growth during that period. LC2 and LD2 give a D_m that is between LS2 and LL2. Also, during the 20 minutes large decrease in number concentration for LP2 and LL2 can be seen (Figure 5.26). Budget of concentration tendency for the 8 layers from LD2 at 10 minutes is shown in Table 5.4. In terms of the concentration, vapor deposition works as a sink due to evaporation of mainly small particles in each layer. Above $z=8$ km, the aggregation process is occurring, but it is compensated by depositional nucleation. This is why that the number concentration does not decrease significantly compared to the lower level. The increase of maximum dimension above 6.5 km is mainly associated with the vapor deposition process of columnar crystals as shown by following PSD analysis. Concentration for layer 6-7 km for LS2, LC2, and LD2 are quasi-steady state as well as maximum dimension. According to Table 5.4, this is because the negative tendency produced by microphysical processes (mainly aggregation) is compensated

by the sedimentation of large particles ($D > 100 \mu\text{m}$) from the above. LL2 shows a small decrease in concentration (about $20 \text{ L}^{-1} \text{ s}^{-1}$) during the 20 minutes between 4 and 6 km because the aggregation tendency is comparable to sedimentation tendency due to the small efficiency. Therefore, it is clear that aggregation efficiency can control the evolution of PSD and that sedimentation of large particles has a significant effect as well.

The data obtained from LL2 are divided into four groups according to the altitude, and analyzed as the extreme case of coalescence efficiency. The PSDs for the four levels at the initial time were obtained in section I as shown in Figure 5.27. Shown in the middle and right columns of the figure are conditional frequencies of types and habits diagnosed given the length. As specified, the slope parameter decreases with height. It can be seen that at the initial time above 6 km, irregular polycrystals dominant over the whole size spectra, at $4 < z < 6$ km the planar crystals dominant in the range of $D > 0.1 \text{ mm}$, and columnar crystals appear in the large side of the spectral at $2 < z < 4$ km. The aggregates in each layer occupy the large side of the PSD and are associated with the dominant habit. After 10 minutes (Figure 5.28), the columnar crystals grow to 0.1 mm above 8 km due to vapor deposition process indicated by the diagnosed type. PSDs, microphysical tendencies, and normalized sedimentation flux for a given size are shown in Figure 5.29. It is clear that PSD above 8 km increased the slope due to the active vapor deposition processes at the level along accompanied by depositional nucleation. As discussed above, the growth of mean maximum dimension from the initial time below 6 km is also associated with decrease of total concentration. Aggregation processes increase concentration of large particles, and also decrease concentration of small particles. It turned out that the vapor deposition and aggregation processes have a similar magnitude of negative

tendency at $D < 100 \mu\text{m}$. As seen from (g) and (j) of Figure 5.30, concentration of $D < 100 \mu\text{m}$ was reduced. Comparison of the right column of Figure 5.29 indicates that aggregation produces large particles at a given level, but those particles also have faster terminal velocity, and thus the large particles may or may not contribute to the increase of concentration of large particles at the level. Local production increases concentration of particle ($D > 1\text{mm}$) at 6-8 km (f), but sedimentation flux divergence is mostly larger than production by microphysical processes at 4-6 km (i) and (l). As the result of local production of large particles, more aggregates of dendrites appear in the largest size at $4 < z < 6$ km (i) in Figure 5.28. The sedimentation effect is indicated by higher conditional frequency of aggregates of irregular polycrystals in $0.1 < D < 1$ mm at $4 < z < 6$ km (see (h) and (i)) than at the initial time, and by virtue of the appearance of aggregates of dendrites in $0.1 < D$ mm at $2 < z < 4$ km. After 20 minutes, PSD are very similar from 10 minutes ago except for the growth of mean diameter at $2 < z < 4$ km. A more obvious difference shows up in the conditional frequency of types and habits. Higher frequency of irregular polycrystals appears in $0.1 < D < 1$ mm than 10 minutes, and aggregates of dendrites and columnar crystals dominate the large size ($0.2 < D$ mm) in the lowest. Note that breakup process becomes more significant in $2 < z < 4$ km than vapor deposition process, which indicates that proper parameterization of breakup process is a priority.

Next, PSDs, types and habits predicted with LS2 are discussed as the slowest extreme of coalescence efficiency. At 10 minutes, PSDs for LS2 in $z > 8\text{km}$ show similar PSD, and conditional frequency of habits and types, and the same explanation can be done as LL2 (Figure 5.30). However, in $6 < z < 8$ km concentration of large particle $2 < D$ mm actually

decreases from the initial time, while it increased for LL2. This indicates that aggregation process is not large enough to compensate sedimentation for LS2 as shown in (e) and (f) of Figure 5.31. Also for LS2, PSDs in $z < 6$ km show decrease of concentration of particles in $D < 0.1$ mm due to vapor deposition and aggregation in the size (see (h) and (k)). Because of the less active aggregation process, production of large aggregates in upper levels is low. Similarly, the concentration flux of large particles from the above, comparing right column of Figure 5.29 and Figure 5.31, is low. This is why aggregates of irregular polycrystals and those of dendrites do not appear to be as frequent as in LL2 at $4 < z < 6$ km and $2 < z < 4$ km, respectively ((i) and (l) of Figure 5.31). Correspondingly, aggregates of columnar crystals can be seen at $2 < z < 4$ km; large end of size spectrum of LS2 has higher frequency of being occupied with the aggregates of habits that are locally produced in the layer than LP2. Thus, aggregation efficiency models affect the habit frequency obtained at a given level. In other words, conditional frequency of habits and types with PSDs should be able to provide useful information on the aggregation efficiency in stratiform clouds.

The evolution of PSDs in section II is described briefly. As shown in Figure 5.23, the high concentration of aggregates at $z = 6$ km and $y = 210$ km corresponds to the active immersion freezing nucleation in the area, which supply high concentration of particles to the initially existing aggregates at the level. Then, riming process are active in $2 < z < 6$ km due to the available supercooled liquid hydrometeors. This can be seen in the average PSD for section II (Figure 5.32). At $6 < z < 8$ km the PSD has higher concentration of large aggregates ($D > 2$ mm) with higher concentration of small crystals due to more active nucleation, vapor deposition and aggregation processes than section I, which makes the PSD looks more super-

exponential. According to the conditional frequency, in $4 < z < 6$ km ($2 < z < 4$ km) the size larger than 3 mm (0.8 mm) are made up of mostly rimed particles. In terms of habit frequency, the main difference is the appearance of planar polycrystals in $6 < z < 8$ km, which corresponds to water saturated environment in the area.

5.4.3 Comparison of PSDs with observation

One way to examine the evolution of particle size distribution (PSD) by microphysical processes is to access parameters of the exponential or gamma distribution fitted to the samples. This study uses the method of moments by Heymsfield et al (2002) to estimate the parameters, which have more weights in large particles. The slope λ and intercept N_0 parameters of exponential size distribution, $N(D) = N_0 \exp(-\lambda D)$, fitted to the horizontally averaged PSD in the entire domain for the five cases are shown in Figure 5.33 and Figure 5.34, respectively. Evolution of the parameters corresponds to the mean maximum dimension and number concentration shown in Figure 5.26 through $D_m = 1/\lambda$ and $N = N_0/\lambda$ if the distribution is adequately approximated to be an exponential distribution. The slope and intercept parameters for LS2 and LD2 show a flat vertical distribution around $z = 6$ km. This is related to positive concentration tendency in these layers. All the simulations show convergence of concentration flux at those levels due to high sedimentation flux of small particles that were produced by active immersion freezing and depositional nucleation processes above. LS2 and LD2 have similarly small efficiency ~ 0.1 at these levels, so that resulting mean maximum dimension is less than the others. However, for LL2, LP2, and LC2 the aggregation process tendency is

large enough to consume that small particles and create large particles, which decrease λ and N_0 .

According to Table 2 of Garvert et al. (2005a), the parameters fitted to the observed PSD along flight tracks are $\lambda = 26.7, 24.62, 23.09, 23.23,$ and 25.55 (cm^{-1}) and $N_0 = 0.278, 0.218, 0.237, 0.316,$ and 0.494 (cm^{-4}) at 6, 5.7, 5.4, 5.2, and 4.9 km, respectively. Woods et al. (2005) suggest that the observed PSDs show increase of small particles with decrease of height due to possible vapor deposition and nucleation processes at that level. SHIPS suggests that the increase is caused by the active nucleation above, sedimentation flux convergence of the particles, and somewhat inefficient aggregation processes to remove the small particles. The simulated profiles of mass content, radar reflectivity and precipitation moderately agree with observation at 10 minutes of simulation for LL2, LP2, LC2, and LD2 (20 minutes for LS2). The parameters at this time are shown in Table 5.5 for quantitative comparison. The slope parameters of LS2, LC2 and LD2 agree with observation in $5 < z < 6$ km, while the intercept parameters of LP2 and LL2 are closer to observed ones. However, qualitatively speaking, LL2, LP2 and LC2 are different from observation in terms of the flatness of these parameters in vertical direction (see Figure 5.33 and Figure 5.34). By comparing Figure 8 of Garvert et al (2005a) and Figure 5.28, Figure 5.30, and Figure 5.32, LP2 and LL2 appear to be missing small particles. PSDs shown in Figure 12 of Woods et al (2005) and Figure 8 of Garvert et al (2005a) have the particles in $D < 0.1$ mm. It is interesting to note that even PSD observed at $2.5 < z < 4$ km over the upwind of crest has a mode in the small size. The lack of particles in $D < 0.1$ mm at low levels in the simulations suggest that deposition-condensational nucleation has to be more active in warm temperature regime ($T < -15^\circ \text{C}$), or that other nucleation

processes are required such as secondary nucleation by collision breakup . Rauber (1987) suggests that cloud ice crystal concentrations may be enhanced by fragmentation during crystal-crystal collisions in snowfall events that are characterized by a large dendrite population. Breakup by turbulence alone may occur for fragile crystals: Griggs and Choulaton (1986) show that dendrites formed on a fixed surface can break up by air current of 2 m s^{-1} . The implication of this in an orographic storm is that dendrites that formed upwind in relatively calm condition can be horizontally advected into area of strong vertical motion, and that they subsequently result in breakup. A parameterization of such breakup may be possible with the use of TKE. Since the observation shows dendrites and their aggregates at 4 km, the fragments may have been left at that altitude without falling and may have contributed to the increase of N_0 .

5.4.4 Trajectory analysis

This subsection discusses evolution of simulated PSDs along trajectories in order to further validate modeled aggregation process and interlocking efficiency models. The trajectories are calculated with the predicted horizontal wind fields and constant downward vertical velocity of 1 m s^{-1} to imitate the Lagrangian spiral decent. The area of interest is the section I ($0 < y < 200 \text{ km}$) where riming process is not active, and microphysical processes are approximately horizontally homogeneous. As shown in Figure 5.35, 10 trajectories started from $y=0.5 \text{ km}$ and $z=7 \text{ km}$ by 11 km apart at 150 s (same as one in the subsection 5.3.3) and they are almost identical among the 5 simulations because the trajectory does not depend on microphysical processes. For each trajectory average PSDs were obtained by considering a

box of 1 km in vertical and 5 km in horizontal centered on the trajectory. The slope parameters of exponential size distribution fitted to the average PSDs are shown in Figure 5.36. Empirical relationships of the slope parameter on temperature of Heymsfield et al. (2002) and Houze et al. (1979) are also shown by thick solid curve and thick dashed curve, respectively. The dotted curves indicate Heymsfield et al. (2002)'s fit to mean \pm one standard deviation of the data. Heymsfield et al. (2002)'s curves are based on samples taken in deep stratiform cloud layers in subtropics and tropics, while Houze et al. (1979) constructed the curve based on precipitating frontal clouds in midlatitude cyclones. It can be seen that the physical-based interlocking cases, LP2, LC2, and LD2 predict dependence of the slope parameter that is confined within the one standard deviation of the Heymsfield et al. (2002)'s data. LS2 shows almost no dependence on temperature warmer than -20°C . LL2 indicates the fastest evolution of the slope parameter compared to the other cases, and they are somewhat smaller than Houze et al. (1979)'s curve. Field (1999) discusses that the rapid decrease of the slope parameter at -15°C is due to the enhancement of aggregation process by dendritic crystals at the level. However, these simulations do not give a clear indication of such decrease in the slope parameter. LS2 may suggest that efficiency should be at least larger than 0.1 in $T > -20^{\circ}\text{C}$.

It is known in the literature that the relationship between the slope and intercept parameters of exponential PSDs indicates dominant microphysical processes. θ ($N_0 \propto \lambda^{\theta}$) has been shown to be $2 < \theta < 3$ in the active aggregation zone of deep stratiform cloud layers (e.g., Lo and Passarelli, 1982; Mitchell, 1988; Field, 1999; Wolde and Vali, 2002). Lo and Passarelli (1982) pointed out that constant θ means conservation of $\theta - 1$ th moment of

exponential PSD. Field and Heymsfield (2003) showed that θ becomes constant in steady-state (precipitation is constant) aggregation-only clouds based on scaling theory of general aggregation phenomena. The relationship between the two parameters N_0 and λ fitted to simulation of LD2 is shown in Figure 5.37. The gradient in the log-log plot corresponds to θ . It can be seen that the gradient of most of trajectories are about 2 before the trajectory reaches around $T = -15^\circ\text{C}$, and it increases to approximately 3 ~ 4 after that temperature, depending on the trajectory. The inflection is expected from the way that interlocking efficiency of LD2 was modeled based on dendritic arm lengths. It suggests that the total maximum dimension (1st moment) is conserved before the trajectories reach $T = -15^\circ\text{C}$ and after that the total area or mass (2nd and 3rd moments) is conserved on the trajectories.

N_0 vs λ is compared for all the simulations in Figure 5.38. The gradients θ were calculated with the two parameters obtained from 10 trajectories and $T < -3^\circ\text{C}$ as shown in Table 5.6. LS2 predicted the gradient of approximately 2 and showed much slower evolution of those parameters than the others. LC2 shows inflection points similar to LD2 around $T = -15^\circ\text{C}$, but LL2 and LP2 do not. The efficiency model of LP2 is not sensitive to the ice crystal habit once it forms aggregates. Since the simulation was started from the initial distribution of ice crystal and aggregates, LP2 does not show the inflection points. All the cases except for LS2 reached $\sim 10\text{ cm}^{-1}$ at the melting layer, which is the value of intercept generally considered to be the minimum in stratiform clouds. Field and Heymsfield (2003) derived an empirical relationship between precipitation rate P and θ by using TRMM, ARM, and FIRE I field observations (see Fig. 7 of their paper):

$$\hat{\theta} = \exp[-1.43 \log_{10}(7P)] + 2.8, \quad (5.2)$$

whereas $\hat{\theta} = 5$ for $P < 0.04$ mm hr⁻¹. First, P was obtained by averaging precipitation rate every 10 minutes for 10 trajectories. By substituting P into the equation, $\hat{\theta}$ for aggregation-dominant steady state clouds was calculated (Table 5.6). The estimates turned out to be somewhat larger than actually predicted with SHIPS. The uncertainty of $\hat{\theta}$ is estimated to be ± 0.6 , according to Field and Heymsfield. Therefore, all cases except for LS2 and HD2 are within the uncertainty for the trajectories starting from the initial time.

More trajectories were started from 2 and 4 hours of simulation at the same position as the above. Also, simulations with IN concentration of 230 and 10 L⁻¹ (HD2 and MD2) were implemented to see any effects of IN concentration. As shown in Table 5.6, all the fitted θ and predicted P except for LS2 and HD2 became smaller than those for the trajectories started in the previous time, and θ and P are positively correlated. Actually, these two parameters were related negatively by Field and Heymsfield (Equation (5.2)). HD2 gives negative correlation between θ and P . Furthermore, growth of the mean mass by each process along the trajectories was investigated. The trajectories, except for HD2, starting at 2 hour and 4 hour indicated that the mean mass growth by aggregation (by decreasing concentration) was less than vapor depositional growth by factor of 10 except for the trajectories near inflow boundary. On the other hand, HD2 still experienced the comparable magnitude of aggregational growth to vapor depositional growth even for trajectories starting at 2 hour simulation because it has high concentration of ice crystals available for aggregation process. Therefore, the discrepancy from Field and Heymsfield's empirical relationship can be

attributed to the existence of steady-state aggregation-dominant cloud layers. It is not clear why fitted θ is much smaller than their estimates for HD2.

Simulations without all microphysical processes except melting and without only aggregation process were also carried out to make sure the relationship between two parameters was produced by mainly aggregation processes. Indeed, the relationship predicted without all microphysical processes stays nearly at one point, and one without aggregation process evolves less than even LS2.

Overall, the above comparisons with observations are not sufficient to determine the aggregation efficiency. However, SHIPS proved that it has ability to realistically predict the evolution of PSDs in stratiform cloud layers and predicted habit and type information can be used in the efficiency model. The size and concentration required to reach aggregation-dominant steady state are not known in literature, although the moments of PSDs in aggregation-dominant clouds have been documented (e.g., Field et al., 2005). They should be studied to understand the evolution of PSDs as well as to validate the aggregation initiation of SHIPS.

5.4.5 Effect of aggregation efficiency, prediction of length, and IN concentration on precipitation

Trajectories calculated with mass weighted terminal velocity turns out to be largely affected by the aggregation efficiency, which make sense because the mass weighted terminal velocity mainly follow large particles produced by aggregation process in this case study. Ten trajectories were calculated in the same way as the above subsection for LS2, LL2 and LD2,

but by using mass-weighted terminal velocity. As shown in Figure 5.39, it is clear that the high efficiency of LL2 leads to faster growth and therefore the ice particles fall faster than the other trajectories. Also, due to the fastest growth, ice particles in the trajectories spend less time in the up and down vertical motion of gravity waves caused by the topography. In contrast, trajectories of LS2 travel the most due to the lowest efficiency of aggregation process. The trajectories of LP2, LS2, and LL2 reach melting level at about 110, 150, and 90 minutes, respectively. Therefore, the aggregation efficiency affects spatial distribution of precipitation, but the question is how much.

The spatial distribution of 6 hour accumulation is shown in (a) and (b) of Figure 5.40. (a) of the figure compares the accumulation among the different efficiency models and degraded version of SHIPS. (b) of the figure compares simulations with different IN concentrations with the efficiency model D. The precipitation in $0 < Y < 100$ km is mostly associated with ice particles in lower and middle levels ($z < 5$ km) of west boundary condition. Since the layer $4 < z < 5$ km has dendrites and this area ($2 < z < 5$ and $0 < y < 50$ km) has little contribution from nucleation over the trajectories, the precipitation is largely affected by the efficiency models. LD2 produced the largest and steepest accumulation over the area, and then LL2, LP2, and LC2 show similarly narrow concentration of precipitation. As expected, LS2 produced flat, widely distributed accumulation over the area. It is speculated that LD2 can keep the high concentration of pristine crystals or aggregates due to the low efficiency for non-dendritic crystals in the beneath of dendritic region, and then the aggregates of dendrites fall into the lower levels and the collection rate can be higher than the other efficiency models due to the high concentration of available particles. In case of LS2, the ice particles do not

grow fast, which results in slower sedimentation and more downwind transport of ice particles. The degraded version of SHIPS (DLD2) stays somewhere between LS2 and LD2 in the area.

The accumulation in $100 < y$ km is associated with ice particles in $z > 5$ km at the inflow boundary and nucleated particles in the domain. Due to the consumption of moisture upwind and advection and sedimentation of irregular polycrystals from above, few dendrites existed over $100 < y$ km except for the first 90 minutes. All simulations show a similar magnitude of accumulation at $y=190$ km. However, the difference becomes more significant in $y > 220$ km where the falling ice particles experience fluctuation in vertical motion and thus moisture conditions. This can be explained by the growth rate of aggregates and terminal velocity. Riming process in $z < 4$ km will preferably enhance the terminal velocity of larger particles. LL2 has the highest efficiency, so the ice particles can grow and fall quickly against the upward motion above the valley ($y \sim 210$ km). DLD2 always diagnoses any ice particles as dendrites in the dendritic growth region ($-16 < T < -12^\circ \text{C}$ and water saturated condition), which leads to constant enhancement of formation of aggregates in the layer over the three crests ($220 < y < 275$ km). In turn, faster falling particles were produced by subsequent riming process, and led to high accumulation over the two crest ($y=245$ km and $y=270$ km).

HD2 shows similar magnitude of accumulation at $y=220$ km ($y=245$ km) to LL2 (DLD2), while the accumulation in the valley ($y=260$ km) is less than LD2 and MD2. From the trajectory analysis, it is speculated that the accumulation at $y=270$ km is largely affected by active immersion freezing process at $y=210$ km and $z > 6$ km, so that the accumulation is least sensitive to IN concentration. On the other hands, the accumulation at the upstream two crests ($y=220$ and $y=245$ km) indicates large sensitivity to IN concentration.

Domain average 6 hour accumulation is shown in Table 5.7. Amount of melt ice particles reaching the ground is sensitive to the choice of the efficiency models and IN concentration. However, the variation of total precipitation is within 10 % of the amount. Therefore, it is speculated that error associated with aggregation efficiency model, habit prediction and IN concentration can cause error to similar degree in spatial distribution of precipitation over mountainous regions with high concentration of supercooled droplets as well as the area where potentially dendrites may exist.

5.5 Summary and conclusions

Two-dimensional idealized simulations were conducted with the cloud-resolving model, UW-NMS. An orographic winter storm over the Oregon Cascade observed during IMPROVE-2 campaign was chosen as a case study. The simulations without ice particle initialization and without riming process showed followings:

1. Aggregation initiation was primarily function of concentration of ice crystals. The effect of terminal velocity difference and cross section area were secondarily important.
2. IN concentration was simulated to have impact on aggregation initiation. The direct effect is through production of the concentration of collector and collected particles. The indirect effect is through change of cross section area by vapor competition. High concentration of IN can lead to depletion of supercooled liquid hydrometeors which could be used for freezing nucleation processes. Low concentration of IN can produce large ice particles by vapor deposition, which may act as collectors in active

nucleation area. Combination of the immersion freezing nucleation and advection of collector ice particles was speculated to be important for small and medium cases of IN concentration.

3. The interlocking efficiency model was able to enhance aggregation initiation given that there is sufficient concentration of ice crystals.
4. Formation of spatial dendrites was modeled through sedimentation of irregular polycrystals into the dendritic zone. They triggered aggregation through the modeled collection efficiency and because of the high concentration nucleated by immersion freezing above the dendritic zone. The pathway to spatial dendrites through sedimentation should be studied in the laboratory because the habit may play an important role in the initiation of aggregation with large planar dendrites.
5. The trajectory analysis showed that habits and types of ice particles predicted in SHIPS can be used as marker of growth history or origin of particle to study the evolution of size distribution.
6. From the ice nucleation process, SHIPS was able to reproduce sub-exponential distribution that consists of pristine crystals and aggregates. The slope and intercept fitted to the predicted PSDs show moderate agreement with observed ones.

The habit frequency analysis was carried out for simulations with all microphysical processes on in order to study effects of aggregation and riming on the frequency. The resulting frequency in terms of number concentration was qualitatively similar to the one obtained with only vapor deposition process except for $T > -10^{\circ}\text{C}$. In the warm temperature, faster sedimentation of aggregates of plates may have resulted in the increase of frequency of

plates. The cases with small IN concentration had high frequency of columnar crystals because active riming process triggered active secondary nucleation process in the temperature. The case with high concentration of CCN shows high concentration of columnar crystals in $T < -30^{\circ}\text{C}$ because nucleated polycrystals were still able to change the growth mode to columnar crystals. SHIPS showed a dependence of simulated mass content of aggregates on the habits produced by freezing nucleation. The average PSDs obtained in the wave cloud section had multiple modes that were similar to typically observed. The inflection points of the PSDs were associated with change of dominant type of ice particles from pristine crystals to aggregates.

Simulations using the initial ice particle distribution to represent the effects of a “seeder” cloud were implemented. The main results are the followings:

1. The simulation with unit efficiency showed the fastest change of concentration and maximum dimension in $z < 6$ km, while the case with lowest constant efficiency indicated the slowest change. Results of three physical-based efficiency models lay in between. Agreement of 10 to 20 minutes simulation with observations suggests that aggregation and riming processes of SHIPS may be able to predict the third and six moments of PSD and mass flux in a realistically consistent way. However, the simulated crystal habit and particle type were located somewhat upward compared to observation at the time.
2. A budget analysis of concentration tendency showed that aggregation efficiency can in fact control the evolution of the PSD and that sedimentation of large particles has a significant effect as well. Concentration and mean maximum dimension of PSDs in

the vertical layer of 6-7 km and $y < 200$ km showed quasi-steady state due to balance between these two processes.

3. It was quantitatively shown that aggregation process produces large particles at a given level, but those particles also have faster terminal velocity, and thus the large particles may or may not contribute to the increase of concentration of large particles at the level. The breakup process became more significant in $2 < z < 4$ km than vapor deposition process, which indicates that proper parameterization of breakup process is important.
4. It was shown that aggregation efficiency models affect the habit frequency obtained at a given level. Thus, analysis of the conditional frequency of habits and types with PSDs should be able to provide useful information on the aggregation efficiency in stratiform clouds.
5. SHIPS suggests that the observed increase in concentration of small particles is caused by the active nucleation above, sedimentation flux convergence of the particles, and somewhat inefficient aggregation process to remove the small particles. However, breakup processes can be another explanation for the increase because it was observed close to dendritic growth region. The lack of particles in $D < 0.1$ mm at low levels in the simulations suggest that deposition-condensational nucleation has to be more active in warm temperature regime ($T < -15^\circ\text{C}$), or that other nucleation processes are required such as secondary nucleation by collision breakup
6. The stochastic collection approach to habit prediction was able to predict the relationships between intercept and slope parameters of exponential PSDs that are

generally observed in deep stratiform cloud layers. All efficiency models but 0.1 efficiency case agree with an empirical dependence of the slope on temperature. It is speculated that efficiency should be at least larger than 0.1 in $T > -20^{\circ}\text{C}$. The predicted habit and type information were shown to be able to be used in efficiency model.

7. Uncertainties associated with aggregation efficiency model, habit prediction and IN concentration can modulate spatial distribution of precipitation to the same degree (<10 %). The affected areas were mountainous regions with high concentration of supercooled droplets as well as the area where dendrites existed.

Some of the above experiments exhibited multi-modal PSDs. It has to be examined more in details if SHIPS can produce typically observed two modes in PSDs in cirrus clouds, orographic wave clouds or stratiform clouds in cloud-resolving simulations, and the mechanisms should be studied quantitatively. Along with it, habit frequency analysis should be conducted and the discrepancy with observations has to be resolved. The habits nucleated by the immersion and homogeneous freezing processes affected aggregation production. Therefore, the habits nucleated from the freezing process and any difference in nucleated habits from deposition nucleation should be investigated in laboratory. The size and concentration of ice particles required to reach aggregation-dominant steady state are not known in literature. They should be studied to understand the evolution of PSDs as well as to validate the aggregation initiation of SHIPS.

Currently, SHIPS is undergoing tests with Arctic boundary layer clouds, and convective clouds. Extension of the cloud-resolving simulation to three dimensions is underway with

parallelization of codes. Finally, outputs from SHIPS are being applied to radiative transfer calculation. Use of the forward calculation can show and validate the value of predicting habits and types of ice particles with SHIPS.

References, Chapter 5

- Bailey, M. and J. Hallett, 2004: Growth rates and habits of ice crystals between -20° and -70° C. *J. Atmos. Sci.*, 61, 514–543.
- Field, P. R., 1999: Aircraft Observations of Ice Crystal Evolution in an Altostratus Cloud. *J. Atmos. Sci.*, 56, 1925–1941.
- , and A. J. Heymsfield, 2003: Aggregation and scaling of ice crystal size distribution. *J. Atmos. Sci.*, 60, 544–560.
- , R. J. Hogan, P. R. A. Brown, A. J. Illingworth, T. W. Choullarton, and R. J. Cotton, 2005: Parameterization of ice-particle size distributions for mid-latitude stratiform cloud. *Quart. J. R. Met. Soc.*, 131, 1997–2017.
- Garvert, M., B. A. Colle, and C. F. Mass, 2005a: The 13-14 December 2001 IMPROVE-2 event. Part I: synoptic and mesoscale evolution and comparison with a mesoscale model simulation. *J. Atmos. Sci.*, 62, 3474–3492.
- , C. P. Woods, B. A. Colle, C. F. Mass, P. V. Hobbs, M. T. Stoelinga, and J. B. Wolfe, 2005b: The 13-14 December 2001 IMPROVE-2 event. Part II: comparisons of MM5 model simulations of clouds and precipitation with observations. *J. Atmos. Sci.*, 62, 3520–3534.
- Heymsfield, A. J., A. Bansemer, P. R. field, S. L. Durden, J. L. Stith, J. E. Dye, W. Hall, and C. A. Grainger, 2002: Observations and parameterizations of particle size distributions in deep tropical cirrus and stratiform precipitating clouds: results from in situ observations in TRMM field campaigns. *J. Atmos. Sci.*, 59, 3457–3491.
- Houze, R. A., P. V. Hobbs, P. H. Herzergh, and D. B. Parsons, 1979: Size distributions of precipitation particles in frontal clouds. *J. Atmos. Sci.*, 36, 156–162.
- Kikuchi, K., and H. Uyeda, 1979: On snow crystals of spatial dendritic type. *J. Meteor. Soc. Japan*, 57, 282–287.
- Mitchell, D. L., 1988: Evolution of Snow-Size Spectra in Cyclonic Storms. Part I: Snow Growth by Vapor Deposition and Aggregation. *J. Atmos. Sci.*, 45, 3431–3451
- , S. K. Chai, Y. Liu, A. J. Heymsfield, and Y. Dong, 1996: Modeling cirrus clouds. Part I: treatment of bimodal size spectra and case study analysis. *J. Atmos. Sci.*, 53, 2952–2966.

- Lo, K. K., and R. E. Passarelli, 1982: The Growth of Snow in Winter Storms: An Airborne Observational Study. *J. Atmos. Sci.*, 39, 697–706.
- Rauber, R. M., 1987: Characteristics of cloud ice and precipitation during wintertime storms over the mountains of northern Colorado. *J. Appl. Meteor.*, 26, 488-524.
- Wolde, M., and G. Vali, 2002: Cloud structure and crystal growth in nimbostratus. *Atmos. Res.*, 61, 49-74.
- Woods, C. P., M. T. Stoelinga, J. D. Locatelli, and P. V. Hobbs, 2005: Microphysical processes and synergistic interaction between frontal and orographic forcing of precipitation during the 13 December 2001 IMPROVE-2 Event over the Oregon Cascades. *J. Atmos. Sci.*, 62, 3493–3519.

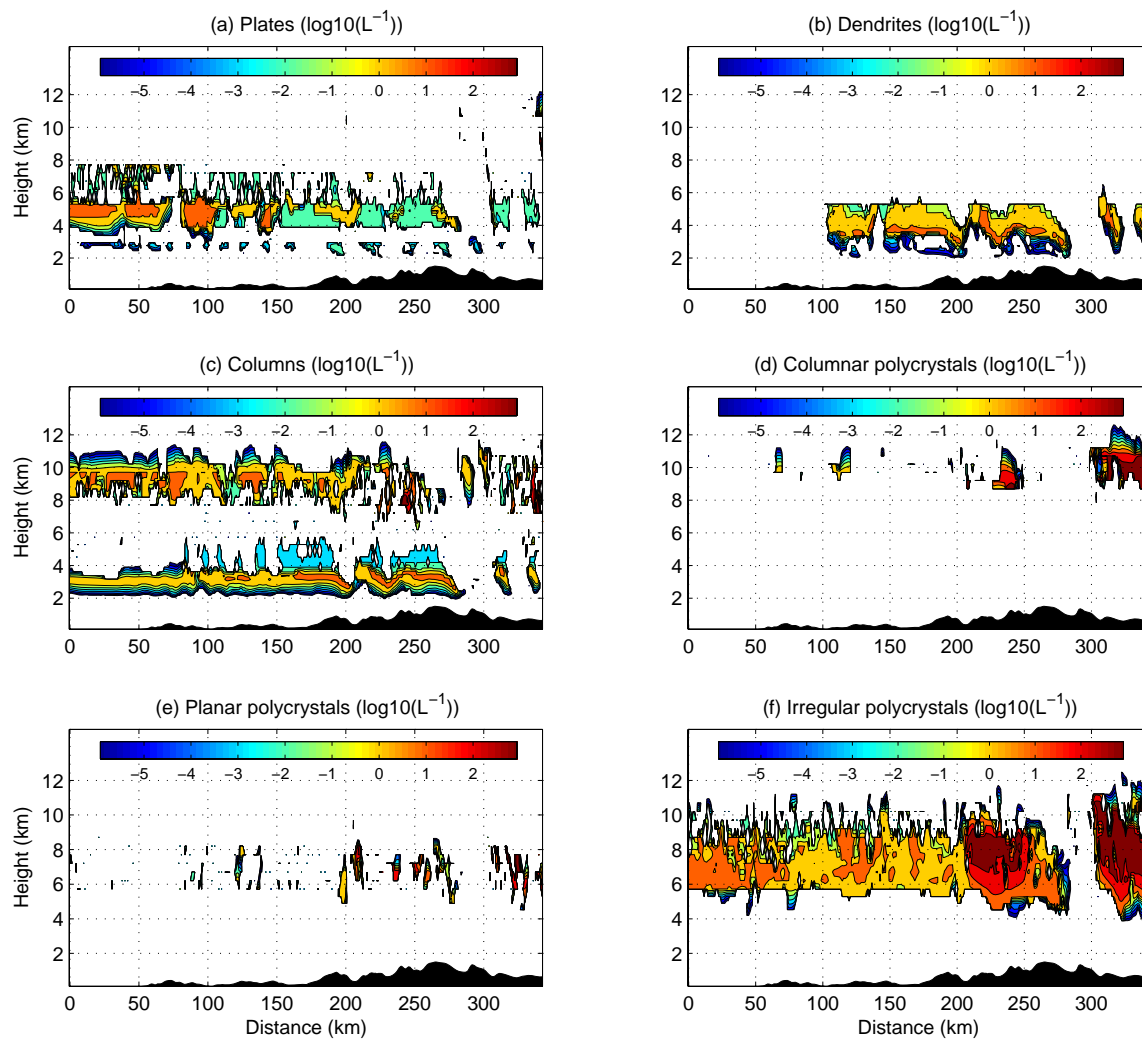


Figure 5.1 Diagnosed habits of all ice particles for MS1 at 20 minutes.

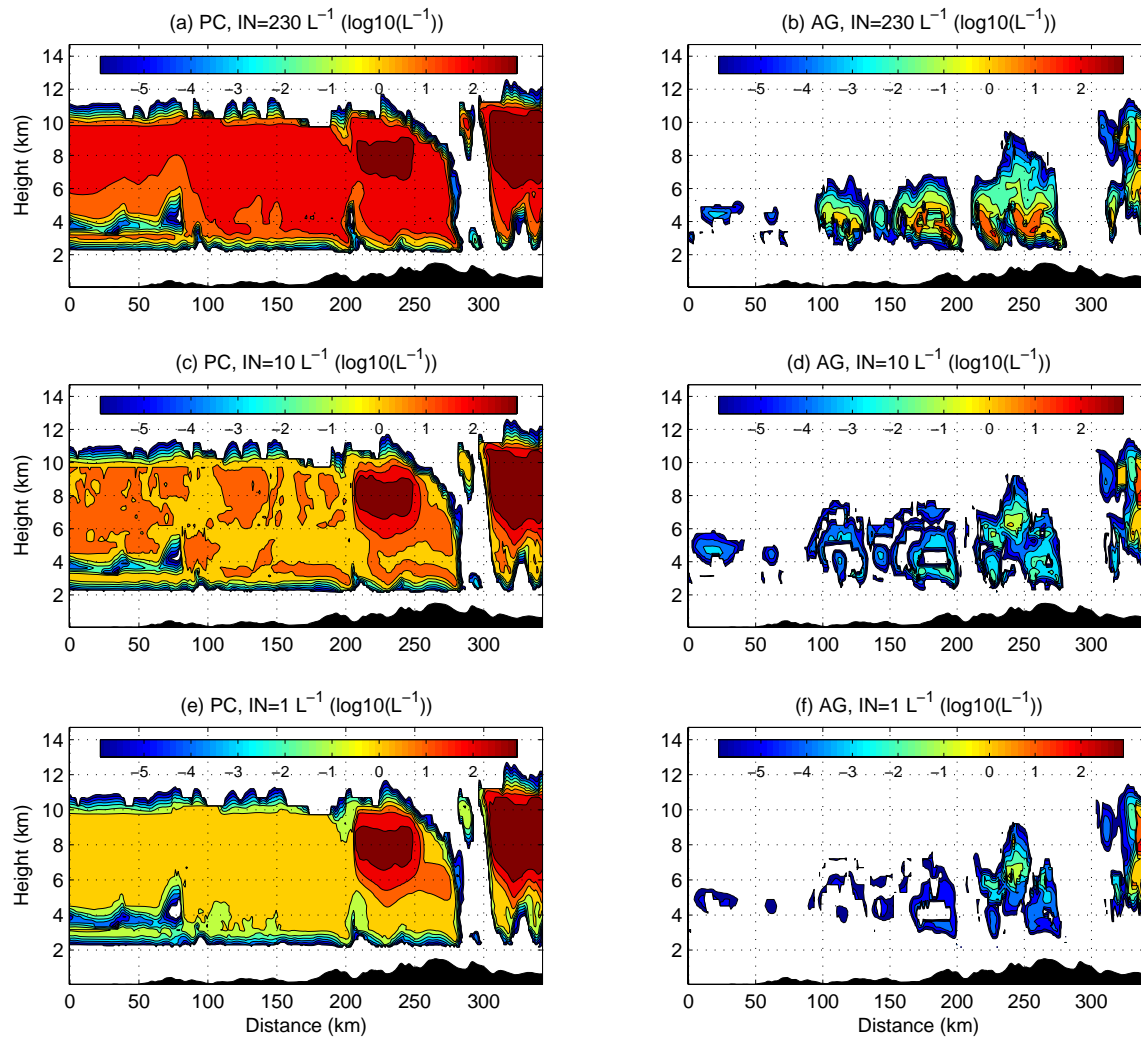


Figure 5.2 Comparison of concentration of diagnosed pristine crystals and aggregates among different IN concentrations with constant efficiency of 0.1 at 20 minutes. (a) and (b) are pristine crystals and aggregates for 230 L^{-1} (HS1), (c) and (d) for 10 L^{-1} (MS1), and (e) and (f) for 1 L^{-1} (LS1).

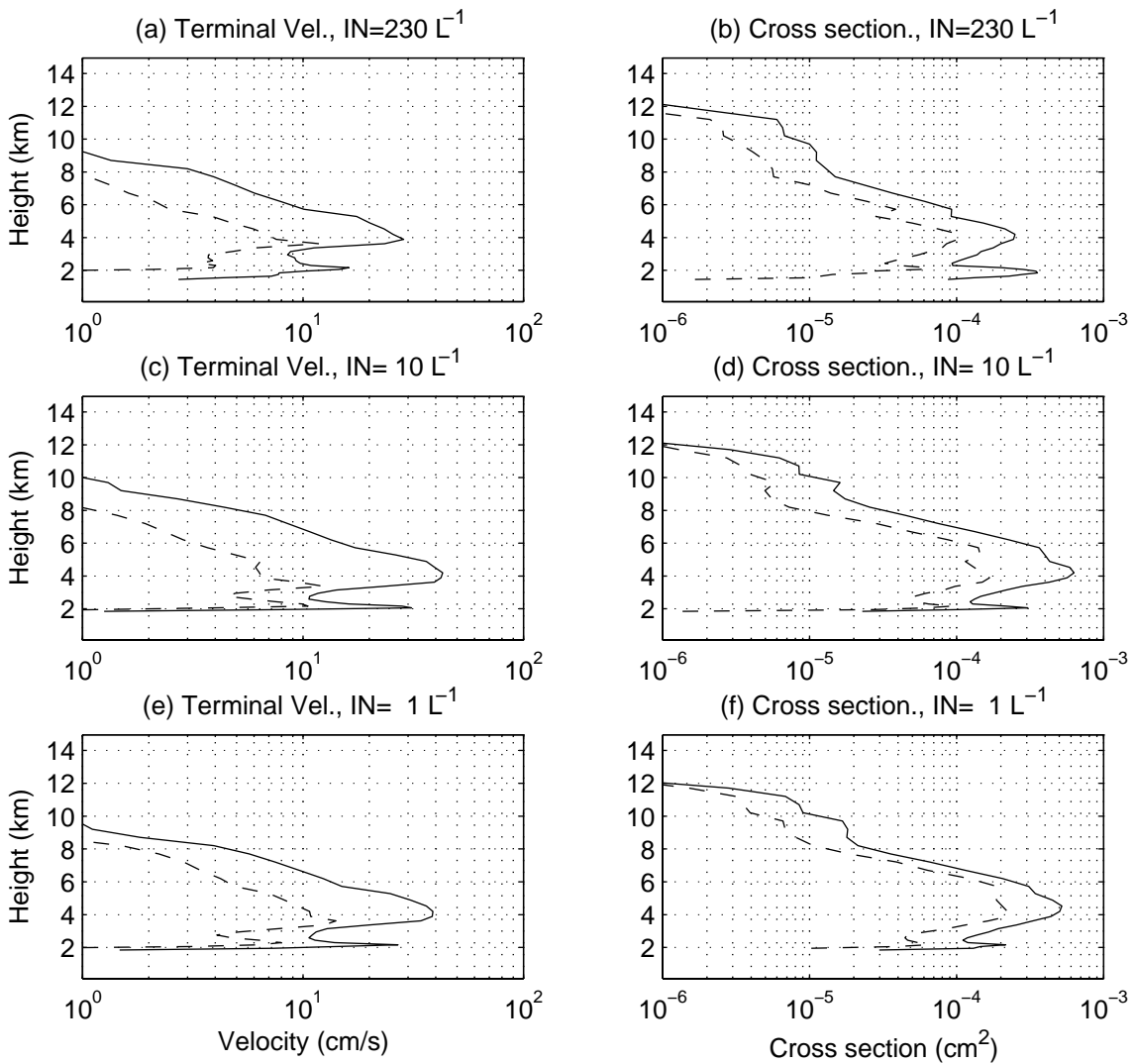


Figure 5.3 Horizontal average of mean (solid line) and standard deviation (dashed line) of terminal velocity and cross section area at each grid cell at 20 minutes.

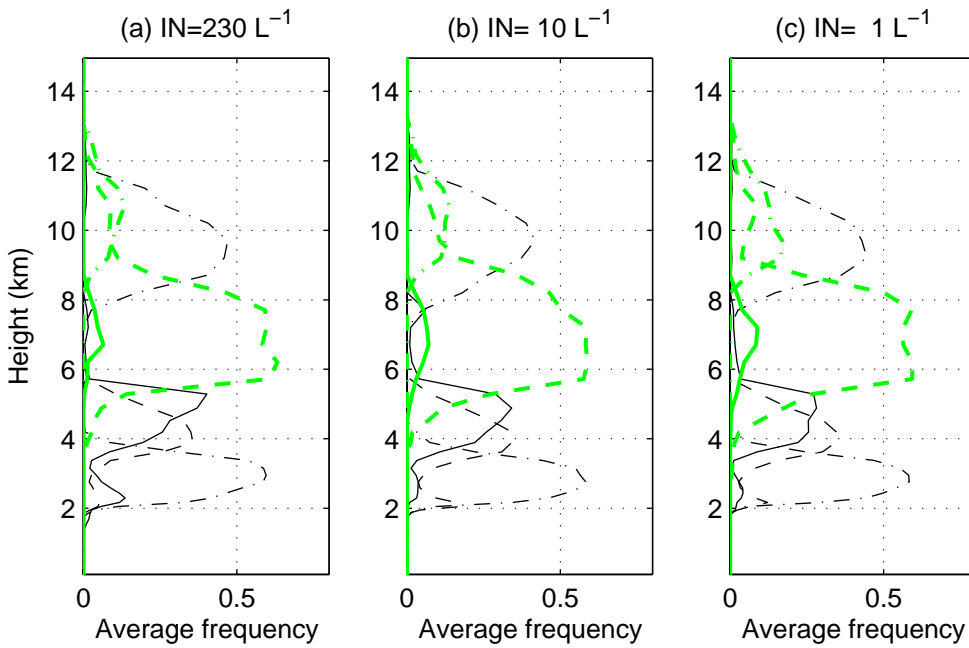


Figure 5.4 Horizontally averaged frequency of habits in terms of cross section area at 20 minutes. Thin solid line indicates plates, thin dashed line dendrites, thin dash-dot line columnar crystals, thick solid line planar polycrystals, thick dash-dot line columnar polycrystals, thick dashed line irregular polycrystals.

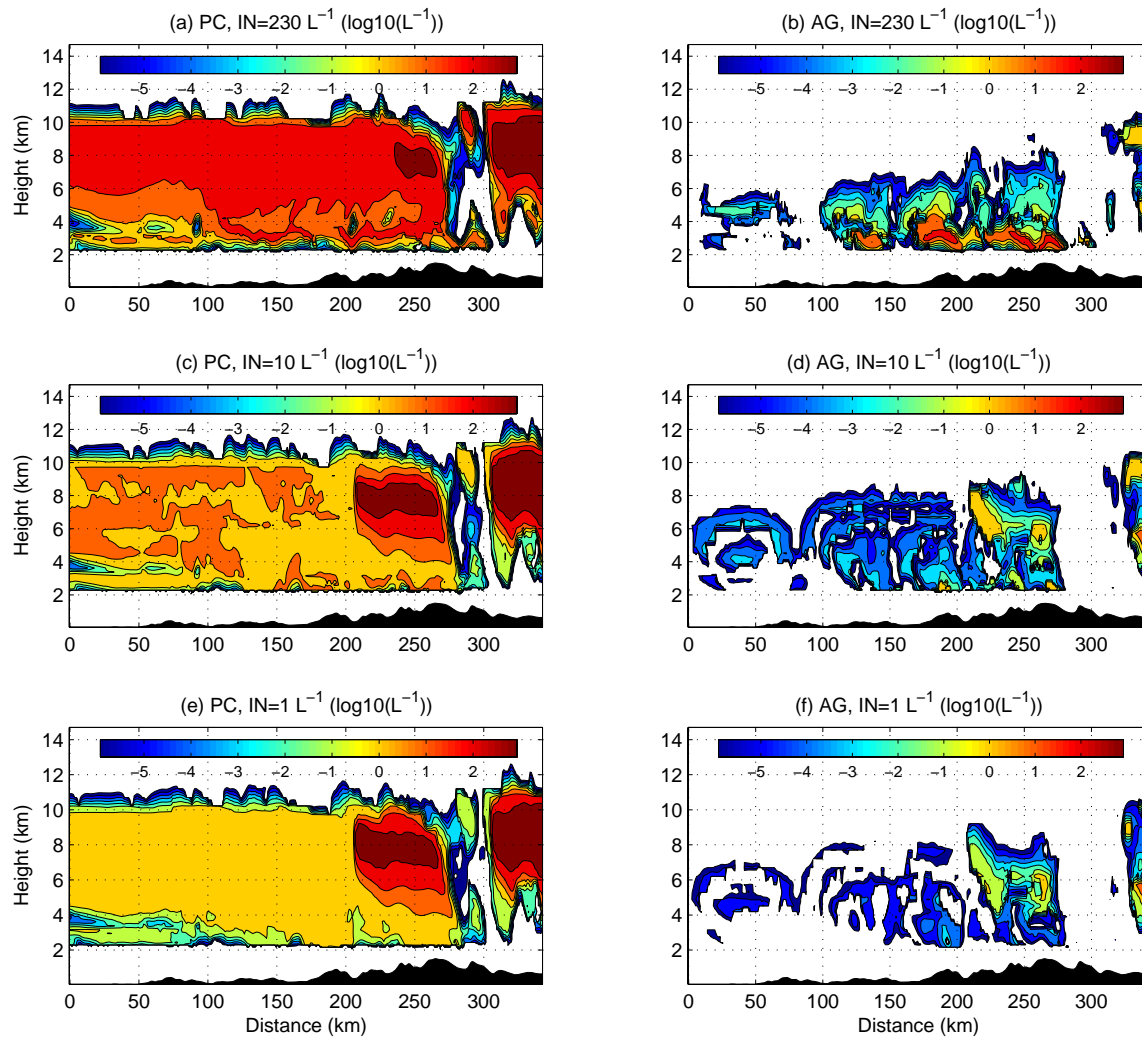


Figure 5.5 Same as Figure 3.12 except that this is a simulation at 40 minutes.

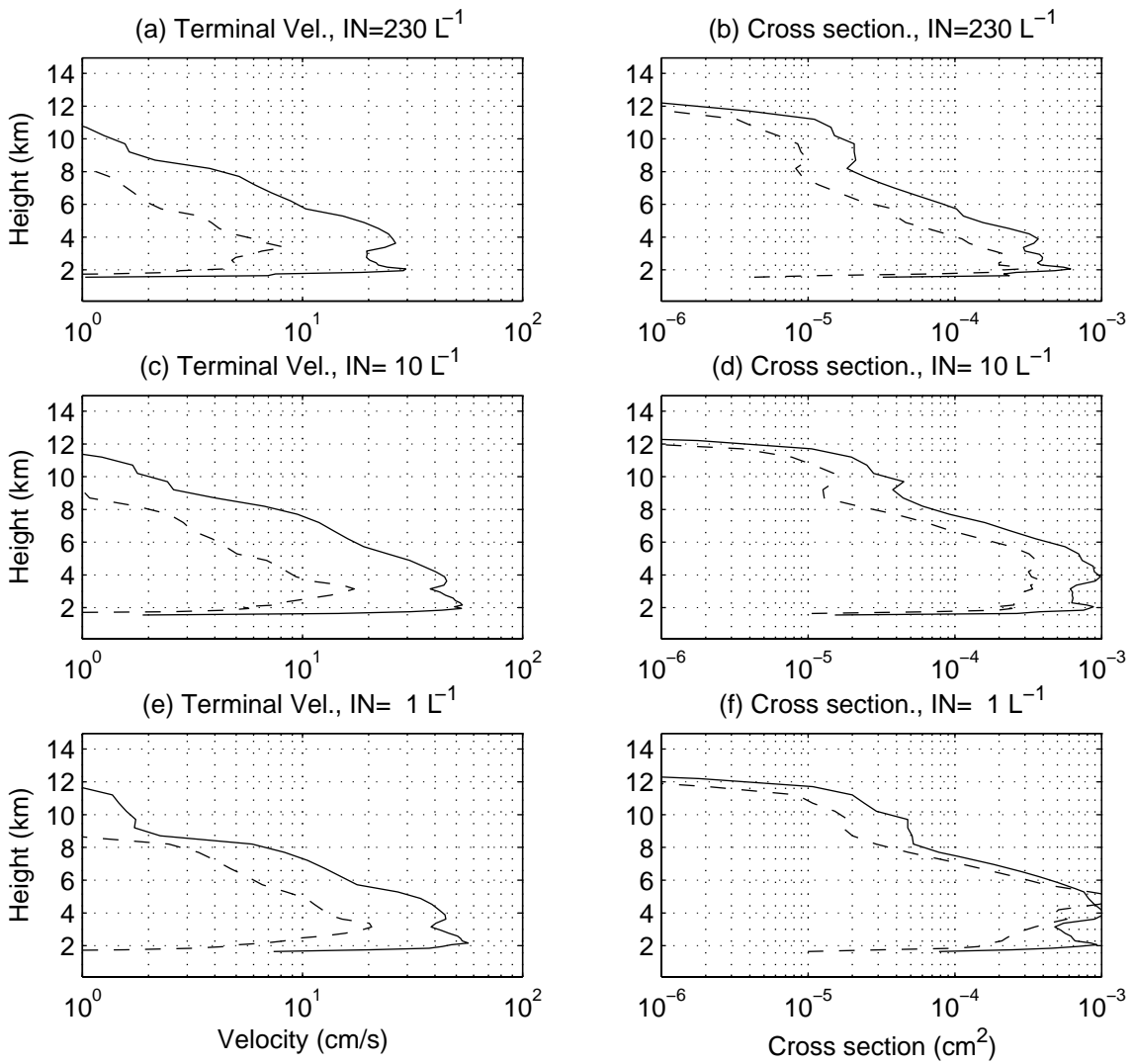


Figure 5.6 Same as Figure 3.13 except that this is at 40 minutes.

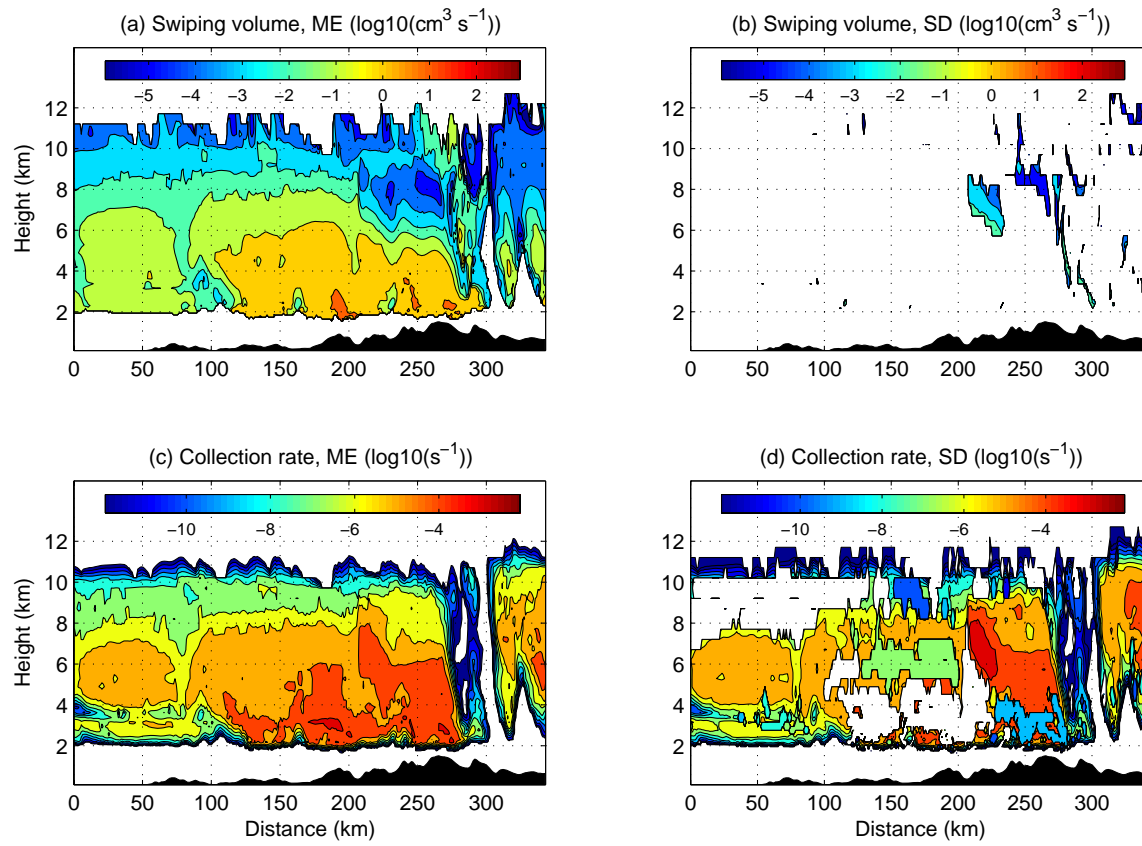


Figure 5.7 Spatial distributions of mean and standard deviation of swiping volume (upper panel) and collection rate (lower panel) for ML1 at 40 minutes.

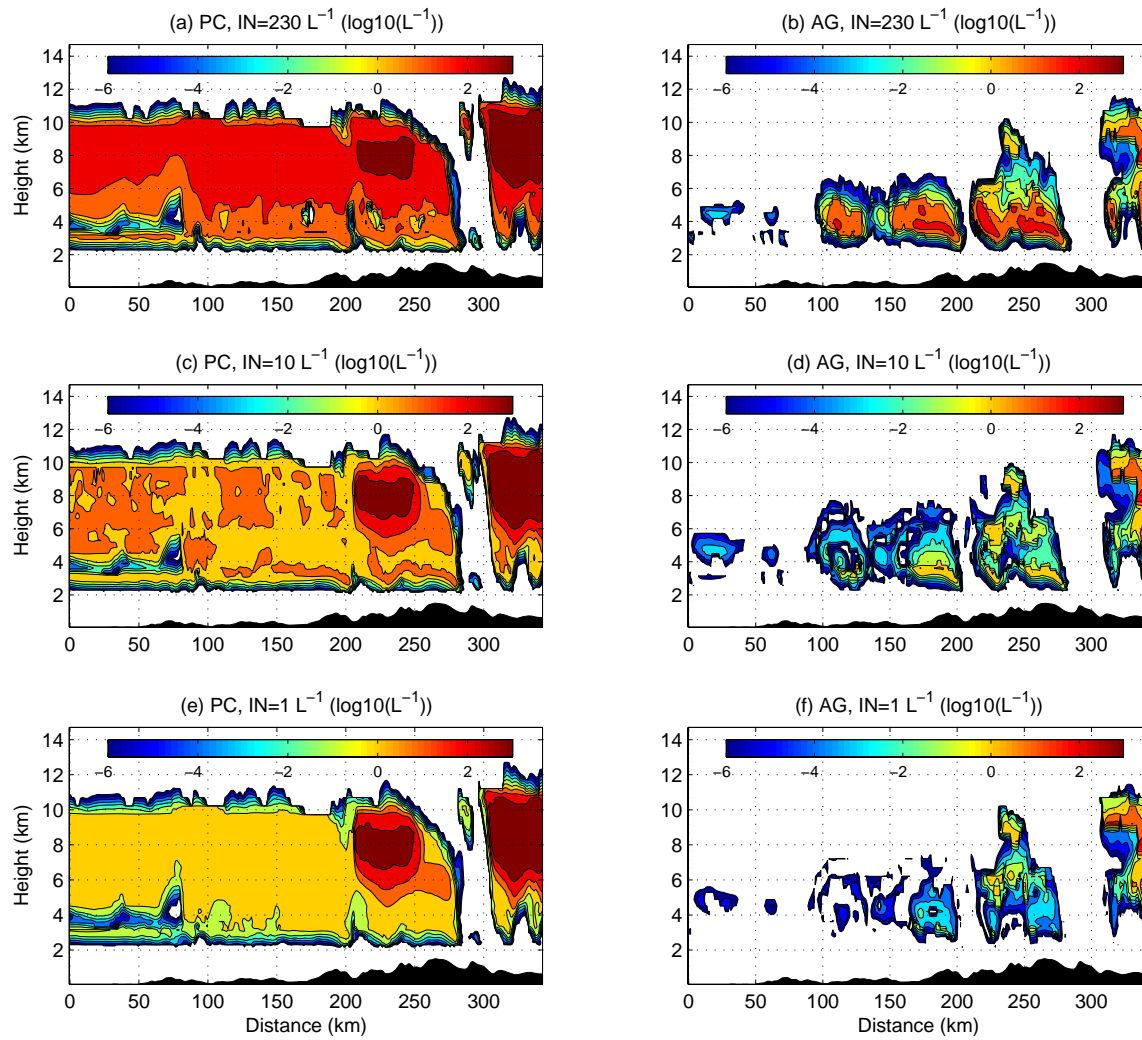


Figure 5.8 Same as Figure 3.12 except that the simulated was implemited with aggregation efficiency model D and at 20 minutes.

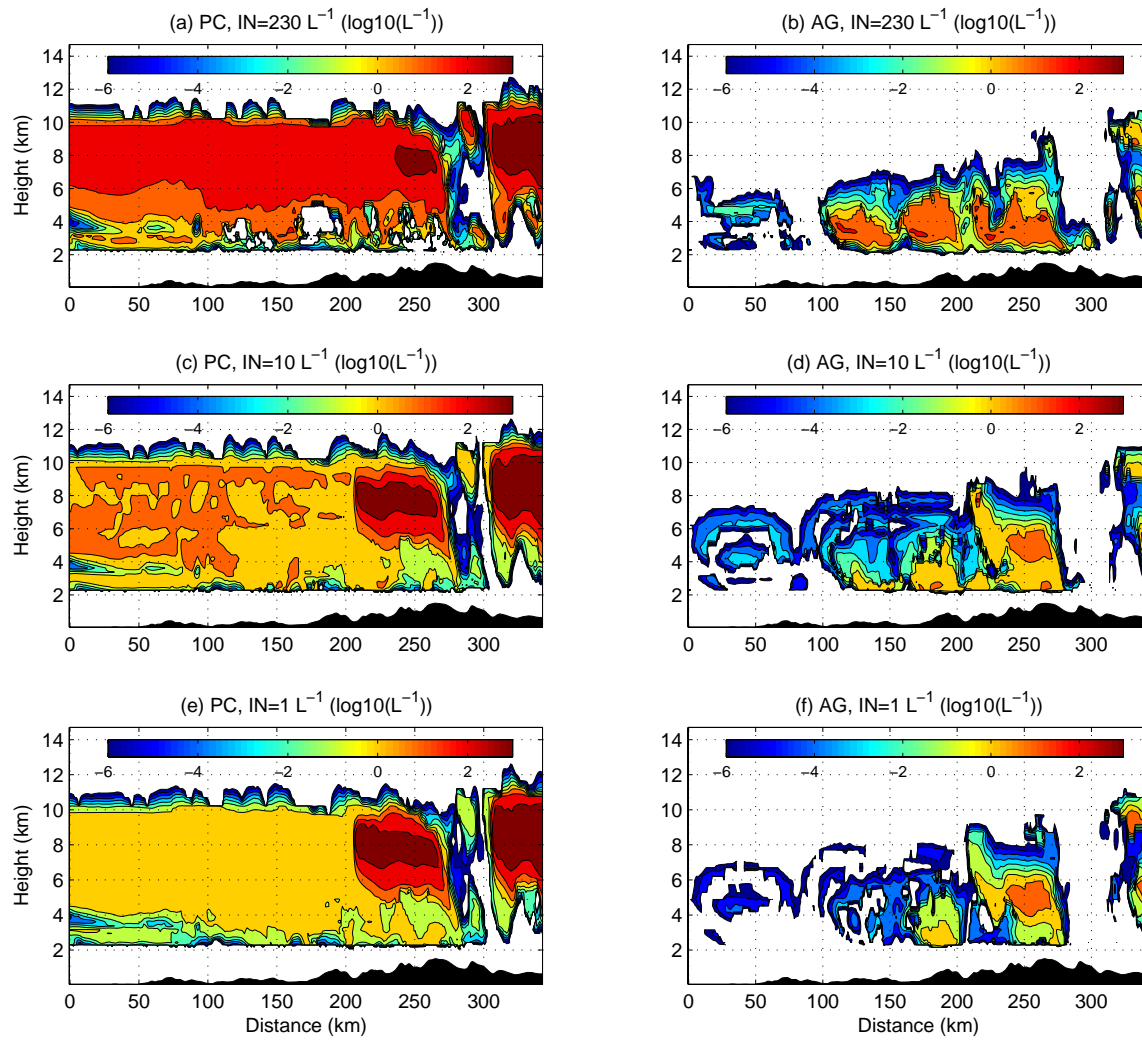


Figure 5.9 Same as Figure 3.12 except that the simulation was implemented with aggregation efficiency model D and at 40 minutes.

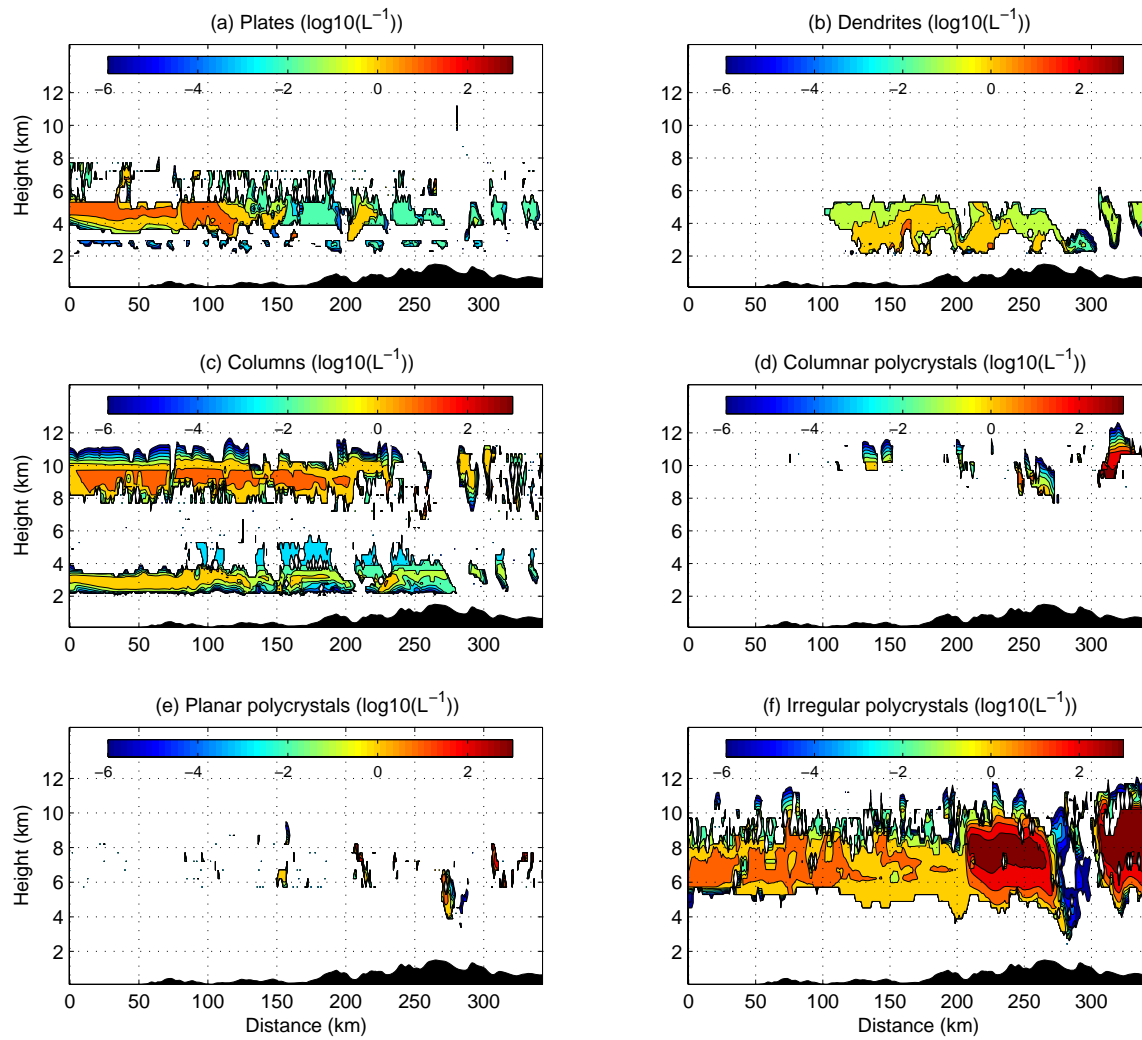


Figure 5.10 Concentration of diagnosed habits only including pristine crystals at 40 minutes of simulation for MD1.

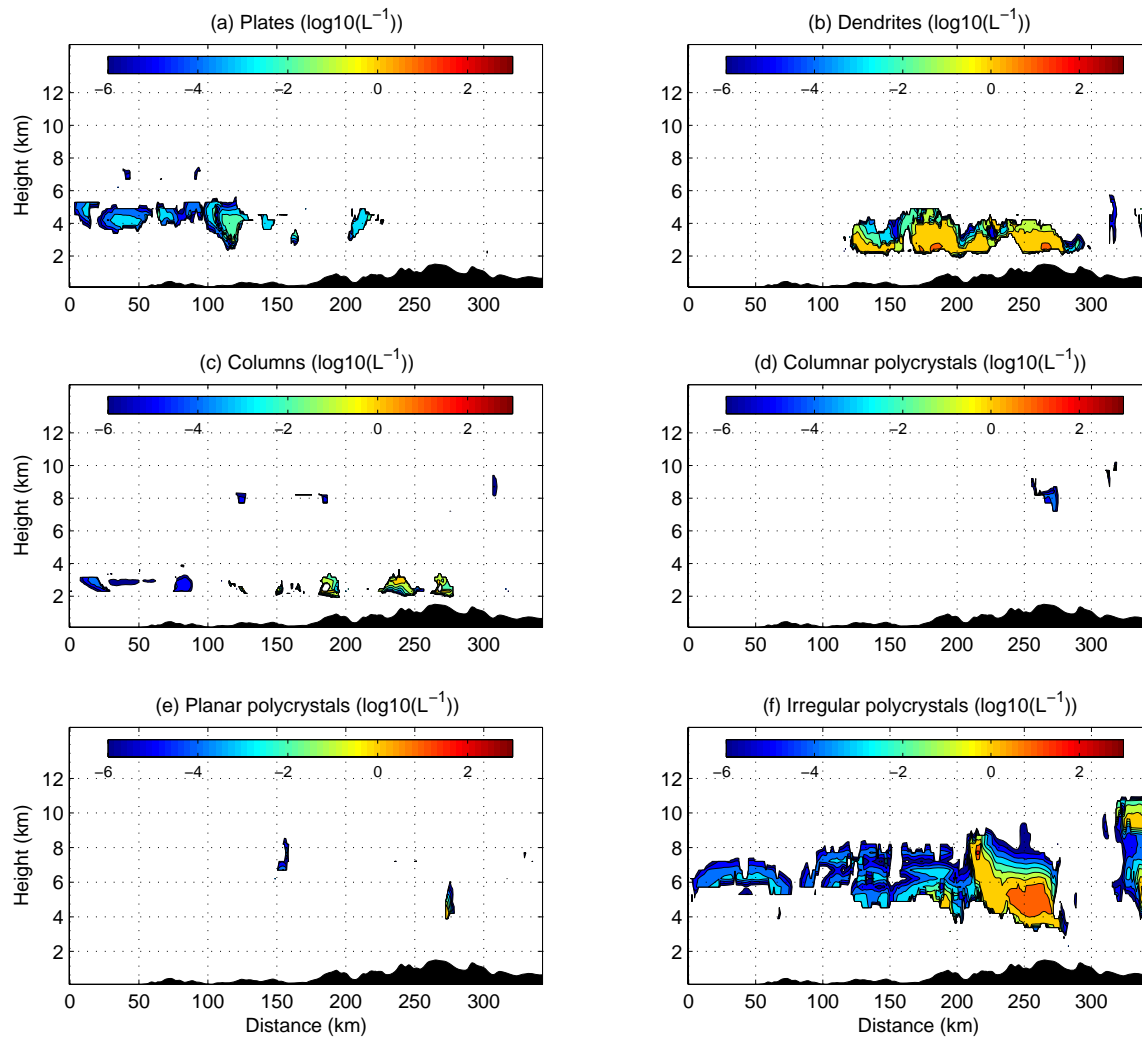


Figure 5.11 Concentration of diagnosed habits only including aggregates at 40 minutes of simulation for MD1.

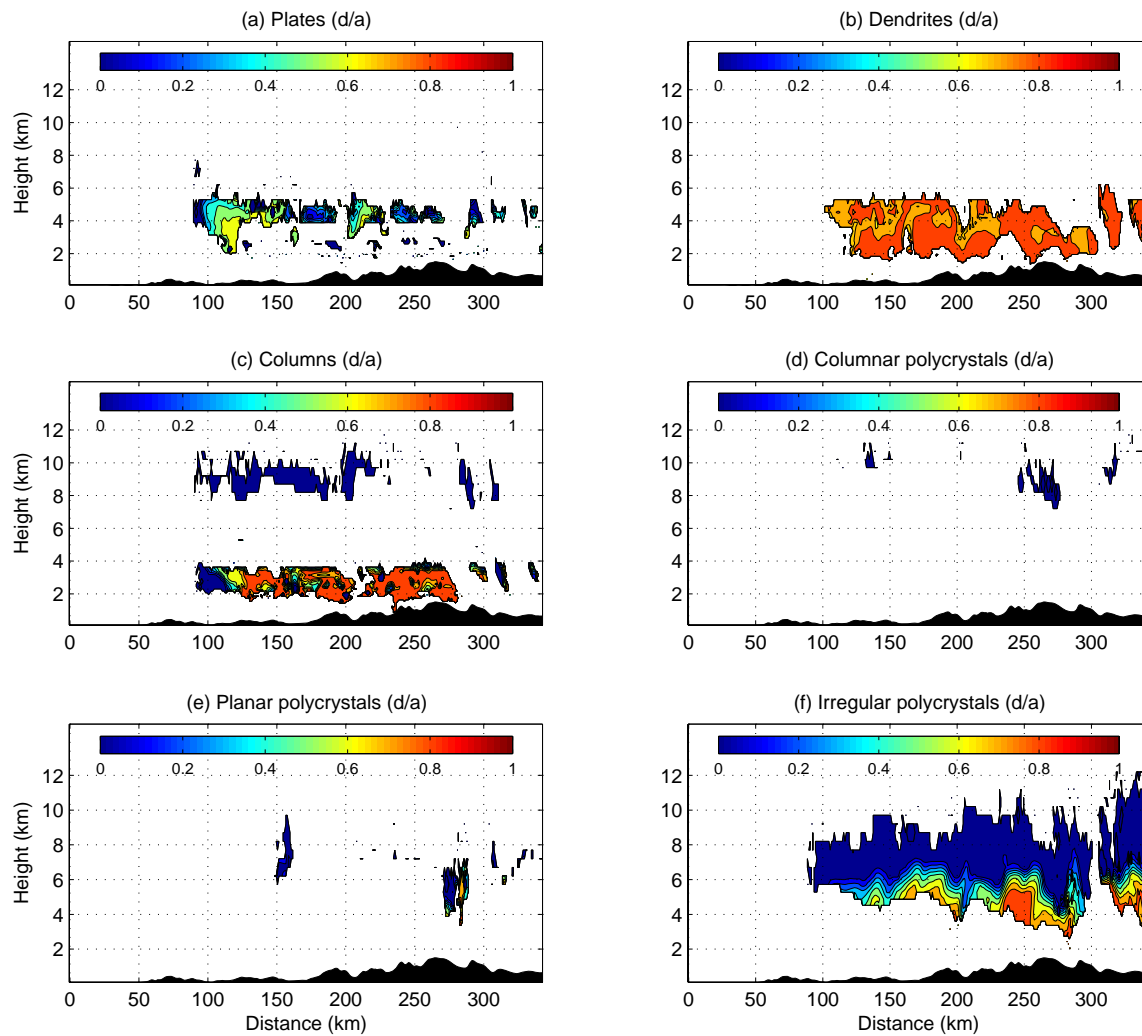


Figure 5.12 Axis ratio $\phi = d/a$ of diagnosed habits including all types of ice particles at 40 minutes of simulation for MD1.

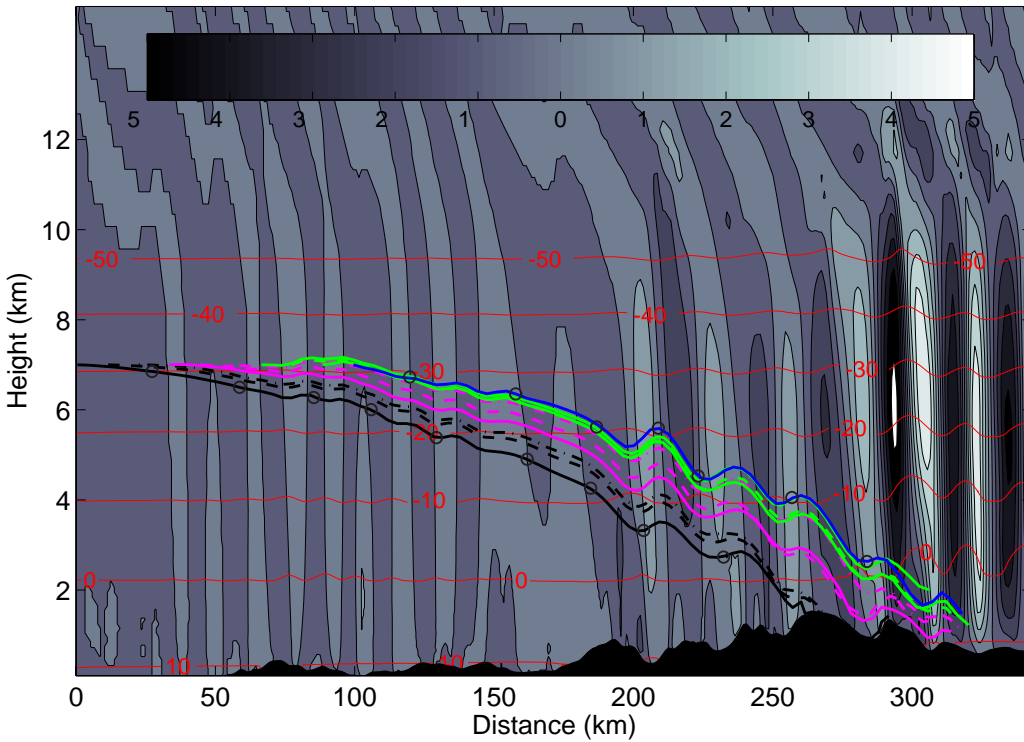


Figure 5.13 Comparison of trajectories for MP1. All trajectories started at $y=0.5$ km $z=7$ km by 11 km apart each other and at the initial time. Trajectories were numbered 1 to 10 from left to right. The circles on trajectory #1 and #10 indicate approximate locations of PSDs shown in Figure 5.14 and Figure 5.15. The time interval is 20 minutes.

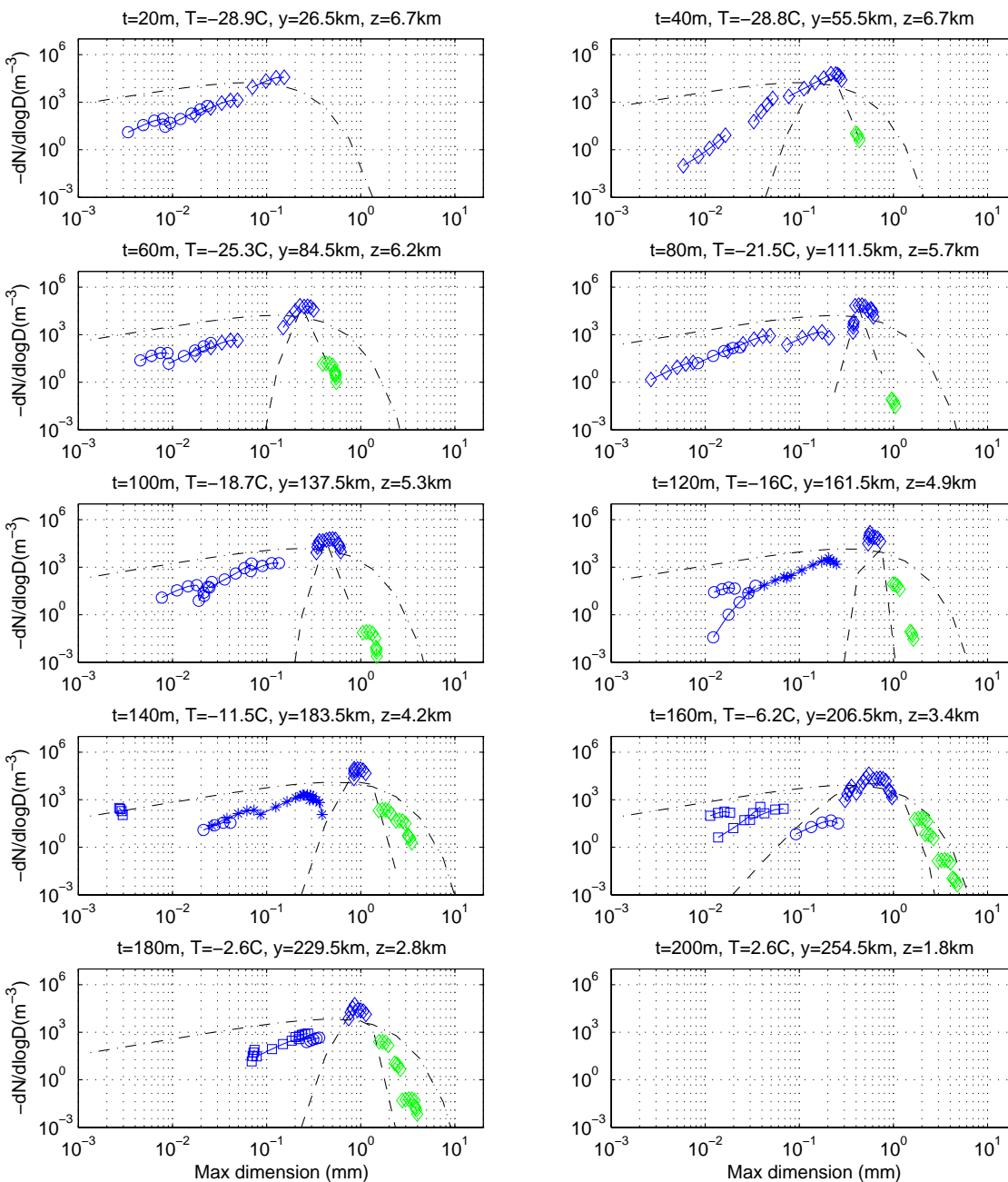


Figure 5.14 Evolution of size distribution along the trajectory #1. Size distribution is shown every 20 minutes starting from 20 minutes of simulation. y and z indicates the middle point of grid cells that the contained the trajectory. Ice crystal habits are indicated with markers; circle markers indicate plates, asterisks dendrites, squares columnar crystals, triangles planar polycrystals, crosses columnar polycrystals, and diamonds irregular polycrystals. Ice particle types are indicated with color; blue is pristine crystals, and green is aggregates. Dashed line (dash-dot line) indicates fitted gamma distribution (exponential distribution) using Heymfield et al. (2002)'s method.

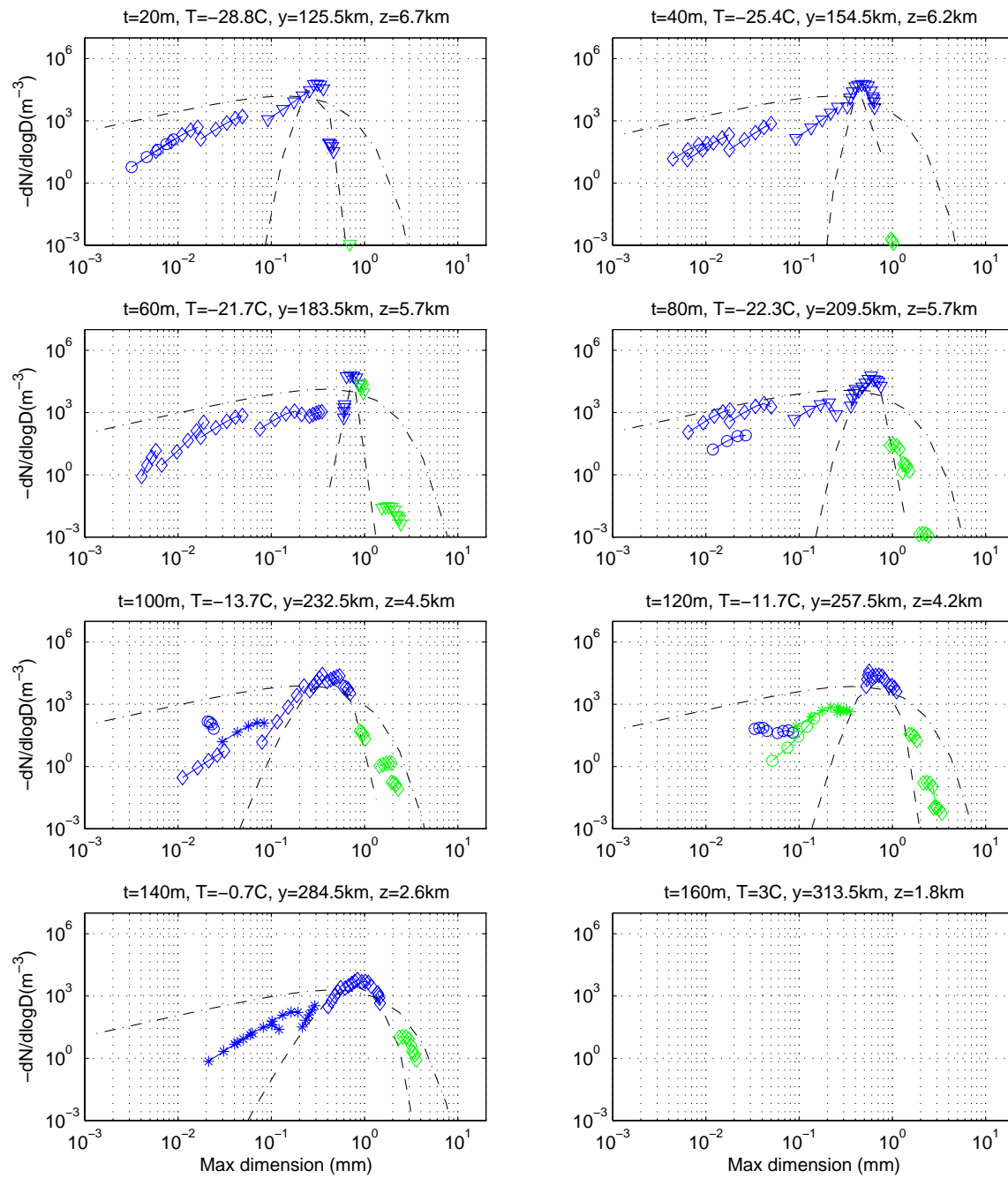


Figure 5.15 Same as Figure 5.14 except for trajectory #10.

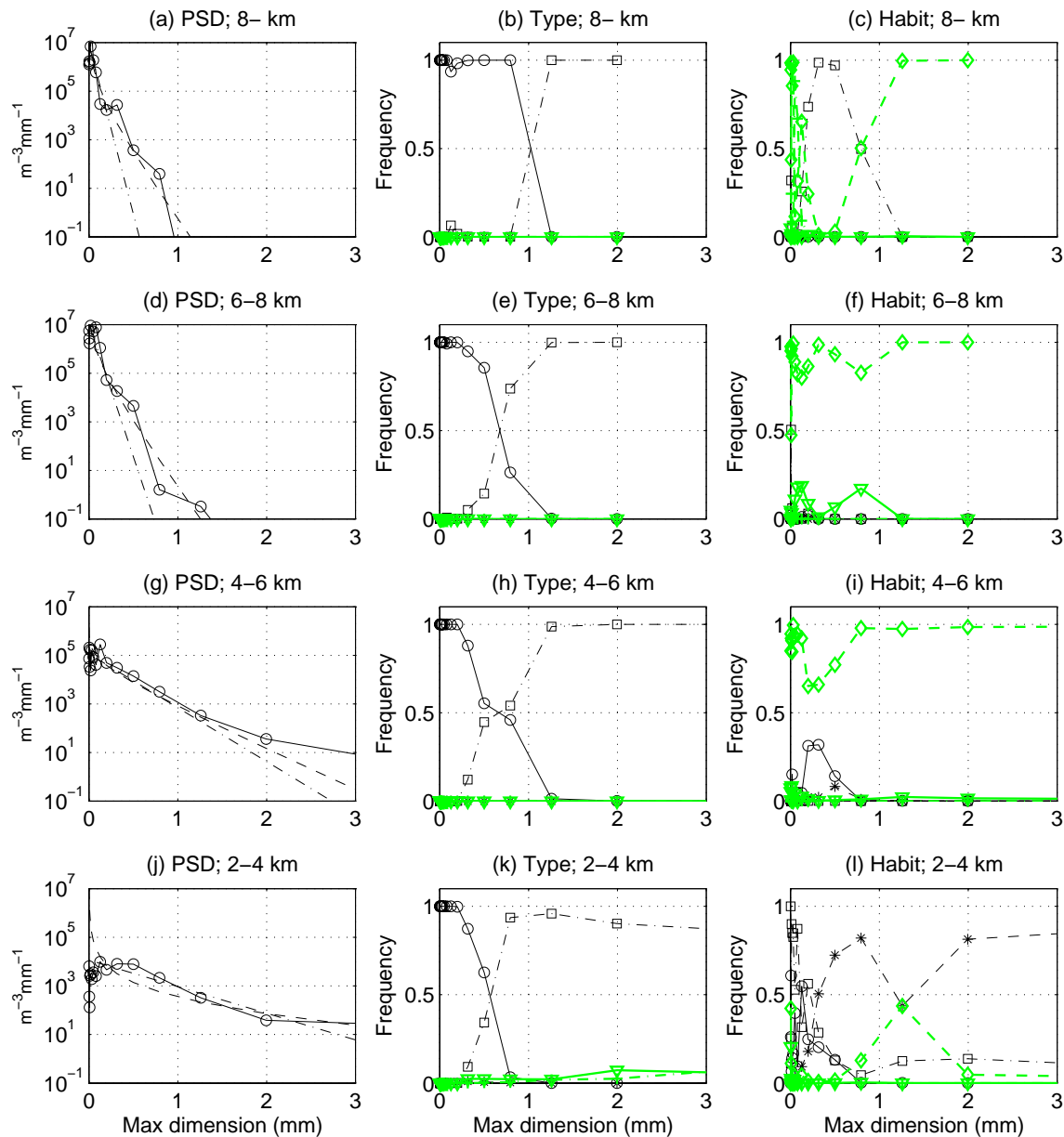


Figure 5.16 Comparison of PSD (left column), and conditional frequencies of types (middle) and habits (right) given maximum dimension at 40 minutes for MD1. They were obtained for vertically grouped samples in the domain. Circle in PSD shows data points, dashed line fitted gamma distribution, and dash-dot lines exponential distribution. For types, circle indicates pristine crystals, asterisks rimed crystals, squares aggregates, crosses rimed aggregates, and triangles graupels. For habits, circle indicates plates, asterisks dendrites, squares columnar crystals, crosses columnar polycrystals, and triangles planar polycrystals, and diamonds irregular polycrystals.

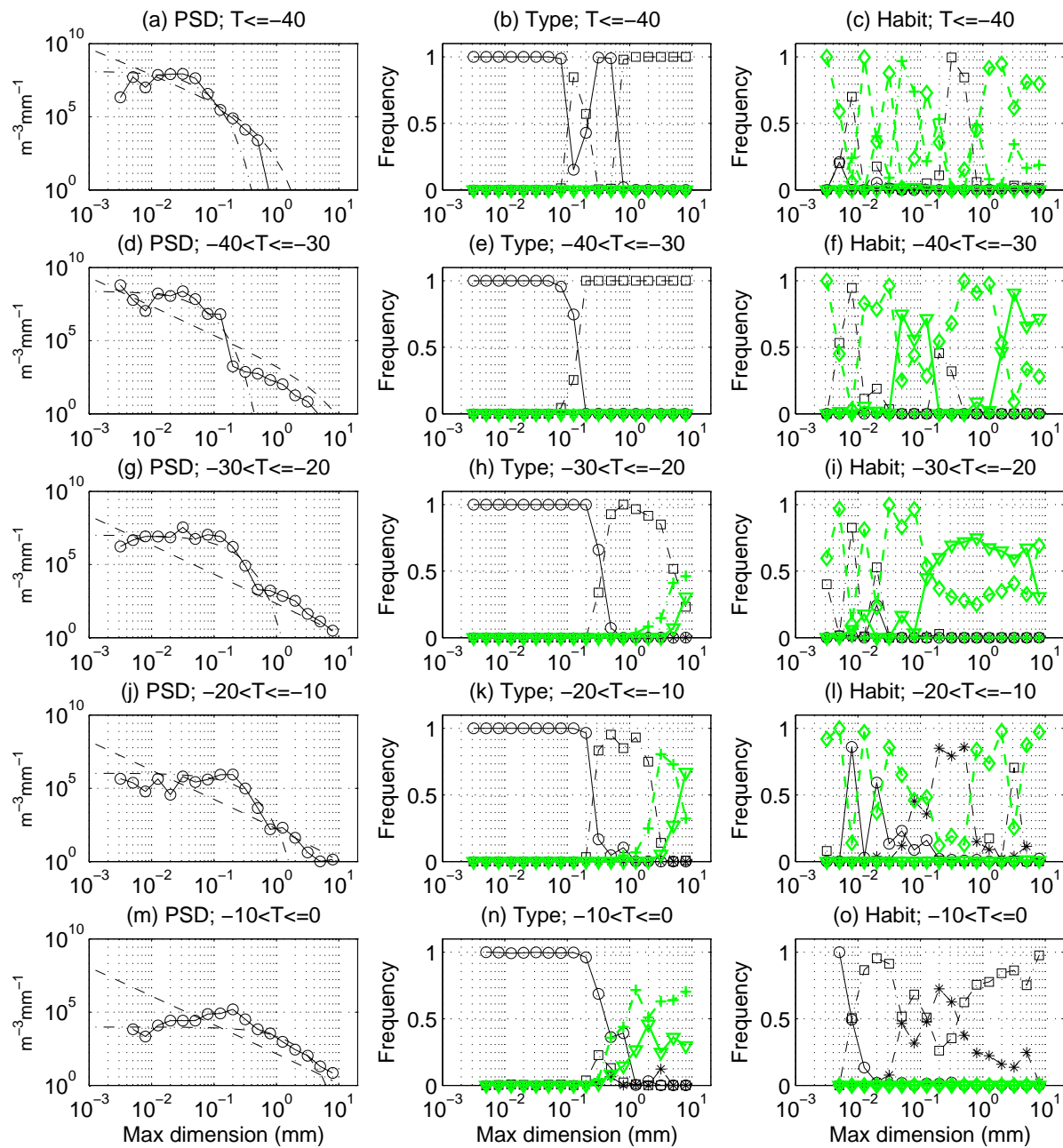


Figure 5.17 Comparison of PSD (left column), and conditional frequencies of types (middle) and habits (right) given maximum dimension at 90 minutes of simulation for PCH. They were obtained by grouping samples in section III ($y > 276$ km) and according to the temperature. See caption of Figure 5.16 for description of the notation.

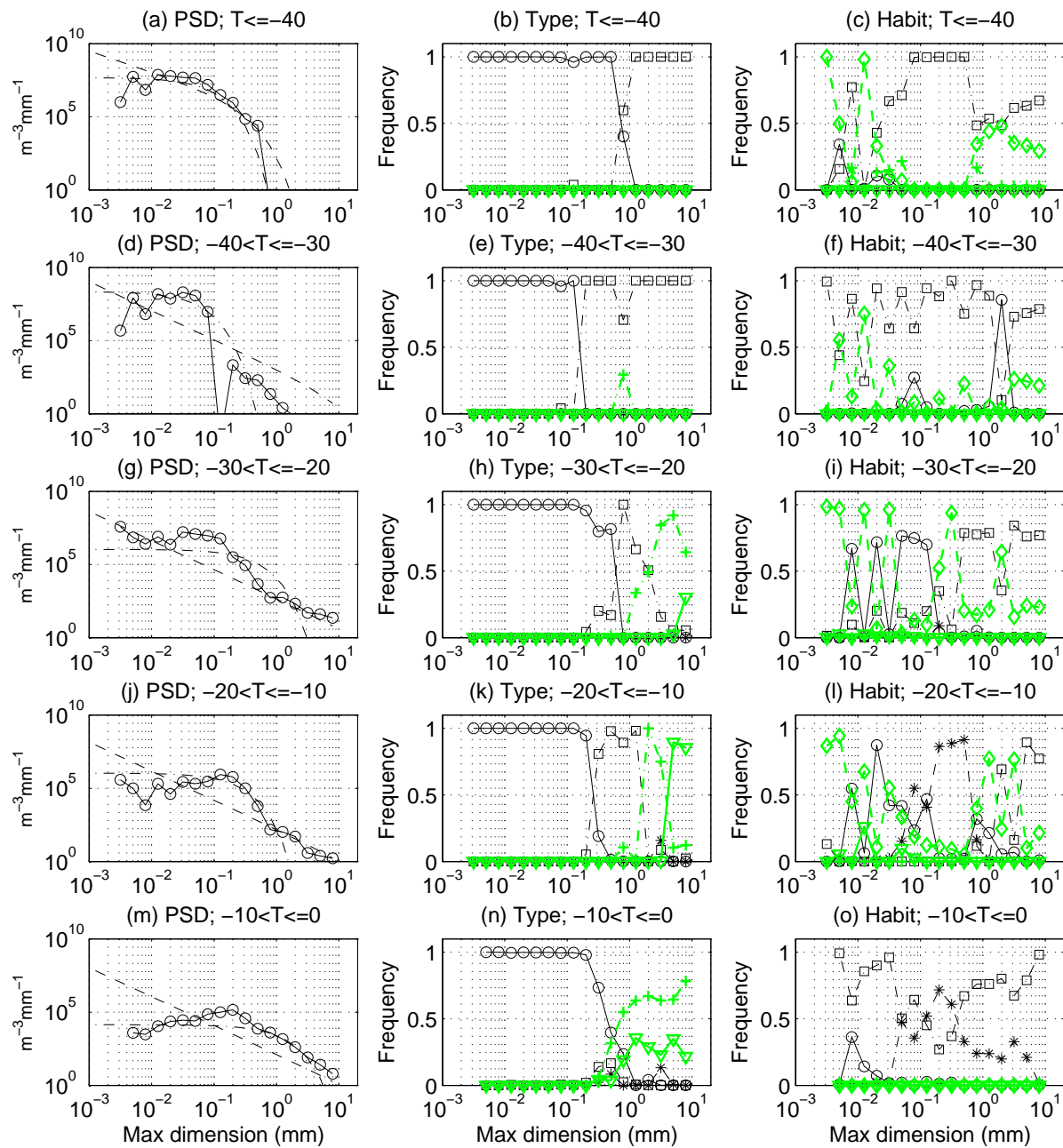


Figure 5.18 Same as Figure 5.17 except that this is for PCHH.

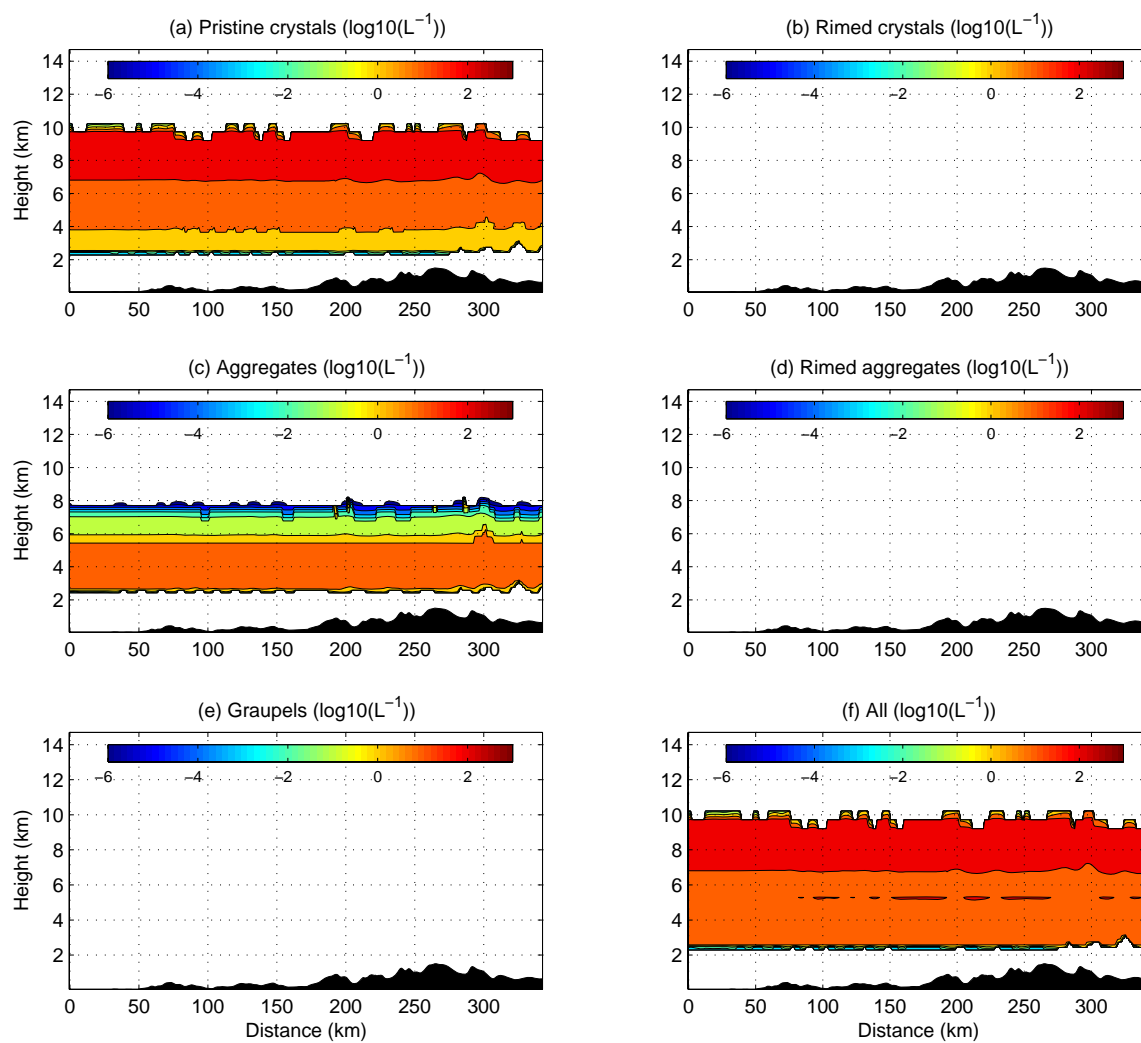


Figure 5.19 Initial concentration of ice particles for each diagnosed type.

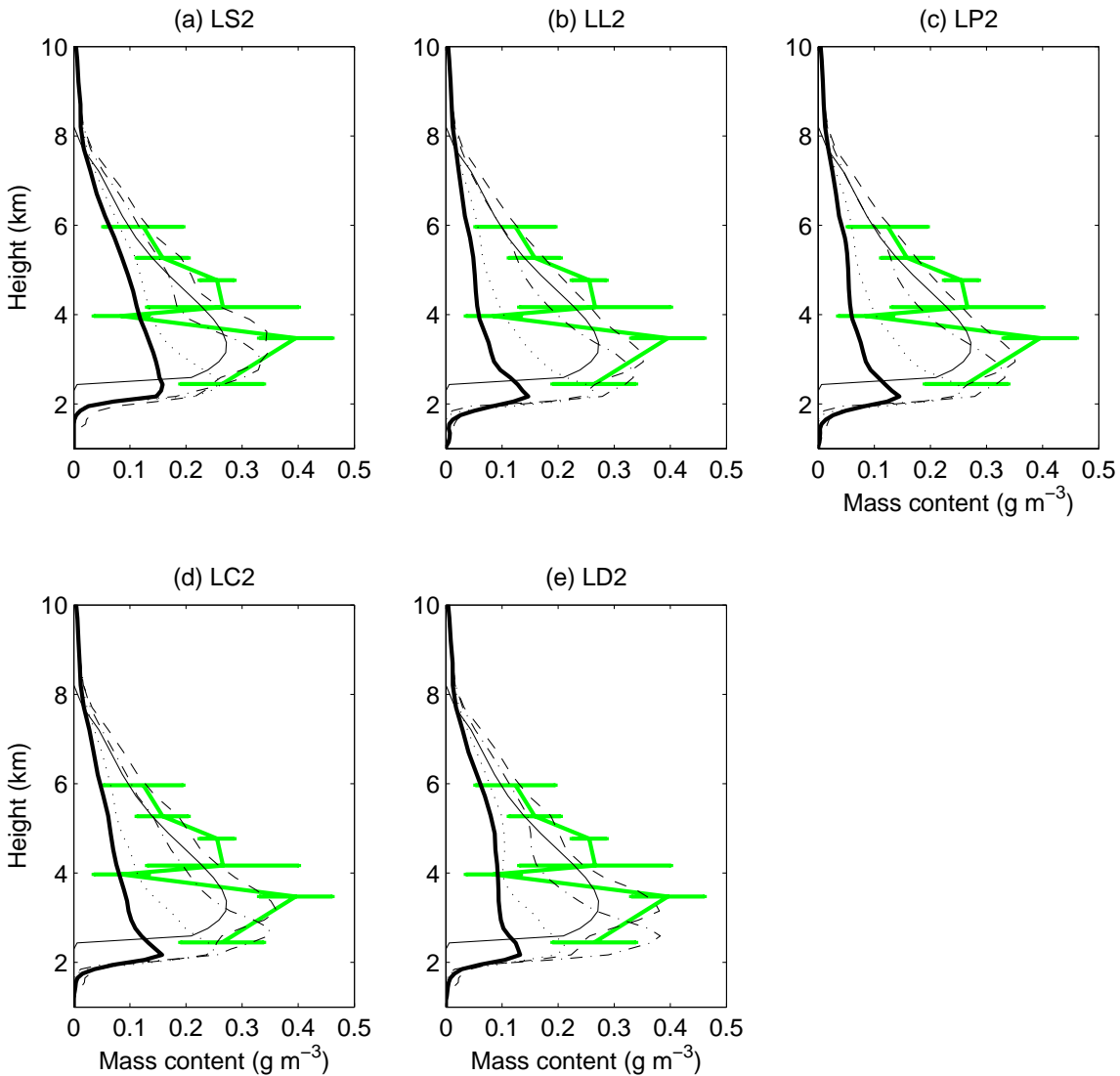


Figure 5.20 Comparison of horizontally averaged mass content for (a) LS2, (b) LL2, (c) LP2, (d) LC2, and (e) LD2. Solid line indicates the initial condition, dashed line 10 minutes, dash-dot line 20 minutes, dotted line 40 minutes, and thick solid line 60 minutes. The mass content estimated by Woods et al. (2005) is shown by thick gray line with standard deviation.

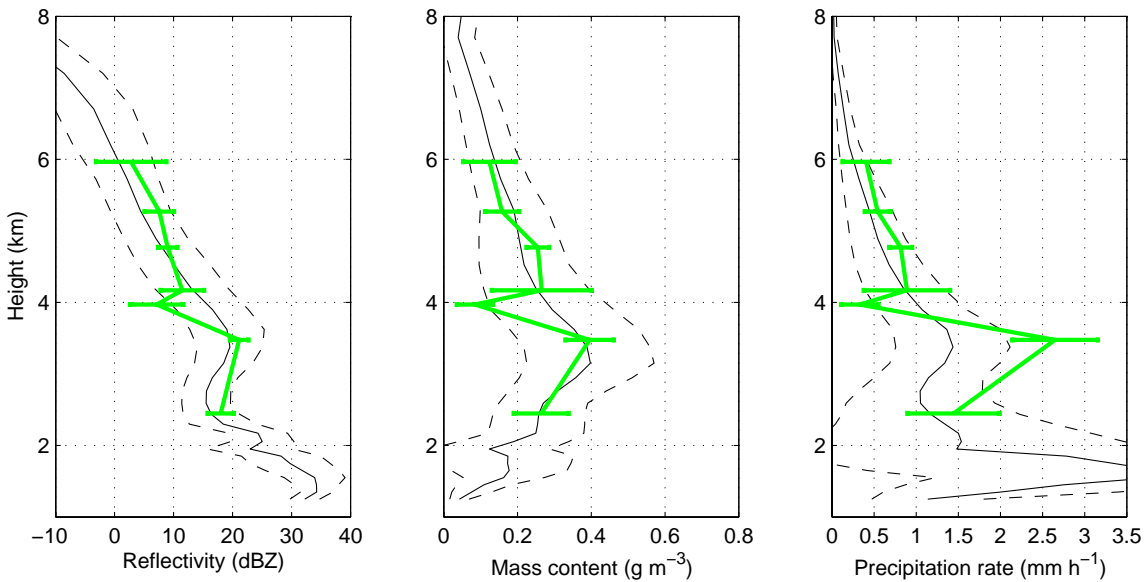


Figure 5.21 Vertical profile of (a) radar reflectivity, (b) mass content, and (c) precipitation rate at 10 minutes for LD2. Solid line denotes horizontal mean and dashed line indicate one standard deviation added or subtracted from the mean. The thick solid line with error bar shows estimates of Woods et al. (2005).

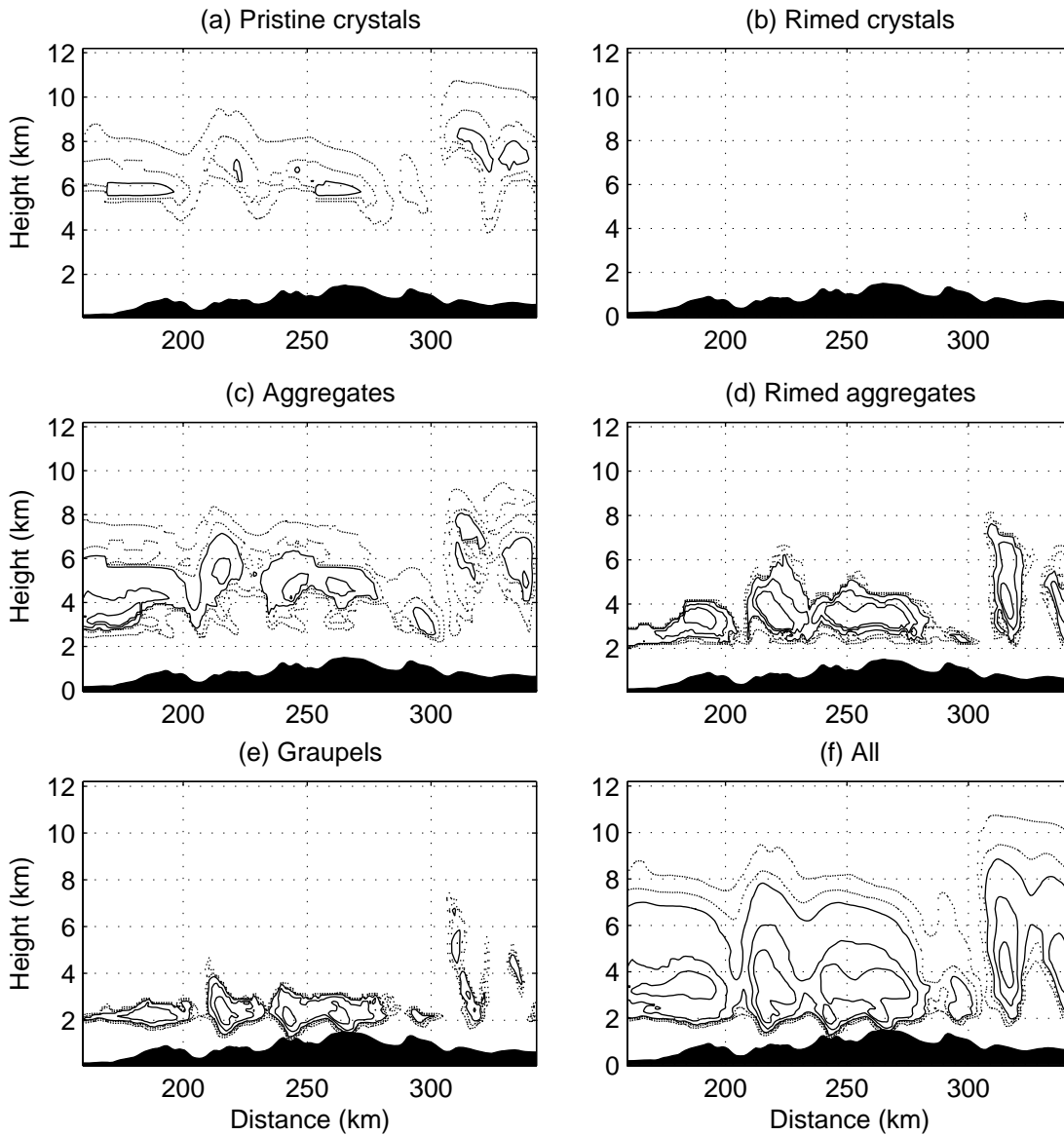


Figure 5.22 Spatial distribution of mass content for each diagnosed type of ice particles for LD2 at 10 minutes. The dotted lines indicate contours of 0.01 and 0.05 gm^{-3} , and the solid lines 0.1, 0.3, and 0.5 gm^{-3} .

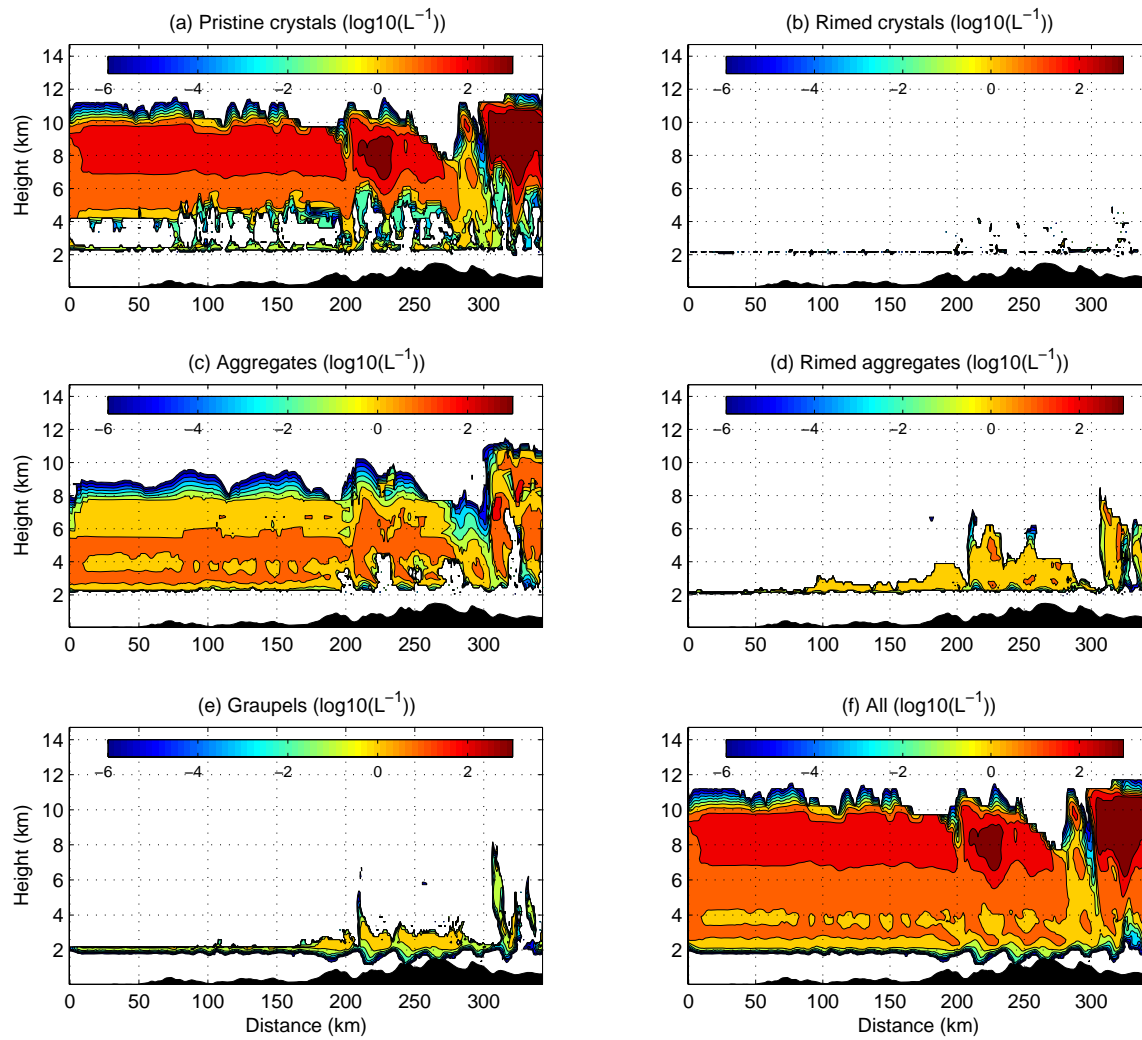


Figure 5.23 Concentration of diagnosed type of ice particles for LD2 at 10 minutes.

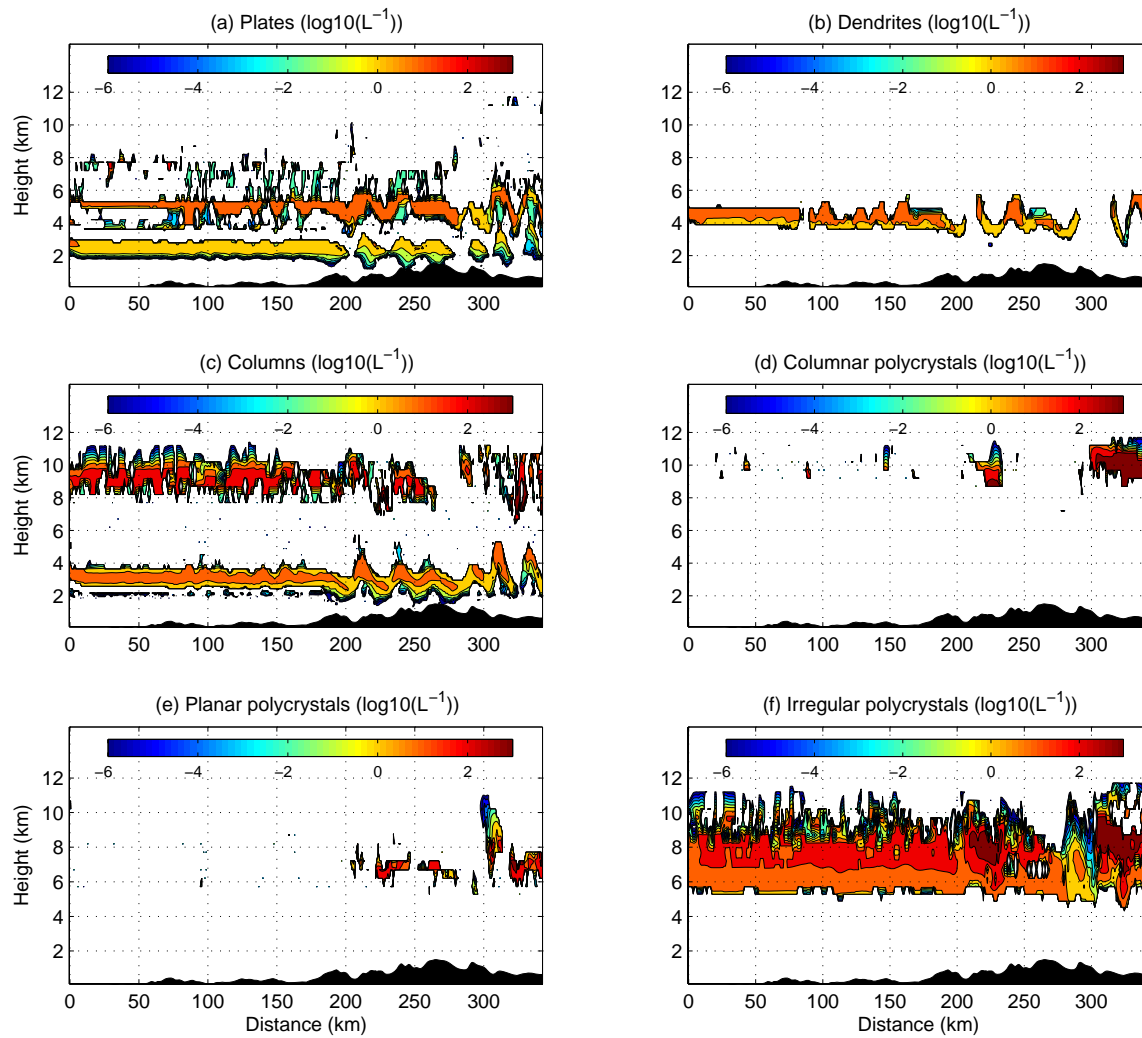


Figure 5.24 Concentration of diagnosed habits of all ice particles for LD2 at 10 minutes

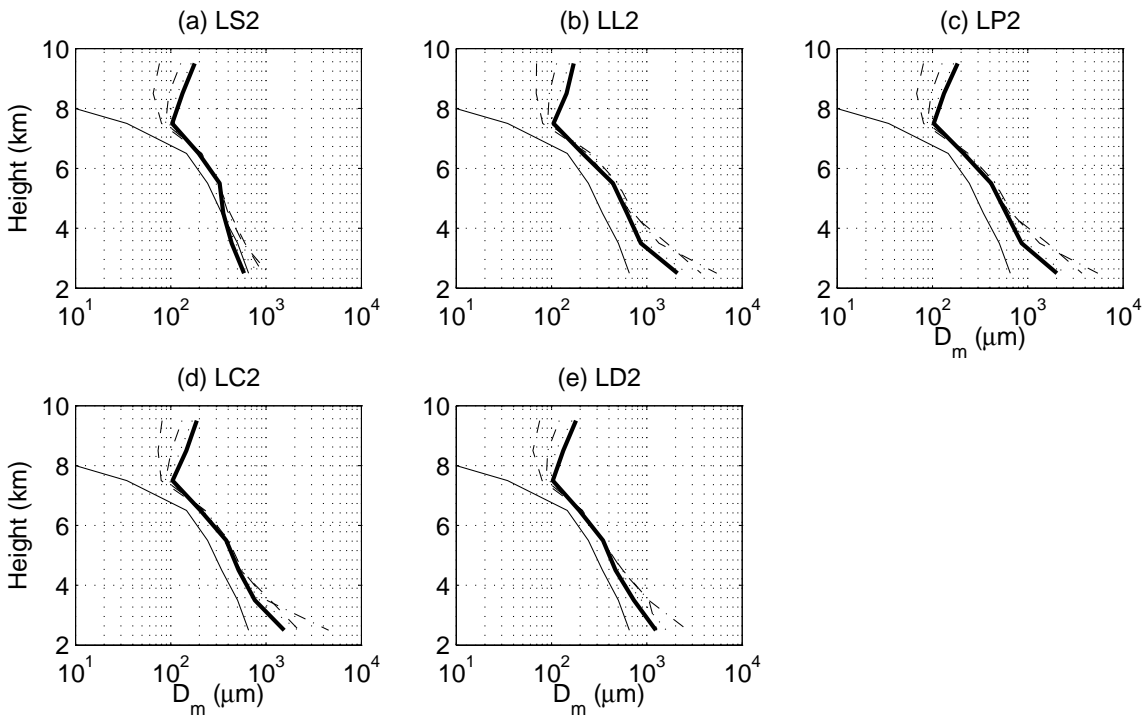


Figure 5.25 Comparison of maximum dimension of horizontally averaged PSD in section I ($0 < y < 200 \text{ km}$). Solid line indicates the initial condition, dashed line 10, dash-dot line 20, dotted line 40, and thick solid line 60 minutes. The values of each layer were plotted in the middle of the layer.

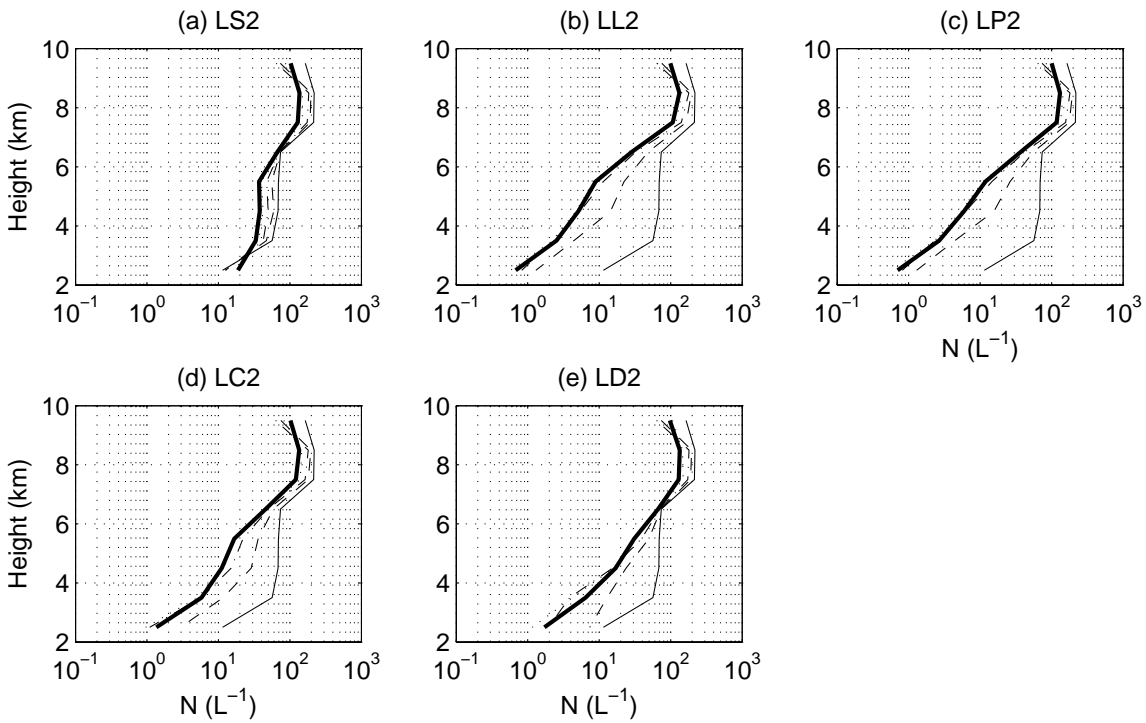


Figure 5.26 Same as Figure 5.25 except that this is for number concentration.

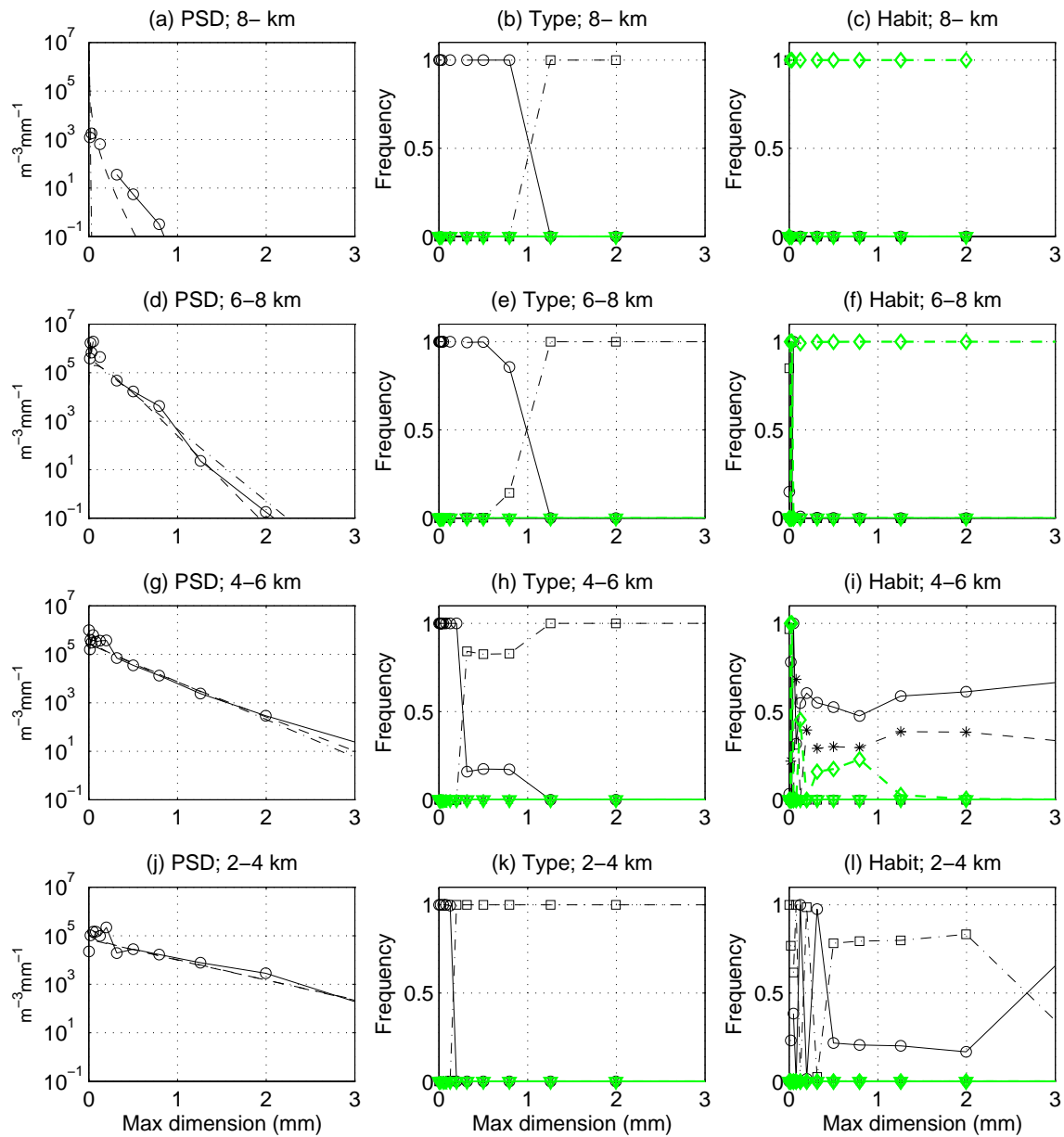


Figure 5.27 Comparison of PSD (left column), and conditional frequencies of types (middle) and habits (right) at the initial time in section I. See Figure 5.16 for description of markers.

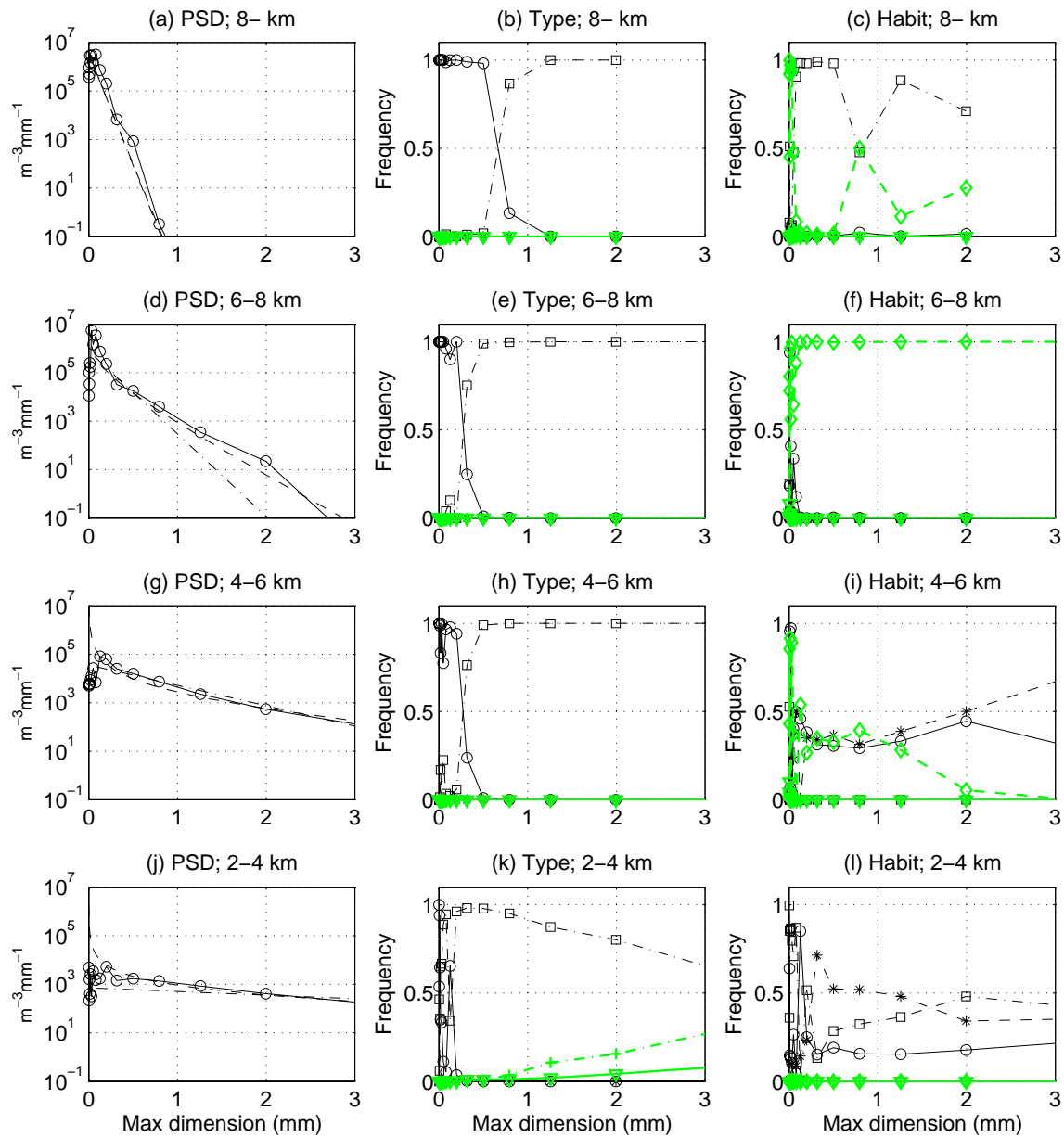


Figure 5.28 Same as Figure 5.27, but at 10 minutes for LL2.

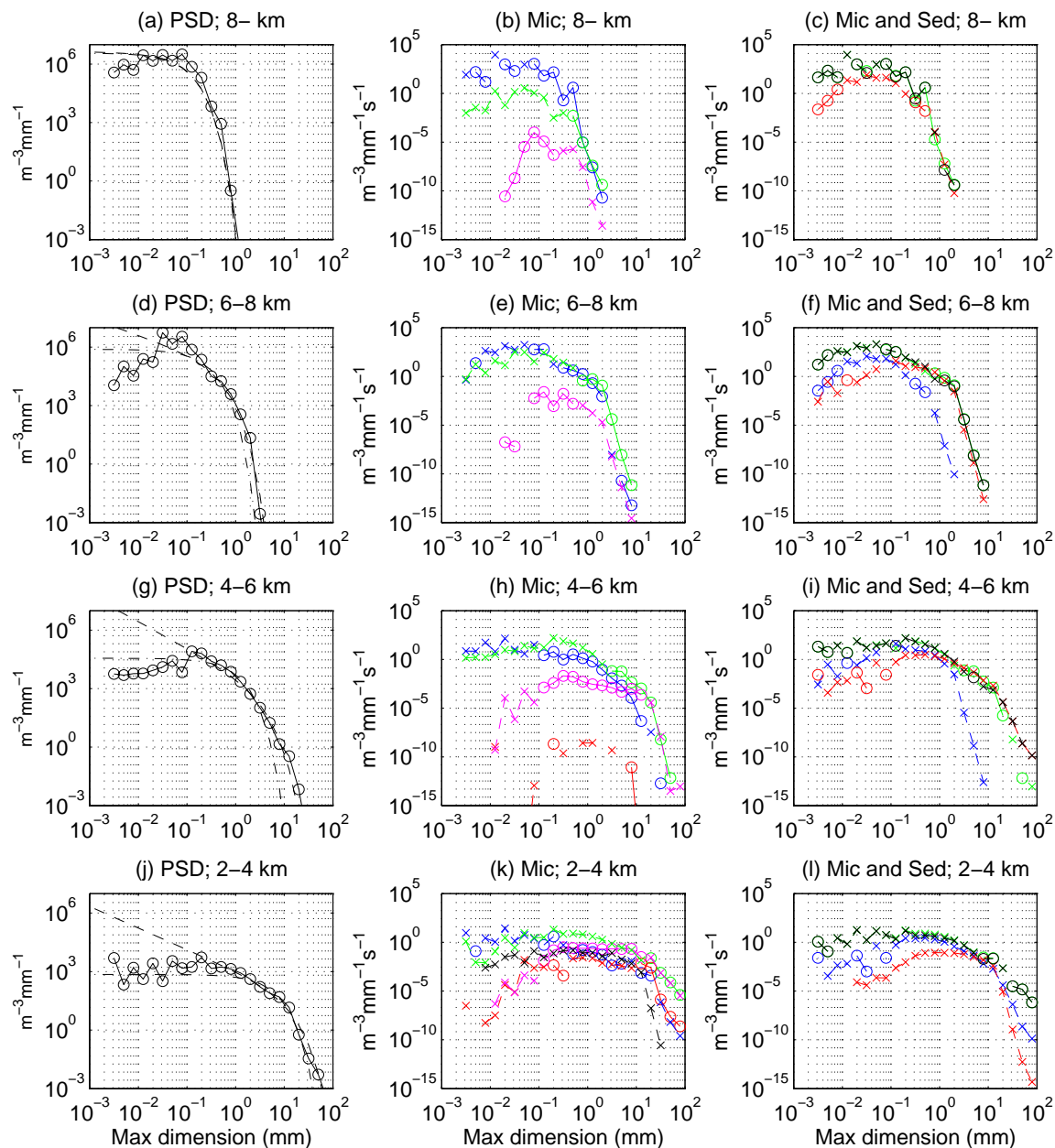


Figure 5.29 Comparison of particle size distribution (left column), concentration tendency of each microphysical process (middle column), and total microphysical tendency and normalized sedimentation flux (right column) for LL2 at 10 minutes of simulation in section I. Circles in PSDs show sample points, and dashed (dash-dotted) line indicates fitted gamma (exponential) distribution. Crosses (circles) in middle and right columns indicate positive (negative) tendency given maximum dimension. In the middle column, blue indicates vapor deposition, green aggregation, magenta breakup, and red riming process. In the right column, green total microphysical tendency, blue sedimentation flux at the upper boundary of the layer, red sedimentation flux at the lower boundary, and black net tendency.

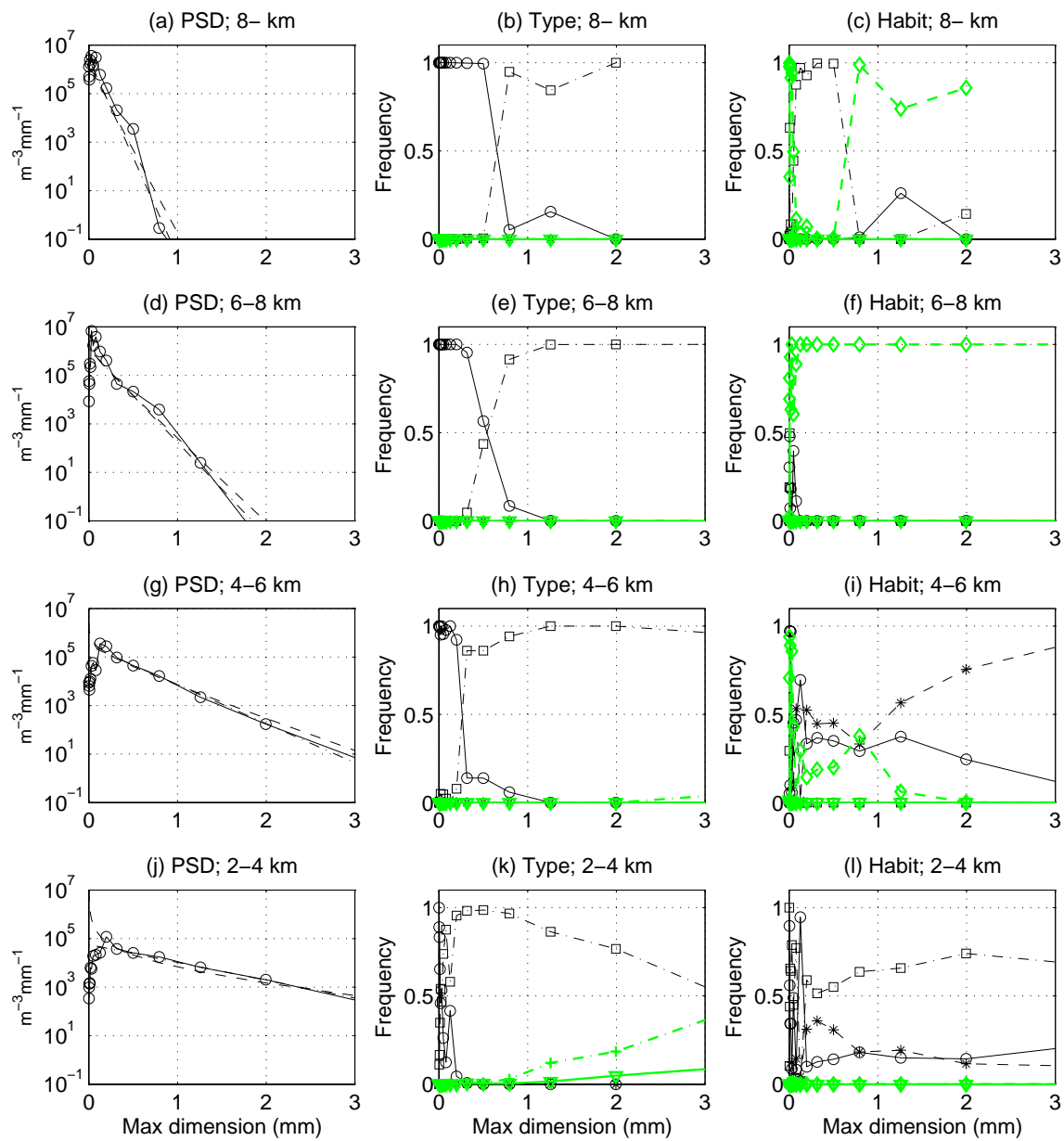


Figure 5.30 Same as Figure 5.27, except that this is for LS2 and at 10 minutes.

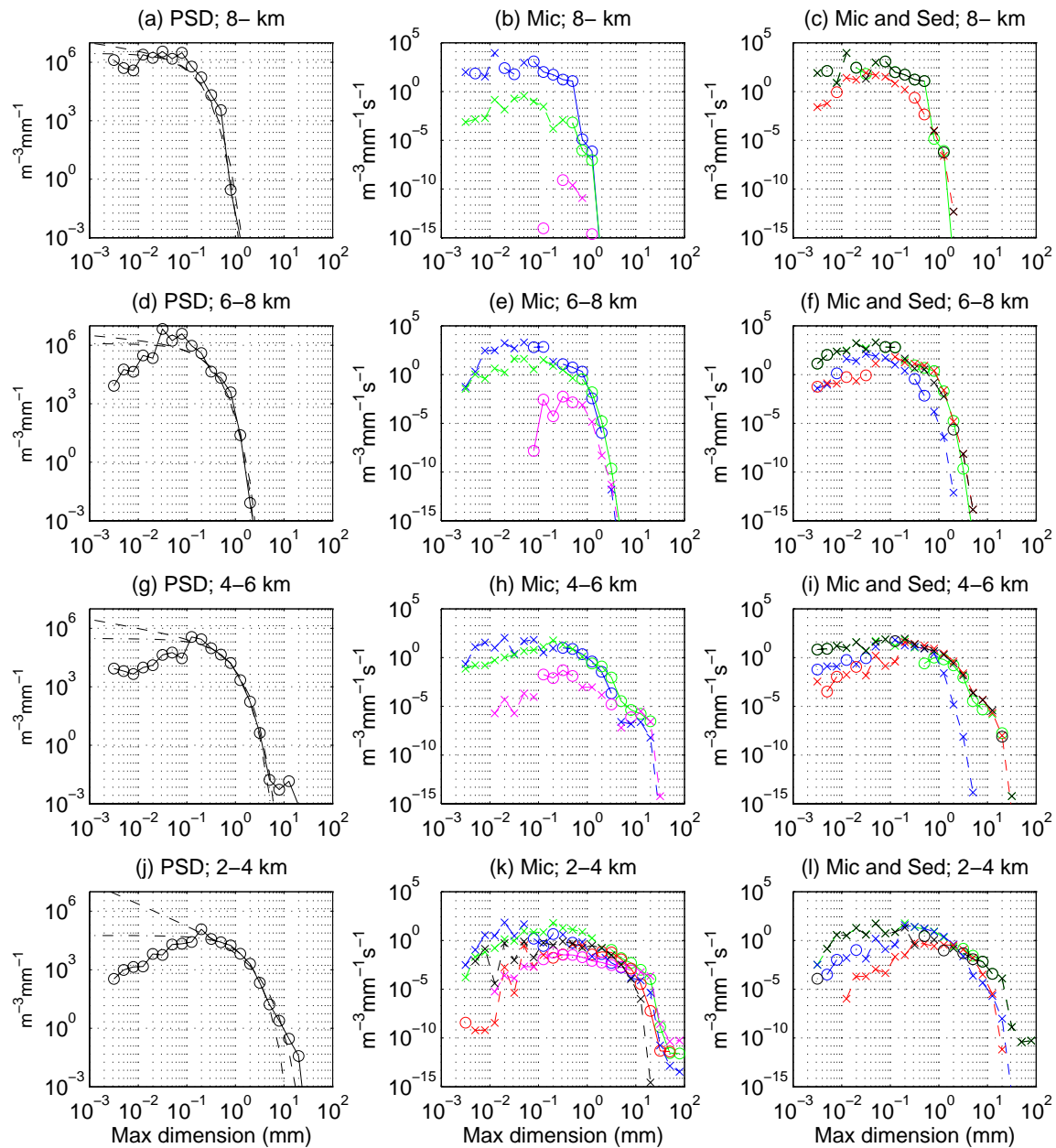


Figure 5.31 Same as Figure 5.29 except that this is for LS2.

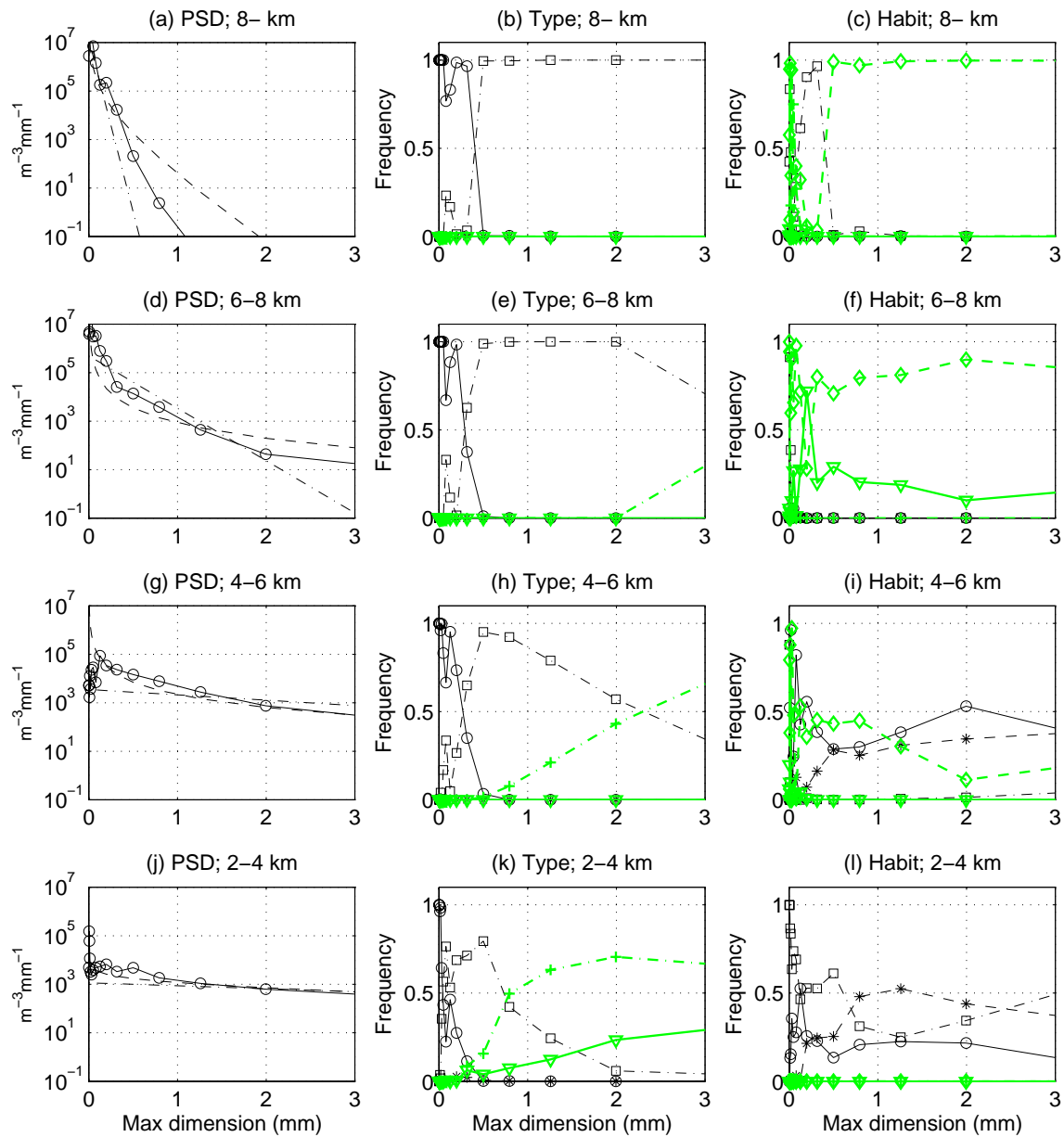


Figure 5.32 Same as Figure 5.27, but for horizontally averaged PSD in section II ($200 < y < 290$ km) at 10 minutes for LL2.

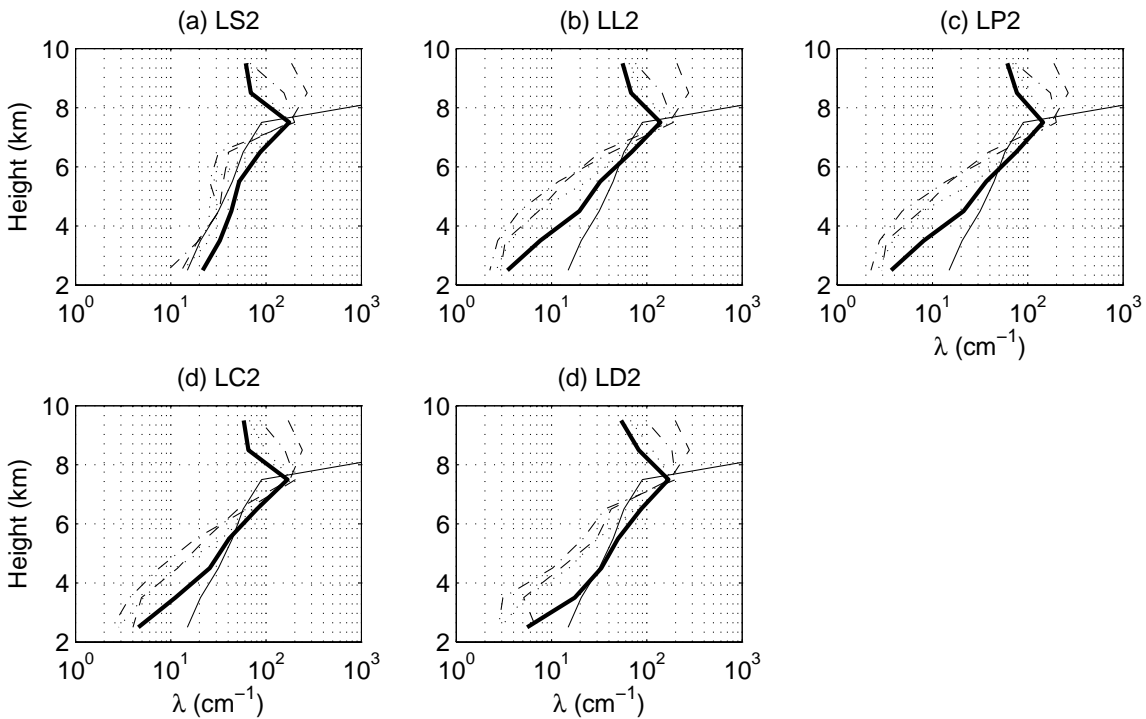


Figure 5.33 Slope parameter of exponential distribution fitted to horizontally averaged PSD over the entire domain ($0 < y < 290 \text{ km}$). Solid line indicates the initial condition, dashed line 10, dash-dot line 20, dotted line 40, and thick solid line 60 minutes. The values of each layer were plotted in the middle of the layer.

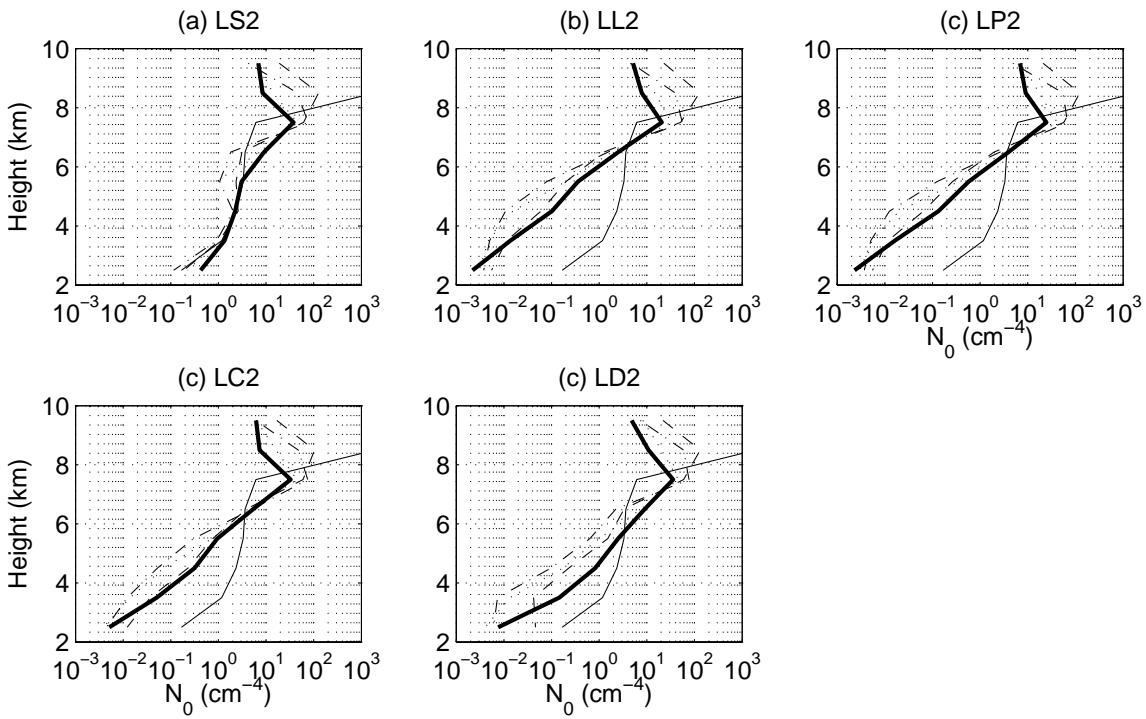


Figure 5.34 Same as Figure 5.33 except that it is the intercept parameter of exponential distribution.

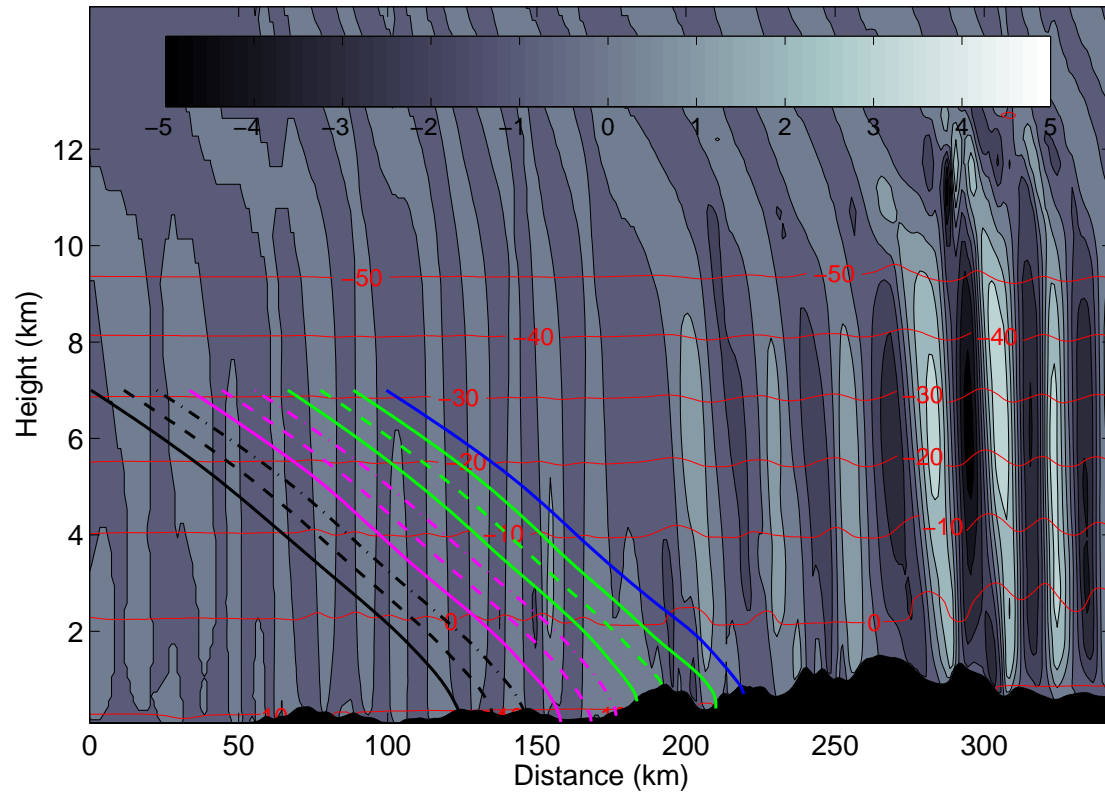


Figure 5.35 Trajectories for LP2 calculated by using constant vertical velocity of 1 m/s.

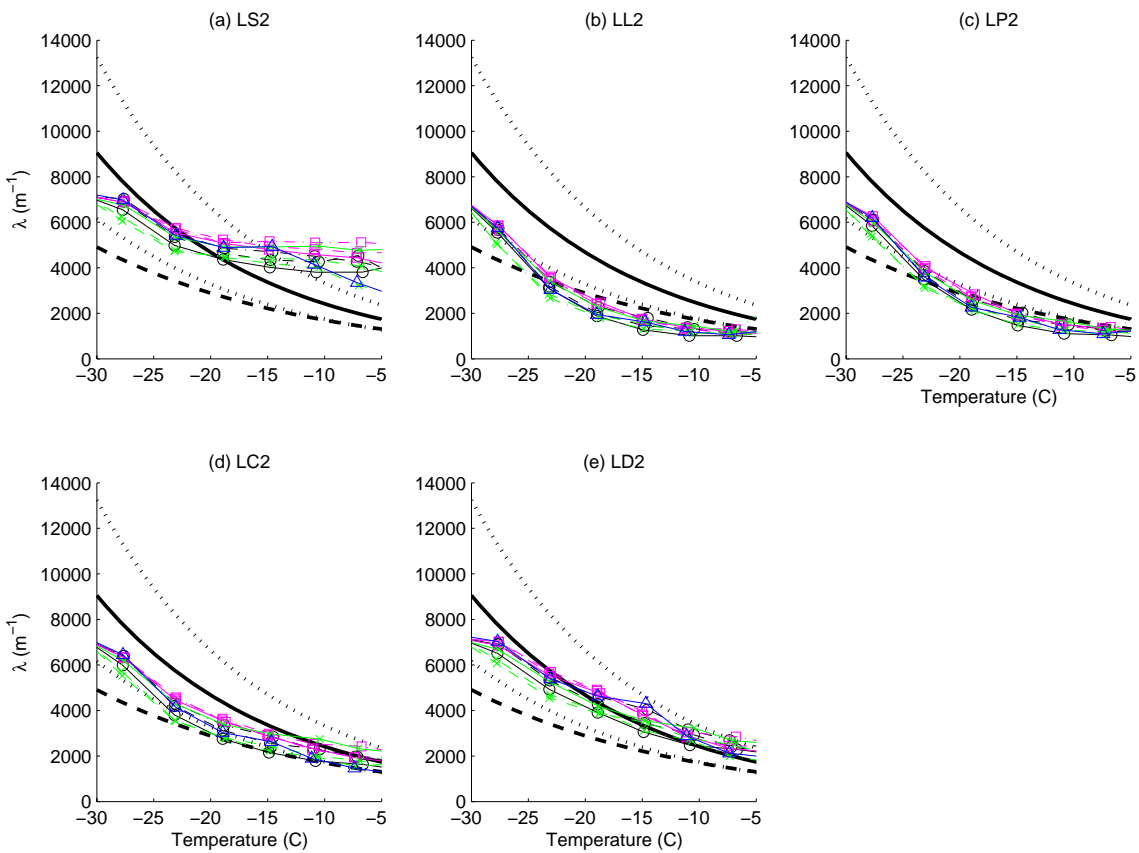


Figure 5.36 Change of slope parameter with temperature fitted the PSDs on the trajectories starting from the initial time. Thick solid curve shows the parameterized slope parameter by Heymsfield et al. (2002) using PSDs from TRMM campaigns, and dotted curves are those fitted to one standard deviation of the data given temperature. Thick dashed curve indicates Houze et al. (1979)'s formula fitted to PSDs taken from frontal clouds.

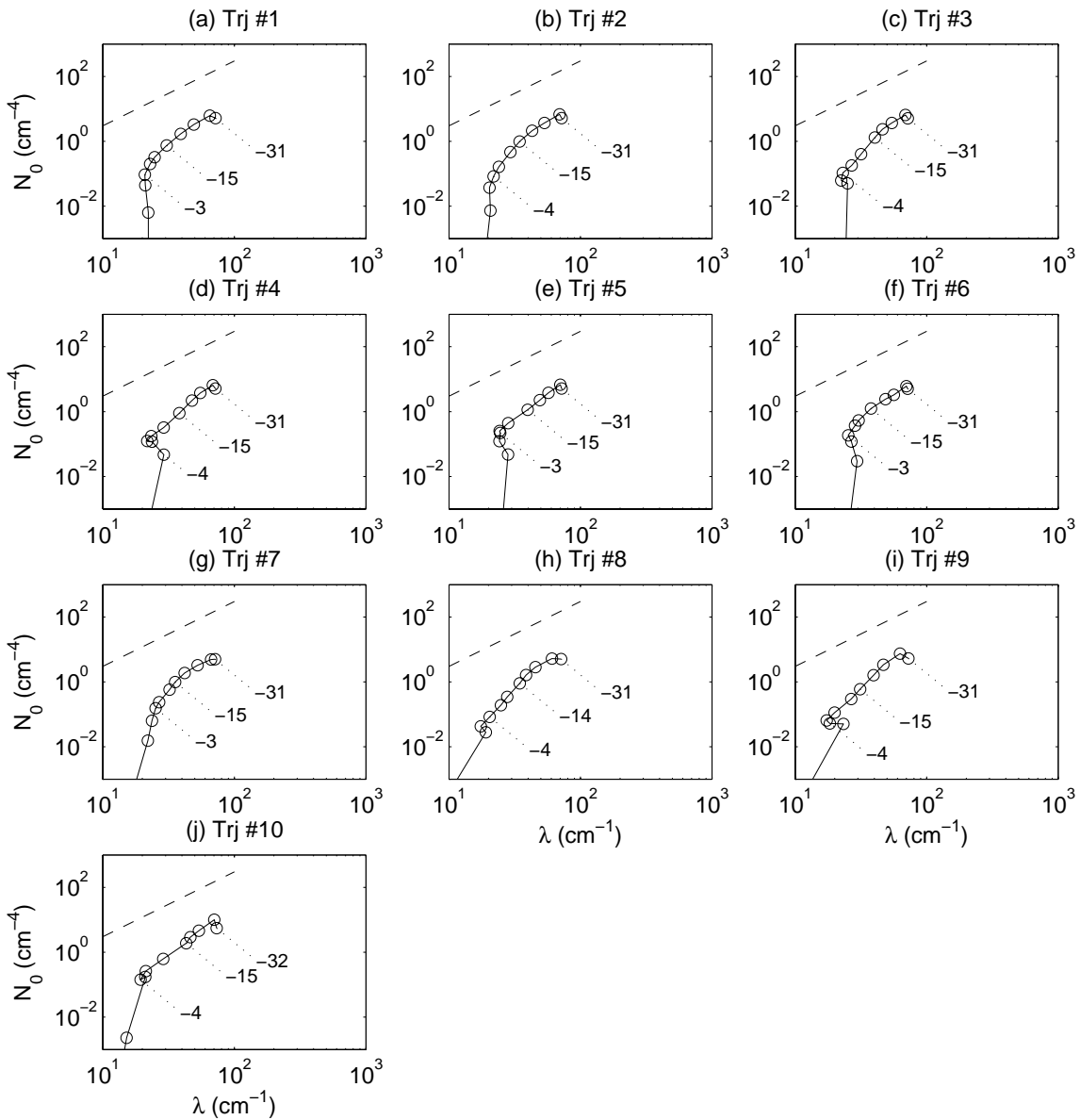


Figure 5.37 N_0 vs λ for each trajectory of LD2 every 10 minutes. The number in the plot indicates the temperature in Celsius. The trajectory numbers are given from left to right in Figure 5.35. The dashed line indicate gradient of 2.

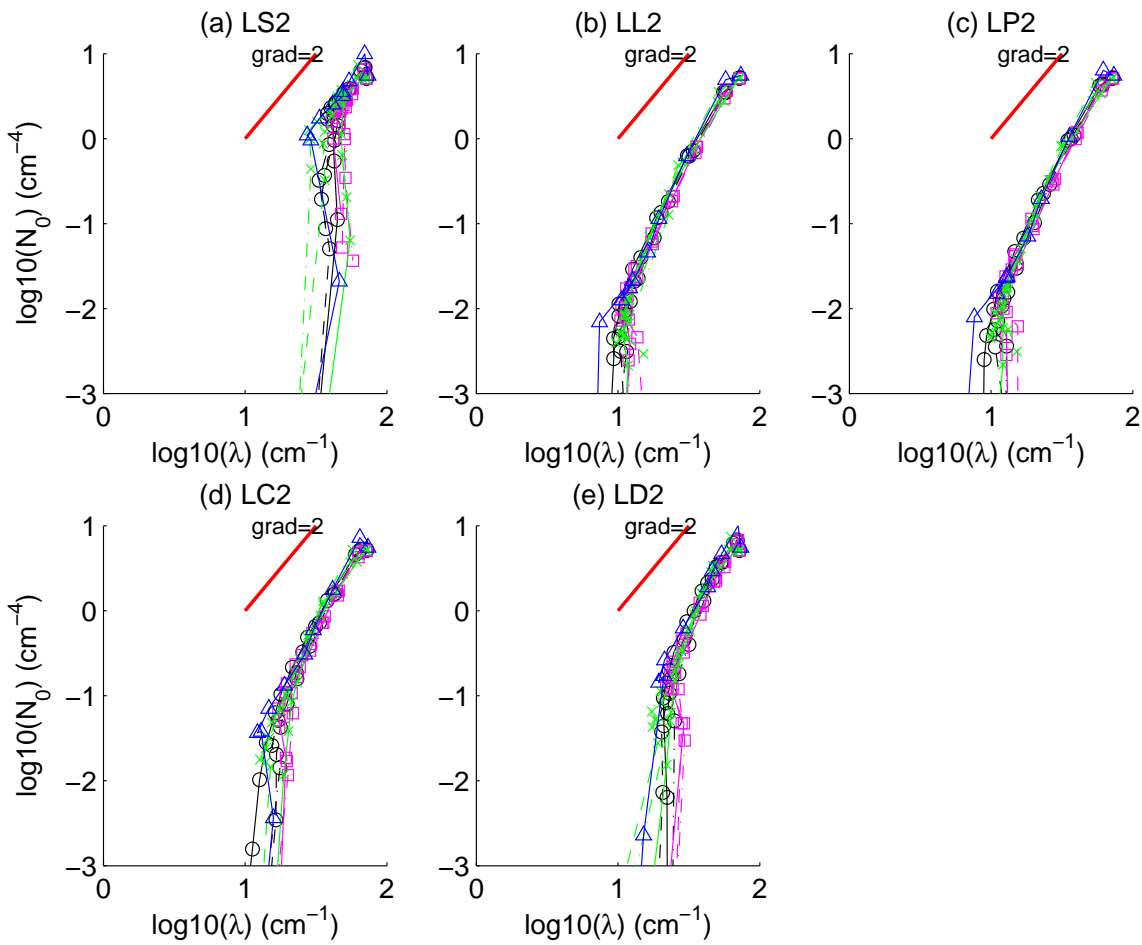


Figure 5.38 N_0 vs λ for trajectories of all simulations every 10 minutes.

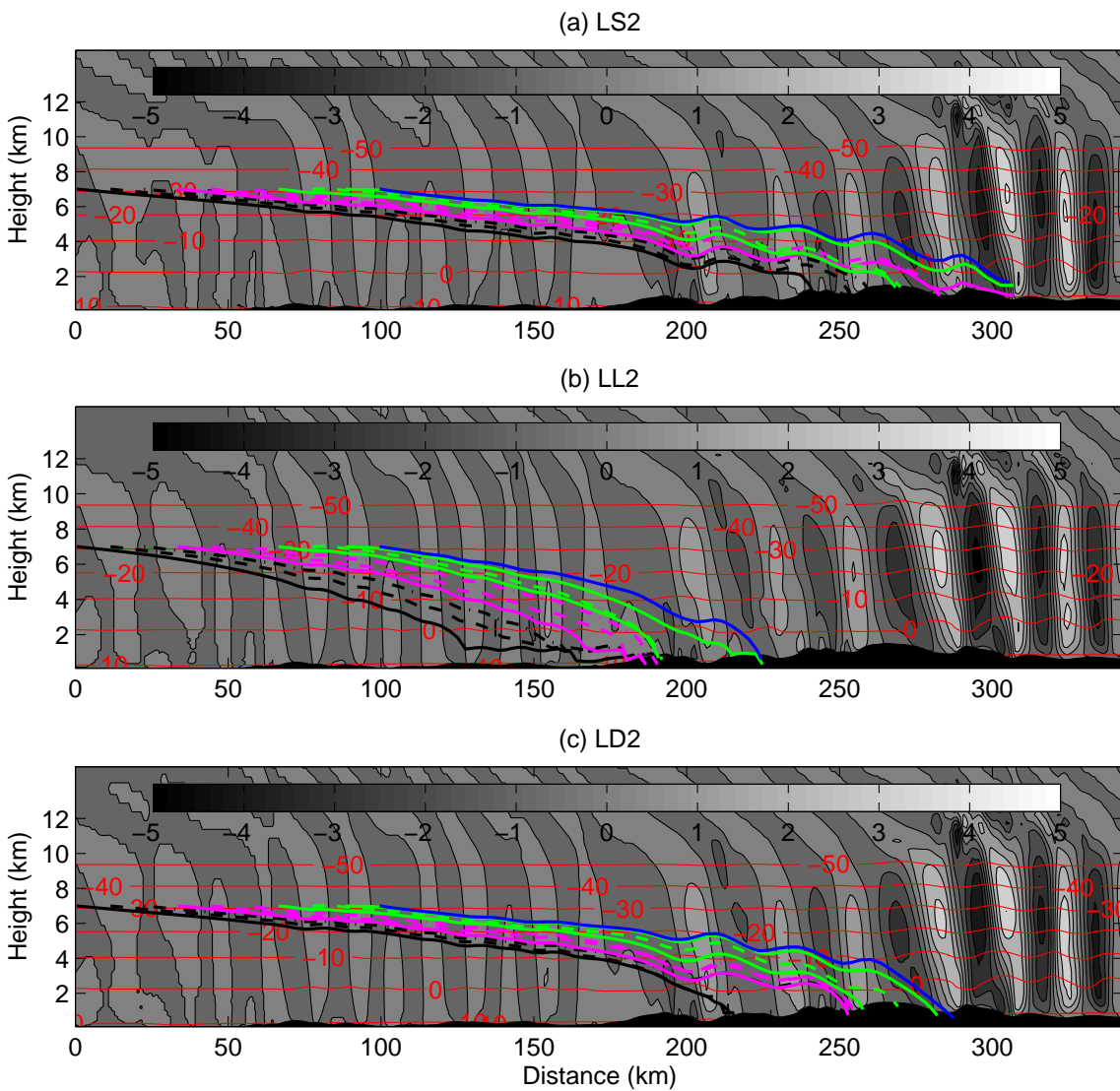


Figure 5.39 Trajectories for (a) LS2, (b) LL2, and (c) LD2 calculated by using mass-weighted terminal velocity. The vertical motion at two hours is depicted in the background.

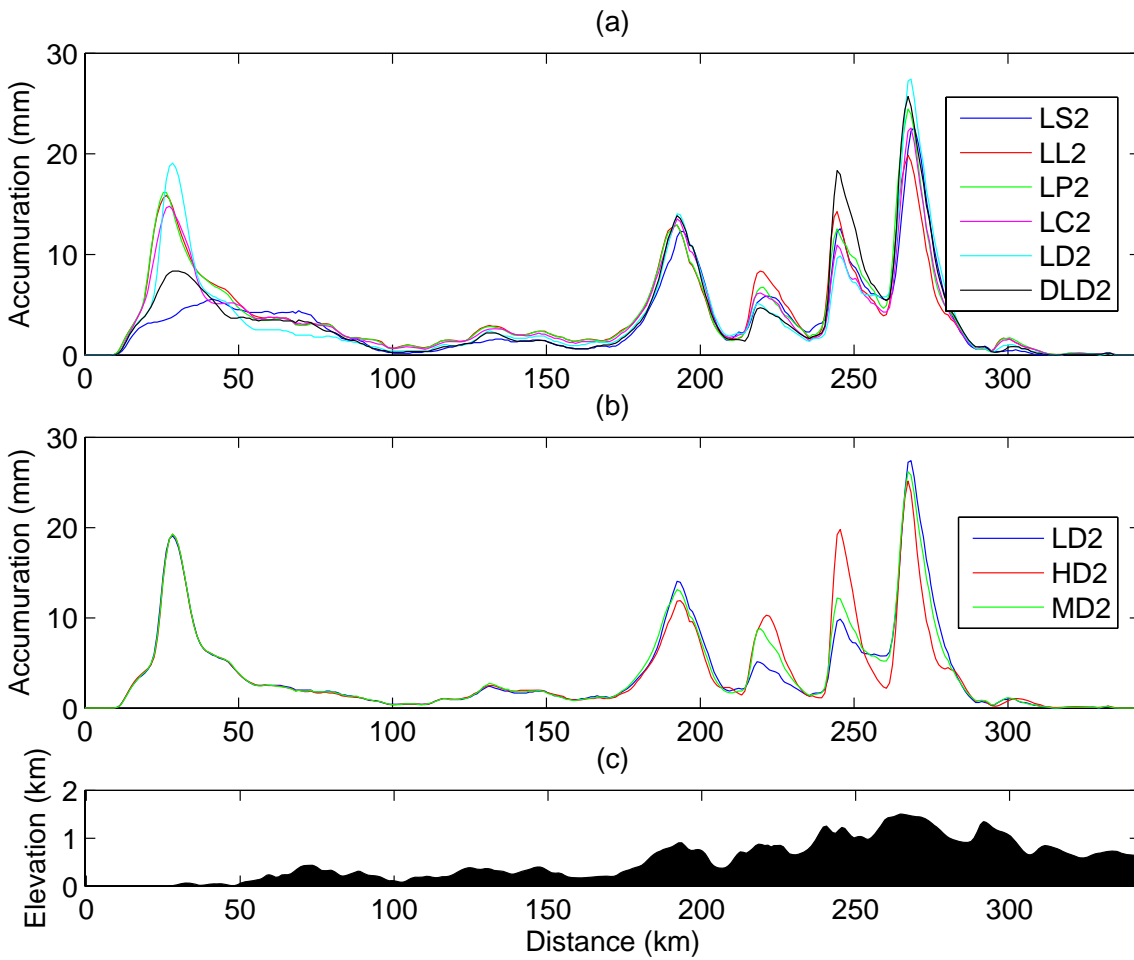


Figure 5.40 Comparison of 6 hour accumulation over the domain.

Table 5.1 Experiment design.

Experiment name	IN concentration (L^{-1})	Aggregation efficiency model	Microphysical processes	Initialization	Ice crystal habit prediction
LL1	1	0.1	No riming	No ice	On
ML1	10	0.1	No riming	No ice	On
HL1	230	0.1	No riming	No ice	On
LD1	1	Model D	No riming	No ice	On
MD1	10	Model D	No riming	No ice	On
HD1	230	Model D	No riming	No ice	On
PCH	230	Model D	All	No ice	On
PCHH	230	Model D	All	No ice	On
PCL	1	Model D	All	No ice	On
PCLH	1	Model D	All	No ice	On
PCH-HCCN	230	Model D	All	No ice	On
LL2	1	0.1	All	Ice	On
LH2	1	1.0	All	Ice	On
LP2	1	Model P	All	Ice	On
LC2	1	Model C	All	Ice	On
LD2	1	Model D	All	Ice	On
MD2	10	Model D	All	Ice	On
HD2	230	Model D	All	Ice	On
DLD2	1	Model D	All	Ice	Off

Table 5.2 Moments of average particle size distribution and concentration frequency of habits for 5 temperature ranges. Concentration (Con), mean maximum dimension (M D) and standard deviation of maximum dimension (SD D) are given in L^{-1} , mm, and mm, respectively. P denotes plates, D dendrites, C columnar crystals, CP columnar polycrystals, PP planar polycrystals, and IP irregular polycrystals. The frequency is in percentage (%). Note all types of ice particles are included in the analysis.

	Con	M D	SD D	P	D	C	CP	PP	IP	
T<-40	PCH	250	0.080	0.111	0	0	29	13	2	56
	PCHH	227	0.105	0.179	1	0	87	2	0	10
	PCL	187	0.051	0.119	1	0	3	32	4	60
	PCLH	168	0.070	0.148	1	0	82	6	0	11
	PCH-HCCN	3632	0.019	0.069	0	0	53	9	2	37
-40<T<-30	PCH	493	0.052	0.155	1	0	5	0	16	78
	PCHH	468	0.055	0.156	5	0	43	0	2	50
	PCL	479	0.041	0.173	0	0	3	0	21	76
	PCLH	360	0.063	0.380	6	0	51	0	2	42
	PCH-HCCN	3410	0.019	0.088	0	0	57	0	8	35
-30<T<-20	PCH	161	0.109	0.288	1	0	1	0	7	91
	PCHH	163	0.104	0.290	17	0	8	0	0	75
	PCL	66	0.109	0.610	0	0	1	0	20	78
	PCLH	44	0.185	1.143	27	2	47	0	0	24
	PCH-HCCN	243	0.088	0.255	1	0	7	0	8	84
-20<T<-10	PCH	51	0.189	0.341	57	17	0	0	0	25
	PCHH	54	0.190	0.228	62	15	0	0	0	22
	PCL	3	0.469	0.768	16	8	1	0	7	68
	PCLH	4	0.435	0.889	35	30	15	0	0	21
	PCH-HCCN	59	0.182	0.162	56	17	0	0	0	27
-10<T	PCH	21	0.354	0.893	26	46	27	0	0	0
	PCHH	20	0.353	0.842	27	43	29	0	0	0
	PCL	2	0.464	0.628	19	21	48	0	1	11
	PCLH	2	0.413	0.400	18	38	39	0	0	5
	PCH-HCCN	24	0.304	0.520	32	43	25	0	0	0

Table 5.3 Mass content and mass content frequency of types for 5 temperature ranges in the entire domain. Mass content (MC) is given in mg m^{-3} . PC denotes pristine crystals, RC rimed crystals, AG aggregates, RA rimed aggregates, GR graupels. The frequency is in percentage (%).

	MC	PC	RC	AG	RA	GR	
T<-40	PCH	5	77	0	23	0	0
	PCHH	5	96	0	4	0	0
	PCL	3	64	0	36	0	0
	PCLH	4	63	0	37	0	0
	PCH-HCCN	8	73	0	27	0	0
-40<T<-30	PCH	18	81	0	19	0	0
	PCHH	18	92	0	8	0	0
	PCL	12	66	0	32	1	0
	PCLH	12	65	0	31	3	0
	PCH-HCCN	26	75	0	22	2	0
-30<T<-20	PCH	32	86	0	11	1	1
	PCHH	31	89	0	10	1	0
	PCL	16	68	0	22	7	3
	PCLH	15	67	0	14	13	5
	PCH-HCCN	44	84	0	6	6	3
-20<T<-10	PCH	40	61	0	37	2	1
	PCHH	40	61	0	38	1	0
	PCL	21	52	3	23	13	9
	PCLH	19	61	4	17	10	8
	PCH-HCCN	47	68	0	28	1	3
-10<T	PCH	64	11	0	42	24	24
	PCHH	62	11	0	44	23	22
	PCL	23	20	4	8	15	54
	PCLH	24	20	5	8	15	52
	PCH-HCCN	69	15	0	48	18	19

Table 5.4 Budget of concentration tendency for 8 layers at 10 minutes of simulation for LD2 in section I. The unit is $\text{m}^{-3}\text{s}^{-1}$. Concentration flux 1 (2) is located at the top (lower) boundary of a layer and were normalized by the volume of the layer.

Layer	Micro Tend	Con Flux 1	Con Flux 2	Conv. C. F.	Total Tend
9 < z	-6.3E+00	0.0E+00	-3.1E+00	-3.1E+00	-9.4E+00
8 < z < 9	-7.9E+00	-6.6E+00	-1.4E+01	-7.2E+00	-1.5E+01
7 < z < 8	-1.1E+01	-1.4E+01	-2.6E+01	-1.3E+01	-2.4E+01
6 < z < 7	-6.5E+00	-2.6E+01	-2.1E+01	5.6E+00	-9.1E-01
5 < z < 6	-2.0E+01	-2.3E+01	-1.2E+01	1.1E+01	-9.1E+00
4 < z < 5	-4.9E+01	-1.1E+01	-1.4E+01	-3.5E+00	-5.3E+01
3 < z < 4	-5.1E+01	-1.4E+01	-8.1E+00	6.2E+00	-4.5E+01
2 < z < 3	-1.4E+01	-7.7E+00	-5.8E+00	2.0E+00	-1.2E+01
Layer	Vap	Agg	Breakup	Melt Shed	Dep Nuc
9 < z	-7.1E+00	-2.8E-03	0.0E+00	0.0E+00	8.1E-01
8 < z < 9	-8.7E+00	-5.2E-02	0.0E+00	0.0E+00	8.8E-01
7 < z < 8	-7.4E+00	-4.0E+00	1.2E-03	0.0E+00	4.6E-01
6 < z < 7	-8.2E-01	-6.1E+00	8.2E-04	0.0E+00	4.2E-01
5 < z < 6	-7.9E-01	-2.1E+01	5.0E-03	0.0E+00	1.4E+00
4 < z < 5	-1.4E+00	-4.9E+01	2.6E-02	0.0E+00	8.5E-01
3 < z < 4	-3.5E-01	-5.2E+01	8.5E-01	0.0E+00	8.1E-01
2 < z < 3	-3.2E-01	-1.3E+01	2.3E-01	-1.4E+00	0.0E+00
Layer	Cont Nuc	Imm Nuc			
9 < z	0.0E+00	0.0E+00			
8 < z < 9	0.0E+00	0.0E+00			
7 < z < 8	0.0E+00	0.0E+00			
6 < z < 7	0.0E+00	0.0E+00			
5 < z < 6	0.0E+00	0.0E+00			
4 < z < 5	0.0E+00	0.0E+00			
3 < z < 4	7.0E-06	0.0E+00			
2 < z < 3	1.6E-04	0.0E+00			

Table 5.5 Fitted parameters of exponential distributions in section $0 < y < 290$ km. The parameters for all but LS2 are obtained at 10 minutes of simulation; the parameters for LS2 are at 20 minutes.

λ	LS2*	LL2	LP2	LC2	LD2
$9 < z$	68.14	207.26	188.12	170.32	198.58
$8 < z < 9$	154.39	275.15	266.03	240.29	279.37
$7 < z < 8$	199.40	171.47	176.27	177.94	174.05
$6 < z < 7$	31.70	32.46	38.85	50.87	42.31
$5 < z < 6$	25.59	13.87	15.20	23.35	29.68
$4 < z < 5$	32.00	7.30	7.49	11.78	12.47
$3 < z < 4$	19.75	3.27	3.31	4.93	5.10
$2 < z < 3$	9.32	2.92	2.94	4.00	6.85
N_0	LS2*	LL2	LP2	LC2	LD2
$9 < z$	4.239	22.901	20.944	16.906	21.961
$8 < z < 9$	45.168	127.797	122.626	104.018	131.213
$7 < z < 8$	75.892	51.029	57.319	59.400	59.222
$6 < z < 7$	1.818	1.254	1.969	3.889	3.330
$5 < z < 6$	1.060	0.201	0.263	0.755	1.509
$4 < z < 5$	2.028	0.060	0.065	0.228	0.228
$3 < z < 4$	0.921	0.011	0.012	0.037	0.042
$2 < z < 3$	0.115	0.006	0.006	0.012	0.046

Table 5.6 Estimated gradients between the parameters of exponential distributions for 10 trajectories. The trajectories started from initial time, 2 hours, 4 hours of simulation. r is the correlation coefficient. P is the average precipitation rate (mm hr^{-1}) for 10 trajectories. $\hat{\theta}$ is estimates by Field and Heymsfield (2003)'s empirical equation. The left column indicates the simulation time when the trajectories started.

		LS2	LL2	LP2	LC2	LD2	HD2	MD2
Init	θ	2.09	3.41	3.41	3.14	3.26	2.42	3.07
	r	0.81	0.99	0.99	0.99	0.98	0.94	0.97
	P	0.23	0.22	0.22	0.22	0.20	0.20	0.20
	$\hat{\theta}$	3.55	3.57	3.58	3.56	3.60	3.61	3.60
2hr	θ	2.55	2.89	2.97	2.77	2.88	2.70	2.68
	r	0.91	0.99	0.98	0.98	0.97	0.96	0.96
	P	0.14	0.16	0.15	0.16	0.15	0.14	0.15
	$\hat{\theta}$	3.81	3.73	3.76	3.73	3.75	3.80	3.76
4hr	θ	1.77	2.85	2.92	2.76	2.62	2.71	1.97
	r	0.81	0.99	0.99	0.99	0.98	0.95	0.88
	P	0.07	0.10	0.10	0.10	0.09	0.08	0.08
	$\hat{\theta}$	4.31	4.03	4.04	4.08	4.15	4.20	4.25

Table 5.7 Domain average 6 hour accumulation.

	LS2	LL2	LP2	LC2	LD2	HD2	MD2	DLD2
Ice	0.0072	0.31	0.38	0.033	0.037	0.18	0.096	0.069
liquid	2.9	2.8	2.8	3.0	2.9	2.7	2.9	3.0
Total	2.9	3.1	3.2	3.0	2.9	2.9	3.0	3.1

Chapter 6 Conclusions and future works

6.1 Concept of SHIPS

The Spectral Habit Ice Prediction System (SHIPS) is designed to retain growth history as conserved particle characteristics that can move throughout the cloud and mix with other particles of different characteristics in a multidimensional Cloud Resolving Model. Rather than assigning ice particles to predefined categories such as cloud ice, pristine crystals or graupel, a distinguishable group of hydrometeors contained within an air parcel is defined only by concentration, mass content, and series of evolved characteristics that reflect the growth history (particle property variables, PPVs). PPVs include mass content components that are individually integrated by vapor deposition, aggregation, riming, and melting processes, length variable components that define habit of ice crystals, volume variable component and aerosol mass content components.

The mass spectrum of solid hydrometeors is divided into bins defined by mass boundaries and each bin has a subdistribution. In this study each mass bin is diagnosed as a single habit of ice crystal and a single type of ice particle based on predicted PPVs. The assumption behind is the implicit mass sorting assumption, which states that different species of solid hydrometeors within a single air parcel are naturally sorted by mass. The limitation is softened, however, by the fact that the mass-habit relationship for a bin can vary over time and between grid cells as a result of microphysical evolution and transport. It is important to note that the average habit

and type of ice particles predicted in SHIPS is not only the result of local microphysical processes, but also result of dynamical transport of ice particles in surrounding grid cells.

6.2 Importance of advection and sedimentation in habit prediction

First, nucleation and vapor deposition of hexagonal ice crystals were simulated in an idealized two dimensional setup of a Cloud Resolving Model, University of Wisconsin Nonhydrostatic Modeling System (UW-NMS). The case simulated is an orographic snow storm over the Oregon Cascade Mountain observed during the IMPROVE-2 campaign. The advection process in the Eulerian dynamics model made growth region of dendrites wider than local atmospheric condition would predict, and revealed the importance of growth conditions of dendritic arms outside of the dendritic regime. The columnar crystals with dendritic arms were diagnosed as capped columns, but the quantitative growth condition of capped columns is not investigated yet in the literature.

A sensitivity test of upper level growth mode of ice crystal habit in $T < -20^{\circ}\text{C}$ indicated that proper simulation of habit of this range of temperature is crucial in orographic storms due to possible high ice crystal concentration at the level and subsequent sedimentation into the altitude of active vapor deposition with dendritic growth mode. A simulation with columnar growth regime of hexagonal crystals defined for $-30 < T < -20^{\circ}\text{C}$ resulted in dominance of columnar crystals in lower levels, which disagrees with the aircraft observation of planar hexagonal crystals and planar polycrystals. The result cast doubt on the role of the columnar growth regime described in the past literature and the definition of a single growth mode given ambient temperature and moisture in $T < -20^{\circ}\text{C}$.

It is well known that habit frequency observed at a given level in stratiform clouds is dominated by irregular particles. It is important to reflect the frequency in the microphysical model because the habits have a large impact in the radiative transfer calculation and sedimentation as well as microphysical processes. This study proposed a framework to predict growth of polycrystals by vapor deposition in a consistent way with simulation of monocrystals based on history of ice crystals and current atmospheric conditions. The inherent growth ratio approach of Chen and Lamb (1994) for hexagonal monocrystals was extended into $T < -20^{\circ}\text{C}$. In $T < -20^{\circ}\text{C}$ during nucleation period ($D < 20\ \mu\text{m}$) crystal habits given one combination of temperature and moisture were determined using a simple stochastic approach based on the habit frequency constructed by Bailey and Hallett (2004).

During the early stage of growth, prediction of only hexagonal monocrystals with extended inherent ratio led to domination of columns in upper levels and plates in middle levels below temperature $T = -20^{\circ}\text{C}$. Prediction of polycrystals introduced the highest concentration of irregular polycrystals above $z = 4\ \text{km}$ ($T = -10^{\circ}\text{C}$), which can be expected from the frequency map given the vertical profile of supersaturation. Also, high concentrations of planar and columnar polycrystals were predicted in the region $6 < z < 8\ \text{km}$ ($-40 < T < -20^{\circ}\text{C}$) and $9 < z < 11\ \text{km}$ ($T < -50^{\circ}\text{C}$), respectively. Concentration of the plates was reduced by order of 2 in the altitudes compared to the case with only hexagonal monocrystals. Concentration of the columnar crystals remained as high as the polycrystals above $z = 8\ \text{km}$ ($T < -50^{\circ}\text{C}$). The difference in the spatial distribution of habits was found even more significant at 90 minutes of simulation due to the sedimentation and mass growth of ice crystals. It is clear that

understanding the frequency of habit formation as well as the growth rate and terminal velocity of habits in middle and upper levels are necessary to understand spatial distribution of ice crystals.

Differences of each nucleation process in spatial patterns, and concentration tendency and initial mass were discussed. The immersion (homogeneous) freezing process was found to be a key process to create planar (columnar and irregular) polycrystals due to the temperature range defined for the polycrystals, and high freezing tendency compared to other nucleation processes in $-35 < T < -20^{\circ}\text{C}$ ($T \leq -35^{\circ}\text{C}$). The freezing processes were quantitatively shown to change the conditional frequency of habits in $10 < D < 100\ \mu\text{m}$. Since concentration of CCN is generally much higher than IN, the freezing nucleation processes can affect habit frequency. Simulations with the formation of polycrystals through the freezing based on Bailey and Hallett (2004a) showed similar frequency of habits to observations in stratiform clouds, and wave and cirrus clouds.

Vapor competition and effect of moisture on habits due to concentration of ice nuclei (IN) were demonstrated. IN concentration may modulate supersaturation by changing concentration of ice crystals, and in turn may change preferable habits given the temperature. In the case study, the effect appeared in area of strong vertical motion with supercooled liquid hydrometeors. Planar and columnar polycrystals indicated higher frequency with lower concentration of IN. Also, IN concentration was able to change the habit frequency analyzed at a given altitude through vapor deposition growth rate and subsequent sedimentation.

6.3 Aggregation and riming process with explicit habit prediction

SHIPS solves the stochastic collection equation with prediction of habits and types of ice particles. Validation of the scheme was conducted in box model simulations and in simulations of an orographic snow storm with UW-NMS.

First, the scheme was assessed in box simulations. The simulations were started from only pristine ice crystals of a single habit. Considered habits included plates, dendrites, columns, planar polycrystals, columnar polycrystals, and irregular polycrystals. Simulations with unit efficiency showed that the collection kernel was largely a function of cross section area, and that having different habits can lead to a difference in collection rate by factor of 10 to 100 at a given mass. Dendrites show the fastest collection rate due to the largest cross section among habits. The stochastic collection model of SHIPS is qualitatively similar to the pure stochastic models of Maruyama and Fujiyoshi (2005) in that the cross section is more important to determine the growth rate of snowflakes than terminal velocity difference. This is the consequence of predicting density of aggregates to decrease with mass.

Three interlocking efficiency models were formed based on bulk crystal density, bulk sphere density and dendritic lengths. They changed evolution of PSD significantly due to nonlinear feedback, even though it ranged between 0 and 1. Mass-dimension, mass-terminal velocity, and diameter-density relationships predicted by SHIPS showed moderate agreement with empirical equations. The relationships were not sensitive to aggregation efficiency if only aggregation processes were considered, but sensitive to the initial PSD. With SHIPS, aggregates of the non-spherical habits grew faster than constant-density sphere aggregates. They also evolved faster than aggregate models of Maruyama and Fujiyoshi (2005) that use ice

sphere as component crystals if the same initial mass distribution was used for the simulation. Therefore, the aggregation process in SHIPS demonstrated sensitivity to efficiency models as well as mass-dimensional relationship of each habit. It was speculated that the emergence of a secondary mode in aggregation simulation may have been an artifact produced by using mean terminal velocity and diameter in the collection kernel. A hydrodynamic breakup process was introduced in order to prevent ice particles from growing unrealistically. The aggregation simulation with breakup process led to an equilibrium size distribution that was similar in terms of mass density among the different habits. The resulting relationships between particle properties remained similar to those without breakup process.

Two-dimensional idealized simulations were conducted with the cloud-resolving model, UW-NMS. As a case study, an orographic winter storm over the Oregon Cascade observed during IMPROVE-2 campaign was chosen. Simulations were run with/without initial and boundary condition of spatial distribution of ice particles. The simulations without ice particle initialization showed sensitivity of aggregation initiation to IN concentration and habit. Aggregation initiation was primarily function of concentration of ice crystals. The effect of terminal velocity difference and cross section area were secondarily important. IN concentration was found to have a significant impact on aggregation initiation. The direct effect is through production of the concentration of collector and collected particles. The indirect effect is through change of cross section area by vapor competition. High concentration of IN can lead to depletion of supercooled liquid hydrometeors which could be used for immersion freezing process and riming process. Low concentration of IN can produce large ice particles by vapor deposition, which may act as collectors in active nucleation

area. Combination of immersion freezing nucleation and advection of collector ice particles was speculated to be important for small and medium cases of IN concentration. The interlocking efficiency models were able to enhance aggregation initiation given that there was sufficient concentration of ice crystals. Formation of spatial dendrites was modeled through sedimentation of irregular polycrystals into the dendritic zone. They triggered aggregation through the modeled collection efficiency and because of the high concentration nucleated by immersion freezing above the dendritic zone. The pathway to form spatial dendrites through sedimentation into dendritic growth regime should be studied in the laboratory because the habit may play an important role in the initiation of aggregation with large planar dendrites. The trajectory analysis showed that habits and types of ice particles predicted in SHIPS can be used as marker of growth history or origin of particle to study the evolution of size distribution. From the ice nucleation process, SHIPS was able to reproduce sub-exponential distribution that consists of pristine crystals and aggregates. The slope and intercept fitted to the predicted PSDs show moderate agreement with observed ones.

The habit frequency analysis was carried out for simulations with all microphysical processes on in order to study effects of aggregation and riming on the frequency. The resulting frequency in terms of number concentration was qualitatively similar to the one obtained with only vapor deposition process except for $T > -10^{\circ}\text{C}$. In the warm temperature, faster sedimentation of aggregates of plates may have resulted in the increase of frequency of plates. The cases with small IN concentration had high frequency of columnar crystals because active riming process triggered active secondary nucleation process in the temperature. The case with high concentration of CCN shows high concentration of columnar crystals in

$T < -30^\circ \text{C}$ since nucleated polycrystals were still able to change the growth mode to columnar crystals. This suggests importance of studying the dependency of growth mode of frozen hydrometeors on the size and environmental conditions. SHIPS showed a dependence of simulated mass content of aggregates on the habits produced by freezing nucleation. The average PSDs obtained in the wave cloud section had multiple modes that were similar to typically observed. The inflection points of the PSDs were associated with change of dominant type of ice particles from pristine crystals to aggregates.

In order to represent the effects of a “seeder” cloud, simulations were initialized with a homogeneous initial distribution of ice particles. The simulation with unit efficiency showed the fastest change of concentration and maximum dimension in $z < 6$ km, while the case with lowest constant efficiency indicated the slowest change. Results of three physical-based efficiency models lay in between. Agreement of 10 to 20 minutes simulation with observations suggests that aggregation and riming processes of SHIPS may be able to predict the third and six moments of PSD and mass flux in a realistically consistent way. A budget analysis of concentration tendency showed that aggregation efficiency can in fact control the evolution of the PSD and that sedimentation of large particles has a significant effect as well. Concentration and mean maximum dimension of PSDs in the vertical layer $6 < z < 7$ km and $y < 200$ km showed quasi-steady state due to balance between these two processes. It was quantitatively shown that aggregation process produces large particles at a given level, but those particles also have faster terminal velocity, and thus the large particles may or may not contribute to the increase of concentration of large particles at the level. The breakup process became more significant in $2 < z < 4$ km than vapor deposition process, which indicates that

proper parameterization of breakup process is important. It was shown that aggregation efficiency models affect the habit frequency obtained at a given level. Thus, analysis of the conditional frequency of habits and types with PSDs should be able to provide useful information on the aggregation efficiency in stratiform clouds. SHIPS suggests that the observed increase in concentration of small particles is caused by the active nucleation above, sedimentation flux convergence of the particles, and somewhat inefficient aggregation process to remove the small particles. However, breakup processes can be another explanation for the increase because it was observed close to dendritic growth region. The lack of particles in $D < 0.1$ mm at low levels in the simulations suggest that deposition-condensational nucleation has to be more active in warm temperature regime ($T < -15^\circ\text{C}$), or that other nucleation processes are required such as secondary nucleation by collision breakup.

The stochastic collection approach to habit prediction was able to predict the relationships between intercept and slope parameters of exponential PSDs that are generally observed in deep stratiform cloud layers. All efficiency models but 0.1 efficiency case agree with an empirical dependence of the slope on temperature. It is speculated that efficiency should be at least larger than 0.1 in $T > -20^\circ\text{C}$. The predicted habit and type information are shown to be able to be used in efficiency model. Uncertainties associated with aggregation efficiency model, habit prediction, and IN concentration can modulate spatial distribution of precipitation to the same degree. The affected areas were mountainous regions with high concentration of supercooled droplets as well as the area where dendrites existed.

6.4 Remarks and future study

This study represents a major leap forward in microphysics modeling. This study developed a numerical framework (SHIPS) to predict variety of habits of ice crystals and types of ice particles explicitly in a numerical weather prediction model or cloud resolving model (CRM). The main philosophy is to retain growth history of ice particles in the Eulerian framework and predict property of ice particles based on fundamental physics. In the past, prediction of ice particles in a CRM relied on predefined categories of ice particles with fixed property over the size distribution. The categorization approach brings computational efficiency, but it is one of the most significant sources of errors that can be found in validation and application of the predicted distribution of ice particles. The SHIPS does not require such categorization and able to reduce the errors caused by categorization.

In the SHIPS the microphysical processes were formulated so that they reflect crystal habit and type of ice particles. This study proposed a framework to predict polycrystals based on habit frequency data constructed in laboratory. Aggregation and riming processes were formulated to simulate the habit dependence by solving stochastic collection equation. This approach of predicting property of ice particles raised many questions regarding to the fundamental microphysical processes that have been ignored or forgotten. With advanced computational resources and observational techniques, the fundamentals should be revisited, and studied. New knowledge should be incorporated into microphysical processes of CRMs.

Various research disciplines will potentially benefit from the SHIPS. Better representation of ice particles in cloud systems can improve radiative transfer calculation of ice

clouds and therefore remote sensing application. Radiative forcing of clouds on the climate system can be studied with realistic representation of habits and types of ice particles. By improving prediction of ice particle property, effects of cloud seeding as well as anthropogenic pollution on precipitation can be studied with smaller uncertainty in the subsequent chain of precipitation process. Data assimilation of clouds can be improved by providing physically sound relationships between radiative fields, and mass and concentration fields.

Suggestions for future research are the followings:

- Because dendrites are a key for aggregation and hence, for physical chain of precipitation process, more quantitative studies of growth condition of dendrites, capped columns and spatial dendrites must be done while varying temperature and humidity.
- Prediction of growth of the a-axis and c-axis lengths in SHIPS relies on the inherent growth rate approach by Chen and Lamb (2004). The scheme was parameterized to match observations under fixed temperature ($T > -30^{\circ}\text{C}$) and moisture conditions. However, its validity in varying environmental conditions has not been proved. It has to be verified quantitatively in a laboratory setting under realistic scenarios of transitioning pressure, temperature and humidity. Also, the extension of the scheme to colder temperature is necessary.
- In order to improve simulation and diagnosis of polycrystals, it is necessary to construct a database in laboratory experiments that provides relationships between characteristic physical parameters and habits as well as the growth rate along the

characteristic parameters. Having the same parameters in model simulation and in measurements would facilitate the comparison.

- This study has developed the habit-dependent aggregation process with use of stochastic collection equation. Even though the predicted relationships between mass, terminal velocity, and maximum dimension showed moderate agreement with observations, no observation of evolution of PSDs is available for specific habits. One way to validate the SHIPS is to use a pure stochastic approach with the real shape of ice crystals used as components of aggregates. However, before it can be implemented, flow field around ice crystals, and collision and coalescence efficiency have to be obtained.
- In SHIPS the aspect ratio and porosity of aggregates, rimed aggregates, and graupels were parameterized based on educational guess. These can change the terminal velocity of ice particles and in turn evolution of PSDs. Thus, observations should be implemented to validate the parameterization.
- Typically, observed PSDs have two modes in cirrus clouds, orographic wave clouds or stratiform clouds. Some of the above experiments exhibited such multi-modal PSDs. Cloud-resolving simulations with finer resolution and SHIPS could help understand the mechanism to form such modes quantitatively as well as observed habit frequency.
- The immersion and homogeneous freezing nucleation processes produced much higher concentration and larger size of ice crystals than other nucleation processes. The assumption of nucleated habit by the freezing processes affected aggregation

production, and it can modulate the radiative heating rate. Therefore, the habits nucleated from the freezing process and any dependence on nucleation processes should be investigated in a laboratory setting.

- An important assumption of SHIPS is the implicit mass sorting which states that ice particles are sorted by mass over particle mass distribution. Based on the assumption, this study further simplifies the mass distribution by diagnosing a single bin as a single habit and type of ice particle. Variation of ice particle property at a given mass has been observed and it has been theoretically proved to enhance aggregation process. Therefore, the variation of property of ice particles in a bin should be investigated and incorporated to SHIPS if necessary.
- One of the most important missing physics in the model is the collision breakup of ice particles. Even though observations show that some habits of crystals and particles are fragile, the fragmentation distribution, and probability of breakup for ice particles have not been investigated in laboratory due to the difficulty of simulating the reality. Another thing that comes with the breakup is coalescence efficiency. These fundamentals should be studied in laboratory experiments.
- It is necessary to understand the quantitative conditions required to initiate aggregation process because the aggregation is a key process in the physical chain of events leading to precipitation. The relationships between ice nuclei concentration, precipitation rate and habit through vapor deposition and aggregation processes can be studied efficiently using a box model setup.

- Evolution of the PSDs by riming process is another important issue especially in convective cloud systems. More tests of SHIPS are necessary for riming process against observation.
- Once the prediction of microphysical processes by SHIPS is validated satisfactorily, SHIPS can be used to train a new habit-dependent bulk microphysical parameterization. The parameterization would reduce the computational cost and could be used in operational forecasts.

References, Chapter 6

- Bailey, M. and J. Hallett, 2004: Growth rates and habits of ice crystals between -20° and -70° C. *J. Atmos. Sci.*, 61, 514–543.
- Chen, J.-P., and D. Lamb, 1994: The theoretical basis for the parameterization of ice crystal habits: Growth by vapor deposition. *J. Atmos. Sci.*, 51, 1206–1221.
- Maruyama, K. and Y. Fujiyoshi, 2005: Monte Carlo simulation of the formation of snowflakes. *J. Atmos. Sci.*, 62, 1529–1544.